

INFLUENCE OF ORGANIC AND INORGANIC PASSIVATION ON THE PHOTOPHYSICS  
OF CADMIUM CHALCOGENIDE AND LEAD CHALCOGENIDE QUANTUM DOTS

A Dissertation  
Submitted to the Graduate Faculty  
of the  
North Dakota State University  
of Agriculture and Applied Science

By

Levi Aaron Lystrom

In Partial Fulfillment of the Requirements  
for the Degree of  
DOCTOR OF PHILOSOPHY

Major Department:  
Chemistry and Biochemistry

May 2020

Fargo, North Dakota

North Dakota State University  
Graduate School

---

**Title**

INFLUENCE OF ORGANIC AND INORGANIC PASSIVATION ON  
THE PHOTOPHYSICS OF CADMIUM CHALCOGENIDE AND LEAD  
CHALCOGENIDE QUANTUM DOT

---

**By**

Levi Aaron Lystrom

---

The Supervisory Committee certifies that this *disquisition* complies with North Dakota  
State University's regulations and meets the accepted standards for the degree of

**DOCTOR OF PHILOSOPHY**

SUPERVISORY COMMITTEE:

Dr. Svetlana V. Kilina

---

Chair

Dr. Dmitri S. Kilin

---

Dr. Wenfang Sun

---

Dr. Erik K. Hobbie

---

Approved:

7/10/2020

---

Date

Dr. Gregory Cook

---

Department Chair

## ABSTRACT

Quantum dots (QDs) are promising materials for photovoltaic (PV) and light-emitting diode (LED) applications due to their unique properties: photostability, size-tunable absorptivity, and narrow line-width emission. These properties are tailored by surface passivations by ligands. However, ligands used in the synthesis of colloidal QDs need to be exchanged with ligands designed for specific applications. The mechanism behind ligand exchange is not well understood. Density functional theory (DFT) is utilized to gain fundamental understanding of ligand exchange (LE) and the resulting effect on the photophysics of QDs. Experimental studies show that phenyldithiocarbamates (PTCs) derivatives can improve the photocurrent of QD-based PVs. Our calculations show that the PTC undergoes decomposition on the CdSe QD surface. Decomposed products of PTCs strongly interact with the surface of QDs, which could cause unforeseen challenges during the implementation of these functionalized QDs in PVs. Secondly, we studied the mechanism of photoluminescence (PL) enhancement by hydride treatment. In experiments, the PL increases by 55 times, but the mechanism is unclear. We found that hydride can interact with surface  $\text{Se}^{2-}$  producing  $\text{H}_2\text{Se}$  gas and passivate surface  $\text{Cd}^{2+}$ . These interactions result in optically active QDs. Thiol derivatives can also improve PL when LE results in low surface coverage of thiols. The PL is quenched if LE is performed at high concentrations and acidic environments. DFT simulations reveal three scenarios for the thiol interacts with QDs: coordination of thiol, networking between surface and/or other ligands, or thiolate formation. It is the last scenario that was found to be responsible for PL quenching. Lastly, PbS(e)/CdS(e) core/shell QDs are investigated to obtain relaxation rates of electron and hole cooling via interactions with phonons. The band structure of the core/shell QDs facilitates carrier multiplication (CM), a process that generates multiple charge carrier pairs per one absorbed

photon. It is thought that CM is facilitated because there are interface associated states that reduce carrier cooling. Non-Adiabatic Molecular Dynamics (NAMD) simulations show that this hypothesis is correct and PbSe/CdSe carrier cooling is about two times slower compared to PbS/CdS due to weaker coupling to optical phonons.

## ACKNOWLEDGEMENTS

I have met many talented research scientists during the time I have attended North Dakota State University (NDSU), I would foremost want to thank my research advisor Dr. Svetlana V. Kilina. She has taught me that a true researcher always asks questions regardless if they are related to the research they are performing. From these questions, I have seen strong collaboration develop that has made me a more well-rounded researcher.

In addition to Dr. Svetlana V. Kilina, I would like to thank my Graduate Supervisory Committee members for their support and advice throughout my graduate career: Dr. Dmitri Kilin, Dr. Wenfang Sun, and Dr. Erik K. Hobbie. I would especially like to thank Dr. Dmitri Kilin, for the time he invested in teaching me theoretical and practical aspects of density functional theory.

I would also like to thank Dr. Wenfang Sun and her research group for the phenomenal research collaboration that was developed during my time at NDSU. I would like to also thank my other collaborators: Dr. Andrea Munro, Dr. Bingqing Liu, Dr. Sergei Tretiak, Dr. Tammie Nelson, Dr. Benjamin Nebgen, Dr. Brendan Gifford, and Dr. Andrew Sifain. Without these collaborators, my impact on the scientific community would be a fraction of what it is.

The current and former Kilina and Kilin group members have a massive influence over the research I currently am, I would like to thank: Dr. Brendan Gifford for his mentorship and pushing me to learn programming, Mohammed Javed for being a sounding board, Dr. Naveen Dandu for his mentorship in computationally simulating CdSe quantum dots, Dr. Dayton Vogel for being a friend and colleague, Aaron Forde, David Graupner, Dr. Patrick Tamukong, Braden Weight, Dr. Peng Cui, Alyssa Roberts, and Rebecca Tomann.

I thank all Chemistry and Biochemistry Graduate Student Association officers for their hard work. Special thanks to Jasmin for helping organize the Lunch of Learning and being a sounding board.

A special thanks for Mrs. Duncan the most supportive teacher I have had the opportunity to learn from. The hope of one day sitting in her chair has pushed me to do great things!

Finally, I would thank my family, without their support I would not have been able to complete graduate school.

**DEDICATION**

My loving Parents and Family

## TABLE OF CONTENTS

ABSTRACT.....	iii
ACKNOWLEDGEMENTS.....	v
DEDICATION.....	vii
LIST OF TABLES.....	xii
LIST OF FIGURES.....	xiv
LIST OF ABBREVIATIONS.....	xxii
LIST OF SYMBOLS.....	xxvii
1. INTRODUCTION.....	1
1.1. Quantum Dots Physical and Chemical Properties.....	1
1.2. Synthetic Methods for II-VI and IV-VI Quantum Dots.....	4
1.2.1. Colloidal QDs.....	4
1.2.2. Colloidal Heterogenous QDs.....	6
1.3. Application of II-IV Quantum Dots in LEDs and PV Devices.....	8
1.3.1. QD based LEDs.....	9
1.3.2. QD based PV.....	10
1.4. References.....	10
2. “DARK SIDE” OF QUANTUM DOTS.....	15
2.1. Surface Passivation of Dangling Bond – “Double-Edged Sword”.....	15
2.2. Surface Passivation by Organic Ligands.....	16
2.2.1. Neutral Ligands.....	17
2.2.2. Ionic Ligand.....	17
2.3. Inorganic Surface Passivation.....	19
2.3.1. X-Type Ligand Exchange – Reactive Ions.....	19
2.3.2. Benefits of Core/Shell QDs for PV and LED Applications.....	19



2.4. Open Research Questions.....	21
2.5. References .....	23
3. COMPUTATIONAL METHODOLOGY .....	27
3.1. Model Systems to Computationally Investigate Complex Systems.....	27
3.2. Computational Methods for Investigating Optoelectronic Properties of QDs.....	27
3.2.1. Density Functional Theory (DFT).....	27
3.2.2. Basis Set .....	31
3.2.3. Excited State Methods.....	32
3.3. Methods and Model Systems Utilized .....	37
3.3.1. Experimental and Theoretical Model of “Magic-Size” Cadmium Chalcogenide .....	37
3.3.2. Theoretical Model for Cadmium Selenide/Cadmium Sulfide Core/Shell QDs .....	40
3.3.3. Experimental and Theoretical Model for PbX/CdX, X = S or Se, Core/Shell QDs.....	41
3.3.4. Methodology Employed for Ground State Optimization and Absorption .....	42
3.3.5. Methodology Employed for Charge Carrier Cooling.....	44
3.4. References .....	47
4. DECOMPOSITION OF PHENYLDITHIOCARBAMATE LIGANDS DURING LIGAND EXCHANGE .....	51
4.1. Motivation .....	52
4.2. Results and Discussion.....	54
4.2.1. Binding Modes of DMPTC to CdSe QDs .....	55
4.3. Influence of Neighboring Ligands on $B_e$ of $VTC^-$ .....	58
4.3.1. Charged $VTC^-$ Neighboring Ligands.....	58
4.3.2. Neutral and Charged Neighboring Ligands.....	59
4.4. Comparing $B_e$ of DMPTC, $DMPTC^-$ and the Decomposition Products .....	60
4.5. Solvent Effects on Binding of DMPTC and $DMPTC^-$ .....	62

4.6. Conclusions .....	63
4.7. References .....	64
<b>5. DFT INSIGHTS INTO BRIGHTENING OF II-VI QUANTUM DOTS BY HYDRIDRIDE TREATMENT .....</b>	<b>67</b>
5.1. Introduction .....	67
5.1.1. Hypothetical Mechanisms of PL Enhancement .....	69
5.2. Results and Discussion.....	70
5.2.1. H <sup>-</sup> Treatment of Stoichiometric QDs.....	70
5.2.2. H <sup>-</sup> Treatment of Non-Stoichiometric QDs .....	83
5.3. Conclusions .....	96
5.4. References .....	97
<b>6. INFLUENCE OF SURFACE THIOL/THIOLATE PASSIVATION ON THE PHOTOPHYSICS OF CDS QUANTUM DOTS .....</b>	<b>99</b>
6.1. Introduction .....	99
6.2. Results and Discussion.....	102
6.2.1. Surface Passivation by a Single Thiol Derivative .....	102
6.2.2. Fully Passivated CdS QDs by HSR and SR <sup>-</sup> /H <sup>+</sup> Ligand .....	111
6.3. Conclusions .....	114
6.4. References .....	115
<b>7. PHONON-DRIVEN ENERGY RELAXATION IN PBS/CDS AND PBSE/CDSE CORE/SHELL QUANTUM DOTS .....</b>	<b>117</b>
7.1. Introduction .....	117
7.2. Result and Discussion .....	119
7.2.1. Ground State Properties.....	119
7.2.2. Thermalization.....	121
7.2.3. Excited State Properties.....	122

7.2.4. NAMD Simulation of Charge Carrier Cooling .....	126
7.3. Conclusion.....	142
7.4. References .....	144
8. CONCLUSION.....	148
8.1. References .....	150

## LIST OF TABLES

<u>Table</u>	<u>Page</u>
1.1. Bohr exciton radius and bandgap for common semiconductors. The semiconductors are listed in decreased Bohr Exciton Radius, modified from Quantum Dots Solar Cells with permission. <sup>11</sup> .....	3
4.1. Binding of VTC <sup>-</sup> to various CdSe QDs surrounded by charged and neutral ligands. Adapted with permission from <sup>22</sup> Copyright 2016 American Chemical Society. ....	60
5.1. Bond lengths, binding energy and RMSD for the three possible binding sites on 2 coordinated Se <sup>2-</sup> , 2 and 3 coordinated Cd <sup>2+</sup> for hydride passivation on Layer A. The RMSD reference geometry is A <sub>1</sub> where A <sub>2</sub> and A <sub>3</sub> are rotated to superimpose over A <sub>1</sub> the values are only QD atoms and ligands without the hydrogens.....	73
5.2. Natural transition orbitals (NTOs) comparing A <sub>1</sub> post-treatment with the Se-H fragment near and far. The NTOs for S <sub>1</sub> and S <sub>2</sub> are plotted with the next two most optically active transitions. ....	75
5.3. NTOs for S <sub>1</sub> transitions plotted in Figure 5.5. surface Se <sup>2-</sup> treatment by H <sup>-</sup> .....	79
5.4. Structure and structural parameters for H <sup>-</sup> reacting with surface Se <sup>2-</sup> on layers A-D.....	80
5.5. NTOs for S <sub>1</sub> transitions plotted in Figure 5.6. surface Cd <sup>2+</sup> treatment by H <sup>-</sup> . ....	83
5.6. NTOs for S <sub>1</sub> transitions plotted in Figure 5.8. surface Se <sup>2-</sup> treatment by two H <sup>-</sup> resulting in neutral QD and H <sub>2</sub> Se. ....	86
5.7. Structural parameters for Cd <sub>33</sub> Se <sub>34</sub> treated by 2 H <sup>-</sup> resulting in neutral QD and H <sub>2</sub> Se.....	86
5.8. NTOs for S <sub>1</sub> transitions plotted in Figure 5.10. surface treatment of Cd <sub>34</sub> Se <sub>33</sub> by H <sup>-</sup> on layer B <sub>1</sub> . ....	89
5.9. NTOs for S <sub>1</sub> transitions plotted in Figure 5.14. surface treatment of Cd <sub>37</sub> Se <sub>33</sub> by H <sup>-</sup> . ....	92
5.10. NTOs for S <sub>1</sub> transitions plotted in Figure 5.14. surface treatment of Cd <sub>37</sub> Se <sub>33</sub> by H <sup>-</sup> . ....	95
6.1. NTOs for S <sub>1</sub> for the QDs with HSR and SR <sup>-</sup> /H <sup>+</sup> initial passivation from Figure 6.6. ....	110
6.2. The instances of HSR, SR <sup>-</sup> /H <sup>+</sup> , N <sub>S</sub> , and N <sub>L</sub> on the surface of CdS QDs fully passivated by thiol derivates based (HSR, and SR <sup>-</sup> /H <sup>+</sup> ) on the bond lengths between sulfurs (ligand and QD's surface) to the H <sup>+</sup> . ....	112
6.3. NTOs for S <sub>1</sub> for QDs initially passivated by HSR and SR <sup>-</sup> /H <sup>+</sup> . The black (red) vertical lines in Figure 6.7 are characterized by NTOs with the name of HSR (SE <sup>-</sup> /H <sup>+</sup> ). ....	113

7.1. Ensemble average of the Non-Adiabatic Coupling Terms (NACTs) and the excited state lifetimes. The average initial NACTs for nearest neighbors (NN), second nearest neighbors (SNN) and average coupling over the entire range for all simulations. The lifetime of the excited states were found by a four-state irreversible kinetic model ( $\tau_{KM}$ ) and single exponential fitting ( $\tau_{SE}$ ).....	128
7.2. Relaxation rates obtained from four-state kinetic model and single exponential fitting. The fitting to the four-state kinetic model shows that relaxation in the PbS/CdS QD is faster than in the PbSe/CdSe QD. The lifetimes found by the single exponential qualitatively agrees with the four-state kinetic model except for hole relaxation at the initial excitation of $1.6 \times E_g$ with hot electrons. This discrepancy is rationalized by the fact that initial conditions for these simulations have the hole populated very close to the frontier MOs, which results in the initial and the final states being almost the same leading to nearly flat ensemble average energy for the hole. ....	137

## LIST OF FIGURES

<u>Figure</u>	<u>Page</u>
3.1. Jacob’s Ladder. The simplistic functional dependency is shown on the left and type of functional on right going from the Hartree world to heaven of chemical accuracy, here the density is represented at $n$ where we refer to the density as $\rho$ . This figure was reprinted with permission. <sup>12</sup> .....	30
3.2. Flow-chart of the FSSH method for NAMD. a) steps to obtain ensemble average of the observable of interest b) splitting the GS BOA MD trajectory into multiple trajectories for the NAMD code, where the horizontal arrows indicate time-steps included for each trajectory of NAMD. The vertical lines show the initial and final timesteps for NAMD trajectories.....	37
3.3. Stoichiometric (CdSe) <sub>33</sub> QDs model. a) optimized bare magic size QDs with layers A-D notations; b) optimized methylamine passivated magic size QDs; c) 2- and 3-coordinated surface Cd <sup>2+</sup> for layers A-D, with black solid lines show 2-coordinated Cd <sup>2+</sup> and grey dashed lines are 3-coordinate Cd <sup>2+</sup> ; d) the C <sub>3</sub> -axis that is perpendicular to the crystallographic layers of A-D.....	39
3.4. Schematic band structure of CdSe/CdS core/shell QDs. a) emissive CdSe core without surface trap states; b) introducing surface trap states results in non-emissive QDs; c) neglecting the CdSe core result in non-emissive QD.....	41
3.5. Ion exchange for magic size (PbSe) <sub>68</sub> creating (PbSe) <sub>16</sub> /(CdSe) <sub>52</sub> core/shell QDs. a) magic size (PbSe) <sub>68</sub> QDs cut from bulk; b) substituting surface Pb <sup>2+</sup> by Cd <sup>2+</sup> in magic size (PbSe) <sub>68</sub> QDs from bulk; c) optimized magic size (PbSe) <sub>68</sub> QD; d) optimized (PbSe) <sub>16</sub> /(CdSe) <sub>52</sub> core/shell QDs.....	42
3.6. Comparing single-particle (SP) and many-particle (MP) absorption spectrum for (PbX) <sub>16</sub> /(CdX) <sub>52</sub> , X =S or Se, core/shell QDs. The average energies of the transitions in the first peaks are shifted to the single-particle average energy and the oscillator strength is normalized by dividing all oscillator strength by the total oscillator strengths relative to the first peak. a) X = S b) X = Se.....	46
3.7. PDOS for PbS/CdS (a-c) and PbSe/CdSe (d-f) core/shell QDs.....	47
4.1. Molecular structure of TEA <sup>+</sup> -DMPTC <sup>-</sup> and its decomposition products that can be catalyzed by the QDs’ surface. ....	52
4.2. H NMR spectrum of free DMPTC and QDs after ligand exchange. a) kinetic study of the decomposition of DMPTC in chloroform and methanol b) signal after ligand exchange of oleate (green) and amine (black) synthesized QDs where the DMA peaks are denoted by blue shaded range, DMPTC, and thiram disulfide are represented by solid and dashed lines respectively. Adapted with permission from <sup>22</sup> Copyright 2016 American Chemical Society. ....	54

4.3. Binding Modes of ligands with two (a-c) and one (d) Lewis acidic atoms. a) bridging b) chelating c) monodentate d) monodentate. Adapted with permission from <sup>22</sup> Copyright 2016 American Chemical Society. ....	56
4.4. Natural bond orbitals (NBOs) of the deprotonated (a-d) and protonated (e-h) DMA and reduced ligands. Bright red (green) indicates atoms with negative (positive) charge. DMA panels a and e, VTC panels e and f, methyl panels c and g, and hydrogen panels d and h. Adapted with permission from <sup>22</sup> Copyright 2016 American Chemical Society. ....	57
4.5. Comparing $B_e$ of the protonated and deprotonated DMPTC and VTC for bridging (Br), chelating (Ct), and monodentate (Md) to bare magic size CdSe QD. Adapted with permission from <sup>22</sup> Copyright 2016 American Chemical Society. ....	57
4.6. $B_e$ of $VTC^-$ to $(CdSe)_{33}$ and $Cd_{39}Se_{33}$ QDs with 12 $VTC^-$ passivating the surface. Adapted with permission from <sup>22</sup> Copyright 2016 American Chemical Society. ....	59
4.7 Average binding energy ( $B_e$ ) of ligand present in experimental studies computation in chloroform to stoichiometric and non-stoichiometric CdSe QDs. Grey circles (red diamonds) indicate binding of a single ligand (reduced ligand VMA or VTC) to the surface of bare $(CdSe)_{33}$ , empty black diamonds indicate fully passivated structure with the reduced ligand, blue (black empty) stars indicate binding of a single ligand (full passivation) to $Cd_{34}Se_{33}$ ( $Cd_{39}Se_{33}$ ) QDs. Adapted with permission from <sup>22</sup> Copyright 2016 American Chemical Society. ....	61
4.8. Binding energies of DMPTC and $DMPTC^-$ attached to the $(CdSe)_{33}$ calculated in methanol and chloroform solvents. Adapted with permission from <sup>22</sup> Copyright 2016 American Chemical Society. ....	63
5.1. Magic size CdSe QDs utilized in this chapter. a) magic size $(CdSe)_{33}$ QD passivated by 21 methylamines labeling Layers A-D. b) magic size $(CdSe)_{33}$ QD without surface passivation demonstrating the $C_3$ -axis symmetry. c) example of $H^-$ passivation of surface $Se^{2-}$ on Layer A d) example of $H^-$ passivation of surface $Cd^{2+}$ on Layer A. ....	71
5.2. Rotating QDs by $0^\circ$ (reference geometry), $120^\circ$ , and $240^\circ$ with various surface passivation demonstrating the $C_3$ -axis of $(CdSe)_{33}$ QDs, hydrogens are omitted in the methylamine. a) 21 methylamines passivated QDs b) hydride passivating 3 coordinated $Se^{2-}$ ions c) hydride passivating 2 coordinated $Cd^{2+}$ ions d) hydride passivating 3 coordinated $Cd^{2+}$ ions. ....	72
5.3. Binding energy of $H^-$ to surface ions in Layer A. The black circles are the binding energy for 3 coordinated surface $Cd^{2+}$ , red cycles are the binding energy for 2 coordinated surface $Cd^{2+}$ , and blue circles are the binding energy for surface $Se^{2-}$ . The positive Binding energy of $H^-$ to surface $Se^{2-}$ in Layer A is likely a result of the increased bond length between the $Se^{2-}$ and neighboring $Cd^{2+}$ . ....	74

5.4. Absorption spectra for (CdSe) <sub>33</sub> QDs with a single H <sup>-</sup> passivating Layer A. a) 2 coordinated Cd <sup>2+</sup> b) 3 coordinated Cd <sup>2+</sup> c) 3 coordinated Se <sup>2-</sup> d) comparing 3 coordinated Se <sup>2-</sup> geometries Near and Far to amine passivated QDs. The Far geometry was obtained by artifactually moving the Se-H fragment from the QDs surface.....	76
5.5. Absorption spectra for pre- and post-treatment of surface Se <sup>2-</sup> with the first three transition oscillator strength plotted with vertical lines. The first state (S <sub>1</sub> ) is optically inactive for A <sub>1</sub> Far Post-treatment and is indicated by the red arrow.....	78
5.6. Absorption spectra for pre- and post-treatment of surface Cd <sup>2+</sup> with the first transition oscillator strength plotted with a vertical line. ....	82
5.7. Schematic surface enriched by a single Se <sup>2-</sup> ions of bare magic size (CdSe) <sub>33</sub> QD followed by surface passivation by 20 methylamines. a) bare magic size (CdSe) <sub>33</sub> QD b) bare Cd <sub>33</sub> Se <sub>34</sub> QD c) methylamine passivated Cd <sub>33</sub> Se <sub>34</sub> QD. ....	84
5.8. Absorption Spectra for Cd <sub>33</sub> Se <sub>34</sub> passivated by methylamine pre- and post-treatment vs. magic size (CdSe) <sub>33</sub> QDs with the first transition oscillator strength is plotted with a vertical line. The dashed (solid) lines represent the pre-treated (post-treated) QDs. a) layer A b) layer B. ....	85
5.9. Schematic surface enriched by a single Cd <sup>2+</sup> ion. This starts from bare magic size (CdSe) <sub>33</sub> QD (a), where a single Cd <sup>2+</sup> is placed on the surface (b). The Cd <sub>34</sub> Se <sub>33</sub> QD surface is then passivation by 22 methylamines (c). The fully passivated QD exchanges the methylamine on the non-stoichiometric Cd <sup>2+</sup> is exchanged for the first H <sup>-</sup> (d). The placement of the second H <sup>-</sup> has four possible binding sites: far Cd <sup>2+</sup> (e), near Cd <sup>2+</sup> (f), near Se <sup>2-</sup> (g), and far Se <sup>2-</sup> (h). ....	87
5.10. Absorption Spectra for Cd <sub>34</sub> Se <sub>33</sub> with pre- (22 methylamine) and post-treatment (21 methylamine and H <sup>-</sup> ) on layer B <sub>1</sub> with the first transition oscillator strength plotted with vertical lines. The first transitions (S <sub>1</sub> ) for the pre-treated systems are indicated by the arrow. a) the second H <sup>-</sup> was place far from the enriched Cd-H fragment b) the second H <sup>-</sup> was place near the enriched Cd-H fragment.....	88
5.11. Schematic surface enriched by a four Se <sup>2-</sup> ions. This starts from bare magic size (CdSe) <sub>33</sub> QD (a), where a four Se <sup>2-</sup> are places on the surface (b). The Cd <sub>33</sub> Se <sub>37</sub> QD surface is then passivation by 17 methylamines (c). Then four H <sup>-</sup> react with the non-stoichiometric Se <sup>2-</sup> (d) followed by a second reaction of four H <sup>-</sup> on the same non-stoichiometric Se <sup>2-</sup> resulting in a neutral system (e). ....	90
5.12. Absorption Spectra of Cd <sub>33</sub> Se <sub>37</sub> Se-enriched QDs pre- and during H <sup>-</sup> treatment compared to magic size (CdSe) <sub>33</sub> QD, where the oscillator strength of S <sub>1</sub> is plotted with the vertical line. ....	91



5.13. Schematic surface enriched by four $\text{Cd}^{2+}$ ions. This starts from bare magic size $(\text{CdSe})_{33}$ QD (a), where a four $\text{Cd}^{2+}$ are places on the surface (b). The $\text{Cd}_{37}\text{Se}_{33}$ QD surface is then passivation by 25 methylamines (c). The fully passivated QD exchanges the four methylamines on the non-stoichiometric $\text{Cd}^{2+}$ ions (d). The second reaction by four $\text{H}^-$ was only performed on far $\text{Cd}^{2+}$ (e) and near $\text{Cd}^{2+}$ (f) ions. ....	93
5.14. Absorption Spectra of $\text{Cd}_{37}\text{Se}_{33}$ Cd-enriched QDs pre- and during $\text{H}^-$ treatment compared to magic size $(\text{CdSe})_{33}$ QD, where the oscillator strength of $S_1$ is plotted with the vertical line. a) configuration 1 b) configuration 2 c) configuration 3.....	94
5.15. Proposed mechanism for enhancement of QY of PL by $\text{H}^-$ treatment.....	96
6.1. Model system used to study surface abstraction of the acidic proton in thiol. a) magic size $(\text{CdS})_{33}$ QD with layers A-D denoted b) single passivated $(\text{CdS})_{33}$ with thiol c) fully passivated $(\text{CdS})_{33}$ with 20 methylamines (MA) and one thiol d) fully passivated $(\text{CdS})_{33}$ with 21 thiol e) Schematic diagram illustrating the three bond lengths shown in Fig. 3. f) Interconversion between thiol and thiolate where the QDs extracts $\text{H}^+$ . ....	101
6.2. Binding energy ( $B_e$ ) of thiol derivative to QDs in propylamine (a) and acetonitrile (b) on layers A-D. Solid (dashed) lines represent passivation by 20 MA (bare) with a single thiol derivative, HSR (black), $\text{SR}^-$ (red), or $\text{SR}^-/\text{H}^+$ (blue) QDs. ....	104
6.3. Bond length of fully passivated (a-c) and bare (d-f) QDs with one HSR or $\text{SR}^-/\text{H}^+$ on the surface. Panels a and d bond length between the surface ( $\text{Cd}^{2+}$ ) and ligand (S), panels b and e bond lengths between the surface and ligand sulfur to $\text{H}^+$ for HSR initial passivation, panels c and f bond lengths between the surface and ligand sulfur to $\text{H}^+$ for $\text{SR}^-$ initial passivation. ....	105
6.4. Projected Density of State (PDOS) for fully passivated QDs and singly passivated of HSR (a and d), $\text{SR}^-$ (b and e), and $\text{SR}^-/\text{H}^+$ (c and f) on layer A in ACN and PAM. The PDOS for the thiol derivatives is multiplied by 3 to aid in visualization. ....	106
6.5. Projected Density of State (PDOS) for fully passivated QDs and singly passivated of HSR (a and d), $\text{SR}^-$ (b and e), and $\text{SR}^-/\text{H}^+$ (c and f) on layer C in ACN and PAM. The PDOS for the thiol derivatives is multiplied by 3 to aid in visualization. ....	107
6.6. Absorption spectra for Layer A and C with a singlet thiol derivative passivating amine and bare QDS.....	109
6.7. Absorption of QDs fully passivated by 21 HSR or $\text{SR}^-/\text{H}^+$ in PAM and ACN. The oscillator strength for $S_1$ is plotted with the vertical lines. ....	112
6.8. PDOS for QDs initially passivated by 21 HSR (a and c) and 21 $\text{SR}^-/\text{H}^+$ (b and d). Dashed black lines QD state, red lines HSR, blue $\text{SR}^-/\text{H}^+$ , black $N_S$ , and grey $N_L$ . ....	114

7.1. Electronic properties of PbX/CdX, X = S or Se, core/shell QDs at the ground state equilibrium geometry. a) atomic structure b) schematic representation c) PDOS for the core/shell QDs d) Normalized radial distribution of electronic density, average of electronic states shaded by colored regions in panel c e) Schematic representation of quasi-type II electronic structure of PbX/CdX QDs.....	120
7.2. Comparing DOS generated by PBE and HSE functionals for PbSe/CdSe core/shell QDs. This comparison was done by shifting the VB by -0.447 eV and CB by 0.242 eV to align the band edges between PBE and HSE.....	121
7.3. Ensemble average of the PDOS evolving in time of PbSe/CdSe (a-c) and PbS/CdS (d-f). (a) and (d) the total DOS; (b) and (e) the PDOS contributed by the atoms in the shell (CdSe and CdS, respectively) and (c) and (f) contributed by the atoms in the core (PbSe and PbS, respectively). The subgaps that distinguishes the core and shell contributions to the electronic states (at $\sim 0.75\text{eV}$ below HOMO) are reduced due to the thermal motion (especially in PbSe/CdSe QD), compared to the DOS at 0 K.....	122
7.4. Absorption spectrum of PbSe/CdSe QDs decomposed into three types of excitations (hot holes, hot electrons, and symmetric). Absorption spectrum at 0 (a) and 300 K averaged over the QD ensemble constructed from 30 randomly selected conformations from NAMD trajectory (b). The vertical black arrows indicate the averaged energy of the HOMO-LUMO gap ( $1.0 \times E_g$ ) and the initial excitations of $1.6 \times E_g$ , $1.9 \times E_g$ , and $2.1 \times E_g$ . These excitation energies were selected as initial conditions for the NAMD simulations that are distinct in their energy and nature having predominantly hot hole and hot electron transitions at $1.9 \times E_g$ and $2.1 \times E_g$ , while significant contributions of symmetric transitions at $1.6 \times E_g$ .....	124
7.5. Absorption spectrum of PbS/CdS QDs decomposed into three types of excitations (hot holes, hot electrons and symmetric). (a) Absorption spectrum at 0 K. Indexes depict the types of the envelope function of the optical transition, according to the effective-mass approximation. (b) Thermalized absorption spectra at 300 K averaged over the QD ensemble constructed from 30 randomly selected conformations from the NAMD trajectories. The vertical black arrows indicate the averaged energy of the HOMO-LUMO gap ( $1.0 \times E_g$ ) and the initial excitations of $1.6 \times E_g$ and $1.9 \times E_g$ .....	125
7.6. Time evolution of the initial excitation at $2.1 \times E_g$ in PbX/CdX QDs. (a)-(c) Relaxation of the average energy of the photoexcited electron-hole in PbS/CdS (black lines) and PbSe/CdSe (red lines), shown as a ratio between the excited energy and the energy gap ( $E/E_g$ ). (d)-(i) Evolution of the electron and the hole wave packets with the magnitude varying from blue (minimum) to red (maximum) according to the rainbow color scheme. The white lines represent the ensemble average energy for the hole (dotted lines) and electron (solid lines) relaxation. The initial excitation includes all optically active transitions at the given energy (a), (d) and (g), optically active transitions involving only high-energy hot electrons (b), (e) and (h), and optically active transitions involving only high-energy hot holes (c), (f) and (i).....	129

- 7.7. Time evolution of the initial excitation at  $1.9 \times E_g$  in PbX/CdX with X=S or Se. (a)-(c) Relaxation of the average energy of the photoexcited electron-hole in PbS/CdS QD (black lines) and PbSe/CdSe QD (red lines), shown as a ratio between the excited energy and the energy gap ( $E/E_g$ ). (d)-(i) Evolution of the electron and the hole wave packets with the magnitude varying from blue (minimum) to red (maximum) according to the rainbow color scheme. The white lines represent the ensemble average energy for the hole (dotted lines) and electron (solid lines) relaxation. The initial excitation includes all optically active transitions at the given energy (a), (d) and (g), optically active transitions involving only high-energy hot electrons (b), (e) and (h), and optically active transitions involving only high-energy hot holes (c), (f) and (i)..... 130
- 7.8. Time evolution of the initial excitation at  $1.9 \times E_g$  in PbX/CdX with X=S or Se. (a)-(c) Relaxation of the average energy of the photoexcited electron-hole in PbS/CdS QD (black lines) and PbSe/CdSe QD (red lines), shown as a ratio between the excited energy and the energy gap ( $E/E_g$ ). (d)-(i) Evolution of the electron and the hole wave packets with the magnitude varying from blue (minimum) to red (maximum) according to the rainbow color scheme. The white lines represent the ensemble average energy for the hole (dotted lines) and electron (solid lines) relaxation. The initial excitation includes all optically active transitions at the given energy (a), (d) and (g), optically active transitions involving only high-energy hot electrons (b), (e) and (h), and optically active transitions involving only high-energy hot holes (c), (f) and (i)..... 131
- 7.9. Population of the excited state during NAMD excited at  $1.6 \times E_g$  in PbX/CdX QDs, with X=S and Se. These populations were used in the four-state kinetic model in Eqs 7.1-7.7. The solid lines represent the ensemble population average obtained from NAMD of excited electrons. Fitting functions obtained from Eqs 7.1-7.7 are indicated by the filled circles. The dashed lines represent the ensemble average populations obtained from NAMD simulations of excited holes. Fitting functions obtained from Eqs 7.1-7.7 are indicated by the empty circles. The time-dependent ensemble populations were generated by monitoring the populations during the NAMD simulations: Line A is comprised of the initially excited states, line C comprises the first three MOs for occupied and unoccupied orbitals (final state), and line B is the sum of the populations of all other orbitals (intermediate states). Population analysis for PbSe/CdSe (a) and PbS/CdS (b) QDs, with initial conditions including all optical transitions at the investigated energy range. Population analysis for PbSe/CdSe (c) and PbS/CdS (d) QDs, with initial conditions including only hot electron transitions at the investigated energy range. Population analysis for (e) PbSe/CdSe and PbS/CdS (f) QDs, with initial conditions including only hot hole transitions at the investigated energy range..... 134

7.10. Time evolution of the population of the state initially excited at  $1.9 \times E_g$  in PbX/CdX QDs, with X=S and Se. These populations were used in the four-state kinetic model in Eqs 7.1-7.7. The solid lines represent the ensemble population average obtained from NAMD of excited electrons. Fitting functions obtained from Eqs 7.1-7.7 are indicated by the filled circles. The dashed lines represent the ensemble average populations obtained from NAMD simulations of excited holes. Fitting functions obtained from Eqs 7.1-7.7 are indicated by the empty circles. The time-dependent ensemble populations were generated by monitoring the populations during the NAMD simulations: Line A is comprised of the initially excited states, line C comprises the first three MOs for occupied and unoccupied orbitals (final state), and line B is the sum of the populations of all other orbitals (intermediate states). Population analysis for PbSe/CdSe (a) and PbS/CdS (b) QDs, with initial conditions including all optical transitions at the investigated energy range. Population analysis for PbSe/CdSe (c) and PbS/CdS (d) QDs, with initial conditions including only hot electron transitions at the investigated energy range. Population analysis for (e) PbSe/CdSe and PbS/CdS (f) QDs, with initial conditions including only hot hole transitions at the investigated energy range..... 135

7.11 Population of the excited state during NAMD excited at  $2.1 \times E_g$  in PbX/CdX QDs, with X=S and Se. These populations were used in the four-state kinetic model in Eqs 7.1-7.7. The solid lines represent the ensemble population average obtained from NAMD of excited electrons. Fitting functions obtained from Eqs 7.1-7.7 are indicated by the filled circles. The dashed lines represent the ensemble average populations obtained from NAMD simulations of excited holes. Fitting functions obtained from Eqs 7.1-7.7 are indicated by the empty circles. The time-dependent ensemble populations were generated by monitoring the populations during the NAMD simulations: Line A is comprised of the initially excited states, line C comprises the first three MOs for occupied and unoccupied orbitals (final state), and line B is the sum of the populations of all other orbitals (intermediate states). Population analysis for PbSe/CdSe (a) and PbS/CdS (b) QDs, with initial conditions including all optical transitions at the investigated energy range. Population analysis for PbSe/CdSe (c) and PbS/CdS (d) QDs, with initial conditions including only hot electron transitions at the investigated energy range. Population analysis for (e) PbSe/CdSe and PbS/CdS (f) QDs, with initial conditions including only hot hole transitions at the investigated energy range..... 136

- 7.12. Electron-phonon couplings contributing from various electron and hole states involved in NAMD simulations of PbX/CdX QDs. The Fourier Transform (FT) of the electronic states evolving along the adiabatic trajectory as a function of the phonon frequency of PbSe/CdSe (a) and PbS/CdS (b) QDs, varying from blue (minimum) to red (maximum) according to the rainbow color scheme. FT data averaged over the final (solid lines) and initial (dotted lines) electron (red) and hole states (black) excited at  $2.1x E_g$  in PbSe/CdSe (c) and PbS/CdS (d) QDs. The values of electron-phonon couplings of PbSe/CdSe QDs are multiplied by 2 for better comparison to those of PbS/CdS QDs. .... 140
- 7.13. Vibrational spectrum for PbSe/CdSe (a) and PbS/CdS (b) QDs decomposed over the contributions of various atom-atom pairs. The low frequency portion of the vibration spectra are dominated by the vibrations between pairs of metals, whereas the high frequency portion originates from the vibration of metal chalcogenides pairs associated with optical phonons. .... 140

## LIST OF ABBREVIATIONS

QDs .....	Quantum Dots.
PV .....	Photovoltaic.
LEDs .....	Light Emitting Diodes.
$E_{PL}$ .....	Emission Energy.
$E_{bandgap}$ .....	Bulk Material Bandgap Energy.
DOS.....	Density of States.
0D.....	Electronic are Confined in All Directions.
1D.....	Electronic are Confined in Two Directions.
2D.....	Electronic are Confined in One Directions.
$a_b^*$ .....	Bohr Exciton Radius.
$a_b$ .....	Bohr Radius.
eV .....	Electron Volts.
nm .....	Nanometer.
SILAR.....	Successive Ionic Layer Adsorption and Reaction.
HTCI.....	High-Temperature Continuous-Injection.
$\xi$ .....	Aspect Ratios.
H.....	Shell Thickness of Core/Shell QD.
R.....	Total Radius of Core/Shell QD.
PL.....	Photoluminescence.
EL.....	Electroluminescence.
CIE .....	Commission Internationale de l'Éclairage.
ps.....	Picosecond.
$\mu$ s.....	Microsecond.
s.....	Second.

$e^-$ .....	Electron.
$h^+$ .....	Hole.
CM .....	Carrier Multiplication.
L-type .....	Ligand Exchange with Neutral Donating Ligand.
Z-type .....	Ligand Exchange with Neutral Accepting Ligand.
X-type .....	Ligand Exchange with Charged Ligand.
BME .....	$\beta$ -mercaptoethanol.
PTC .....	Phenyldithiocarbamate.
QY .....	Quantum Yield.
MEG .....	Multiexciton Generation.
DFT .....	Density Functional Theory.
VB .....	Valance Band.
CB .....	Conduction Band.
TDDFT .....	Time-Depended Density Functional Theory.
NAMD .....	Nonadiabatic Molecular Dynamics.
BOA .....	Bohr-Oppenheimer Approximation.
$\rho_0$ .....	Ground State Density.
KS .....	Kohn-Sham.
SP-KS .....	Independent Particle Absorption.
LDA .....	Local-Density Approximation.
GGA .....	Generalized Gradient Approximation.
STOs .....	Slater-type orbitals.
GTOS .....	Gaussian-type orbitals.
$v_i(\mathbf{r}, t)$ .....	Time-Dependent External Potentials.
$c(t)$ .....	Time-Dependent Constant.

$\rho(r_i, t)$	Time-Dependent Density.
$\rho^{GS}$	Ground State Electron Density.
$\rho(r_i, \omega)$	Transition Density.
$\delta P_{ab}$	Expansion Coefficients.
$\delta P_{ba}$	Expansion Coefficients.
$\theta_a$	Occupied Orbitals ( $\varphi_a(r_i; \{R_I\})$ ).
$\theta_b$	Unoccupied Orbitals ( $\varphi_b(r_i; \{R_I\})$ ).
$X$	Expansion Coefficients Vector.
$Y$	Expansion Coefficients Vector.
FSSH	Fewest Switching Surface Hopping.
GS	Ground State.
MD	Molecular Dynamics.
$\Delta\varepsilon_{\alpha\beta}$	Energy Difference Between Orbital $\alpha$ and $\beta$ .
$B_e$	Binding Energy.
CPCM	Conductor Polarized Continuum Model
$Abs(\varepsilon)$	Absorption Spectra.
MOs	Molecular Orbitals.
NTOs	Natural Transition Orbitals.
VASP	Vienna Ab-Initio Simulation Package.
PAW	Projector-Augmented Wave.
Å	Angstrom.
SP	Single-Particle.
MP	Many-Particle.
TEA <sup>+</sup>	Triethylammonium.
TEA	Triethylamine.



DMPTC <sup>-</sup> .....	Deprotonated 3,5-dimethylphenyldithiocarbamate.
DMPTC .....	Protonated 3,5-dimethylphenyldithiocarbamate.
DMA .....	3,5-dimethylaniline.
PTC-PTZ .....	4-phenothiazin-10-yl-dithiocarbamate.
BA-PTZ .....	4-phenothiazin-10-yl-benzonic acid.
MNR .....	Nuclear Magnetic Resonance.
VTC <sup>-</sup> .....	Deprotonated Vinylthiocarbamate.
VTC .....	Protonated Vinylthiocarbamate.
NBOs .....	Natural Bond Orbitals.
Dimer .....	Thiruram Disulfide DMPTC.
VMA .....	Vinylmethylaniline.
H <sup>-</sup> .....	Hydride.
ZB .....	Zinc Blende.
D <sup>-</sup> .....	Deuterated H <sup>-</sup> .
WZ .....	Wurtzite.
RMSD .....	Root-Mean-Square Deviation.
meV .....	millielectronvolt.
CT .....	Charge Transfer.
A <sub>n</sub> .....	Attachment of Ligand on Surface A.
B <sub>n</sub> .....	Attachment of Ligand on Surface B.
C <sub>n</sub> .....	Attachment of Ligand on Surface C.
D <sub>n</sub> .....	Attachment of Ligand on Surface D.
S <sub>n</sub> .....	n <sup>th</sup> Singlet Excited State.
H <sup>+</sup> .....	Proton.
MA .....	Methylamine.

PAM.....	Propylamine
ACN.....	Acetonitrile.
HSR.....	Thiol.
SR <sup>-</sup> .....	Thiolate.
SR/H <sup>+</sup> .....	Thiolate with Proton on Surface.
N <sub>L</sub> .....	Neighboring Ligands.
N <sub>S</sub> .....	Surface Networking.
EMA.....	Effective Mass Approximation.
NACT.....	Non-Adiabatic Coupling Term.
$A(t)$ .....	Population of Initial Excited State.
$B'(t)$ .....	Population of First Intermediate Excited State.
$B''(t)$ .....	Population of Second Intermediate Excited State.
$C(t)$ .....	Population of Final Excited State.
FFT.....	Fast Fourier Transform.

## LIST OF SYMBOLS

$\hbar$ .....	Reduced Planck's Constant.
$r$ .....	QD radius.
$m_e$ .....	Effective Mass of the Conduction Band.
$m_h$ .....	Effective Mass of the Valence Band.
$\epsilon$ .....	Relative Permittivity of the Bulk Material.
$\epsilon_0$ .....	Vacuum Permittivity.
$m$ .....	Mass of a Freely Moving Electron.
$\hat{H}$ .....	Hamiltonian Operator.
$\Psi(r_1, \dots, r_M, R_1, \dots, R_N)$ .....	Many-Body Wavefunction.
$E$ .....	Eigenvalues.
$r_n$ .....	Coordinate of the $n^{\text{th}}$ electron.
$R_n$ .....	Coordinate of the $n^{\text{th}}$ nuclei.
$\hat{H}_e$ .....	Electronic Hamiltonian Operator.
$\varphi(r_i; \{R_I\})$ .....	Electronic Wavefunction.
$\{R_I\}$ .....	Nuclear Parameterization.
$v_{\text{ext}}(\mathbf{r})$ .....	External Potential.
$v_{\text{eff}}(\mathbf{r})$ .....	Local Effective Potential.
$E[\rho(r_i)]$ .....	Energy Functional.
$v_{xc}(\mathbf{r})$ .....	Exchange-Correlation Potential.
$E_{xc}^{\text{exact}}[\rho(r_i)]$ .....	Hartree-Fock Exact Exchange Functional.
$E_x^{\text{GGA}}[\rho(r_i)]$ .....	Exchange Functionals.
$E_c^{\text{GGA}}[\rho(r_i)]$ .....	Correlation Functional.
$\mathcal{A}[\Phi]$ .....	Action Integral.
$\Phi$ .....	Time-Dependent Wavefunction $\Psi(r_i, t; \{R_I\})$ .

$\hat{H}^{GS}$ .....	Ground State Hamiltonian.
$\hat{H}^1(t)$ .....	Time-Dependent Perturbation Hamiltonian.
$\mu_z$ .....	Dipole Along the Z-Axis.
$\varphi_\alpha(r_i; \{R_i(t)\})$ .....	Adiabatic Basis Orbitals.
$\dot{R}d_{\alpha\beta}$ .....	Non-Adiabatic Coupling Term.
$c_\alpha(t)$ .....	Time-Dependent Expansion Coefficients.
$g_{\alpha\beta}$ .....	Hopping Probability.
$a_{\alpha\beta}^*(t)$ .....	$c_\alpha(t)^* c_\beta(t)$ .
$a_{\alpha\alpha}(t)$ .....	$c_\alpha(t) c_\alpha(t)^*$ .
$a_{ij}(t)$ .....	$c_i(t) c_j^*(t)$ .
$a_{jj}(t)$ .....	Time-Dependent Population of Excited State $j$ .
$E_s(t)$ .....	Time-Dependent Energy of Charge Carrier $s$ .
$P_{s,j}(t)$ .....	Time-Dependent Population of State $j$ for Charge Carrier $s$ .
$k_B$ .....	Boltzmann Constant.
T .....	Temperature.
$\Delta t$ .....	Time-step.
$E^I$ .....	Energy of Interacting System.
$E_{Fragment}^{NI}$ .....	Energy of Noninteracting Fragment.
$n$ .....	Number of Ligands.
$PDOS_{Frag}(\varepsilon)$ .....	PDOS of a Specific Fragment.
$N$ .....	Gaussian Normalization Factor.
$F_{Frag,i}$ .....	Percentage of Fragment to $i^{\text{th}}$ Electronic State.
$\sigma$ .....	Line-Width of the Gaussian.
$f_i$ .....	Oscillator Strength of the $i^{\text{th}}$ Transition.

$k_B T$	.....	Thermal Fluctuations at a specific T.
$\Delta E$	.....	Symmetry of a Transition.
$ E_h $	.....	Energy of Hole Compared to VB Edge.
$ E_e $	.....	Energy of Hole Compared to CB Edge.
$E_g$	.....	Bandgap.
$k_1$	.....	Rate Between $A(t)$ and $B'(t)$ .
$k_2$	.....	Rate Between $B'(t)$ and $B''(t)$ .
$k_3$	.....	Rate Between $B''(t)$ and $C(t)$ .
$\alpha$	.....	$k_2 - k_1$ .
$\beta$	.....	$k_3 - k_1$ .
$\gamma$	.....	$k_3 - k_2$ .
$\tau_{lt}$	.....	Total Excited-State Lifetime.
$\tau_{SE}$	.....	Single-Exponential Fitted Excited-State Lifetime.

# 1. INTRODUCTION

## 1.1. Quantum Dots Physical and Chemical Properties

The discovery and characterization of colloidal quantum dots (QDs), also named as semiconducting nanoparticles, in the 1980s<sup>1-2</sup> initiated the widespread investigation by the scientific community for incorporating QDs in various applications, including photovoltaic (PV) and light emitting diode (LED) devices.<sup>3-9</sup> QDs are particularly suited for these applications because of their unique photophysical properties, with one of the most important being size-tunable optoelectronic properties.<sup>10</sup> The early characterization by Brus highlights the sensitivity of the electronic states in QDs to their size, where small QDs absorption and emission is blue shifted compared to the bulk material while large QDs optical properties are similar to the bulk material.<sup>2</sup> The emission energy ( $E_{PL}$ ) of QDs can be approximated by considering the bulk band gap and radius:

$$E_{PL} = E_{bandgap} + \frac{\hbar^2\pi^2}{2r^2} \left( \frac{1}{m_e} + \frac{1}{m_h} \right) - \frac{1.8e^2}{4\pi\epsilon\epsilon_0r} \quad (1.1)$$

Where  $E_{bandgap}$  is the energy of the bulk material's bandgap,  $\hbar$  is the reduced Planck's constant,  $r$  is the radius of the QD,  $m_e$  ( $m_h$ ) is the effective mass of the conduction (valence) band,  $e$  is the charge of the electron,  $\epsilon$  is the relative permittivity of the bulk material,  $\epsilon_0$  is the vacuum permittivity.<sup>11</sup> The first term in equation 1.1 is straightforward, it is the bandgap of the bulk material. The second and thirst terms are dependent on the QDs' size, where the second term is the energy increase due to quantum confinement and the third is the exciton binding energy (Coulombic attraction between the electron and hole). Typically, the third term can be neglected because quantum confinement dominates the difference in emission energy because at small particle size confinement grows as  $r^{-2}$  while Coulombic attraction is only  $r^{-1}$ , which results in the energy increase dominating the shift in emission energy. The second term is derived based on the

quantum mechanical model of “particle in a box,” where the boundaries of the box modify the wavefunction resulting in the quantization of energy levels. The density of states (DOS) predicted for particles in 0D (electrons are confined in all directions), 1D (electrons are confined in two directions), and 2D (electrons are confined in one direction) boxes have provided a rough explanation of the optical spectra of various nanomaterials, such as organic conjugated dyes (typically 1D or 2D),<sup>12-14</sup> carbon nanotubes (1D),<sup>15-17</sup> nanoplatelets (2D)<sup>18</sup> and QDs (0D).<sup>2, 19-20</sup>

Quantum mechanical confinement occurs whenever a dimension of particle is comparable or smaller than the Bohr exciton radius ( $a_b^*$ ):

$$a_b^* = \varepsilon m \left( \frac{1}{m_e} + \frac{1}{m_h} \right) a_b \quad (1.2)$$

Where  $\varepsilon$  is the relative permittivity of the bulk material,  $m$  is the mass of a freely moving electron,  $m_e$  ( $m_h$ ) is the effective mass of the conduction (valence) band, and  $a_b$  is the Bohr radius.<sup>21</sup> The Bohr exciton radius is the distance where the electron and hole interact via Coulombic interactions, resulting in a bounded electron hole pair. The quantum mechanical confinement region for QDs is material dependent because the relative permittivity and effective masses are different for various semiconducting materials, thus, the Bohr exciton radius can vary from 5-40 nm.<sup>11</sup> For QDs with particle size that are comparable to the Bohr exciton radius the energy of the excited states are greatly influenced leading to size-tunable properties. Table 1.1 has examples of common semiconductors' Bohr exciton radius.

Table 1.1. Bohr exciton radius and bandgap for common semiconductors. The semiconductors are listed in decreased Bohr Exciton Radius, modified from Quantum Dots Solar Cells with permission.<sup>11</sup>

Semiconductor	Bohr Exciton Radius (nm)	Bandgap (eV)
PbS	40.0	0.41
GaAs	28.0	1.43
CdTe	15.0	1.50
CdSe	10.6	1.74
ZnSe	8.4	2.58
CdS	5.6	2.53

Experimental studies investigating the photophysical properties of QDs tend to focus on QDs with radii from 1 to 10 nm, depending on the QD's chemical composition, because these QDs are strongly confined.<sup>3, 22</sup> This strong confinement causes the emission energy to be very sensitive to the QDs' size. This sensitivity requires the QDs to be highly monodispersed when implementing into LED devices. This requires advanced synthetic procedures for designing QD-based devices.

The synthesis of QDs in general are either top-down or bottom-up techniques. Top-down methods include molecular beam epitaxy, ion implantation, e-beam lithography and X-ray lithography.<sup>23</sup> Top-down methods typically involve reaction conditions that require advanced equipment and high voltage supplies. Techniques for bottom-up synthesis can be done under mild conditions with common laboratory glassware, making bottom-up synthesis ideal for widespread research into QDs properties. QDs synthesized using bottom-up techniques result in colloidal QDs where self-assembly of dissolved precursors nucleate.<sup>23</sup> Bottom-up synthesis methods of QDs are capable of synthesizing monodispersed QDs that can be utilized in PV and LEDs devices.<sup>3-9, 22</sup>



In this thesis, II-VI (cadmium chalcogenide) and IV-VI (lead chalcogenide) colloidal QDs were studied because these QDs were the most intensively studied for the last decade with the focus on applications in LED and PV devices. For LED applications cadmium chalcogenide QDs are of interest because they can be synthesized to emit throughout most/all of the visible light spectrum.<sup>6, 11, 24</sup> For PV applications QDs should absorb light in the near-infrared region making cadmium chalcogenides not ideal because bulk cadmium selenide (cadmium sulfide) bandgap is 1.74 (2.53) eV, Table 1.1.<sup>11</sup> Lead sulfide bandgap on the other hand is 0.41 eV, Table 1.1.<sup>11</sup> and is a broadband absorber with high molar absorptivity,<sup>4, 12, 25-26</sup> thus lead sulfide (chalcogenide) QDs are ideal candidates for PV applications.

## **1.2. Synthetic Methods for II-VI and IV-VI Quantum Dots**

The synthesis of QDs via bottom-up methods result in QDs that are surrounded by ligands that coordinate with reactive ions, these ligands result in colloidal suspension of the QDs. The incorporation of the colloidal QDs into devices can be achieved by introducing bi-functional ligands that result in closely packed QD structures.<sup>27</sup> The ligand coordinate with reactive surface ions because there are dangling bonds that are passivated during synthesis for QDs comprised of a single or multiple (heterogenous) semiconducting material. The passivation of dangling bonds is not necessarily beneficial to the optical properties of QDs. In Chapter 2, the downside of surface passivation will be discussed leading to open research questions regarding the influence of ligands on QDs photophysical properties.

### **1.2.1. Colloidal QDs**

The initial discovery of CdS colloidal QDs by Henglein in 1982<sup>1</sup> and characterization by Louis<sup>2</sup> was performed on CdS QDs. The most wide-spread method to synthesize colloidal QDs is hot injection.<sup>4, 28</sup> This method typically involves dissolving the cation precursors in a thermally-

stable solvents such as oleic acid and octadecene.<sup>28</sup> Thermally-stable solvents are required because the reaction vessel is heated between 150-350°C.<sup>4</sup> Once the cationic precursors solution is at the desired temperature, the chalcogenide precursors, such as, trioctylphosphine selenide/sulfide or bis(trimethylsilyl) selenide/sulfide, are quickly added. The rapid injection of the chalcogenide precursor resulting in nucleation and a reduction in temperature, which prevents continued nucleation and promotes particle growth. Controlling the temperature after injecting the chalcogenide precursor will in part determine the size of the QDs, and as a result, the QDs' emission energy relative to the bulk material.<sup>3-4, 28-29</sup>

Although, hot injection is straightforward there are drawbacks associated with the simplicity of the method. The first being that the batch-to-batch reproducibility can be difficult to achieve because slight changes in concentration, temperatures, and injection rates can cause the particles' sizes to dramatically vary; therefore, their optoelectronic properties vary from batch-to-batch.<sup>30</sup> The process of heating the cation precursor solution to high temperatures also is time consuming and the precursors used can be extremely toxic.<sup>31</sup> The last drawback of hot injection are the thermally-stable ligands that are typically insulating ligands. The insulating ligands make extracting charge carriers somewhat difficult. This can be addressed by performing ligand exchange of the insulating ligands, also referred to as “native” ligands, by ligands designed to increase extraction rates.<sup>32</sup> Additional discussion on ligand exchange can be found in Chapter 2.2.3.

Microwave synthesis of QDs can partially address some of the drawbacks of hot injections. Microwave synthesis of QDs was reported to reduce the health risk, and dramatically reduce the time associated with heating the cationic precursors, while producing QDs of similar quality as hot injection.<sup>28</sup> Microwave synthesis requires producing cadmium and chalcogenide

solutions similar to hot injection; however, the nucleation and growth of the QDs are performed within a microwave reaction vial. Utilizing the microwave reaction chamber greatly reduces the reaction time from hours or day<sup>28</sup> to several minutes.<sup>31</sup> The resulting CdSe QDs emission energy range from red (605 nm) to green/cyan (509 nm) with the emission spectra dominated from band edge emission with some contribution of trap state emission.<sup>28</sup> The benefit of microwave synthesized QDs is the relatively short nucleation and growth compare to hot injection and reduced health issues associated with synthesis. However, the major drawback of this method is it requires access to microwave reaction vessel(s).

Colloidal QDs that are monodisperse ranging from several to tens of nm that are highly emissive can be achieved via the relatively simple methods as describe above. In section 1.2.2., methods to synthesis heterogeneous QDs will be discussed.

### **1.2.2. Colloidal Heterogeneous QDs**

Heterogeneous QDs are comprised of multiple semiconducting materials and can broadly be classified into two categories core/shell and Janus QDs. The first category core/shell QDs, are QDs that have an inner core comprised of one semiconducting material covered by a second semiconducting material (shell). The second category Janus QDs are QDs that have comprised of two quasi-hemispheres of differing semiconducting materials. For both categories of heterogeneous QDs, the relative ratio of the semiconducting materials can be manipulated during QD synthesis, which greatly influences the photophysical properties.

#### **1.2.2.1. Core/shell QDs**

The synthesis of core/shell QDs can be accomplished in two scenarios, the first is encapsulation of core by the shell that increases the particles' size and the second is ion exchange which does not increase the particles' size because surface ions are replaced by the desired shell

material. The encapsulation of the core can be performed by several methods, here I will focus on successive ionic layer adsorption and reaction (SILAR)<sup>30, 33</sup> and high-temperature continuous-injection (HTCI).<sup>6, 34</sup> These methods have been studied for LED applications because they can generate so-called “giant” core/shell QDs.<sup>6, 8-9, 24, 35-36</sup> Both methods utilize cores that are synthesized by hot injections, but differ when adding the shell material. In the SILAR process, a single monolayer of either the cation or anion is added repetitively till the desired thickness is achieved.<sup>30, 33, 37</sup> The HTCI utilizes chalcogenide precursors where there is a strong covalent bonds that must be broken in order to deposit additional monolayers to the growing shell.<sup>6, 24, 34</sup> Cleaving the covalent bond in the HTCI synthesis and the sequential addition of monolayers in the SILAR synthesis enables these methods to generate monodisperse core/shell QDs with the shell thickness that can vary from a monolayer<sup>30</sup> to several nanometers.<sup>24</sup>

The synthesis of PbSe/CdSe core/shell QDs that have been studied for PV applications are typically synthesized via ion exchange. As the name suggests, ions near the surface of the QD are exchanged for ions in the solvent, in this example Pb<sup>2+</sup> is replaced by Cd<sup>2+</sup> resulting in PbSe/CdSe core/shell QDs. The resulting QDs have a total radius of approximately 4 nm, with the shell thickness ranging from 1 to 2 nm.<sup>38</sup> Ion exchange is employed over encapsulation because the shell thickness can be manipulated by changing the temperature of the reaction during ion exchange which results in reproducible aspect ratios ( $\rho=H/R$ , where H is the shell thickness and R is the total radius of the QD).<sup>38</sup> Core/shell QDs synthesized by encapsulation or ion exchange results in batches with samples with similar morphology and photophysical properties. Additionally, core/shell QDs have been shown to increase the CM efficiencies of QDs. For PV applications CM is an important process because multiple charge carrier pairs can be generated by a single photon that increase the upper limit of efficiency from 33%<sup>39</sup> to 46%.<sup>40</sup>

### ***1.2.2.2. Janus QDs***

The name of Janus comes from the Roman god Janus that is depicted with two-faces; this two-faced depiction describes the combination of the quasi-hemispheres that comprise this class of heterogenous QDs. The synthesis of Janus QDs is performed by ion exchange with lead chloride because cadmium and chlorine direct the reaction to preferentially attaches the PbSe(111) surface.<sup>41</sup> The preferentiality of attack is not seen when utilizing cadmium oxide which result in core/shell PbSe/CdSe QDs.<sup>38</sup> The choose of lead chloride results in Janus QDs where the grain boundary is co-plainer with both PbSe(111) and CdSe(111) crystallography surfaces.<sup>42</sup> The electronic properties of PbX/CdX, X = S or Se, core/shell and Janus QDs are similar, but the structure of Janus QDs allows for more readily hole extraction. The PbX, X = S or Se, quasi-hemispheres in Janus QDs means that the hole can easily migrate to the surface, while the PbX, X = S or Se, core localizes the hole on the interior core preventing hole extraction. This makes Janus QDs more practical for PV applications.<sup>42</sup>

The synthesis of Janus and core/shell QDs are similar,<sup>6, 26, 38, 41-42</sup> but the resulting QDs' structures of Janus and core/shell QDs are very different. Fundamentally understanding how the reactive ligands interact with the surface of the QD is crucial in controlling the resulting morphology of the QDs. Understanding how to manipulate the morphology of QDs will aid and improve QD-based LED and PV devices. The next section will discuss what properties makes QDs particularly suited for LEDs or PV applications.

## **1.3. Application of II-IV Quantum Dots in LEDs and PV Devices**

The unique photophysical and optoelectronic properties of QDs has enticed the scientific community to study QDs for a wide range of applications because they are broadband absorption with high molar absorptivity,<sup>4, 12, 25-26, 43</sup> have narrow emission spectra,<sup>4, 44-45</sup> are resistant to

photodegradation,<sup>46</sup> can be easily functionalized by ligand exchange,<sup>32, 47-49</sup> can undergo multi-exciton generation,<sup>7, 26, 41, 50-53</sup> and electronic structure can be engineered by structure modification such as: core/shell<sup>26, 50, 53</sup> and Janus<sup>38, 41-42</sup> heterogenous QDs.

### 1.3.1. QD based LEDs

QD based LEDs undergo either photoluminescence (PL, emission in response to photoexcitation) or electroluminescence (EL, emission in response to electric current or electric field).<sup>54</sup> QDs-based LEDs are superior to organic-based LEDs because QDs are photostable.<sup>55</sup> Additionally, QDs also have narrow line-width of their emission spectra, which results in displays with high color purity and depth.<sup>56</sup> The resulting displays, therefore, increase the area within the Commission Internationale de l'Éclairage (CIE) chromaticity diagram increasing the number of possible colors resolved by the human eye. However, colloidal QDs luminosity varies on short (ps)<sup>57</sup> and long ( $\mu$ s-s) timescales,<sup>24</sup> which are contributed to charging<sup>57</sup> and disproportion of ligands<sup>43</sup> resulting in trap states that are non-emissive. The short timescale blinking caused by charge is difficult to mitigate when exciting QDs with high influence of photons or electrical current, but the long timescale blinking has been addressed by encapsulating the light emitting core by a thick shell, so-called “giant” core/shell QDs, reducing the effect of the surface on the optoelectronic properties near the band gap.<sup>6, 9, 33-35</sup> However, “giant” core/shell QDs synthesized by HTCI utilizing thiol derivatives for the sulfur precursors show irreversible photobleaching upon exposure to intense heat and irradiation.<sup>24</sup> The mechanism for this photobleaching is unknown but is likely caused by the ligands that passivated the surface of the “giant” core/shell QDs.

### 1.3.2. QD based PV

The theoretical limit of a single junction solar cell is 33% (the Shockley-Queisser limit),<sup>39</sup> this is based on the generation of a single pair of charge carrier (electron ( $e^-$ ) and hole ( $h^+$ )). However, the theoretical limit can go from 33%<sup>39</sup> to 46%<sup>40</sup> if multiple pairs of charge carriers are generated. The dramatic increase in the theoretical limit along with QDs' ability to absorb energy photons without undergoing photodegradation<sup>46</sup> makes QDs highly promising to solar cell applications. Lead chalcogenide QDs (PbS and PbSe) are particular promising for solar cell applications due to their relatively low bandgap<sup>4</sup> and capability of undergoing carrier multiplication (CM), the process of generating several pairs of charge carriers from a single photon.<sup>7, 26, 41, 50-53</sup> The extraction of the charge carriers remains challenging for QD based PV devices. This can be partially addressed by functionalizing the surface of QDs with organic ligands. The Weiss group has investigated the impact of aryl-dithiocarbamate on the extraction of the hole, resulting in extraction rates of the hole that are similar to the extraction of the electron.<sup>32, 47-48, 58-60</sup> However, the process of functionalization of QDs (ligand exchange) is not well understood. In the next Chapter, I will discuss both the benefits and drawbacks of surface passivation by organic and inorganic ligands.

### 1.4. References

1. Henglein, A. Photochemistry of colloidal cadmium sulfide. 2. Effects of adsorbed methyl viologen and of colloidal platinum. *J. Phys. Chem.* **1982**, 86 (13), 2291-2293.
2. Brus, L. E. A simple model for the ionization potential, electron affinity, and aqueous redox potentials of small semiconductor crystallites. *J. Chem. Phys.* **1983**, 79 (11), 5566-5571.
3. Evans, C. M.; Guo, L.; Peterson, J. J.; Maccagnano-Zacher, S.; Krauss, T. D. Ultrabright PbSe magic-sized clusters. *Nano Lett.* **2008**, 8 (9), 2896-2899.
4. Hetsch, F.; Zhao, N.; Kershaw, S. V.; Rogach, A. L. Quantum dot field effect transistors. *Mater. Today* **2013**, 16 (9), 312-325.
5. de Mello Donegá, C.; Liljeroth, P.; Vanmaekelbergh, D. Physicochemical evaluation of the hot-injection method, a synthesis route for monodisperse nanocrystals. *Small* **2005**, 1 (12), 1152-1162.

6. Chen, Y.; Vela, J.; Htoon, H.; Casson, J. L.; Werder, D. J.; Bussian, D. A.; Klimov, V. I.; Hollingsworth, J. A. "Giant" multishell CdSe nanocrystal quantum dots with suppressed blinking. *J. Am. Chem. Soc.* **2008**, *130* (15), 5026-5027.
7. Garcí'a-Santamarí'a, F.; Chen, Y.; Vela, J.; Schaller, R. D.; Hollingsworth, J. A.; Klimov, V. I. Suppressed Auger Recombination in Giant Nanocrystals Boosts Optical Gain Performance. *Nano Lett.* **2009**, 3482-3488.
8. Pal, B. N.; Ghosh, Y.; Brovelli, S.; Laocharoensuk, R.; Klimov, V. I.; Hollingsworth, J. A.; Htoon, H. 'Giant' CdSe/CdS core/shell nanocrystal quantum dots as efficient electroluminescent materials: strong influence of shell thickness on light-emitting diode performance. *Nano Lett.* **2012**, *12* (1), 331-336.
9. Vela, J.; Htoon, H.; Chen, Y.; Park, Y. S.; Ghosh, Y.; Goodwin, P. M.; Werner, J. H.; Wells, N. P.; Casson, J. L.; Hollingsworth, J. A. Effect of shell thickness and composition on blinking suppression and the blinking mechanism in 'giant' CdSe/CdS nanocrystal quantum dots. *J. Biophotonics* **2010**, *3* (10-11), 706-717.
10. Bakueva, L.; Musikhin, S.; Hines, M.; Chang, T.-W.; Tzolov, M.; Scholes, G. D.; Sargent, E. Size-tunable infrared (1000–1600 nm) electroluminescence from PbS quantum-dot nanocrystals in a semiconducting polymer. *Appl. Phys. Lett.* **2003**, *82* (17), 2895-2897.
11. Jasim, K. E. Quantum dots solar cells. *Solar Cells-New Approaches and Reviews* **2015**.
12. Kaeser, A.; Schenning, A. P. Fluorescent nanoparticles based on self-assembled  $\pi$ -conjugated systems. *Adv. Mater.* **2010**, *22* (28), 2985-2997.
13. Rasmussen, S. C.; Mulholland, M. E.; Schwiderski, R. L.; Larsen, C. A. Thieno [3, 4-b] pyrazines and Its Extended Analogs: Important Building Blocks for Conjugated Materials. *Journal of Heterocyclic Chemistry* **2012**, *49* (3), 479-493.
14. Gierschner, J.; Cornil, J.; Egelhaaf, H. J. Optical bandgaps of  $\pi$ -conjugated organic materials at the polymer limit: experiment and theory. *Adv. Mater.* **2007**, *19* (2), 173-191.
15. Mintmire, J.; White, C. Universal density of states for carbon nanotubes. *Phys. Rev. Lett.* **1998**, *81* (12), 2506.
16. Weisman, R. B.; Bachilo, S. M. Dependence of optical transition energies on structure for single-walled carbon nanotubes in aqueous suspension: an empirical Kataura plot. *Nano Lett.* **2003**, *3* (9), 1235-1238.
17. Dresselhaus, M. S.; Avouris, P. Introduction to carbon materials research. In *Carbon nanotubes*, Springer: 2001; pp 1-9.
18. Ithurria, S.; Tessier, M.; Mahler, B.; Lobo, R.; Dubertret, B.; Efros, A. L. Colloidal nanoplatelets with two-dimensional electronic structure. *Nat. Mater.* **2011**, *10* (12), 936-941.
19. Klimov, V. I. *Semiconductor and metal nanocrystals: synthesis and electronic and optical properties*. CRC Press: 2003.
20. Yoffe, A. D. Semiconductor quantum dots and related systems: electronic, optical, luminescence and related properties of low dimensional systems. *Adv. Phys.* **2001**, *50* (1), 1-208.
21. Ashcroft, N. W.; Mermin, N. D. Solid state physics [by] Neil W. Ashcroft [and] N. David Mermin. New York: Holt, Rinehart and Winston: 1976.
22. Kasuya, A.; Sivamohan, R.; Barnakov, Y. A.; Dmitruk, I. M.; Nirasawa, T.; Romanyuk, V. R.; Kumar, V.; Mamykin, S. V.; Tohji, K.; Jeyadevan, B. Ultra-stable nanoparticles of CdSe revealed from mass spectrometry. *Nat. Mater.* **2004**, *3* (2), 99-102.



23. Valizadeh, A.; Mikaeili, H.; Samiei, M.; Farkhani, S. M.; Zarghami, N.; Akbarzadeh, A.; Davaran, S. Quantum dots: synthesis, bioapplications, and toxicity. *Nanoscale Res. Lett.* **2012**, *7* (1), 480.
24. Orfield, N. J.; Majumder, S.; McBride, J. R.; Yik-Ching Koh, F.; Singh, A.; Bouquin, S. J.; Casson, J. L.; Johnson, A. D.; Sun, L.; Li, X. Photophysics of thermally-assisted photobleaching in “giant” quantum dots revealed in single nanocrystals. *ACS Nano* **2018**, *12* (5), 4206-4217.
25. Nootz, G.; Padilha, L. A.; Levina, L.; Sukhovatkin, V.; Webster, S.; Brzozowski, L.; Sargent, E. H.; Hagan, D. J.; Van Stryland, E. W. Size dependence of carrier dynamics and carrier multiplication in PbS quantum dots. *Phys. Rev. B* **2011**, *83* (15), 155302.
26. Cirloganu, C. M.; Padilha, L. A.; Lin, Q.; Makarov, N. S.; Velizhanin, K. A.; Luo, H.; Robel, I.; Pietryga, J. M.; Klimov, V. I. Enhanced carrier multiplication in engineered quasi-type-II quantum dots. *Nat. Commun.* **2014**, *5* (1), 1-8.
27. Xiao, F.-X.; Miao, J.; Wang, H.-Y.; Liu, B. Self-assembly of hierarchically ordered CdS quantum dots–TiO<sub>2</sub> nanotube array heterostructures as efficient visible light photocatalysts for photoredox applications. *J. Mater. Chem. A* **2013**, *1* (39), 12229-12238.
28. Yu, W. W.; Peng, X. Formation of high-quality CdS and other II–VI semiconductor nanocrystals in noncoordinating solvents: tunable reactivity of monomers. *Angew. Chem. Int. Ed. Engl.* **2002**, *41* (13), 2368-2371.
29. Hines, M. A.; Scholes, G. D. Colloidal PbS nanocrystals with size-tunable near-infrared emission: observation of post-synthesis self-narrowing of the particle size distribution. *Adv. Mater.* **2003**, *15* (21), 1844-1849.
30. Wei, H. H.-Y.; Evans, C. M.; Swartz, B. D.; Neukirch, A. J.; Young, J.; Prezhdo, O. V.; Krauss, T. D. Colloidal semiconductor quantum dots with tunable surface composition. *Nano Lett.* **2012**, *12* (9), 4465-4471.
31. Thomas, D.; Lee, H. O.; Santiago, K. C.; Pelzer, M.; Kuti, A.; Jenrette, E.; Bahoura, M. Rapid Microwave Synthesis of Tunable Cadmium Selenide (CdSe) Quantum Dots for Optoelectronic Applications. *J. Nanomater* **2020**, 2020.
32. Lian, S.; Weinberg, D. J.; Harris, R. D.; Kodaimati, M. S.; Weiss, E. A. Subpicosecond photoinduced hole transfer from a CdS quantum dot to a molecular acceptor bound through an exciton-delocalizing ligand. *ACS Nano* **2016**, *10* (6), 6372-6382.
33. Mahler, B.; Spinicelli, P.; Buil, S.; Quelin, X.; Hermier, J.-P.; Dubertret, B. Towards non-blinking colloidal quantum dots. *Nat. Mater.* **2008**, *7* (8), 659-664.
34. Chen, O.; Zhao, J.; Chauhan, V. P.; Cui, J.; Wong, C.; Harris, D. K.; Wei, H.; Han, H.-S.; Fukumura, D.; Jain, R. K. Compact high-quality CdSe–CdS core–shell nanocrystals with narrow emission linewidths and suppressed blinking. *Nat. Mater.* **2013**, *12* (5), 445-451.
35. Ghosh, Y.; Mangum, B. D.; Casson, J. L.; Williams, D. J.; Htoon, H.; Hollingsworth, J. A. New insights into the complexities of shell growth and the strong influence of particle volume in nonblinking “giant” core/shell nanocrystal quantum dots. *J. Am. Chem. Soc.* **2012**, *134* (23), 9634-9643.
36. Jeong, S.; Achermann, M.; Nanda, J.; Ivanov, S.; Klimov, V. I.; Hollingsworth, J. A. Effect of the thiol–thiolate equilibrium on the photophysical properties of aqueous CdSe/ZnS nanocrystal quantum dots. *J. Am. Chem. Soc.* **2005**, *127* (29), 10126-10127.
37. Reiss, P.; Protiere, M.; Li, L. Core/shell semiconductor nanocrystals. *small* **2009**, *5* (2), 154-168.

38. Lin, Q.; Makarov, N. S.; Koh, W.-k.; Velizhanin, K. A.; Cirloganu, C. M.; Luo, H.; Klimov, V. I.; Pietryga, J. M. Design and synthesis of heterostructured quantum dots with dual emission in the visible and infrared. *ACS Nano* **2014**, *9* (1), 539-547.
39. Shockley, W.; Queisser, H. J. Detailed balance limit of efficiency of p-n junction solar cells. *J. Appl. Phys.* **1961**, *32* (3), 510-519.
40. Hanna, M.; Nozik, A. Solar conversion efficiency of photovoltaic and photoelectrolysis cells with carrier multiplication absorbers. *J. Appl. Phys.* **2006**, *100* (7), 074510.
41. Zhang, J.; Gao, J.; Church, C. P.; Miller, E. M.; Luther, J. M.; Klimov, V. I.; Beard, M. C. PbSe quantum dot solar cells with more than 6% efficiency fabricated in ambient atmosphere. *Nano Lett.* **2014**, *14* (10), 6010-6015.
42. Zhang, J.; Chernomordik, B. D.; Crisp, R. W.; Kroupa, D. M.; Luther, J. M.; Miller, E. M.; Gao, J.; Beard, M. C. Preparation of Cd/Pb Chalcogenide Heterostructured Janus Particles via Controllable Cation Exchange. *ACS Nano* **2015**, *9* (7), 7151-7163.
43. Hostetler, M. J.; Wingate, J. E.; Zhong, C.-J.; Harris, J. E.; Vachet, R. W.; Clark, M. R.; Londono, J. D.; Green, S. J.; Stokes, J. J.; Wignall, G. D. Alkanethiolate gold cluster molecules with core diameters from 1.5 to 5.2 nm: core and monolayer properties as a function of core size. *Langmuir* **1998**, *14* (1), 17-30.
44. Jang, E.; Jun, S.; Chung, Y.; Pu, L. Surface treatment to enhance the quantum efficiency of semiconductor nanocrystals. *J. Phys. Chem. B* **2004**, *108* (15), 4597-4600.
45. Somers, R. C.; Bawendi, M. G.; Nocera, D. G. CdSe nanocrystal based chem-/bio-sensors. *Chem. Soc. Rev.* **2007**, *36* (4), 579-591.
46. Doose, S.; Tsay, J. M.; Pinaud, F.; Weiss, S. Comparison of photophysical and colloidal properties of biocompatible semiconductor nanocrystals using fluorescence correlation spectroscopy. *Anal. Chem.* **2005**, *77* (7), 2235-2242.
47. Frederick, M. T.; Amin, V. A.; Cass, L. C.; Weiss, E. A. A molecule to detect and perturb the confinement of charge carriers in quantum dots. *Nano Lett.* **2011**, *11* (12), 5455-5460.
48. Morris-Cohen, A. J.; Frederick, M. T.; Lilly, G. D.; McArthur, E. A.; Weiss, E. A. Organic surfactant-controlled composition of the surfaces of CdSe quantum dots. *J. Phys. Chem. Lett.* **2010**, *1* (7), 1078-1081.
49. Munro, A. M.; Chandler, C.; Garling, M.; Chai, D.; Popovich, V.; Lystrom, L.; Kilina, S. Phenylthiocarbamate Ligands Decompose During Nanocrystal Ligand Exchange. *J. Phys. Chem. C* **2016**, *120* (51), 29455-29462.
50. Lin, Q.; Makarov, N. S.; Koh, W. K.; Velizhanin, K. A.; Cirloganu, C. M.; Luo, H.; Klimov, V. I.; Pietryga, J. M. Design and synthesis of heterostructured quantum dots with dual emission in the visible and infrared. *ACS Nano* **2015**, *9* (1), 539-47.
51. Midgett, A. G.; Luther, J. M.; Stewart, J. T.; Smith, D. K.; Padilha, L. A.; Klimov, V. I.; Nozik, A. J.; Beard, M. C. Size and Composition Dependent Multiple Exciton Generation Efficiency in PbS, PbSe, and PbS x Se1-x Alloyed Quantum Dots. *Nano Lett.* **2013**, *13* (7), 3078-3085.
52. Padilha, L. A.; Stewart, J. T.; Sandberg, R. L.; Bae, W. K.; Koh, W.-K.; Pietryga, J. M.; Klimov, V. I. Aspect ratio dependence of auger recombination and carrier multiplication in PbSe nanorods. *Nano Lett.* **2013**, *13* (3), 1092-1099.
53. Stewart, J. T.; Padilha, L. A.; Bae, W. K.; Koh, W.-K.; Pietryga, J. M.; Klimov, V. I. Carrier multiplication in quantum dots within the framework of two competing energy relaxation mechanisms. *J. Phys. Chem. Lett.* **2013**, *4* (12), 2061-2068.

54. Hoshino, K.; Gopal, A.; Glaz, M. S.; Vanden Bout, D. A.; Zhang, X. Nanoscale fluorescence imaging with quantum dot near-field electroluminescence. *Appl. Phys. Lett.* **2012**, *101* (4), 043118.
55. Talapin, D. V.; Lee, J.-S.; Kovalenko, M. V.; Shevchenko, E. V. Prospects of colloidal nanocrystals for electronic and optoelectronic applications. *Chem. Rev.* **2010**, *110* (1), 389-458.
56. Choi, M. K.; Yang, J.; Hyeon, T.; Kim, D.-H. Flexible quantum dot light-emitting diodes for next-generation displays. *npj Flexible Electronics* **2018**, *2* (1), 1-14.
57. Galland, C.; Ghosh, Y.; Steinbrück, A.; Sykora, M.; Hollingsworth, J. A.; Klimov, V. I.; Htoon, H. Two types of luminescence blinking revealed by spectroelectrochemistry of single quantum dots. *Nature* **2011**, *479* (7372), 203-207.
58. Frederick, M. T.; Amin, V. A.; Swenson, N. K.; Ho, A. Y.; Weiss, E. A. Control of exciton confinement in quantum dot–organic complexes through energetic alignment of interfacial orbitals. *Nano Lett.* **2013**, *13* (1), 287-292.
59. Frederick, M. T.; Amin, V. A.; Weiss, E. A. Optical properties of strongly coupled quantum dot–ligand systems. *J. Phys. Chem. Lett.* **2013**, *4* (4), 634-640.
60. Morris-Cohen, A. J.; Malicki, M.; Peterson, M. D.; Slavin, J. W.; Weiss, E. A. Chemical, structural, and quantitative analysis of the ligand shells of colloidal quantum dots. *Chem. Mater.* **2013**, *25* (8), 1155-1165.

## 2. “DARK SIDE” OF QUANTUM DOTS

### 2.1. Surface Passivation of Dangling Bond – “Double-Edged Sword”

In this chapter, I will discuss the benefits of surface passivation by both organic (section 2.2.) and inorganic ligands (section 2.3). Surface passivation of II-VI and IV-VI colloidal QDs is needed to passivate the highly reactive surface caused by the increased ratio between the surface area to volume of the QDs.<sup>1</sup> The QDs’ surface also is reactive because surface ions are under-passivated by neighboring semiconducting ions that result in dangling bonds.<sup>2</sup> To some extent the confinement of the QD distorts the bulk crystalline structure,<sup>3-5</sup> commonly referred to as surface “self-healing.” Such surface reconstruction decreases the number of surface-associated trap states (optically inactive states)<sup>6-7</sup> to decrease, but ligands are still needed to passivate the remaining dangling bonds and suspend the QDs in the solvent.<sup>7</sup> However, the ligands used to suspend the QDs in the solvent dynamically passivate the surface, and their adsorption and desorption result in the process known as blinking.<sup>7-13</sup> Blinking can also occur when the QD becomes charged which opens additional pathways for optically dark recombination via trions.<sup>14</sup> Blinking is not ideal for LEDs due to the variation in the luminosity of the display. In addition to impacting the emissive properties of QDs for LED devices, ligands can be used to improve the efficiencies of PV devices where QDs are the photo-active materials.<sup>15-17</sup>

The ligand associated blinking can be eliminated by core/shell heterogenous QDs making them candidates for incorporation into QD-based LEDs.<sup>8-10, 12</sup> However, heterogenous QDs (core/shell or Janus) have an additional source of “trap states” that are associated with the interface between the different materials. These interfacial associated states mainly originate from strain on the lattice near the interface and/or vacant or additional ions.<sup>8, 18-22</sup> In the remainder of this chapter, I will discuss specific studies where ligands are used to impact the

photophysical properties of QDs highlighting results and the resulting questions from incorporating organic and inorganic ligands. Then I will outline my research objectives to address the resulting questions.

## **2.2. Surface Passivation by Organic Ligands**

From the discussion on the synthesis of colloidal QDs in section 1.2., during the nucleation and growth the surface is partially or fully passivated by compounds present in the reaction vessel.<sup>8, 13, 23-27</sup> These ligands are selected for their thermal-stable solvents or are precursors, but are not necessarily suitable to optimize the QDs' properties for LED and PV devices. Thus, these "native" ligands are replaced by ligands that improve the desired properties by a process called ligand exchange.<sup>28-30</sup> The ligands that are desired to be on the QDs surface are typically not suitable for the harsh conditions experienced in colloidal synthesis of QDs, thus, they are exchanged for the "native" ligands utilized in the synthesis.<sup>28</sup> Ligand exchange can be classified into three main categories: L-, Z- and X-type.<sup>29</sup> Ligands that undergo L-type ligand exchange are neutral and donate lone pair electrons which passivates the dangling bonds of surface metals, phosphenes, and amines such ligands. Z-type are also neutral like L-type but, they accept lone pair electrons from surface chalcogenides or surface anions. Z-type ligands are primarily the metal solvent complexes such as  $\text{Cd}(\text{O}_2\text{CR})_2$ , and  $\text{PbCl}_2$ . Finally, X-type are charged ligands that balance the overall charge of the QD-ligand system while donating lone pair electrons capping the dangling bonds of surface metals.<sup>29</sup> For each type of ligand exchange, both experimental and theoretical methods have been used to understare the mechanism more in-depth.<sup>29, 31</sup> These mechanisms are system specific, but understanding the basis of ligands exchange is vital to build a foundation for studying new and novel ligand-QD systems.

### 2.2.1. Neutral Ligands

The synthesis utilizing neutral coordinating ligands, typically primary amine and phosphenes, has been shown to produce QDs with neutral surfaces with a ratio of cation and anions approximately equal to one.<sup>28</sup> In this scenario, the surface primarily undergoes L-type ligand exchange where the “native” ligands are replaced by designer ligands that are neutral and donate lone pairs to the dangling bonds of the surface metals. L-type ligand exchange has shown to improve the emissive properties of CdSe/ZnS core/shell QDs by replacing the “native” phosphine chalcogenide with a thiol derivative ( $\beta$ -mercaptoethanol, BME).<sup>32</sup> Unfortunately, this improvement can result in QDs that are initially optically active but over time become non-emissive or weakly emissive.<sup>32</sup> From this report, the BME ligand that was thought to improve the photophysical properties underwent multiple reaction pathways that lead to a reduction in emissive properties at high surface concentration.<sup>32</sup> The quenching of the emission is thought to be the result of thiol formation when the QD-BME is transferred to the aqueous phase.<sup>32</sup> Additionally, determining what is occurring on the surface of the QDs is difficult to study experimentally.<sup>32-33</sup> This is why joint experimental and theoretical studies are now being performed to better understand the surface of the QDs in particular experimental conditions.<sup>1-2, 34-</sup>

35

### 2.2.2. Ionic Ligand

The exchange of charged “native” ligands primarily occurs on metal-enriched QDs because charged chelating ligands are used to dissolve the metal precursors during synthesis and the metal solvent complex is deposited on the surface of the QDs.<sup>29, 31, 36-37</sup> The charged surface of the QDs in metal-enriched QDs allows for strong Coulomb interaction to charged ligands.<sup>29, 31</sup> X-type of ligand exchange is sub-divided into two groups, conjugate bases to organic acids and

reactive ions. The first group, conjugate bases, are widely studied and can interact with the charged surface via Coulomb interactions, the strong Coulomb forces on the surface dictate how ligands are distributed.<sup>31</sup> When acetate ions (reduces model for oleate ions) interact with Cd-enriched CdSe QDs, theoretical calculations showed the most stable scenario of passivation is when there is a single acetate ion bond to the additional Cd<sup>2+</sup> ions and the second acetate ion is passivating neighboring surface Cd.<sup>31</sup> When both acetate ions were placed on the excess Cd<sup>2+</sup> ion there was a tendency to desorb,<sup>31</sup> this desorption was observed experimentally.<sup>29</sup> The Weiss group has investigated phenyldithiocarbamates (PTCs) ligands (X-type ligand exchange) on CdS, CdSe and PbS QDs for PV devices because PTCs were found to increase the rate of hole extraction to the same order of magnitude as electron extraction.<sup>38-40</sup> However, PTCs are quasi-stable when dissolved in protic solvents because PTCs can readily be converted into carbon disulfide and aniline derivatives in the presence of protons.<sup>28</sup>

The last X-type conjugate bases I will discuss are organic dyes utilized in dye-sensitized QD solar cells, where the organic dyes are not necessary ionic but carboxylic anchoring groups can be used to increase the intermolecular forces and electronic coupling between the dye (ligand) and QD.<sup>40-41</sup> The function of the organic dye in dye-sensitized QD solar cells is to facilitate charge separation<sup>42</sup> Strong electronic coupling between the dye and QD is crucial for efficient charge carrier transfer. The correct energy alignment between QD and dye states can thermodynamically drive charge separation.<sup>16-17, 43</sup>

The second group of X-type ligand exchange, reaction ions, tend to be inorganic compounds such as hydride generating compounds,<sup>44</sup> and salts (halide, chalcogenide and/or metal).<sup>19, 22, 29</sup> Thus, I will discuss them in the next section.

### **2.3. Inorganic Surface Passivation**

This section will continue the discussion on ligand exchange for X-type ligands that are reactive ions, followed by the effect of converting QD (core) with a second semiconducting material (shell) which results in a core/shell heterogenous core/shell QDs.

#### **2.3.1. X-Type Ligand Exchange – Reactive Ions**

As discussed in section 1.2.2., there are two classes of X-type ligand exchange conjugate bases of organic acids and reactive ions. The latter can dramatically modify surface morphology of the QD being studied resulting in etching of the surface,<sup>45</sup> metal oxide layer(s),<sup>44</sup> converting the surface into shell material of different semiconducting materials (i.e. PbSe is converted into CdSe),<sup>46</sup> or removal of passivating ligands causing the QDs from precipitating.<sup>47</sup> One example of X-type ligand exchange that greatly impacts the photophysics of cadmium chalcogenides QDs is the surface treatment by hydride generating compounds which resulted in orders of magnitude increase in the PL quantum yield (QY). This enhancement of PL QY was explained by the generation of cadmium oxide shell, that insulated the light-emitting core from the environment because cadmium oxide is a wide bandgap material.<sup>44</sup> Later this conclusion was put in question without providing a new mechanism for the enhancement.<sup>45, 47</sup> These studies once again highlights that the surface of QDs is extremely complicated and difficult to probe experimentally, while fundamentally understanding of the surface during ligand exchange is crucial for improving the implementation of QDs in PV and LED applications.

#### **2.3.2. Benefits of Core/Shell QDs for PV and LED Applications**

There are multiple benefits for encapsulating QDs in a second semiconducting material or insulating solid, these include but are not limited to reduced blinking,<sup>8-9, 11, 13-14, 24, 48</sup> reduced toxicity of photo-active core,<sup>49</sup> increased QY of PL,<sup>50</sup> increased photostability,<sup>51</sup> band



engineering,<sup>21, 35, 46, 52-53</sup> etc. Of these benefits, reduced blinking and band engineering are the most promising for LED and PV applications.

The incorporation of QDs in LEDs has been investigated, but QDs have suffered from blinking or fluctuations in the PL intensity. This blinking is believed to originate from the dynamic ligand passivation by organic ligands.<sup>8, 24</sup> Blinking has been somewhat addressed by so-called “giant” core/shell CdSe/CdS QDs, where the thick shell reduces the impact of ligands on the light-emitting core resulting in non-blinking QDs.<sup>8-9, 11, 13-14, 24, 48</sup> Unfortunately, blinking is not the only hurdle QDs have when utilizing them in LEDs as the photo-active materials. LEDs require QDs to be photothermal stable because electrically exciting QDs likely produce heat. The synthesis of “giant” core/shell QDs by the HTCI method initially outperforms once created by SILAR, however, under intense photo and thermal conditions the emissive properties of HTCI QDs are irreversibly bleached while SILAR QDs can recover.<sup>12</sup> The difference in photothermal stability between HTCI and SILAR QDs is not well understood.

As discussed in section 1.3.2, the theoretical limit of single-junction solar cells is predicted to be 33% (the Shockley-Queisser limit),<sup>54</sup> but utilizing QDs as the photo-active material can increase the limit to 46% due to multiexciton generation (MEG) or carrier multiplication (CM).<sup>55</sup> CM is the process where a photon with more than twice the bandgap results in more than one pair of charge carriers. Bulk PbS can undergo CM through impact ionization, but CM is enhanced in QDs due to the confinement of the charge carriers and increased coupling between carriers.<sup>20, 53</sup> Although, bulk PbS and PbS QDs undergo CM, its efficiency remains relatively low and the threshold for CM can range from 2.5-5 times the bandgap.<sup>56</sup> The increase in the threshold compared to the theoretical minimum of 2 times the bandgap is the result of carrier cooling, where the excess excitonic energy is converted to

phonons and lost as heat. Thus, one route to improving CM efficiencies is to reduce carrier cooling. It has been shown that band engineering of core/shell QDs can result in decreasing the rate of carrier cooling in PbSe/CdSe QDs, resulting in increased efficiencies of CM in the core/shell QDs compared to bulk PbSe and PbSe QD.<sup>21, 35, 46, 52-53</sup>

The properties of Core/shell QDs are improved over their homogenous counterparts, but several questions arise from studying them for PV and PLE applications. In the next sections, open research questions will be posted, and brief conclusions will be discussed.

#### **2.4. Open Research Questions**

Here we employ computational methods to simulate the effect of surface passivation by organic and inorganic ligands. As shown above, fundamentally understanding the surface of QDs is vital to understanding the impact of ligands on the photophysical properties of QDs for PV and LED applications, but experimentally probing the surface of QDs can be difficult. This is where atomic level simulation can provide insight and can help to explain intriguing trends observed in experimental methods. Density functional theory (DFT) based calculations, see Chapter 3 for details, was utilized to investigate how organic and inorganic surface passivations influences the photophysical properties of II-VI and IV-VI QDs and stability of the passivating groups.

In Chapter 4, the stability of PTC derivative during ligand exchange on CdSe QDs was investigated. From experimental work, the PTC derivatives are observed to decompose.<sup>38, 40</sup> The two questions we investigated were 1) Do the decomposition products can interact with the surface of the QDs? 2) What effect do solvents have on the interaction between the ligand(s) and QD? We found that the decomposition products can strongly interact with the surface which is not ideal for ligand exchange, and the interaction between the ligand and QDs is strongly dependent on the solvent.

In chapter 5, hydride treatment of CdSe QDs was investigated to explain the orders of magnitude enhancement of the QY of PL.<sup>44</sup> From literature, the mechanism of PL enhancement is unclear.<sup>44-45, 47</sup> We are interested in answering, how hydride interacts with the QDs, and what products are formed during/after hydride treatment. Our DFT simulations, provide support for two scenarios of hydride interaction with the surface of QDs. The first is removing surface  $\text{Se}^{2-}$  as  $\text{H}_2\text{Se}$  gas which removes  $\text{Se}^{2-}$  trap states, and the second strongly passivating  $\text{Cd}^{2+}$  dangling bonds. These scenarios result in increasing the oscillator strength of the lowest transitions and explain the enhancement in PL observed in experimental studies.

In chapter 6, the irreversible photo-thermal bleaching of HTCI core/shell QDs was investigated.<sup>12</sup> From experimental single dot spectroscopy it is unknown what causes the irreversible bleaching of HTCI compared to SILAR QDs.<sup>12</sup> We hypothesize that HTCI has thiols passivating the surface while SILAR has oleic acid passivated surfaces. The question we addressed is whether the formation of thiolate results in ligand-based trap states that are formed when the QDs undergo high-intensity laser pump and strong heating? From our simulations, the ligand-based states shift from deep within the VB to the VB edge when thiol is converted to thiolate. These thiolate-based states are likely the reason for the irreversible photo-thermal bleaching of HTCI.

In chapter 7, the relaxation of charge carriers in  $\text{PbX/CdX}$ ,  $\text{X} = \text{S}$  or  $\text{Se}$ , core/shell QDs are investigated to understand the effect of the interfacial associated states. From experimental studies the CM efficiencies are improved for the  $\text{PbSe/CdSe}$  core/shell QDs; this improvement is thought to be the result of reduced carrier cooling through the interfacial associated states allowing CM to outcompete carrier cooling.<sup>18, 20-21, 52-53</sup> To investigate the cooling of charge carriers, Non-Adiabatic Molecular Dynamic (NAMMD) was utilized to understand whether the

interfacial associated states are long-lived reducing the cooling to the band edge and the effect of chemical composition of QDs on relaxation rates. NAMD simulations revealed that interfacial states are long-lived allows CM to compete with carrier cooling and the lighter PbS/CdS core/shell QDs excited state lifetimes are significantly reduced compared to PbSe/CdSe core/shell QDs.

## 2.5. References

1. Kilina, S.; Velizhanin, K. A.; Ivanov, S.; Prezhdo, O. V.; Tretiak, S. Surface Ligands Increase Photoexcitation Relaxation Rates in CdSe Quantum Dots. *ACS Nano* **2012**, *6* (7), 6515-6524.
2. Kilina, S.; Ivanov, S.; Tretiak, S. Effect of Surface Ligands on Optical and Electronic Spectra of Semiconductor Nanoclusters. *J. Am. Chem. Soc.* **2009**, *131* (22), 7717-7726.
3. Sapra, S.; Nanda, J.; Pietryga, J. M.; Hollingsworth, J. A.; Sarma, D. D. Unraveling internal structures of highly luminescent PbSe nanocrystallites using variable-energy synchrotron radiation photoelectron spectroscopy. *J. Phys. Chem. B* **2006**, *110* (31), 15244-15250.
4. Winkler, U.; Eich, D.; Chen, Z.; Fink, R.; Kulkarni, S.; Umbach, E. Detailed investigation of CdS nanoparticle surfaces by high-resolution photoelectron spectroscopy. *Chem. Phys. Lett.* **1999**, *306* (1-2), 95-102.
5. Ip, A. H.; Thon, S. M.; Hoogland, S.; Voznyy, O.; Zhitomirsky, D.; Debnath, R.; Levina, L.; Rollny, L. R.; Carey, G. H.; Fischer, A. Hybrid passivated colloidal quantum dot solids. *Nat. Nanotechnol.* **2012**, *7* (9), 577.
6. Puzder, A.; Williamson, A.; Gygi, F.; Galli, G. Self-healing of CdSe nanocrystals: first-principles calculations. *Phys. Rev. Lett.* **2004**, *92* (21), 217401.
7. Kilina, S. V.; Tamukong, P. K.; Kilin, D. S. Surface Chemistry of Semiconducting Quantum Dots: Theoretical Perspectives. *Acc. Chem. Res.* **2016**, *49* (10), 2127-2135.
8. Chen, Y.; Vela, J.; Htoon, H.; Casson, J. L.; Werder, D. J.; Bussian, D. A.; Klimov, V. I.; Hollingsworth, J. A. "Giant" multishell CdSe nanocrystal quantum dots with suppressed blinking. *J. Am. Chem. Soc.* **2008**, *130* (15), 5026-5027.
9. Ghosh, Y.; Mangum, B. D.; Casson, J. L.; Williams, D. J.; Htoon, H.; Hollingsworth, J. A. New insights into the complexities of shell growth and the strong influence of particle volume in nonblinking "giant" core/shell nanocrystal quantum dots. *J. Am. Chem. Soc.* **2012**, *134* (23), 9634-9643.
10. Pal, B. N.; Ghosh, Y.; Brovelli, S.; Laocharoensuk, R.; Klimov, V. I.; Hollingsworth, J. A.; Htoon, H. 'Giant' CdSe/CdS core/shell nanocrystal quantum dots as efficient electroluminescent materials: strong influence of shell thickness on light-emitting diode performance. *Nano Lett.* **2012**, *12* (1), 331-336.
11. Vela, J.; Htoon, H.; Chen, Y.; Park, Y. S.; Ghosh, Y.; Goodwin, P. M.; Werner, J. H.; Wells, N. P.; Casson, J. L.; Hollingsworth, J. A. Effect of shell thickness and composition on blinking suppression and the blinking mechanism in 'giant' CdSe/CdS nanocrystal quantum dots. *J. Biophotonics* **2010**, *3* (10-11), 706-717.

12. Orfield, N. J.; Majumder, S.; McBride, J. R.; Yik-Ching Koh, F.; Singh, A.; Bouquin, S. J.; Casson, J. L.; Johnson, A. D.; Sun, L.; Li, X. Photophysics of thermally-assisted photobleaching in “giant” quantum dots revealed in single nanocrystals. *ACS Nano* **2018**, *12* (5), 4206-4217.
13. Chen, O.; Zhao, J.; Chauhan, V. P.; Cui, J.; Wong, C.; Harris, D. K.; Wei, H.; Han, H.-S.; Fukumura, D.; Jain, R. K. Compact high-quality CdSe–CdS core–shell nanocrystals with narrow emission linewidths and suppressed blinking. *Nat. Mater.* **2013**, *12* (5), 445-451.
14. Galland, C.; Ghosh, Y.; Steinbrück, A.; Sykora, M.; Hollingsworth, J. A.; Klimov, V. I.; Htoon, H. Two types of luminescence blinking revealed by spectroelectrochemistry of single quantum dots. *Nature* **2011**, *479* (7372), 203-207.
15. Barkhouse, D. A. R.; Pattantyus-Abraham, A. G.; Levina, L.; Sargent, E. H. Thiols passivate recombination centers in colloidal quantum dots leading to enhanced photovoltaic device efficiency. *ACS Nano* **2008**, *2* (11), 2356-2362.
16. Cui, P.; Javed, M.; Vogel, D. J.; Kilina, S. Phonon-Mediated Ultrafast Hole Transfer from Photoexcited CdSe Quantum Dots to Black Dye. In *Computational Photocatalysis: Modeling of Photophysics and Photochemistry at Interfaces*, American Chemical Society: 2019; Vol. 1331, pp 137-156.
17. Cui, P.; Tamukong, P. K.; Kilina, S. Effect of Binding Geometry on Charge Transfer in CdSe Nanocrystals Functionalized by N719 Dyes to Tune Energy Conversion Efficiency. *ACS Appl. Nano Mater.* **2018**, *1* (7), 3174-3185.
18. Midgett, A. G.; Luther, J. M.; Stewart, J. T.; Smith, D. K.; Padilha, L. A.; Klimov, V. I.; Nozik, A. J.; Beard, M. C. Size and Composition Dependent Multiple Exciton Generation Efficiency in PbS, PbSe, and PbS x Se1–x Alloyed Quantum Dots. *Nano Lett.* **2013**, *13* (7), 3078-3085.
19. Zhang, J.; Chernomordik, B. D.; Crisp, R. W.; Kroupa, D. M.; Luther, J. M.; Miller, E. M.; Gao, J.; Beard, M. C. Preparation of Cd/Pb chalcogenide heterostructured janus particles via controllable cation exchange. *ACS Nano* **2015**, *9* (7), 7151-7163.
20. Zhang, J.; Gao, J.; Church, C. P.; Miller, E. M.; Luther, J. M.; Klimov, V. I.; Beard, M. C. PbSe quantum dot solar cells with more than 6% efficiency fabricated in ambient atmosphere. *Nano Lett.* **2014**, *14* (10), 6010-6015.
21. Cirloganu, C. M.; Padilha, L. A.; Lin, Q.; Makarov, N. S.; Velizhanin, K. A.; Luo, H.; Robel, I.; Pietryga, J. M.; Klimov, V. I. Enhanced carrier multiplication in engineered quasi-type-II quantum dots. *Nat. Commun.* **2014**, *5* (1), 1-8.
22. Lin, Q.; Makarov, N. S.; Koh, W.-k.; Velizhanin, K. A.; Cirloganu, C. M.; Luo, H.; Klimov, V. I.; Pietryga, J. M. Design and synthesis of heterostructured quantum dots with dual emission in the visible and infrared. *ACS Nano* **2014**, *9* (1), 539-547.
23. Hetsch, F.; Zhao, N.; Kershaw, S. V.; Rogach, A. L. Quantum dot field effect transistors. *Mater. Today* **2013**, *16* (9), 312-325.
24. Mahler, B.; Spinicelli, P.; Buil, S.; Quelin, X.; Hermier, J.-P.; Dubertret, B. Towards non-blinking colloidal quantum dots. *Nat. Mater.* **2008**, *7* (8), 659-664.
25. Thomas, D.; Lee, H. O.; Santiago, K. C.; Pelzer, M.; Kuti, A.; Jenrette, E.; Bahoura, M. Rapid Microwave Synthesis of Tunable Cadmium Selenide (CdSe) Quantum Dots for Optoelectronic Applications. *J. Nanomater* **2020**, 2020.
26. Wei, H. H.-Y.; Evans, C. M.; Swartz, B. D.; Neukirch, A. J.; Young, J.; Prezhdo, O. V.; Krauss, T. D. Colloidal semiconductor quantum dots with tunable surface composition. *Nano Lett.* **2012**, *12* (9), 4465-4471.

27. Yu, W. W.; Peng, X. Formation of high-quality CdS and other II–VI semiconductor nanocrystals in noncoordinating solvents: tunable reactivity of monomers. *Angew. Chem. Int. Ed. Engl.* **2002**, *41* (13), 2368-2371.
28. Munro, A. M.; Chandler, C.; Garling, M.; Chai, D.; Popovich, V.; Lystrom, L.; Kilina, S. Phenylthiocarbamate Ligands Decompose During Nanocrystal Ligand Exchange. *J. Phys. Chem. C* **2016**, *120* (51), 29455-29462.
29. Anderson, N. C.; Hendricks, M. P.; Choi, J. J.; Owen, J. S. Ligand exchange and the stoichiometry of metal chalcogenide nanocrystals: spectroscopic observation of facile metal-carboxylate displacement and binding. *J. Am. Chem. Soc.* **2013**, *135* (49), 18536-18548.
30. De Roo, J.; Ibáñez, M.; Geiregat, P.; Nedelcu, G.; Walravens, W.; Maes, J.; Martins, J. C.; Van Driessche, I.; Kovalenko, M. V.; Hens, Z. Highly dynamic ligand binding and light absorption coefficient of cesium lead bromide perovskite nanocrystals. *ACS Nano* **2016**, *10* (2), 2071-2081.
31. Tamukong, P. K.; Peiris, W. D.; Kilina, S. Computational insights into CdSe quantum dots' interactions with acetate ligands. *Phys. Chem. Chem. Phys.* **2016**, *18* (30), 20499-20510.
32. Jeong, S.; Achermann, M.; Nanda, J.; Ivanov, S.; Klimov, V. I.; Hollingsworth, J. A. Effect of the thiol–thiolate equilibrium on the photophysical properties of aqueous CdSe/ZnS nanocrystal quantum dots. *J. Am. Chem. Soc.* **2005**, *127* (29), 10126-10127.
33. Kilina, S.; Kilin, D.; Tretiak, S. Light-driven and phonon-assisted dynamics in organic and semiconductor nanostructures. *Chem. Rev.* **2015**, *115* (12), 5929-5978.
34. Albert, V. V.; Ivanov, S. A.; Tretiak, S.; Kilina, S. V. Electronic structure of ligated cdse clusters: Dependence on dft methodology. *J. Phys. Chem. C* **2011**, *115* (32), 15793-15800.
35. Piryatinski, A.; Ivanov, S. A.; Tretiak, S.; Klimov, V. I. Effect of quantum and dielectric confinement on the exciton–exciton interaction energy in type II core/shell semiconductor nanocrystals. *Nano Lett.* **2007**, *7* (1), 108-115.
36. Fritzing, B.; Capek, R. K.; Lambert, K.; Martins, J. C.; Hens, Z. Utilizing self-exchange to address the binding of carboxylic acid ligands to CdSe quantum dots. *J. Am. Chem. Soc.* **2010**, *132* (29), 10195-10201.
37. Azpiroz, J. M.; De Angelis, F. Ligand induced spectral changes in CdSe quantum dots. *ACS Appl. Mater. Interfaces* **2015**, *7* (35), 19736-19745.
38. Frederick, M. T.; Amin, V. A.; Swenson, N. K.; Ho, A. Y.; Weiss, E. A. Control of exciton confinement in quantum dot–organic complexes through energetic alignment of interfacial orbitals. *Nano Lett.* **2013**, *13* (1), 287-292.
39. Morris-Cohen, A. J.; Malicki, M.; Peterson, M. D.; Slavin, J. W.; Weiss, E. A. Chemical, structural, and quantitative analysis of the ligand shells of colloidal quantum dots. *Chem. Mater.* **2013**, *25* (8), 1155-1165.
40. Lian, S.; Weinberg, D. J.; Harris, R. D.; Kodaimati, M. S.; Weiss, E. A. Subpicosecond photoinduced hole transfer from a CdS quantum dot to a molecular acceptor bound through an exciton-delocalizing ligand. *ACS Nano* **2016**, *10* (6), 6372-6382.
41. Kalyanasundaram, K.; Grätzel, M. Applications of functionalized transition metal complexes in photonic and optoelectronic devices. *Coord. Chem. Rev.* **1998**, *177* (1), 347-414.

42. Morris-Cohen, A. J.; Aruda, K. O.; Rasmussen, A. M.; Canzi, G.; Seideman, T.; Kubiak, C. P.; Weiss, E. A. Controlling the rate of electron transfer between a quantum dot and a tri-ruthenium molecular cluster by tuning the chemistry of the interface. *Phys. Chem. Chem. Phys.* **2012**, *14* (40), 13794-13801.
43. Rodríguez-Pérez, M.; Canto-Aguilar, E. J.; García-Rodríguez, R.; De Denko, A. T.; Oskam, G.; Osterloh, F. E. Surface photovoltage spectroscopy resolves interfacial charge separation efficiencies in ZnO dye-sensitized solar cells. *J. Phys. Chem. C* **2018**, *122* (5), 2582-2588.
44. Jang, E.; Jun, S.; Chung, Y.; Pu, L. Surface treatment to enhance the quantum efficiency of semiconductor nanocrystals. *J. Phys. Chem. B* **2004**, *108* (15), 4597-4600.
45. Subila, K.; Kishore Kumar, G.; Shivaprasad, S.; George Thomas, K. Luminescence properties of CdSe quantum dots: role of crystal structure and surface composition. *J. Phys. Chem. Lett.* **2013**, *4* (16), 2774-2779.
46. Lin, Q.; Makarov, N. S.; Koh, W. K.; Velizhanin, K. A.; Cirloganu, C. M.; Luo, H.; Klimov, V. I.; Pietryga, J. M. Design and synthesis of heterostructured quantum dots with dual emission in the visible and infrared. *ACS Nano* **2015**, *9* (1), 539-47.
47. Tsui, E. Y.; Hartstein, K. H.; Gamelin, D. R. Selenium Redox Reactivity on Colloidal CdSe Quantum Dot Surfaces. *J. Am. Chem. Soc.* **2016**, *138* (35), 11105-11108.
48. Zhang, A.; Dong, C.; Liu, H.; Ren, J. Blinking behavior of CdSe/CdS quantum dots controlled by alkylthiols as surface trap modifiers. *J. Phys. Chem. C* **2013**, *117* (46), 24592-24600.
49. Zhu, C.; Chen, Z.; Gao, S.; Goh, B. L.; Samsudin, I. B.; Lwe, K. W.; Wu, Y.; Wu, C.; Su, X. Recent advances in non-toxic quantum dots and their biomedical applications. *Progress in Natural Science: Materials International* **2020**.
50. Ratnesh, R.; Mehata, M. S. Investigation of biocompatible and protein sensitive highly luminescent quantum dots/nanocrystals of CdSe, CdSe/ZnS and CdSe/CdS. *Spectrochim. Acta A* **2017**, *179*, 201-210.
51. Cho, J.; Jung, Y. K.; Lee, J.-K.; Jung, H.-S. Highly efficient Blue-Emitting CdSe-derived Core/Shell Gradient Alloy Quantum Dots with Improved Photoluminescent Quantum Yield and Enhanced Photostability. *Langmuir* **2017**, *33* (15), 3711-3719.
52. García-Santamaría, F.; Chen, Y.; Vela, J.; Schaller, R. D.; Hollingsworth, J. A.; Klimov, V. I. Suppressed Auger Recombination in Giant Nanocrystals Boosts Optical Gain Performance. *Nano Lett.* **2009**, 3482-3488.
53. Stewart, J. T.; Padilha, L. A.; Bae, W. K.; Koh, W.-K.; Pietryga, J. M.; Klimov, V. I. Carrier multiplication in quantum dots within the framework of two competing energy relaxation mechanisms. *J. Phys. Chem. Lett.* **2013**, *4* (12), 2061-2068.
54. Shockley, W.; Queisser, H. J. Detailed balance limit of efficiency of p-n junction solar cells. *J. Appl. Phys.* **1961**, *32* (3), 510-519.
55. Hanna, M.; Nozik, A. Solar conversion efficiency of photovoltaic and photoelectrolysis cells with carrier multiplication absorbers. *J. Appl. Phys.* **2006**, *100* (7), 074510.
56. Nootz, G.; Padilha, L. A.; Levina, L.; Sukhovatkin, V.; Webster, S.; Brzozowski, L.; Sargent, E. H.; Hagan, D. J.; Van Stryland, E. W. Size dependence of carrier dynamics and carrier multiplication in PbS quantum dots. *Phys. Rev. B* **2011**, *83* (15), 155302.

### 3. COMPUTATIONAL METHODOLOGY

#### 3.1. Model Systems to Computationally Investigate Complex Systems

In the previous chapter, we discussed the effect of ligands either organic or inorganic on the photophysical properties of QDs, and the challenges and open questions from experimental work investigating QDs for the photo-active material in PV and LEDs devices. In this chapter, we will first outline the computational methods, followed by the model systems and specific methods used to study the complex surface chemistry of CdS, CdSe and PbX/CdX, X = S or Se, QDs to answer the open research questions that were posed in section 2.4.

#### 3.2. Computational Methods for Investigating Optoelectronic Properties of QDs

In this section, we will discuss the computational framework used in this thesis. The methods utilized in this thesis are density functional theory (DFT),<sup>1</sup> time-dependent DFT (TDDFT)<sup>2-5</sup> and nonadiabatic molecular dynamics (NAMD).<sup>6-9</sup> This section will be sub-divided into three parts where each method will be described.

##### 3.2.1. Density Functional Theory (DFT)

The necessity for DFT originated in the many-body problem where the electrons are coupled and have correlated motion, this problem makes solving the electronic structure of the most realistic system impossible. The time-independent Schrödinger equation takes the following form for a system with N nuclei and M electrons:

$$\hat{H}\Psi(r_1, \dots, r_M, R_1, \dots, R_N) = E\Psi(r_1, \dots, r_M, R_1, \dots, R_N) \quad (3.1.)$$

Where  $\hat{H}$  is the Hamiltonian operator,  $\Psi$  is the many-body wavefunction,  $r_n$  represents the coordinates of the n<sup>th</sup> electron, and  $R_n$  represents the coordinates of the n<sup>th</sup> nuclei. The Bohr-Oppenheimer approximation (BOA) significantly simplifies the many-body wavefunction by



decoupling the electronic and nuclear wavefunctions, which allows for solving the time-independent Schrödinger equation at a fixed nuclear configuration:<sup>10</sup>

$$\hat{H}_e \varphi(r_i; \{R_I\}) = E \varphi(r_i; \{R_I\}) \quad (3.2.)$$

Where  $\hat{H}_e$  is the electronic Hamiltonian operator,  $\varphi$  is the antisymmetric electronic wavefunction that depends parametrically on the nuclear coordinates, the electronic and nuclear coordinates are simplified represented by  $r_i$  and  $\{R_I\}$  ( $r_i$  has  $3M$  degrees of freedom and  $\{R_I\}$  has  $3N$  degrees of freedom). Although, the BOA greatly simplifies solving for the electronic wavefunction the electronic Hamiltonian operator still contains terms where the motion of the electrons are coupled and correlated:

$$\hat{H}_e = -\frac{\hbar^2}{2m_e} \sum_{j=1}^M \nabla_j^2 + \sum_{j,k=1, j \neq k}^M \frac{e^2}{|r_j - r_k|} - \sum_{j,k=1}^{M,N} \frac{Z_k e^2}{|r_j - r_k|} \quad (3.3.)$$

Where the first term is the kinetic energy of all the electrons in the system, the second term is the Coulombic repulsion between electrons and the last term is the Coulombic attraction between the electrons and fixed nuclei. DFT addresses in part the coupled and correlated electrons by representing the electronic ground state as a density ( $\rho(r)$ ) instead of the explicated electronic wavefunction:

$$\rho(r) = \iint \dots \iint |\varphi(r, r_2, \dots, r_M; \{R_I\})|^2 dr_2 \dots dr_M \quad (3.4.)$$

The integration over  $r_2$  through  $r_M$  provides the  $\rho(r)$ , if one is interested in  $\rho(r_2)$  the same method can be applied integrating  $r$  and  $r_3$  through  $r_M$ . The  $\rho(r)$  representation of the electronic wavefunction is the key to DFT, this representation relies on the two famous theorems of Hohenberg and Kohn.<sup>1</sup> The first states that given an external potential ( $v_{\text{ext}}(r)$ ), the  $\rho(r)$  of a system uniquely maps to the  $\varphi(r_i; \{R_I\})$ . The second states there is an energy functional of the  $\rho$  that provides the energy of a many electron system. Kohn-Sham (KS) DFT goes further,

assuming that the many-body system can be approximated by non-interacting single particles in a local effective potential ( $v_{\text{eff}}(r)$ ), where the energy functional takes:

$$E[\rho(r)] = T[\rho(r)] + \int dr v_{\text{ext}}(r)\rho(r) + \frac{1}{2} \iint \frac{\rho(r)\rho(r')}{|r-r'|} dr' dr + E_{xc}[\rho(r)] \quad (3.4.)$$

Where the first term is the energy functional, the second term is the kinetic energy of the electron, the third term in the interaction term, the fourth term is the electron-electron repulsion and the fifth term is the exchange-correlation functional. The energy obtained via the energy functional can be used variationally to obtain the ground state geometry by solving the one-particle KS equation:

$$\left(-\frac{\hbar^2}{2m_e}\nabla^2 + v_{KS}\right)\varphi_j(r_i; \{R_I\}) = \varepsilon_j\varphi_j(r_i; \{R_I\}) \quad (3.5.)$$

Where  $\varphi_j(r_i; \{R_I\})$  are the single-particle KS orbitals (eigenvectors),  $\varepsilon_j$  are the single-particle KS orbital energies (eigenvalues), and  $v_{KS}(r)$  is the KS potential:

$$v_{KS}(r) = v_{\text{eff}}(r) + \int dr' \frac{\rho(r')}{|r-r'|} + v_{xc}(r) \quad (3.6.)$$

Where  $v_{xc}(r)$  is the exchange-correlation potential:

$$v_{xc}(r) = \frac{\delta E_{xc}[\rho(r)]}{\delta \rho(r)} \quad (3.7.)$$

Formally, KS DFT is exact, however, the form of the exchange-correlation ( $E_{xc}[\rho(r_i)]$ ) functional is unknown meaning in practicality DFT is an approximate method for electronic structure theory calculations<sup>11</sup> and the single-particle KS orbitals are linear-combination of basis sets. The functional form of the  $E_{xc}[\rho(r_i)]$  determines the accuracy of the results, initial implementations used the local-density approximation (LDA) which was derived from the homogenous electron gas model. LDA functional depends only on the  $\rho$  which can cause the energy predictions to have significant error. The generalized gradient approximation (GGA) class of functional can reduce this error by including how the  $\rho$  varies locally by including both

the  $\rho$  and the derivative of the  $\rho$ . Further, improvements can be made by hyper-GGA functionals where the Hartree-Fock exact exchange functional ( $E_{xc}^{exact}[\rho(r_i)]$ ), exchange functionals ( $E_x^{GGA}[\rho(r_i)]$ ), and correlation functional ( $E_c^{GGA}[\rho(r_i)]$ ) are linearly combined. The so-called Jacob's Ladder organizes these classes of functional in increased accuracy, Figure 3.1.<sup>12</sup>

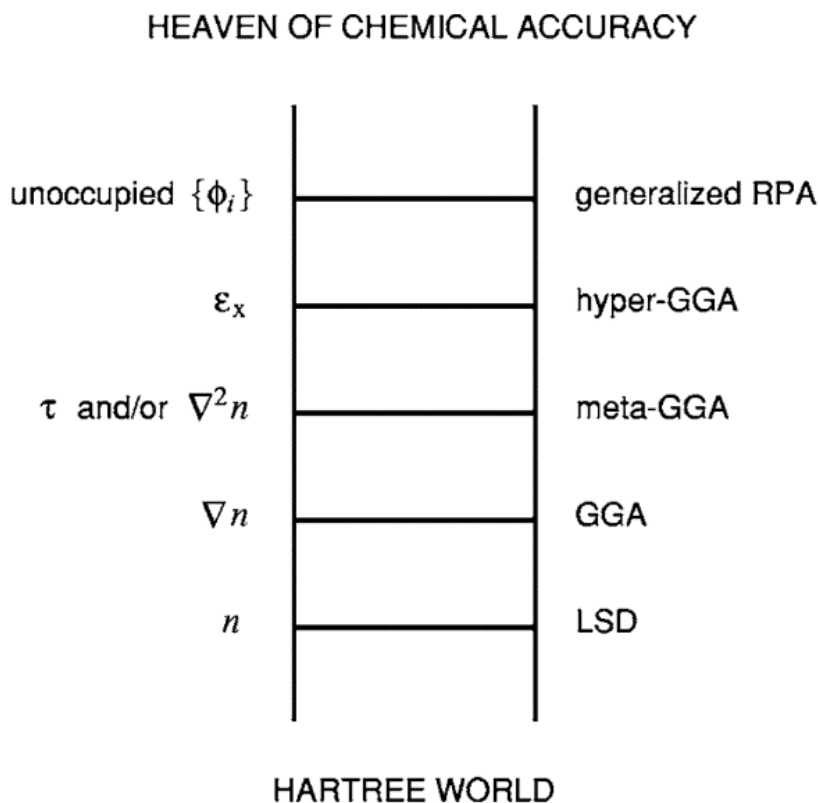


Figure 3.1. Jacob's Ladder. The simplistic functional dependency is shown on the left and type of functional on right going from the Hartree world to heaven of chemical accuracy, here the density is represented at  $n$  where we refer to the density as  $\rho$ . This figure was reprinted with permission.<sup>12</sup>

In this thesis, we will utilize two functionals that have been widely utilized for QDs, which are PBE (GGA)<sup>13</sup> and PBE0 (hyper-GGA, also called hybrid functional).<sup>14-15</sup> The choice of these functionals was based on the improved energy prediction of GGA and hybrid functional

compared to LDA and the computational efficiency of these functionals compared to more advanced functionals.<sup>12</sup>

### 3.2.2. Basis Set

In the previous section, we discussed the framework of DFT where the energy prediction of the system is depended on the functional used to determine the total energy of the system. If the exact functional form of the  $E_{xc}[\rho(r_i)]$  was found, DFT would still be an approximant method because the KS orbitals are a linear combination of basis sets. Any practical implementation of DFT would not reach the complete basis set limit, meaning that DFT will remain an approximant method.<sup>11</sup> Basis sets are either a linear combination of atomic orbitals (local basis) or plane waves (non-local basis), the basis sets are used to describe the electrons in the system, but pseudopotentials can replace the core electrons dramatically reducing the computational cost of the electronic structure calculations.<sup>16</sup> Common local basis sets are Slater-type orbitals (STOs) and Gaussian-type orbitals (GTOs), GTOs are by far the most common because their mathematical representation leads to efficient implementation. STOs can be approximated by the product of GTOs that leads to the Pople basis sets.<sup>17</sup> The Pople basis sets are widely utilized for light elements and are named as X-YZg, where X is the number of primitive Gaussians comprising each core atomic orbitals, Y is the number of primitive Gaussian functions for the first composed of the linear combination for the valance orbitals and Z is the number of primitive Gaussian functions for the second composed of the linear combination for the valance orbitals.<sup>17</sup> Another common basis set used for heavy elements is LANL2DZ that utilizes pseudopotentials to reduce the computational cost.<sup>16</sup> Local basis sets are primarily used for non-periodic systems such as molecules, system with periodic unit cells plane wave basis sets are typically selected. Plane waves basis sets are linear combinations of plan waves, typically an

energy cut off is set and only plane waves with energies less than the cut off are included in the basis set.<sup>18</sup>

The orbitals, orbital energies, and total energy obtained by DFT can be used to describe many ground-state properties and a deeper understanding of the system being investigated. However, DFT is a ground state method due to the variational principle used to obtain the optimized geometry. Thus, additional methods are needed to describe the excited state. In the next section, two methods will briefly be discussed to investigate the excited state properties of systems.

### **3.2.3. Excited State Methods**

In this section, TDDFT and NAMD will discuss, methods used to probe the excited state properties of systems. Often the observable of interest can be obtained with a few or even a single confirmation, in the most part, the absorption spectra can be simulated with a single geometry obtained by DFT where this geometry is provided to TDDFT. TDDFT is based on the Runge-Gross theorem that minimizes the quantum mechanical action (action integral).<sup>19</sup> In cases, where the excited state properties such as non-radiative relaxation, photodegradation, intersystem crossing between spin manifolds, and pump-probe simulations NAMD is needed.

#### **3.2.3.1. TDDFT**

The first Hohenberg and Kohn theorem<sup>1</sup> can be generalized to the time-dependent domain, this was done by Runge and Gross.<sup>19</sup> In the Runge-Gross theorem, the excited state of a many-electron system that evolves from an initial condition, then the resulting time-dependent properties will be different if subjected to different time-dependent external potentials,  $v_1(\mathbf{r}, t)$  and  $v_2(\mathbf{r}, t)$ , that differ more than a time-dependent constant ( $c(t)$ ) from the identical initial conditions:<sup>3, 19</sup>

$$v_1(r_i, t) \neq v_2(r_i, t) + c(t) \Leftrightarrow \rho_1(r_i, t) \neq \rho_2(r_i, t) \quad (3.8.)$$

The time-dependent potential can be obtained using the Runge-Gross theorem. However, applying the variational principle to this potential would result in obtaining the ground state, so the term minimized via the variational principle is the action integral:

$$\mathcal{A}[\Phi] = \int_{t_0}^{t_1} dt \left\langle \Phi \left| \frac{i\partial}{\partial t} - \hat{H}(r_i, t) \right| \Phi \right\rangle \quad (3.9.)$$

Where  $\Phi$  is the time-dependent wavefunction  $\Psi(r_i, t; \{R_I\})$ , when solving the time-dependent Schrödinger equation (3.8.) the action integral must equal zero.

$$\frac{i\partial}{\partial t} \Psi(r_i, t; \{R_I\}) = \hat{H} \Psi(r_i, t; \{R_I\}) \quad (3.10.)$$

Based on the Runge-Gross theorem and action integral, linear-response TDDFT obtains the excitation energy and probabilities (oscillator strengths) for the ground state perturbed by a small perturbation.<sup>20</sup> This perturbation is an external electromagnetic field and the Hamiltonian is:

$$\hat{H} = \hat{H}^{GS} + \hat{H}^1(t) \quad (3.11.)$$

Where  $\hat{H}^{GS}$  is the ground state Hamiltonian and  $\hat{H}^1(t)$  is the perturbation caused by the oscillating field in the electric dipole approximation:

$$\hat{H}^1(t) = -\mu_z E \cos(\omega t) \quad (3.12.)$$

Here  $\mu_z$  is the dipole along the z-axis, E is the strength of the electric field and  $\omega$  is the frequency of the electric field. From this Hamiltonian, the time-dependent electron density ( $\rho(r_i, t)$ ) can be written as:

$$\rho(r_i, t) = \rho^{GS} + \rho(r_i, \omega) \cos(\omega t) \quad (3.13.)$$

Where  $\rho^{GS}$  is the ground-state electron density and  $\rho(r_i, \omega)$  is the transition density. From the time-dependent density, the change in the electronic density upon excitation can be obtained:

$$\delta\rho(r_i, \omega) = \sum_{a,b} \delta P_{ab}(\omega) \theta_a \theta_b^* + \sum_{b,a} \delta P_{ba}(\omega) \theta_b \theta_a^* \quad (3.14.)$$

Where  $\delta P_{ab}$  and  $\delta P_{ba}$  are the expansion coefficients,  $\theta_a$  are the occupied orbitals ( $\varphi_a(r_i; \{R_I\})$ ) and  $\theta_b$  are the unoccupied orbitals ( $\varphi_b(r_i; \{R_I\})$ ). These expansion coefficients can be obtained by diagonalizing the Casida equation:

$$\begin{bmatrix} A & B \\ B & A \end{bmatrix} \begin{bmatrix} X \\ Y \end{bmatrix} = \omega_I \begin{bmatrix} 1 & 0 \\ 0 & -1 \end{bmatrix} \begin{bmatrix} X \\ Y \end{bmatrix} \quad (3.14.)$$

Here the expansion coefficients  $X = \delta P_{ab}$  and  $Y = \delta P_{ba}$ , and the transition frequencies  $\omega_I$  can be obtained. From the expansion coefficients and oscillator strength (the probability that a transition occurs) can be computed.<sup>20</sup>

### 3.2.3.2. Excited State Dynamics

In this section we will discuss a method that can describe the excited state dynamics of charge carriers in QDs, this method has several approximations that makes it ill-suited to describe photochemical reaction which causes the excited state to differ greatly compared to the ground state. This method is based on the fewest switching surface hopping (FSSH) first introduced by Tully,<sup>8</sup> which was later adapted to satisfy detailed balance.<sup>7</sup> This detailed balance is a result of performing the FSSH algorithm on an ensemble of trajectory in a stochastic method.<sup>6</sup> FSSH is framed in the time-domain Kohn-Sham theory which provides the quantum master equation that couples the electron to phonon motion via non-adiabatic coupling. The excited-state wavefunctions are expanded in terms of the adiabatic basis, the adiabatic states are readily computable:

$$\Psi(r_i; \{R_I(t)\}) = \sum_{\alpha} c_{\alpha}(t) \varphi_{\alpha}(r_i; \{R_I(t)\}) \quad (3.15.)$$

Where  $c_{\alpha}(t)$  are the time-dependent expansion coefficients and  $\varphi_{\alpha}(r_i; \{R_I(t)\})$  are the adiabatic orbitals obtain from ground-state DFT. The time-dependend Schrödinger equation then acts on the wavefunction and the expansion coefficients can be obtained:<sup>21</sup>

$$\frac{i\hbar\partial}{\partial t} \sum_{\alpha} c_{\alpha}(t) \varphi_{\alpha}(r_i; \{R_I(t)\}) = \hat{H}_e \sum_{\alpha} c_{\alpha}(t) \varphi_{\alpha}(r_i; \{R_I(t)\}) \quad (3.16.)$$

This equation can be simplified by multiplying the set of conjugated basis sets resulting in a system of coupled equations and the non-adiabatic coupling term (NACTs,  $\dot{R}d_{\alpha\beta}$ ) between state  $\alpha$  and  $\beta$ :

$$i\hbar \left[ \frac{\partial}{\partial t} c_{\beta}(t) + \sum_{\beta} c_{\beta}(t) \dot{R}d_{\alpha\beta} \right] = c_{\beta}(t) \varepsilon_{\beta} \quad (3.17.)$$

Where  $\dot{R}d_{\alpha\beta} = \langle \varphi_{\beta} | \frac{\partial}{\partial t} \varphi_{\alpha} \rangle$ . As state above, the implementation of FSSH is designed for systems like QDs because the adiabatic orbitals are obtained from a single ground state trajectory. This approximation is valued for QDs because the bond is rigid and the density of the VB and CB are quite high.<sup>21</sup> In addition to this approximation, the many-body excited state found by such methods as TDDFT is found by the independent particle approach (SP-KS), which means that the dynamics of the electron and hole are decoupled and Coulombic forces are neglected. The confinement of the electron and hole in QDs results in the kinetic energy of the charge carriers is the more important term and the electrostatic interaction can be neglected at the zeroth-order approximation of charge carrier dynamics in QDs.<sup>21</sup> In section 3.3.4., we will discuss the neglect of Coulomb interaction future.

The implementation of the FSSH with the approximation stated above is illustrated in Figure 3.2. where the first state is to obtain the adiabatic basis functions and  $\dot{R}d_{\alpha\beta}$  from the ground state (GS) BOA molecular dynamics (MD). The GS BOA MD is then split into trajectories, Figure 3.2.b, where the time-dependent expansion coefficients are found by equation 3.17. The expansion coefficients determine whether the electron will go from state  $\alpha$  to  $\beta$ , typically referred to as hopping between state  $\alpha$  and  $\beta$ . When  $g_{\alpha\beta}$  is larger than a stochastic value the electron will switch from state  $\alpha$  to state  $\beta$  and the particle propagates on state  $\beta$ .<sup>6</sup>

$$g_{\alpha\beta} = \frac{-2\text{Re}(a_{\alpha\beta}^*(t)\dot{R}d_{\alpha\beta})\Delta t}{a_{\alpha\alpha}(t)} \exp \left[ -\frac{\Delta\varepsilon_{\alpha\beta}}{k_B T} \right] \quad (3.18.)$$



Where  $a_{\alpha\beta}^*(t)$  and  $a_{\alpha\alpha}(t)$  are found by  $a_{ij}(t) = c_i(t)c_i^*(t)$ , and the exponential term accounts for detailed balance driving the charge carriers towards the band edges. This formulism was designed to reduce the number of surface switching during the excited state dynamics.<sup>8</sup> By solving the system of coupled differential equation 3.17. for all trajectories, the time-dependent expansion coefficients ( $c_i(t)$ ,  $i$  ranges over all adiabatic states) for the adiabatic basis sets are found. The  $c_i(t)$  are then used to find the time-dependent population ( $a_{jj}(t)$ ) of the excited states during the dynamics:<sup>8</sup>

$$a_{jj}(t) = c_i(t)c_i^*(t) \quad (3.19.)$$

The excited state populations are then used to compute the ensemble average of the observable of interest, in this work we are interested in time-dependent charge carriers' energies ( $E_{s,T}(t)$  s is for hole or electron charge carrier for trajectory T), time-dependent population of the excited states ( $a_{jj}(t)$ ), and charge carriers' excited state lifetimes. The time-dependent charge carriers' energies are obtained by a weighted averaging of the time-dependent energy of the adiabatic basis:

$$E_{s,T}(t) = \sum_j a_{jj,T}(t)\varepsilon_{j,T}(t) \quad (3.20.)$$

To obtain the ensemble average energy ( $\langle E_s(t) \rangle$ ) for the charge carriers (s is for electron and hole) the  $E_{s,T}(t)$  is simply averaged:

$$\langle E_s(t) \rangle = \sum_T E_{s,T}(t) \quad (3.21.)$$

Interpreting the population of hundreds of excited states by merely plotting the time-dependent  $a_{jj}(t)$  is visually difficult, to aid in interpreting the dynamics of the excited states a time-dependent density of population (DOP(t)) is constructed by dressing the adiabatic states with gaussian functions weighted by the populations of the states:

$$DOP(t) = \sum_j a_{jj,T}(t)\delta(\varepsilon - \varepsilon_{j,T}(t)) \quad (3.22.)$$

Where  $\delta$  denotes a normalized Gaussian distribution. The ensemble average  $\langle \text{DOP}(t) \rangle$  is obtained similarly to average charge carrier energy.

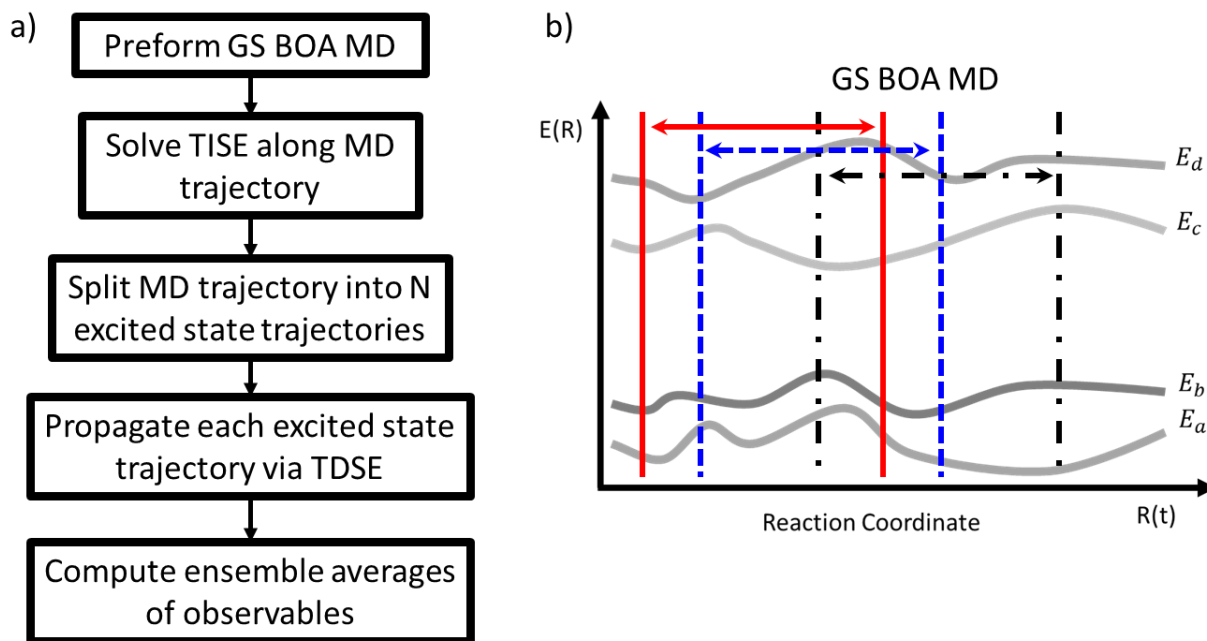


Figure 3.2. Flow-chart of the FSSH method for NAMD. a) steps to obtain ensemble average of the observable of interest b) splitting the GS BOA MD trajectory into multiple trajectories for the NAMD code, where the horizontal arrows indicate time-steps included for each trajectory of NAMD. The vertical lines show the initial and final timesteps for NAMD trajectories.

### 3.3. Methods and Model Systems Utilized

In this section, we will discuss the model system used in our research and the specific methodology utilized to gain fundamental insights into experimental results for QDs that can be used in PV and LED devices.

#### 3.3.1. Experimental and Theoretical Model of “Magic-Size” Cadmium Chalcogenide

CdX, X = S, Se or Te, QDs used in experimental investigations range from several nanometers to tens of nanometers, these QDs are computational prohibitive to simulations.<sup>22-23</sup> The smallest stable QDs, so-called magic-size QDs, have been detected by mass spectroscopy as (CdSe)<sub>33</sub> and (CdSe)<sub>34</sub> QDs.<sup>24</sup> The major peak in the mass spectroscopy spectra corresponds to (CdSe)<sub>34</sub> and followed by a shoulder peak corresponding to (CdSe)<sub>33</sub>. This investigation predicts

a crystalline core of  $(\text{CdSe})_6$  with a  $(\text{CdSe})_{28}$  cage that has the crystalline structure that is greatly perturbed from bulk CdSe.<sup>24</sup> This quasi-amorphous cage greatly differ from the surface structure of larger and experimentally relevant QDs. Therefore, the magic size  $(\text{CdSe})_{33}$  will be used to investigate the surface of QDs. The surface of  $(\text{CdSe})_{33}$  QDs retains the bulk-like crystalline structure, where the surface undergoes “self-healing” perturbing the crystalline lattice structure, Figure 3.3.<sup>23, 25-27</sup> The process of self-healing reduces the number of dangling bonds on the surface when the quasi-spherical  $(\text{CdSe})_{33}$  is cut from bulk materials, Figure 3.3.a-b. There are 2- and 3- coordinated surface ions, where the bulk wurtzite crystal has only 4-coordinated ones.<sup>22</sup> This model has been widely utilized to study the surface chemistry of CdSe QDs as well as CdS QDs. Bulk CdS has similar crystal structure, which we assume would result in the similar magic size  $(\text{CdS})_{33}$  QDs.<sup>21-23, 25-26, 28-34</sup> Cutting the quasi-spherical  $(\text{CdX})_{33}$ , X = S, Se or Te, QDs for bulk wurtzite crystal results in QDs with crystallographic layers commonly referred to as layer A-D, where layer A is terminated with  $\text{Cd}^{2+}$  that are either 2- or 3-coordinated, layer B and D are terminated by  $\text{Cd}^{2+}$  that are 3-coordinated and layer C is terminated with 2-coordinated  $\text{Cd}^{2+}$ , Figure 3.3.c shows the coordination number of various surface  $\text{Cd}^{2+}$ . This means that L-type ligands such as phosphenes and amines ligands tend to bind the strongest to the most reactive layers A and C having the lowest coordination number.<sup>23</sup> This binding energy ( $B_e$ ) is computed by obtaining the total energy of the optimized system that is interacting ( $E^I$ ) and subtracting the optimized energy of the non-interacting fragments ( $E_{\text{Fragment}}^{NI}$ ):

$$B_e = \frac{E^I - E_{\text{QD}}^{NI} - nE_{\text{Ligand}}^{NI}}{n} \quad (3.23.)$$

Here the average binding energy of n ligands is found, when a single ligand is passivating the surface, n is set to 1.

Additionally, this model has a  $C_3$ -axis that lays perpendicular to the planes created by layers A-D. This symmetry means that investigating every surface ion is not needed and only non-symmetrically equivalent ions need to be simulated. In Figure 3.3.d, the symmetrically equivalent ions are shown by highlighting the three portions of the  $(CdSe)_{33}$  that differ by rotating about the  $C_3$ -axis, the atoms highlighted by red are equivalent to the green (blue) highlighted atoms by rotation about the  $C_3$ -axis by  $120^\circ$  ( $-120^\circ$ ). This means among 21 surface  $Cd^{2+}$  and  $Se^{2-}$  that there are only 7  $Cd^{2+}$  and 7  $Se^{2-}$  that need to be investigated for stoichiometric  $(CdX)_{33}$ ,  $X = S, Se$  or  $Te$ , QDs (see additional discussion in Chapter 5).

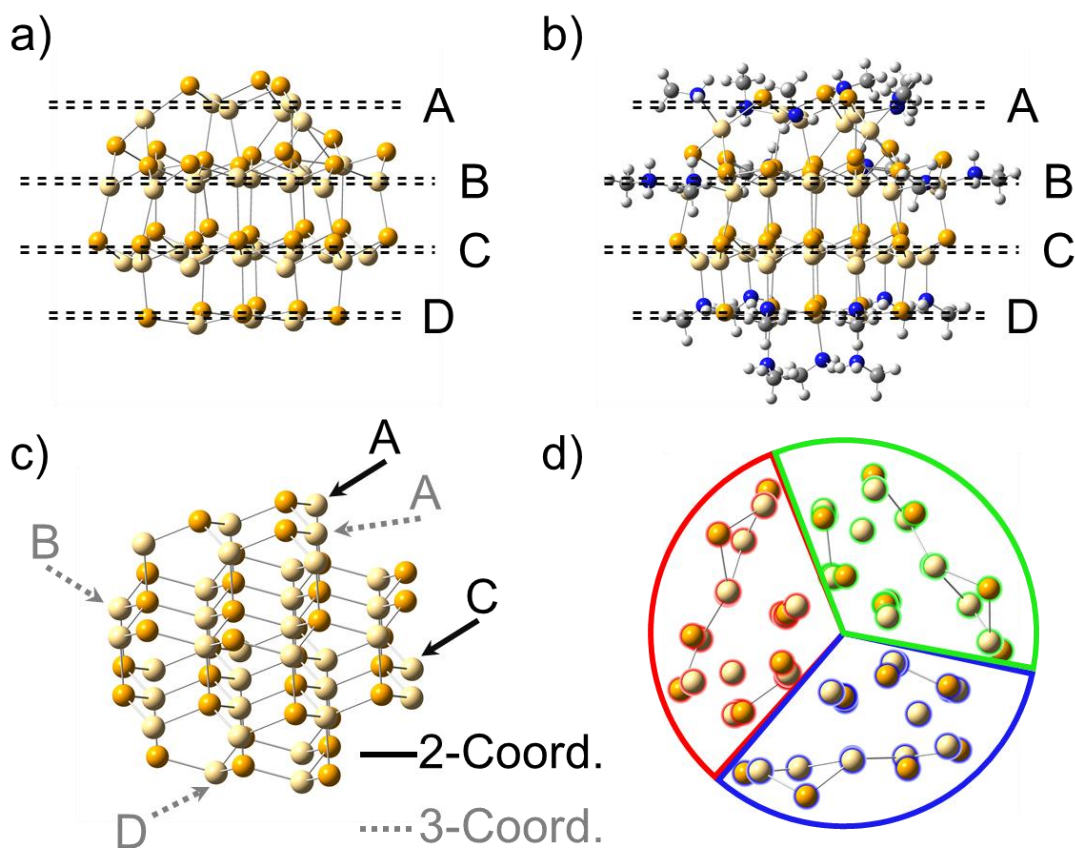


Figure 3.3. Stoichiometric  $(CdSe)_{33}$  QDs model. a) optimized bare magic size QDs with layers A-D notations; b) optimized methylamine passivated magic size QDs; c) 2- and 3-coordinated surface  $Cd^{2+}$  for layers A-D, with black solid lines show 2-coordinated  $Cd^{2+}$  and grey dashed lines are 3-coordinated  $Cd^{2+}$ ; d) the  $C_3$ -axis that is perpendicular to the crystallographic layers of A-D.

### 3.3.2. Theoretical Model for Cadmium Selenide/Cadmium Sulfide Core/Shell QDs

In the previous section, we connected experimental result for magic size CdSe and stated that magic size CdS have similar bulk crystal structure.<sup>24</sup> However, adding an additional monolayer on the surface of  $(\text{CdX})_{33}$ ,  $\text{X} = \text{S}$  or  $\text{Se}$ , resulting in  $(\text{CdSe})_{111}$  would dramatically increase the computational cost.<sup>21</sup> With passivating ligands, this increase by a single monolayer would result in the system going from  $\text{Cd}_{33}\text{Se}_{33}(\text{NH}_2\text{CH}_3)_{21}$  to  $\text{Cd}_{111}\text{Se}_{111}(\text{NH}_2\text{CH}_3)_{78}$ . However, we suspect that the irreversible bleaching is likely caused by surface passivation of thiolate on the “giant” CdSe/CdS core/shell QDs.<sup>35-36</sup> Thus, we will investigate the surface of  $(\text{CdS})_{33}$  QDs with the assumption that if there are surface-associated trap states, these trap states would appear within the band gap of the light emitting core and will cause non-radiative relaxation through surface mediated states. This assumption is illustrated in Figure 3.4, where the bright transition of the core is no longer the lowest excited state. Therefore, simulating magic size QDs would provide a reasonable model for studying the formation of surface trap states in the “giant” CdSe/CdS core/shell QDs.<sup>35-37</sup>

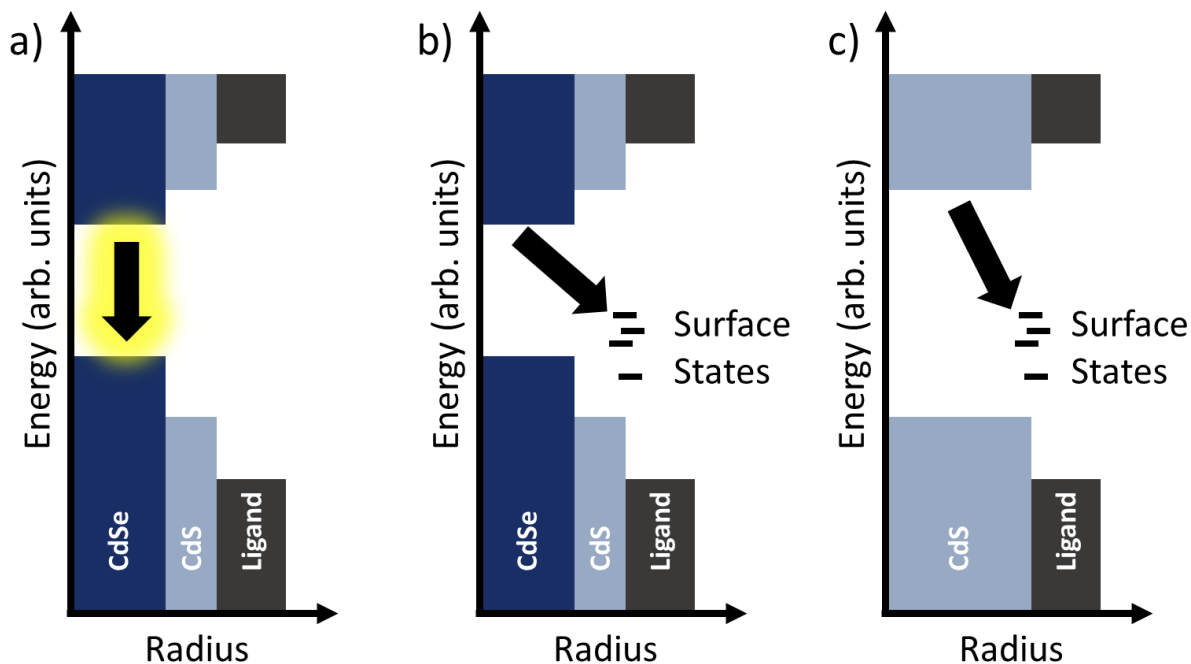


Figure 3.4. Schematic band structure of CdSe/CdS core/shell QDs. a) emissive CdSe core without surface trap states; b) introducing surface trap states results in non-emissive QDs; c) neglecting the CdSe core result in non-emissive QD.

### 3.3.3. Experimental and Theoretical Model for PbX/CdX, X = S or Se, Core/Shell QDs

The synthesis of the PbSe/CdSe QDs is performed by reactive ions exchange, where surface  $\text{Pb}^{2+}$  ions are replaced by  $\text{Cd}^{2+}$  ions through ion exchange resulting in the core/shell structure. The ion exchange also reduces the number of vacant ions sites in the lattice. In our work, the magic size  $(\text{PbX})_{68}$ , X = S or Se, was used as the initial structure before ion exchange resulting in  $(\text{PbX})_{16}(\text{CdX})_{52}$ , X = S or Se, core/shell QDs, as illustrated in Figure 3.5. The homogenous PbSe magic size QDs<sup>38</sup> have been simulated directly to study the photophysics of charged carriers.<sup>21, 30, 32, 39</sup>

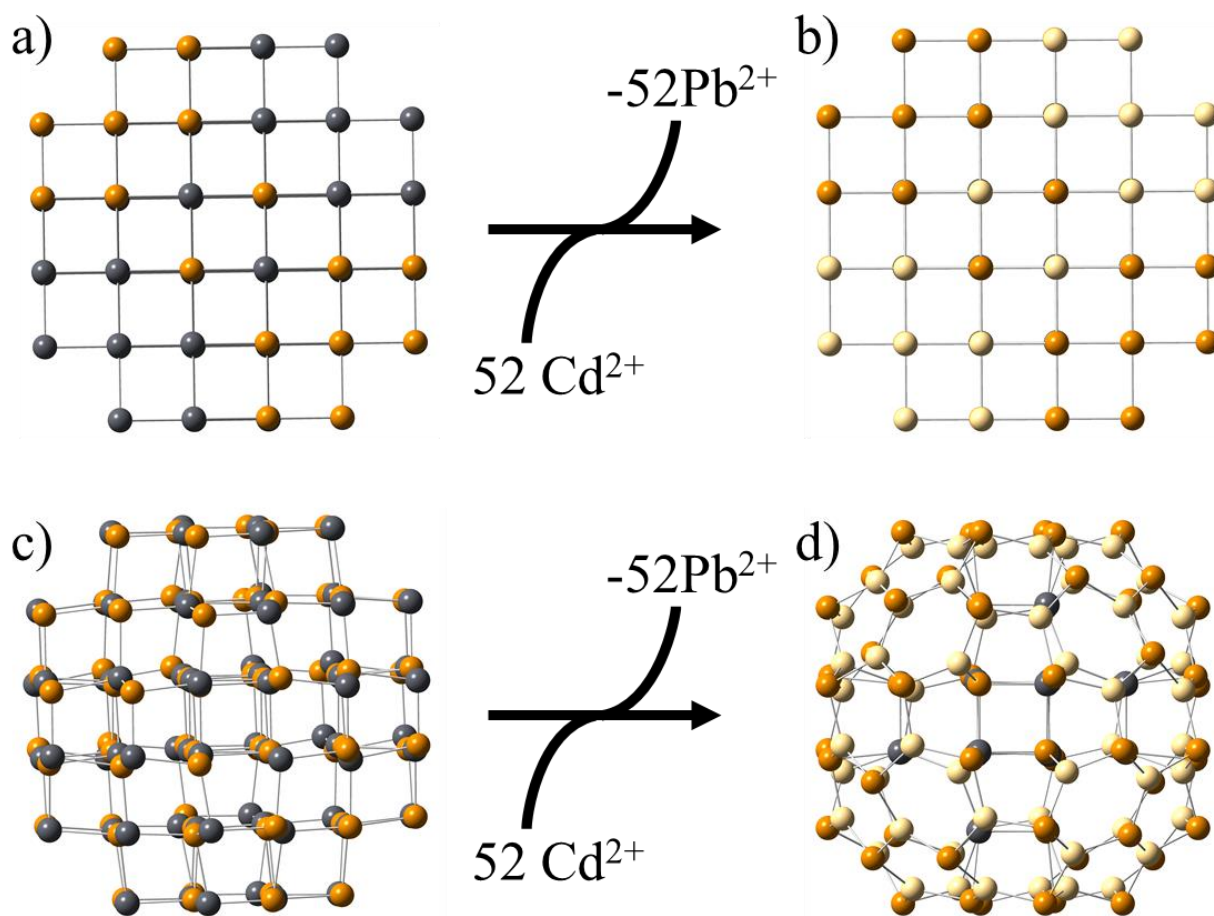


Figure 3.5. Ion exchange for magic size  $(\text{PbSe})_{68}$  creating  $(\text{PbSe})_{16}/(\text{CdSe})_{52}$  core/shell QDs. a) magic size  $(\text{PbSe})_{68}$  QDs cut from bulk; b) substituting surface  $\text{Pb}^{2+}$  by  $\text{Cd}^{2+}$  in magic size  $(\text{PbSe})_{68}$  QDs from bulk; c) optimized magic size  $(\text{PbSe})_{68}$  QD; d) optimized  $(\text{PbSe})_{16}/(\text{CdSe})_{52}$  core/shell QDs.

### 3.3.4. Methodology Employed for Ground State Optimization and Absorption

In section 2.4., we outlined the open research questions we will address in this thesis. In our calculations on CdSe and CdS magic size QDs we utilized Gaussian09<sup>40</sup> and Gaussian16<sup>41</sup> software packages to perform DFT and TDDFT calculations with the PBE0<sup>15</sup> functional and mixed basis sets LANL2DZ (Cd, S and Se atoms)<sup>16</sup> and 6-31g\* (H, C, and N).<sup>17, 42</sup> This methodology has been utilized for CdSe and CdS QDs.<sup>28</sup> Solvent effects were implicitly included via the Conductor Polarized Continuum Model (CPCM)<sup>43-44</sup> as implemented in Gaussian09<sup>40</sup> and Gaussian16.<sup>41</sup> Utilizing the methodology provides the total energy, electronic energies and

orbitals, and excited state energies with their corresponding oscillator strengths via TDDFT. The total energy is used to compute the  $B_e$  of the ligands to the surface of the QD being investigated. The impact of surface passivation on the electronic structure is primarily investigated by either density of states (DOS) or projected DOS (PDOS), PDOS is the procedure where the electronic states are projected onto portions of the system. PDOS are generated by broadening the electronic states by a weighted gaussian broadening:

$$PDOS_{Fragment}(\varepsilon) = N \sum_{i=1} F_{Fragment,i} \exp \left[ -\frac{1}{2} \left( \frac{\varepsilon - \varepsilon_i}{\sigma} \right)^2 \right] \quad (3.24.)$$

Where  $PDOS_{Fragment}(\varepsilon)$  is the PDOS of a specific fragment,  $N$  is the gaussian normalization factor,  $F_{Fragment,i}$  is the amount that a specific fragment contributes to the  $i^{\text{th}}$  electronic state,  $\varepsilon_i$  is the energy of the  $i^{\text{th}}$  electronic state and  $\sigma$  is the line-width of the Gaussian. PDOS can aid in understanding the system's photophysical properties because there is spatial information encoded into the spectra when projected the electron density on fragments (portions) of the system. This spatial information can provide an intuitive understanding of whether the QD is likely to be emissive, emissive systems should have the edges of the VB and CB located on the same portion of the molecule because the oscillator strength is proportional to the overlap of the electron and hole squared.

Investigating the excited state via TDDFT provides the energy and oscillator strength of the transitions and the contribution of orbitals to the optical transitions by diagonalizing the Casida equation.<sup>20</sup> The energy and oscillator strength of optical excitations are similarly broadened as PDOS to generate the absorption spectra ( $Abs(\varepsilon)$ ) but the  $F_{Fragment,i}$  is replaced by the oscillator of the transition:

$$Abs(\varepsilon) = N \sum_{i=1} f_i \exp \left[ -\frac{1}{2} \left( \frac{\varepsilon - \varepsilon_i}{\sigma} \right)^2 \right] \quad (3.25.)$$



Where  $f_i$  is the oscillator strength of the  $i^{\text{th}}$  optical transition. Characterizing the nature of the transition by comparing multiple molecule orbitals (MOs) is uncomfortable for transitions where many MOs contribute. To elevate this discomfort, we will compute the Natural Transition Orbitals (NTOs) that performs a rotation in the basis set that typically results in one or two transition orbitals that characterize the optical transition.<sup>45</sup> The visualization of MOs and NTOs was performed in VMD with isosurface value of 0.02.<sup>46</sup> Visualization of the geometry obtained from geometry optimization was done in VMD,<sup>46</sup> Jmol<sup>47</sup> and GaussView 5.<sup>48</sup>

### 3.3.5. Methodology Employed for Charge Carrier Cooling

The simulation of charge carrier cooling was performed using the NAMD described in section 3.2.3.2, here we will provide the specifics on our calculations and add additional justification that the independent particle approximation is valid for PbX/CdX, X = S or Se, core/shell QDs.

We will first provide the specifics of our NAMD calculations that are in the basis of adiabatic orbitals, with the adiabatic orbitals obtained from the Vienna ab initio simulation package (VASP) plane wave quantum mechanical software package<sup>49</sup> utilizing the PBE GGA functional<sup>13</sup> and projector-augmented wave (PAW) pseudopotentials<sup>50</sup> at the gamma k-point. There is at least 8 Å of vacuum between the repeating images of the core/shell QDs. The BOA GS MD trajectory was prepared by optimizing the core/shell QDs to have less than 0.01 eV/Å forces on each atom, then the systems was heated to 300K until thermal equilibrium was reached ( $\pm 25\text{K}$ ) by rescaling the ions' velocities utilizing energy conserving dynamics.<sup>21</sup> This was then propagated for 4 ps with 5 fs time-steps using BOA GS MD. The obtained trajectory was then split into 300 initial conditions for the ensemble used in the FSSH NAMD trajectory. We investigated 80 KS orbitals states above and below the band edges; 80 states for both the electron

and hole. NAMD based on FSSH were then performed on the 300 trajectories, afterwards the ensemble averaging was conducted to obtain observables of interest.

It has been reported for  $(\text{CdSe})_{33}$  QDs that the absorption spectrum computed by single-particle KS (SP-KS) and linear response TDDFT have similar spectral features and the peaks are only shifted by a constant.<sup>22</sup> This spectral shift could result in overestimating the NACTs because NACTs are inversely proportional to the difference in energy gaps. Figure 3.6 compares the absorption spectra of  $\text{PbX/CdX}$ ,  $X = \text{S or Se}$ , core/shell QDs calculated by TDDFT (implemented in Gaussian 16 software)<sup>41</sup> at the PBE and PBE0 functional with LANL2DZ basis sets to the SP-KS absorption spectrum obtained by PBE and plane wave basis set in VASP. There is a more complicated relationship between the SP-KS and TDDFT approach compared to the clear trends for  $(\text{CdSe})_{33}$  QDs. The spectral features of the SP-KS and TDDFT are similar, although the energy of the peaks is shifted non-linearly going from SP-KS to TDDFT. The second band indicated by the arrows in Figure 3.6. are comprised of the transitions between  $1\text{P}_h - 1\text{S}_e$  or  $1\text{S}_h - 1\text{P}_e$ . The energy sub-gaps for  $\text{PbS/CdSe}$  core/shell QDs in Figure 3.7. at the PBE0 level and local basis set are larger compared to PBE utilizing local or plane wave basis sets. This explains why the second peak for  $\text{PbS/CdS}$  using TDDFT within the PBE0 local basis set is blue-shifted compared to PBE predicted energies. The first bright peak originates from the  $1\text{D}_h - 1\text{S}_e$  transitions; the energy of this transition increases with more advanced methodology because of the sub-gaps increase. Comparing the second and first bright optical bands show a more complicated relationship than a constant shift observed for the  $(\text{CdSe})_{33}$  QDs but the overall trend is consistent with the ground state electronic energies.<sup>22</sup> As such, we conclude that SP-KS approach is justified for describing the excited state properties of  $\text{PbX/CdX}$ ,  $X = \text{S or Se}$ , core/shell QDs because there is similarities in the absorption spectrum comparing SP-KS and

linear response TDDFT. The main difference between the spectrum originate from the energy difference of bands for  $1D_h$ ,  $1P_h$ ,  $1S_h$ ,  $1S_e$  and  $1P_e$ . Utilizing the SP-KS approach within the NAMD method significantly reduces the computational cost of NAMD enabling us to investigate the carrier cooling in  $PbX/CdX$ ,  $X = S$  or  $Se$ , core/shell QDs.

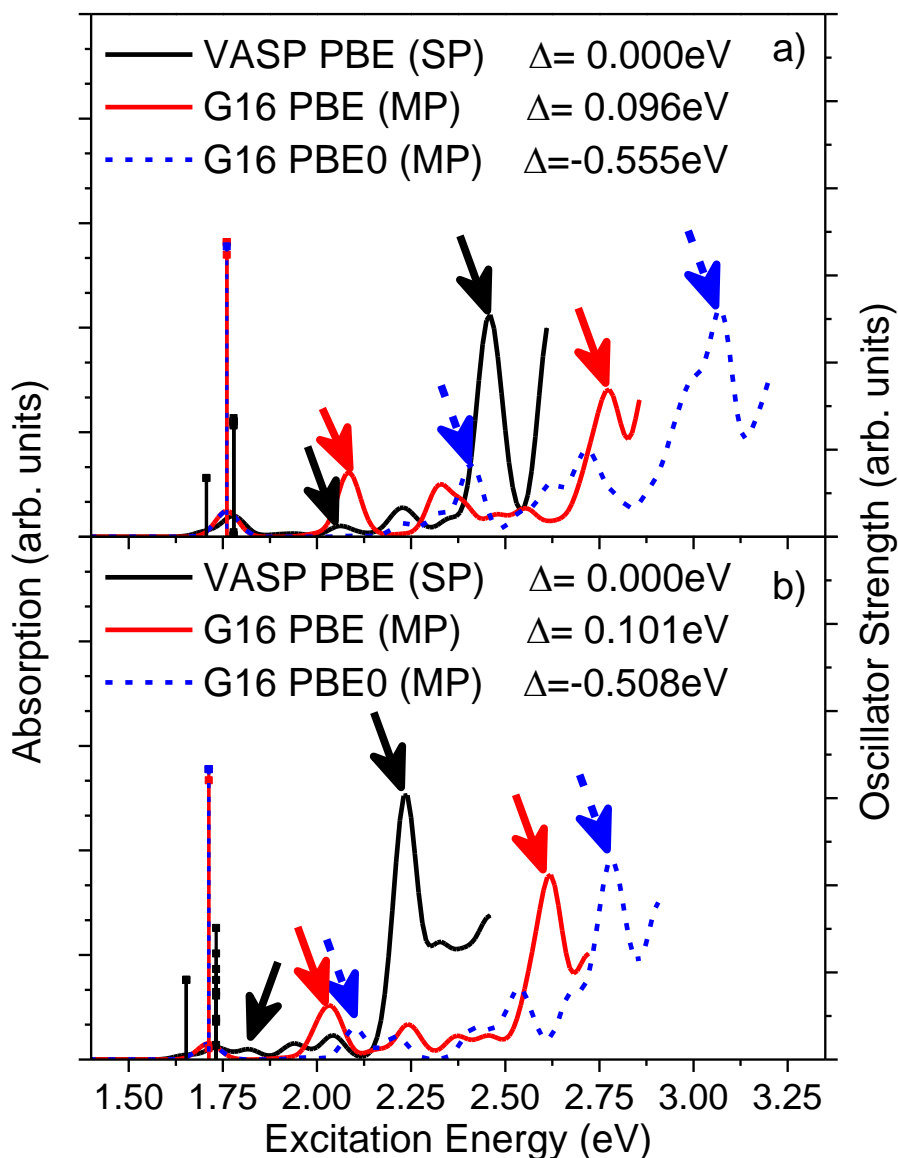


Figure 3.6. Comparing single-particle (SP) and many-particle (MP) absorption spectrum for  $(PbX)_{16}/(CdX)_{52}$ ,  $X = S$  or  $Se$ , core/shell QDs. The average energies of the transitions in the first peaks are shifted to the single-particle average energy and the oscillator strength is normalized by dividing all oscillator strength by the total oscillator strengths relative to the first peak. a)  $X = S$  b)  $X = Se$ .

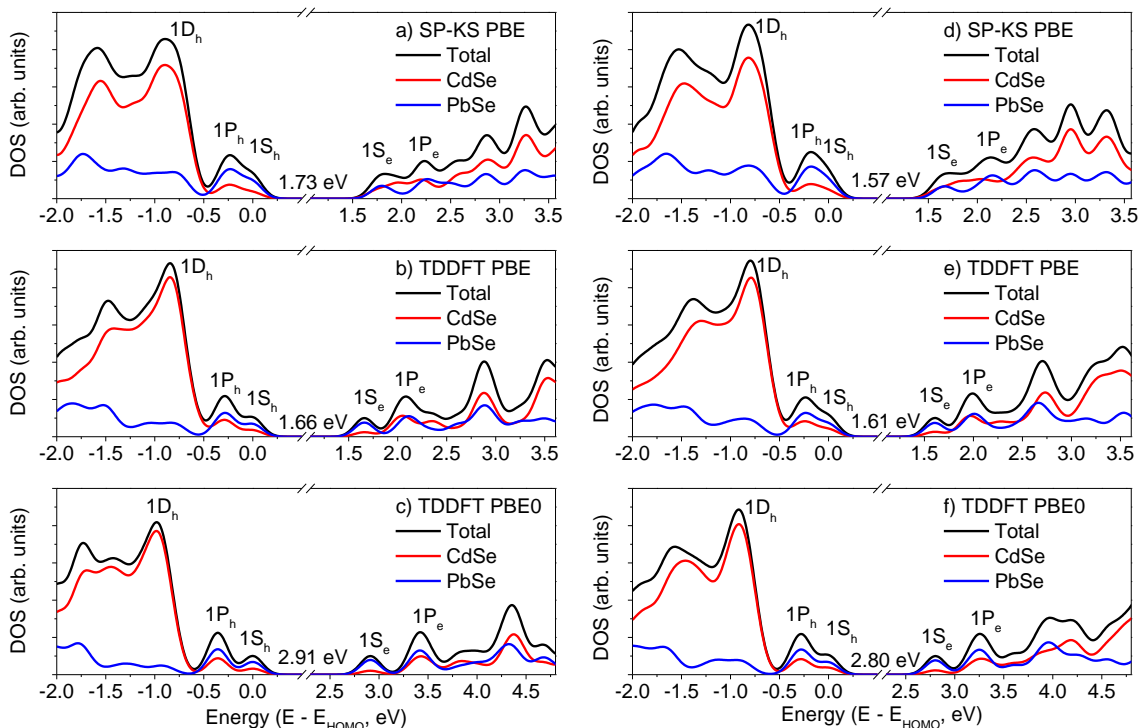


Figure 3.7. PDOS for PbS/CdS (a-c) and PbSe/CdSe (d-f) core/shell QDs.

### 3.4. References

1. Hohenberg, P.; Kohn, W. Inhomogeneous Electron Gas. *Phys. Rev.* **1964**, *136* (3B), B864-B871.
2. Runge, E.; Gross, E. K. Density-functional theory for time-dependent systems. *Phys. Rev. Lett.* **1984**, *52* (12), 997.
3. van Leeuwen, R. Mapping from densities to potentials in time-dependent density-functional theory. *Phys. Rev. Lett.* **1999**, *82* (19), 3863.
4. Casida, M. E. Time-dependent density functional response theory for molecules. In *Recent Advances In Density Functional Methods: (Part I)*, World Scientific: 1995; pp 155-192.
5. Marques, M. A.; Gross, E. K. Time-dependent density functional theory. *Annu. Rev. Phys. Chem.* **2004**, *55*, 427-455.
6. Craig, C. F.; Duncan, W. R.; Prezhdo, O. V. Trajectory surface hopping in the time-dependent Kohn-Sham approach for electron-nuclear dynamics. *Phys. Rev. Lett.* **2005**, *95* (16), 163001.
7. Parandekar, P. V.; Tully, J. C. Mixed quantum-classical equilibrium. *J. Chem. Phys.* **2005**, *122* (9), 094102.
8. Tully, J. C. Molecular dynamics with electronic transitions. *J. Chem. Phys.* **1990**, *93* (2), 1061-1071.
9. Hammes-Schiffer, S.; Tully, J. C. Proton transfer in solution: Molecular dynamics with quantum transitions. *J. Chem. Phys.* **1994**, *101* (6), 4657-4667.

10. Born, M.; Oppenheimer, R. Zur quantentheorie der molekeln. *Annalen der physik* **1927**, 389 (20), 457-484.
11. Garrick, R.; Natan, A.; Gould, T.; Kronik, L. Exact Generalized Kohn-Sham Theory for Hybrid Functionals. *Physical Review X* **2020**, 10 (2), 021040.
12. Perdew, J. P.; Ruzsinszky, A.; Tao, J.; Staroverov, V. N.; Scuseria, G. E.; Csonka, G. I. Prescription for the design and selection of density functional approximations: More constraint satisfaction with fewer fits. *J. Chem. Phys.* **2005**, 123 (6), 062201.
13. Perdew, J. Electronic Structure of Solids' 91, edited by Ziesche, P. and Eschrig, H.(Berlin: Akademie-Verlag) p. 11; Perdew, JP and Wang, Y., 1992. *Phys. Rev. B* **1991**, 45 (13), 244.
14. Perdew, J. P.; Ernzerhof, M.; Burke, K. Rationale for mixing exact exchange with density functional approximations. *J. Chem. Phys.* **1996**, 105 (22), 9982-9985.
15. Perdew, J. P.; Burke, K.; Ernzerhof, M. Generalized gradient approximation made simple. *Phys. Rev. Lett.* **1996**, 77 (18), 3865.
16. Hay, P. J.; Wadt, W. R. Ab initio effective core potentials for molecular calculations. Potentials for the transition metal atoms Sc to Hg. *J. Chem. Phys.* **1985**, 82 (1), 270-283.
17. Ditchfield, R.; Hehre, W. J.; Pople, J. A. Self-consistent molecular-orbital methods. IX. An extended Gaussian-type basis for molecular-orbital studies of organic molecules. *J. Chem. Phys.* **1971**, 54 (2), 724-728.
18. Paier, J.; Hirschl, R.; Marsman, M.; Kresse, G. The Perdew–Burke–Ernzerhof exchange–correlation functional applied to the G2-1 test set using a plane-wave basis set. *J. Chem. Phys.* **2005**, 122 (23), 234102.
19. Runge, E.; Gross, E. K. U. Density-Functional Theory for Time-Dependent Systems. *Phys. Rev. Lett.* **1984**, 52 (12), 997-1000.
20. Petersilka, M.; Gossmann, U. J.; Gross, E. K. U. Excitation Energies from Time-Dependent Density-Functional Theory. *Phys. Rev. Lett.* **1996**, 76 (8), 1212-1215.
21. Kilina, S. V.; Kilin, D. S.; Prezhdo, O. V. Breaking the phonon bottleneck in PbSe and CdSe quantum dots: time-domain density functional theory of charge carrier relaxation. *ACS Nano* **2009**, 3 (1), 93-99.
22. Fischer, S. A.; Crotty, A. M.; Kilina, S. V.; Ivanov, S. A.; Tretiak, S. Passivating ligand and solvent contributions to the electronic properties of semiconductor nanocrystals. *Nanoscale* **2012**, 4 (3), 904-914.
23. Kilina, S.; Ivanov, S.; Tretiak, S. Effect of surface ligands on optical and electronic spectra of semiconductor nanoclusters. *J. Am. Chem. Soc.* **2009**, 131 (22), 7717-7726.
24. Kasuya, A.; Sivamohan, R.; Barnakov, Y. A.; Dmitruk, I. M.; Nirasawa, T.; Romanyuk, V. R.; Kumar, V.; Mamykin, S. V.; Tohji, K.; Jeyadevan, B. Ultra-stable nanoparticles of CdSe revealed from mass spectrometry. *Nat. Mater.* **2004**, 3 (2), 99-102.
25. Kilina, S.; Velizhanin, K. A.; Ivanov, S.; Prezhdo, O. V.; Tretiak, S. Surface Ligands Increase Photoexcitation Relaxation Rates in CdSe Quantum Dots. *ACS Nano* **2012**, 6 (7), 6515-6524.
26. Kilina, S. V.; Tamukong, P. K.; Kilin, D. S. Surface Chemistry of Semiconducting Quantum Dots: Theoretical Perspectives. *Acc. Chem. Res.* **2016**, 49 (10), 2127-2135.
27. Puzder, A.; Williamson, A.; Gygi, F.; Galli, G. Self-healing of CdSe nanocrystals: first-principles calculations. *Phys. Rev. Lett.* **2004**, 92 (21), 217401.

28. Albert, V. V.; Ivanov, S. A.; Tretiak, S.; Kilina, S. V. Electronic structure of ligated cdse clusters: Dependence on dft methodology. *J. Phys. Chem. C* **2011**, *115* (32), 15793-15800.
29. Cui, P.; Tamukong, P. K.; Kilina, S. Effect of Binding Geometry on Charge Transfer in CdSe Nanocrystals Functionalized by N719 Dyes to Tune Energy Conversion Efficiency. *ACS Appl. Nano Mater.* **2018**, *1* (7), 3174-3185.
30. Kamisaka, H.; Kilina, S. V.; Yamashita, K.; Prezhdo, O. V. Ab initio study of temperature and pressure dependence of energy and phonon-induced dephasing of electronic excitations in CdSe and PbSe quantum dots. *J. Phys. Chem. C* **2008**, *112* (21), 7800-7808.
31. Kilina, S.; Cui, P.; Fischer, S. A.; Tretiak, S. Conditions for directional charge transfer in CdSe quantum dots functionalized by Ru (II) polypyridine complexes. *J. Phys. Chem. Lett.* **2014**, *5* (20), 3565-3576.
32. Kilina, S. V.; Kilin, D. S.; Prezhdo, V. V.; Prezhdo, O. V. Theoretical study of electron-phonon relaxation in PbSe and CdSe quantum dots: evidence for phonon memory. *J. Phys. Chem. C* **2011**, *115* (44), 21641-21651.
33. Munro, A. M.; Chandler, C.; Garling, M.; Chai, D.; Popovich, V.; Lystrom, L.; Kilina, S. Phenylthiocarbamate Ligands Decompose During Nanocrystal Ligand Exchange. *J. Phys. Chem. C* **2016**, *120* (51), 29455-29462.
34. Tamukong, P. K.; Peiris, W. D.; Kilina, S. Computational insights into CdSe quantum dots' interactions with acetate ligands. *Phys. Chem. Chem. Phys.* **2016**, *18* (30), 20499-20510.
35. Orfield, N. J.; Majumder, S.; McBride, J. R.; Yik-Ching Koh, F.; Singh, A.; Bouquin, S. J.; Casson, J. L.; Johnson, A. D.; Sun, L.; Li, X. Photophysics of thermally-assisted photobleaching in “giant” quantum dots revealed in single nanocrystals. *ACS Nano* **2018**, *12* (5), 4206-4217.
36. Jeong, S.; Achermann, M.; Nanda, J.; Ivanov, S.; Klimov, V. I.; Hollingsworth, J. A. Effect of the thiol- thiolate equilibrium on the photophysical properties of aqueous CdSe/ZnS nanocrystal quantum dots. *J. Am. Chem. Soc.* **2005**, *127* (29), 10126-10127.
37. Pal, B. N.; Ghosh, Y.; Brovelli, S.; Laocharoensuk, R.; Klimov, V. I.; Hollingsworth, J. A.; Htoon, H. ‘Giant’CdSe/CdS core/shell nanocrystal quantum dots as efficient electroluminescent materials: strong influence of shell thickness on light-emitting diode performance. *Nano Lett.* **2012**, *12* (1), 331-336.
38. Evans, C. M.; Guo, L.; Peterson, J. J.; Maccagnano-Zacher, S.; Krauss, T. D. Ultrabright PbSe magic-sized clusters. *Nano Lett.* **2008**, *8* (9), 2896-2899.
39. Kilina, S. V.; Craig, C. F.; Kilin, D. S.; Prezhdo, O. V. Ab initio time-domain study of phonon-assisted relaxation of charge carriers in a PbSe quantum dot. *J. Phys. Chem. C* **2007**, *111* (12), 4871-4878.
40. Frisch, M. J.; Trucks, G. W.; Schlegel, H. B.; Scuseria, G. E.; Robb, M. A.; Cheeseman, J. R.; Scalmani, G.; Barone, V.; Mennucci, B.; Petersson, G. A., et al. *Gaussian 09*, Gaussian, Inc.: Wallingford, CT, USA, 2009.
41. Frisch, M. J.; Trucks, G. W.; Schlegel, H. B.; Scuseria, G. E.; Robb, M. A.; Cheeseman, J. R.; Scalmani, G.; Barone, V.; Petersson, G. A.; Nakatsuji, H., et al. *Gaussian 16 Rev. C.01*, Wallingford, CT, 2016.

42. Francel, M. M.; Pietro, W. J.; Hehre, W. J.; Binkley, J. S.; Gordon, M. S.; DeFrees, D. J.; Pople, J. A. Self-consistent molecular orbital methods. XXIII. A polarization-type basis set for second-row elements. *J. Chem. Phys.* **1982**, *77* (7), 3654-3665.
43. Barone, V.; Cossi, M.; Tomasi, J. Geometry optimization of molecular structures in solution by the polarizable continuum model. *J. Comput. Chem.* **1998**, *19* (4), 404-417.
44. Cossi, M.; Barone, V.; Cammi, R.; Tomasi, J. Ab initio study of solvated molecules: a new implementation of the polarizable continuum model. *Chem. Phys. Lett.* **1996**, *255* (4-6), 327-335.
45. Martin, R. L. Natural transition orbitals. *J. Chem. Phys.* **2003**, *118* (11), 4775-4777.
46. Humphrey, W.; Dalke, A.; Schulten, K. VMD: visual molecular dynamics. *J. Mol. Graph.* **1996**, *14* (1), 33-38.
47. Hanson, R. M.; Prilusky, J.; Renjian, Z.; Nakane, T.; Sussman, J. L. JSmol and the next-generation web-based representation of 3D molecular structure as applied to proteopedia. *Israel Journal of Chemistry* **2013**, *53* (3-4), 207-216.
48. Hratchian, H.; Dennington II, R.; Keith, T.; Millam, J.; Nielsen, A.; Holder, A.; Hiscocks, J. GaussView 5 Reference **2009**.
49. Kresse, G.; Furthmüller, J. Efficiency of ab-initio total energy calculations for metals and semiconductors using a plane-wave basis set. *Comput. Mater. Sci.* **1996**, *6* (1), 15-50.
50. Vanderbilt, D. Soft self-consistent pseudopotentials in a generalized eigenvalue formalism. *Phys. Rev. B* **1990**, *41* (11), 7892.

#### 4. DECOMPOSITION OF PHENYLDITHIOCARBAMATE LIGANDS DURING LIGAND EXCHANGE

As stated in section 2.4, this chapter will investigate the effect that ligand exchange has on a PTC derivative. Due to the quasi-stable nature of PTC in protic solvents, such as methanol, methanol is used to cause the QDs to crash out of suspension in the colloidal mixture.<sup>1-3</sup> The PTC derivative considered in this study is triethylammonium 3,5-dimethylphenyldithiocarbamate ( $\text{TEA}^+\text{-DMPTC}^-$ ). The counter ion  $\text{TEA}^+$  can protonate the nitrogen in the aniline group resulting in bond cleavage producing TEA, 3,5-dimethylaniline (DMA), and carbon disulfide; these molecules are shown in Figure 4.1. The decomposition products of  $\text{TEA}^+\text{-DMPTC}^-$  can undergo L-type ligand exchange. However, the conventional “mass-action” mechanism assumes that only the PTC ligands exchange with “native” ligands.<sup>4-6</sup> Nonetheless, the decomposition products TEA and DMA could also exchange with “native” ligands could impact the photophysical properties of CdSe QDs in PV applications.



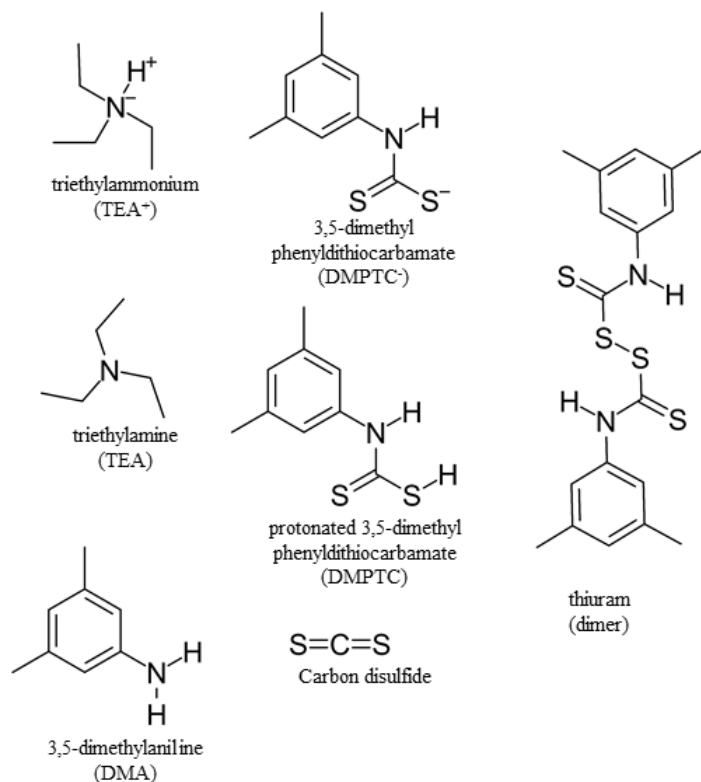


Figure 4.1. Molecular structure of TEA<sup>+</sup>-DMPTC<sup>-</sup> and its decomposition products that can be catalyzed by the QDs' surface.

#### 4.1. Motivation

Employing QDs as the photo-active material in LED and PV applications typically involves surface modification, this modification can be achieved by ligand exchange of the “native” ligands for ligands designed to improve the photophysical properties of the QDs.<sup>7-10</sup> For PV applications, the designed ligands enhance charge transfer that is responsible for generating the photocurrent of the device. One class of such ligands are PTC that have been widely investigated.<sup>11-18</sup> The Weiss group has reported that triethylammonium 4-phenothiazin-10-yl-dithiocarbamate (PTC-PTZ) results in a red-shift of the first optical band and sub-picosecond photoinduced hole transfer for QDs with PTC-PTZ passivating the surface while the carboxylic derivative 4-phenothiazin-10-yl-benzonic acid (BA-PTZ) does not couple to the QDs surface which decreases the hole transfer rates.<sup>18</sup> The red-shift of the first optical band has been

attributed to the delocalization of the hole into the PTC-PTZ ligand shell.<sup>12, 15-17</sup> The sub-picosecond hole transfer is important because this is comparable to the electron transfer, the comparable rates for the electron and hole transfer are crucial to prevent the building up of charge which leads to inefficient PV devices.<sup>19-21</sup> However, the ligand exchange process has a lack of fundamental understanding that could be problematic when implementing PTC derivatives in PV devices because it is unknown what ligands are passivating the surface.

To address this lack of fundamental knowledge, Munro and co-workers performed nuclear magnetic resonance (NMR) studies on free ligand and QDs after ligand exchange.<sup>22</sup> They studied two types of CdSe QDs amine and oleate passivated QDs to compare if the nature of the surface impacts ligands exchange because amine passivated QDs should undergo L-type ligand exchange while oleate passivated QDs undergo X-type ligand exchange.<sup>5</sup> In their NMR studies, they found that the free ligands undergo decomposition in both protic (methanol) and aprotic (chloroform) solvents with half-lives of 2 and 6 hours, respectively. The relative short half-life of 2 hours for methanol is significant because methanol is commonly used in ligand exchange.<sup>14</sup><sup>15</sup> The half-life was found by fitting the concentration of DMPTC obtained via NMR in methanol and chloroform to the pseudo-first-order integrated rate law, Figure 4.2.a. Conducting NMR on amine and oleate passivated QDs after ligand exchange shows that multiple peaks are not associated with the “native” ligands or DMPTC, which implies that the simple mass-action picture of ligands exchange of PTC derivatives does not capture ligand exchange fully. Interestingly, DMA appears to be coordinated to both amine and oleate synthesized QDs which means that the aniline derivative (DMA) tightly binds to the surface of stoichiometric (roughly 1:1 ratio of cations and anions, amine synthesized QDs) and non-stoichiometric (none 1:1 ratio of cations and anions, oleate synthesized QDs) surfaces, Figure 4.2.b.

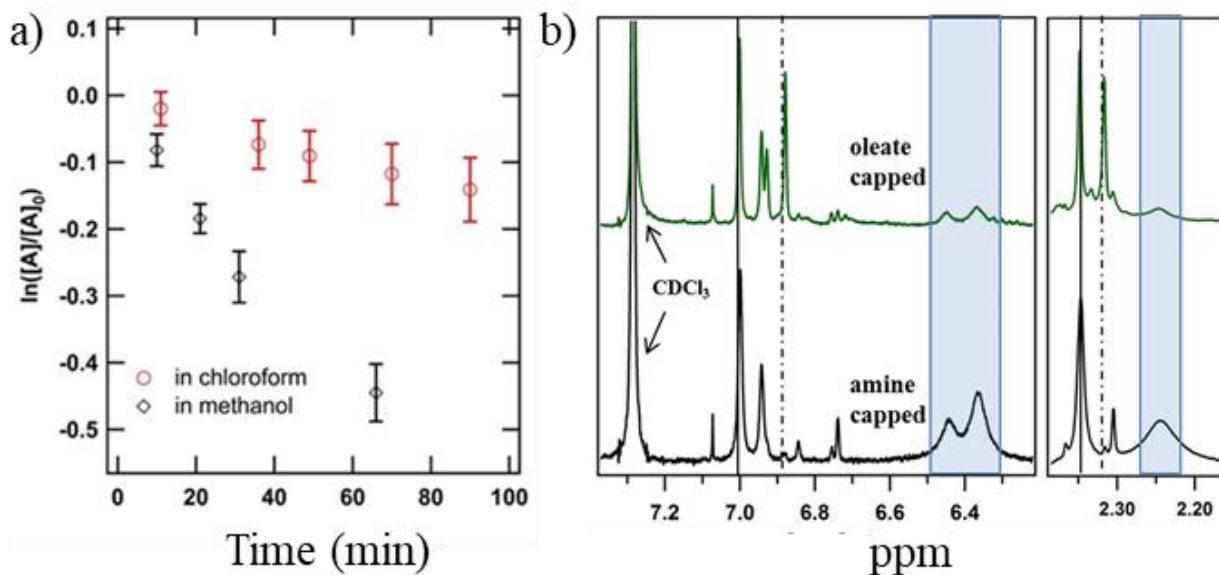


Figure 4.2.  $^1\text{H}$  NMR spectrum of free DMPTC and QDs after ligand exchange. a) kinetic study of the decomposition of DMPTC in chloroform and methanol b) signal after ligand exchange of oleate (green) and amine (black) synthesized QDs where the DMA peaks are denoted by blue shaded range, DMPTC, and thiram disulfide are represented by solid and dashed lines respectively. Adapted with permission from <sup>22</sup> Copyright 2016 American Chemical Society.

The experimental NMR study by Munro and co-workers<sup>22</sup> demonstrate that ligand exchange for PTC is not as simple as the mass-action picture, mass-action is where the QDs are exposed to high concentrations of the ligand of interest which results in desorption of the “native” ligand and adsorption of the ligand of interest. Here we will perform DFT simulations on the decomposition products and QD catalyzed products to further the fundamental knowledge of ligand exchange for the PTC class of ligands. The computational methodology utilized in this work is stated in section 3.3.4., where the calculations were performed by Gaussian09 on stoichiometric magic size  $(\text{CdSe})_{33}$  and non-stoichiometric  $\text{Cd}_{34}\text{Se}_{33}$  and  $\text{Cd}_{39}\text{Se}_{33}$  QDs.

## 4.2. Results and Discussion

Atomic-level simulations via DFT calculations can provide fundamental understanding into the binding of ligands to the surface of QDs synthesized and studied experimentally. QDs synthesized in oleate solvents are known to have Cd-enriched surfaces.<sup>5, 12, 23-25</sup> Thus, the magic

size  $(\text{CdSe})_{33}$  should be modified to simulate QDs with Cd-enriched surfaces, Tamukong and co-workers have addressed and studied acetate (model system for oleate ligands) passivated QDs by placing  $\text{Cd}^{2+}$  on the surface of magic size  $(\text{CdSe})_{33}$  QDs. They found that acetate ligands are the most stable when distributed around the surface of the QD with one passivating the non-stoichiometric  $\text{Cd}^{2+}$  ion.<sup>25</sup> We will use this method to generate  $\text{Cd}_{34}\text{Se}_{33}$ ,  $\text{Cd}_{35}\text{Se}_{33}$  and  $\text{Cd}_{39}\text{Se}_{33}$  Cd-enriched QDs synthesized in oleate solvents and magic size  $(\text{CdSe})_{33}$  QDs for QDs synthesized in amine solvents. The binding of DMPTC,  $\text{DMPTC}^-$  and the decomposition products of  $\text{TEA}^+\text{DMPTC}^-$  will be investigated by comparing the  $B_e$  of the ligands to QDs. We will first introduce a model ligand to reduce the computational cost of simulating the binding of DMPTC in its protonated and deprotonated form, followed by comparing the  $B_e$  of various ligands. In sections 4.2. through 4.4., the solvent used in the CPCM solvent model is chloroform because this is the solvent used to suspend the QD during ligand exchange. In section 4.5, the effect of methanol is investigated where we compute the  $B_e$  in both chloroform and methanol.

#### **4.2.1. Binding Modes of DMPTC to CdSe QDs**

When investigating ligands with multiple Lewis acidic atoms that can bind to the surface of the QD, the type of binding mode can dictate how the electronic properties will change upon passivation.<sup>25</sup> Here we studied three binding modes:<sup>25</sup> chelating between surface  $\text{Cd}^{2+}$ , bidentate and monodentate as illustrated in Figure 4.3.a-c. Monodentate binding is typical for ligands with only one Lewis acidic atom, such as TEA or DMA, Figure 4.3.d. In Figure 4.3., the  $\text{DMPTC}^-$  is represented by deprotonated vinylthiocarbamate ( $\text{VTC}^-$ ), Azpiroz and co-workers studied PTCs by simplifying it to aminomethanedithioic acid.<sup>11</sup> This simplification removes the aromatic portion of the molecule which facilitates hole transfer, simplifying DMPTC ligands will significantly reduce the computational cost of simulating QDs where the surface is fully

passivated by PTC derivatives. Here we analyzed the electron distribution via the natural bond orbitals (NBO) method<sup>26</sup> in a set of simplified models. The set of models investigated are aminomethanedithioic acid (hydrogen), methyl[sulfanyl(carbonothioyl)]amine (methyl), and ethenyl[sulfanyl(carbonothioyl)]amine (vinyl). The NBOs for the optimized ligands are shown in Figure 4.4. This figure shows that the electronic distribution of the reduced VTC<sup>-</sup> model is the most similar to DMPTC<sup>-</sup>. Thus, we will investigate the  $B_e$  for both protonated and deprotonated versions of VTC and DMPTC. This will be done with a single ligand passivating the bare magic size (CdSe)<sub>33</sub> QD, Figure 4.5.

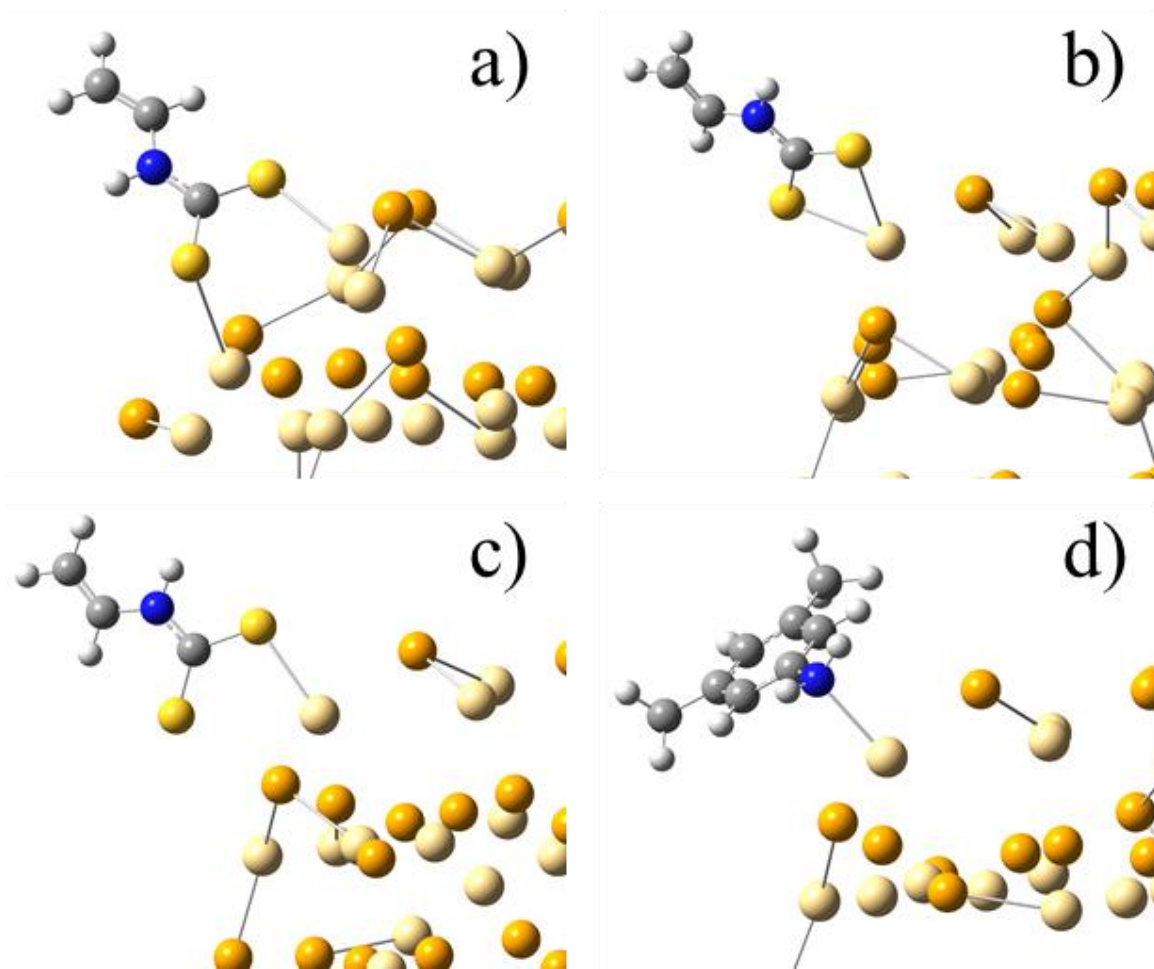


Figure 4.3. Binding Modes of ligands with two (a-c) and one (d) Lewis acidic atoms. a) bridging b) chelating c) monodentate d) monodentate. Adapted with permission from <sup>22</sup> Copyright 2016 American Chemical Society.

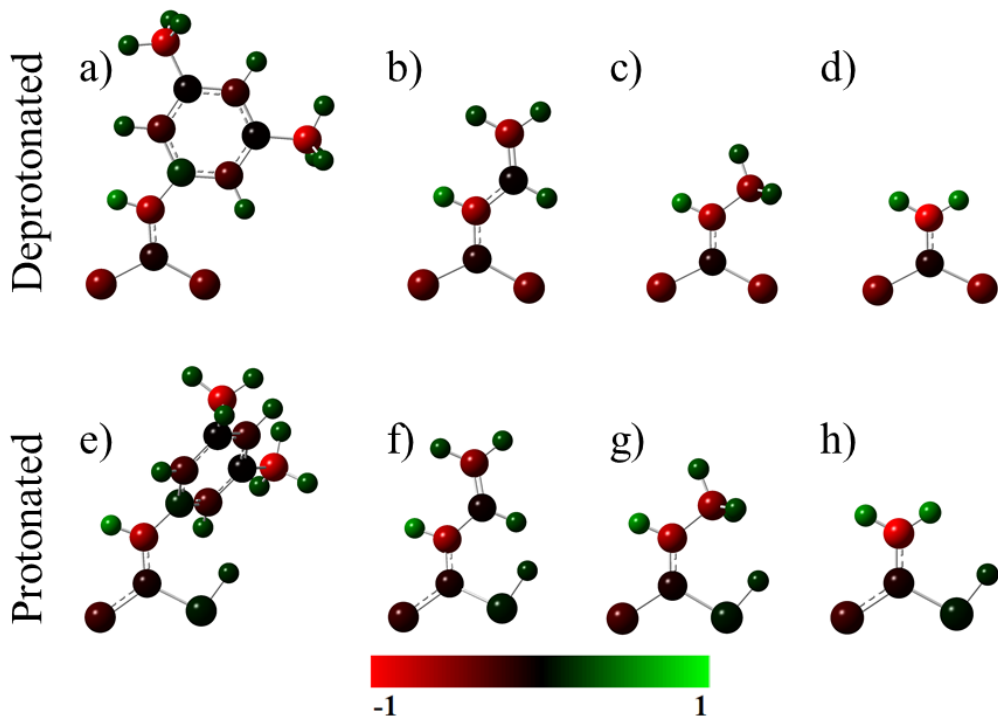


Figure 4.4. Natural bond orbitals (NBOs) of the deprotonated (a-d) and protonated (e-h) DMA and reduced ligands. Bright red (green) indicates atoms with negative (positive) charge. DMA panels a and e, VTC panels e and f, methyl panels c and g, and hydrogen panels d and h. Adapted with permission from <sup>22</sup> Copyright 2016 American Chemical Society.

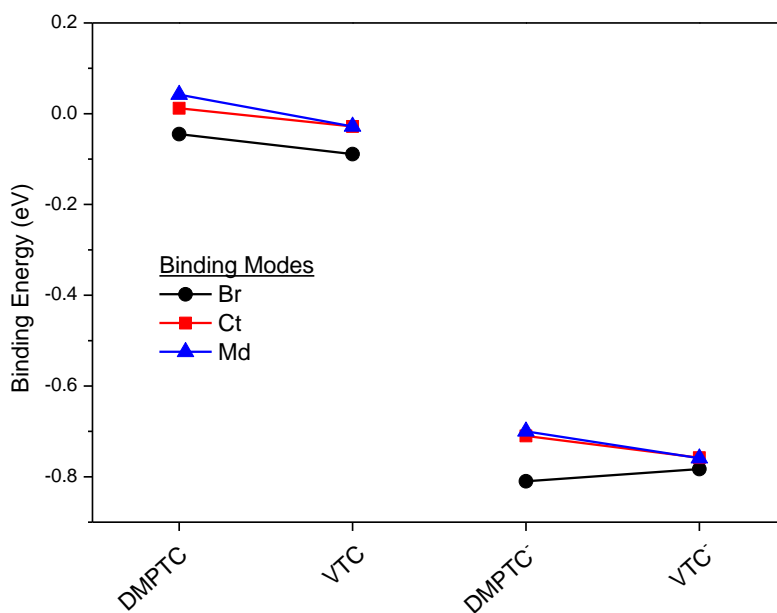


Figure 4.5. Comparing  $B_e$  of the protonated and deprotonated DMPTC and VTC for bridging (Br), chelating (Ct), and monodentate (Md) to bare magic size CdSe QD. Adapted with permission from <sup>22</sup> Copyright 2016 American Chemical Society.

From Figure 4.5, we can see that comparing to DMPTC, VTC systematically overestimates the  $B_e$  on the order of thermal fluctuation. DMPTC prefers to bind in the bridging mode but the difference between the other modes is on the order of thermal fluctuation that was observed by Azpiroz and co-workers, where their aminomethanedithioic acid reduced model interchanges between binding modes. This was not the case when they investigated formic acid (reduced model for oleate), where the structure remained in bridging mode.<sup>11</sup> The trend of very rigid binding of acetate ion to the surface of Cd-enriched QDs was also computationally predicted by Tamukong and co-workers; in their study, they found that acetate ions that balance the charge of the Cd-enriched QDs bind the strongest when distributed along the surface and when two acetate ions are on the non-stoichiometric  $Cd^{2+}$  the  $[Cd^{2+}(acetate^-)_2]$  complex weakly binds and can undergo Z-type ligand exchange.<sup>25</sup>

### **4.3. Influence of Neighboring Ligands on $B_e$ of $VTC^-$**

In the previous section, we have shown that VTC can be used to model the DMPTC ligand, which can significantly reduce the computational cost. In this section, we will use VTC and  $VTC^-$  to model ligand exchange on stoichiometric and non-stoichiometric CdSe QDs. This was done to investigate the effect of the neighboring ligands. First, we will consider passivating stoichiometric and non-stoichiometric CdSe QDs by 12  $VTC^-$ , then we will investigate the effect of neutral neighboring ligands.

#### **4.3.1. Charged $VTC^-$ Neighboring Ligands**

It has been reported that oleate synthesized QDs are Cd-enriched, while the positive charge of the surface is balanced by a shell of negatively charged ligands, such as oleate, acetate, and DMPTC.<sup>5, 12, 23-25</sup> Tamukong and co-workers showed that  $[Cd^{2+}(acetate^-)_2]$  weakly binds to the surface of the stoichiometric surface.<sup>25</sup> Here we investigate the  $B_e$  of  $VTC^-$  ligands to magic

size  $(\text{CdSe})_{33}$  and Cd-enriched  $\text{Cd}_{39}\text{Se}_{33}$  QDs, Figure 4.6. To balance the charge in the Cd-enriched QDs 3  $\text{VTC}^-$  were bounded to each layer resulting in 12  $\text{VTC}^-$  that balanced the 6  $\text{Cd}^{2+}$  ions. Using this model, we found that the  $B_e$  dependence on the specific layer roughly follows the intuitive trend of 2- and 3-coordinated  $\text{Cd}^{2+}$ , with the strongest ligand-QD interactions observed for 2-coordinated A and C layers. However, the  $B_e$  of  $\text{VTC}^-$  to the magic size QDs is highly repulsive due to the electrostatic repulsion of the neighboring ligands. In contrast, the  $\text{VTC}^-$  is strongly bond to the Cd-enriched QD resulting in large negative  $B_e$ . Additionally, the average  $B_e$  is significantly stronger compared to the individual  $B_e$  implying that there are strong intermolecular forces between the  $\text{VTC}^-$  ligands.

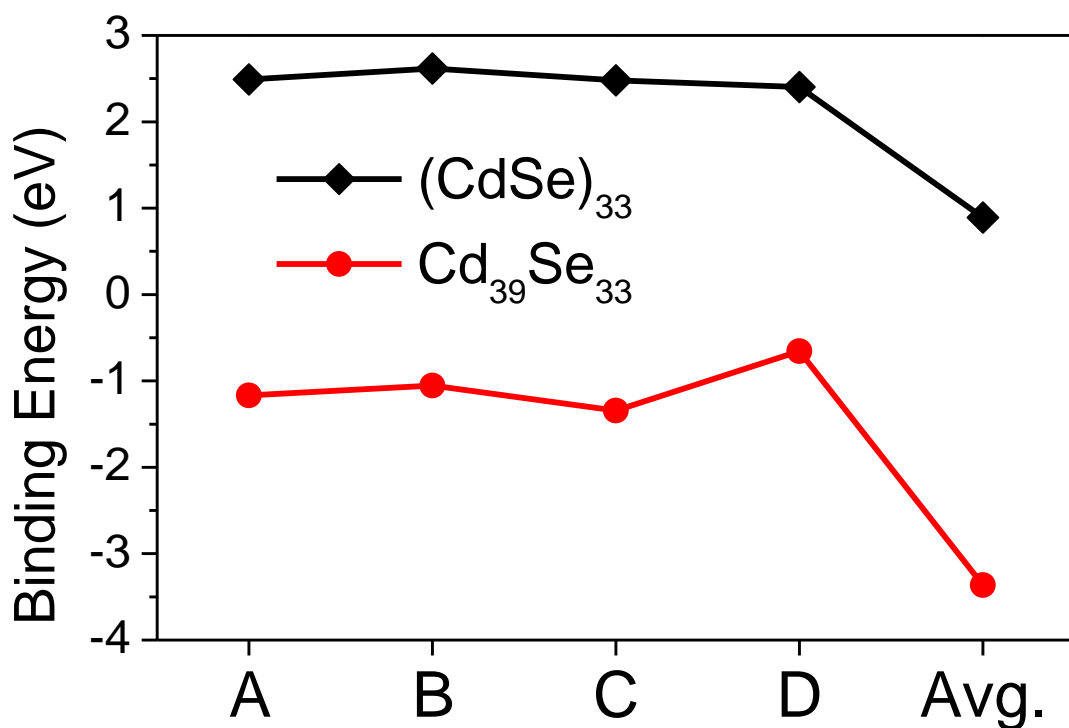


Figure 4.6.  $B_e$  of  $\text{VTC}^-$  to  $(\text{CdSe})_{33}$  and  $\text{Cd}_{39}\text{Se}_{33}$  QDs with 12  $\text{VTC}^-$  passivating the surface. Adapted with permission from <sup>22</sup> Copyright 2016 American Chemical Society.

#### 4.3.2. Neutral and Charged Neighboring Ligands

In this section, we will focus on the different stoichiometries of the QDs to investigate the effect of the QD's charge on the binding of  $\text{VTC}^-$  in the presence of various ligands. Comparing



the  $B_e$  for  $VTC^-$  surrounded by 3 TEA, we found nearly three times increase in the  $B_e$  going from -0.67 eV to -1.55 eV, Table 4.1. This dramatic increase in  $B_e$  is expected due to the increase in electrostatic forces between two optically charge ions. Comparing the  $B_e$  of  $VTC^-$  surrounded by 2 vinylamine (VA) to 2 DMA, there is a slight decrease in  $B_e$  which is likely the result of increased steric hindrance when including the functionalized phenyl ring. Comparing the  $B_e$  for the 2 VA to 2 acetate ions shows that the electrostatic repulsion between  $VTC^-$  and acetate decreases the  $B_e$  roughly by half going from -1.55 eV to -0.77 eV. Finally, when the ligand balances the charge of the QD, the  $B_e$  of  $VTC^-$  increases from -0.77 eV to -1.25 eV. From the  $B_e$  in Table 4.1, we can conclude that (1)  $VTC^-$  binds strongly to  $Cd_{33}Se_{33}$  and this binding increases when attached to  $Cd_{34}Se_{33}$  when surrounded by neutral ligands, (2) the  $B_e$  of  $VTC^-$  when surrounded by charged ligands significantly weakens the interaction with  $Cd_{33}Se_{33}$ , (3) and the weakened interaction can be increased when bound to non-stoichiometric QDs that balance the charge of the ligand shell.

Table 4.1. Binding of  $VTC^-$  to various CdSe QDs surrounded by charged and neutral ligands. Adapted with permission from <sup>22</sup> Copyright 2016 American Chemical Society.

	Binding Energy ( $B_e$ , eV)		
	$(CdSe)_{33}$	$Cd_{34}Se_{33}$	$Cd_{35}Se_{33}$
3 TEA	-0.67	-1.55	--
2 VA	--	-1.58	--
2 DMA	--	-1.55	--
2 acetate <sup>-</sup>	--	-0.77	--
3 acetate <sup>-</sup>	--	--	-1.25

#### 4.4. Comparing $B_e$ of DMPTC, $DMPTC^-$ and the Decomposition Products

To this point, we only investigated the interaction between CdSe QDs and DMPTC ( $VTC$ ) either protonated or deprotonated. Here we compute the  $B_e$  of the products of the decomposition and demonstrate that  $CS_2$ , dimer (thiruram disulfide DMPTC), and protonated

DMPTC weakly bind to the surface of the bare (CdSe)<sub>33</sub> QD, grey circles in Figure 4.7. This is in contrast with the relatively strong interaction between the QD and TPA, DMA (VMA), and DMPTC<sup>-</sup> (VTC<sup>-</sup>), grey circles in Figure 4.7. However, oleate binds significantly stronger compared to all the ligands investigated, except when a single DMPTC<sup>-</sup> binds to the surface of Cd<sub>34</sub>Se<sub>33</sub> QDs, black empty star in Figure 4.7.

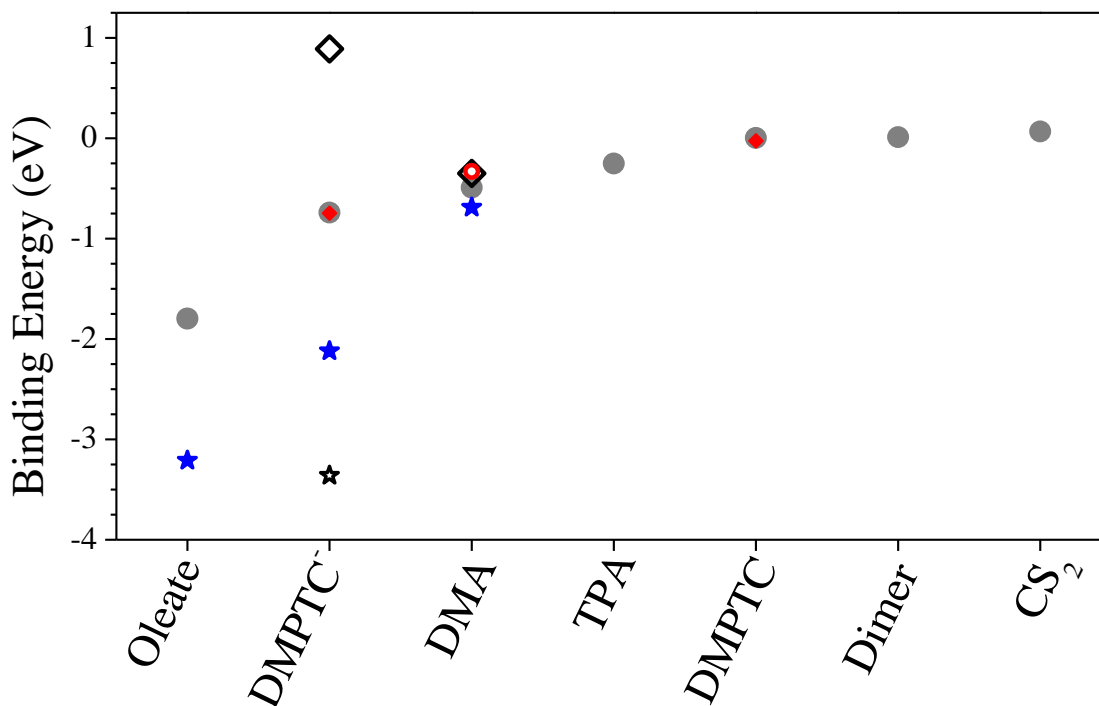


Figure 4.7 Average binding energy ( $B_e$ ) of ligand present in experimental studies computation in chloroform to stoichiometric and non-stoichiometric CdSe QDs. Grey circles (red diamonds) indicate binding of a single ligand (reduced ligand VMA or VTC) to the surface of bare (CdSe)<sub>33</sub>, empty black diamonds indicate fully passivated structure with the reduced ligand, blue (black empty) stars indicate binding of a single ligand (full passivation) to Cd<sub>34</sub>Se<sub>33</sub> (Cd<sub>39</sub>Se<sub>33</sub>) QDs. Adapted with permission from <sup>22</sup> Copyright 2016 American Chemical Society.

From Figure 4.7, we can conclude that during ligand exchange if TEA<sup>+</sup>DMPTC<sup>-</sup> undergo decomposition, then TEA and DMA are likely passivating the surface of the QD regardless of the surface stoichiometry. This is supported by the NMR data obtained by Munro and co-workers,<sup>22</sup> where DMA peaks were observed for both amine and oleate capped QDs. Our  $B_e$

prediction suggest that DMPTC<sup>-</sup> would strongly bind to the surface of Cd-enriched QDs.

However, NMR data does not show these peaks. This could be rationalized by the very strong electronic coupling, as reported by the Weiss Group,<sup>12, 15-18</sup> which could make the NMR peaks for DMPTC<sup>-</sup> unresolvable.

#### **4.5. Solvent Effects on Binding of DMPTC and DMPTC<sup>-</sup>**

The final simulations we performed was comparing the  $B_e$  of DMPTC and DMPTC<sup>-</sup> in methanol because methanol is a common solvent to cause precipitation of QDs is a critical step in ligand exchange. The precipitation of QDs is thought to be the result of surface ligands desorbing from the surface which results in the loss of the colloidal nature of the QDs. This idea is conferred by computing the  $B_e$  in methanol which results in the  $B_e$  of DMPTC<sup>-</sup> going from -0.74 eV (chloroform) to -0.039 eV (methanol). The  $B_e$  of DMPTC<sup>-</sup> is on the order of thermal fluctuation, Figure 4.8. The trend of decreasing the interaction between the ligand and the QD is also observed for DMPTC but to a lesser degree.

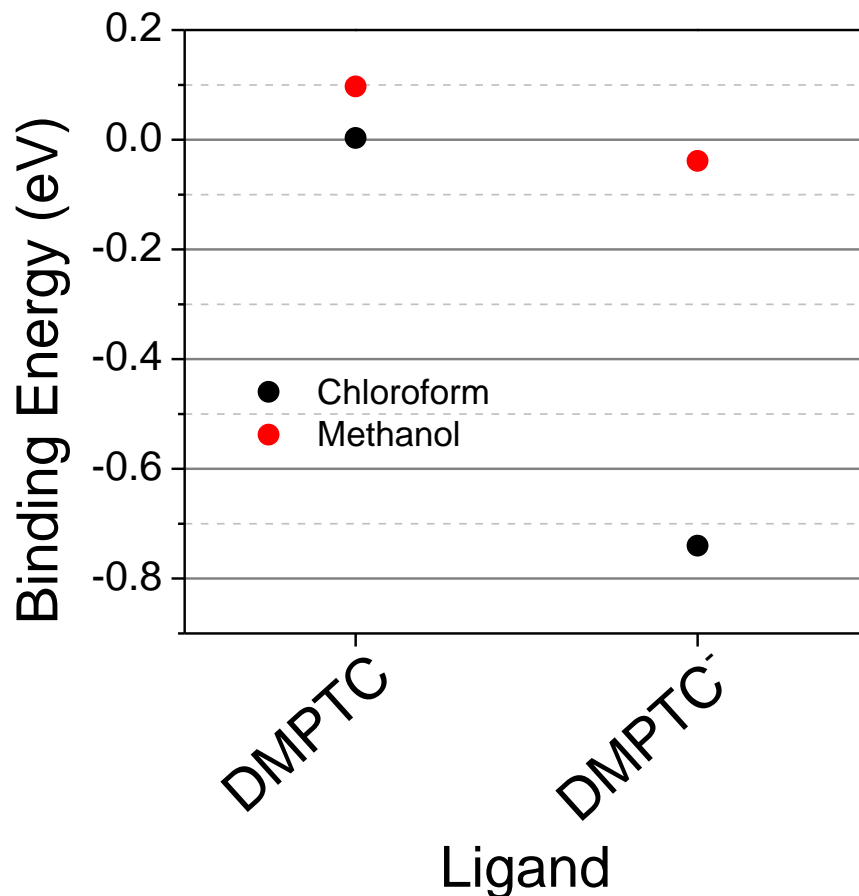


Figure 4.8. Binding energies of DMPTC and DMPTC<sup>-</sup> attached to the (CdSe)<sub>33</sub> calculated in methanol and chloroform solvents. Adapted with permission from <sup>22</sup> Copyright 2016 American Chemical Society.

#### 4.6. Conclusions

The process of ligand exchange of “native” ligand with DMPTC was investigated at the atomic level through DFT simulations of stoichiometric and non-stoichiometric CdSe QDs with various decomposition products of TEA<sup>+</sup>-DMPTC<sup>-</sup>, Figure 4.1. We found that DMPTC can be simplified to VTC which reduces the computational cost, while retaining the electronic distribution and predicting the  $B_e$  on the order of thermal fluctuations. This simplification allowed for investigating the effect of the surrounding ligands, where we found that VTC<sup>-</sup> prefers to bind the Cd-enriched surfaces and be surrounded by neutral ligands. When VTC<sup>-</sup> is

surrounded by charged ligands (acetate), the  $B_e$  is significantly reduced causing destabilization of the QD-ligand bond. We also found that the decomposition products, such as DMA and TEA, can strongly bind to the surface of the QD, which makes ligand exchange by PTC derivatives more complicated than the mass-action picture previously imaged.<sup>5</sup> Finally, we showed that methanol results in dramatic decreasing in the interaction between DMPTC<sup>-</sup> and the magic size CdSe QDs supporting the experimental observation of precipitation of colloidal QDs.

From our simulations and experimental results it appears that future research into ligand exchange of PTC should consider counter ions that are very weak acids and develop new protocols to exchange “native” ligands for desired ligands for improving QDs properties and long-term stability of the QD-based PV devices.<sup>22</sup>

#### 4.7. References

1. Humeres, E.; Debacher, N. A.; Sierra, M. M. d. S.; Franco, J. D.; Schutz, A. Mechanisms of acid decomposition of dithiocarbamates. 1. Alkyl dithiocarbamates. *J. Org. Chem.* **1998**, *63* (5), 1598-1603.
2. Humeres, E.; Debacher, N. A.; Franco, J. D.; Lee, B. S.; Martendal, A. Mechanisms of acid decomposition of dithiocarbamates. 3. Aryldithiocarbamates and the torsional effect. *J. Org. Chem.* **2002**, *67* (11), 3662-3667.
3. Joris, S. J.; Aspila, K. I.; Chakrabarti, C. L. On the mechanism of decomposition of dithiocarbamates. *J. Phys. Chem.* **1970**, *74* (4), 860-865.
4. Balazs, D. M.; Dirin, D. N.; Fang, H.-H.; Protesescu, L.; ten Brink, G. H.; Kooi, B. J.; Kovalenko, M. V.; Loi, M. A. Counterion-mediated ligand exchange for PbS colloidal quantum dot superlattices. *ACS Nano* **2015**, *9* (12), 11951-11959.
5. Anderson, N. C.; Hendricks, M. P.; Choi, J. J.; Owen, J. S. Ligand exchange and the stoichiometry of metal chalcogenide nanocrystals: spectroscopic observation of facile metal-carboxylate displacement and binding. *J. Am. Chem. Soc.* **2013**, *135* (49), 18536-18548.
6. De Roo, J.; Ibáñez, M.; Geiregat, P.; Nedelcu, G.; Walravens, W.; Maes, J.; Martins, J. C.; Van Driessche, I.; Kovalenko, M. V.; Hens, Z. Highly dynamic ligand binding and light absorption coefficient of cesium lead bromide perovskite nanocrystals. *ACS Nano* **2016**, *10* (2), 2071-2081.
7. Debnath, R.; Tang, J.; Barkhouse, D. A.; Wang, X.; Pattantyus-Abraham, A. G.; Brzozowski, L.; Levina, L.; Sargent, E. H. Ambient-processed colloidal quantum dot solar cells via individual pre-encapsulation of nanoparticles. *J. Am. Chem. Soc.* **2010**, *132* (17), 5952-5953.

8. Kramer, I. J.; Sargent, E. H. The architecture of colloidal quantum dot solar cells: materials to devices. *Chem. Rev.* **2014**, *114* (1), 863-882.
9. Greenham, N. C.; Peng, X.; Alivisatos, A. P. Charge separation and transport in conjugated-polymer/semiconductor-nanocrystal composites studied by photoluminescence quenching and photoconductivity. *Phys. Rev. B* **1996**, *54* (24), 17628.
10. Kovalenko, M. V.; Manna, L.; Cabot, A.; Hens, Z.; Talapin, D. V.; Kagan, C. R.; Klimov, V. I.; Rogach, A. L.; Reiss, P.; Milliron, D. J. Prospects of nanoscience with nanocrystals. ACS Publications: 2015.
11. Azpiroz, J. M.; De Angelis, F. Ligand induced spectral changes in CdSe quantum dots. *ACS Appl. Mater. Interfaces* **2015**, *7* (35), 19736-19745.
12. Frederick, M. T.; Amin, V. A.; Cass, L. C.; Weiss, E. A. A molecule to detect and perturb the confinement of charge carriers in quantum dots. *Nano Lett.* **2011**, *11* (12), 5455-5460.
13. Teunis, M. B.; Dolai, S.; Sardar, R. Effects of surface-passivating ligands and ultrasmall CdSe nanocrystal size on the delocalization of exciton confinement. *Langmuir* **2014**, *30* (26), 7851-7858.
14. Zotti, G.; Vercelli, B.; Berlin, A.; Virgili, T. Multilayers of CdSe Nanocrystals and Bis (dithiocarbamate) Linkers Displaying Record Photoconduction. *J. Phys. Chem. C* **2012**, *116* (49), 25689-25693.
15. Frederick, M. T.; Amin, V. A.; Swenson, N. K.; Ho, A. Y.; Weiss, E. A. Control of exciton confinement in quantum dot–organic complexes through energetic alignment of interfacial orbitals. *Nano Lett.* **2013**, *13* (1), 287-292.
16. Frederick, M. T.; Amin, V. A.; Weiss, E. A. Optical properties of strongly coupled quantum dot–ligand systems. *J. Phys. Chem. Lett.* **2013**, *4* (4), 634-640.
17. Morris-Cohen, A. J.; Malicki, M.; Peterson, M. D.; Slavin, J. W.; Weiss, E. A. Chemical, structural, and quantitative analysis of the ligand shells of colloidal quantum dots. *Chem. Mater.* **2013**, *25* (8), 1155-1165.
18. Lian, S.; Weinberg, D. J.; Harris, R. D.; Kodaimati, M. S.; Weiss, E. A. Subpicosecond photoinduced hole transfer from a CdS quantum dot to a molecular acceptor bound through an exciton-delocalizing ligand. *ACS Nano* **2016**, *10* (6), 6372-6382.
19. Kamat, P. V.; Christians, J. A.; Radich, J. G. Quantum dot solar cells: hole transfer as a limiting factor in boosting the photoconversion efficiency. *Langmuir* **2014**, *30* (20), 5716-5725.
20. Wu, K.; Chen, Z.; Lv, H.; Zhu, H.; Hill, C. L.; Lian, T. Hole removal rate limits photodriven H<sub>2</sub> generation efficiency in CdS-Pt and CdSe/CdS-Pt semiconductor nanorod–metal tip heterostructures. *J. Am. Chem. Soc.* **2014**, *136* (21), 7708-7716.
21. Tseng, H.-W.; Wilker, M. B.; Damrauer, N. H.; Dukovic, G. Charge transfer dynamics between photoexcited CdS nanorods and mononuclear Ru water-oxidation catalysts. *J. Am. Chem. Soc.* **2013**, *135* (9), 3383-3386.
22. Munro, A. M.; Chandler, C.; Garling, M.; Chai, D.; Popovich, V.; Lystrom, L.; Kilina, S. Phenylthiocarbamate Ligands Decompose During Nanocrystal Ligand Exchange. *J. Phys. Chem. C* **2016**, *120* (51), 29455-29462.
23. Fritzing, B.; Capek, R. K.; Lambert, K.; Martins, J. C.; Hens, Z. Utilizing self-exchange to address the binding of carboxylic acid ligands to CdSe quantum dots. *J. Am. Chem. Soc.* **2010**, *132* (29), 10195-10201.

24. Sluydts, M.; De Nolf, K.; Van Speybroeck, V.; Cottenier, S.; Hens, Z. Ligand addition energies and the stoichiometry of colloidal nanocrystals. *ACS Nano* **2016**, *10* (1), 1462-1474.
25. Tamukong, P. K.; Peiris, W. D.; Kilina, S. Computational insights into CdSe quantum dots' interactions with acetate ligands. *Phys. Chem. Chem. Phys.* **2016**, *18* (30), 20499-20510.
26. Reed, A. E.; Curtiss, L. A.; Weinhold, F. Intermolecular interactions from a natural bond orbital, donor-acceptor viewpoint. *Chem. Rev.* **1988**, *88* (6), 899-926.

## 5. DFT INSIGHTS INTO BRIGHTENING OF II-VI QUANTUM DOTS BY HYDRIDRIDE TREATMENT

In the previous chapter, we investigated ligand exchange of  $\text{TEA}^+\text{DMPTC}^-$ , where we found that the simple mass-action picture lacks key processes during ligand exchange of the quasi-stable  $\text{TEA}^+\text{DMPTC}^-$  ligands in methanol. The atomic simulation revealed that both  $\text{DMPTC}^-$ , and its decomposition products (DMA and TEA) bind to the surface during ligand exchange which could be problematic when implementing ligand exchange with TPCs on QDs in PV applications. Here we will focus on the X-type ligand exchange with hydride (H), a reactive ion that undergoes X-type inorganic ligand exchange, resulting in order of magnitude increase in the PL QY of CdS QDs going from 1.4% to 78% QY of PL, 55.7 times enhancement.<sup>1</sup> This enhancement of the QY could be used for QDs synthesized in large batches more suited to LED applications. However, the mechanism for this enhancement is unclear due to conflicting reports,<sup>2-3</sup> here we will investigate the mechanism of PL enhancement using atomic simulations.

### 5.1. Introduction

Implementing QDs in LED applications has been sought-after for years because QDs have narrow emission line-widths,<sup>1, 4-6</sup> and size-tunable emission properties, these properties could produce LEDs that are increased color combinations.<sup>7</sup> However, the surface of QDs complicates the implementation because it can result in trap states leading to optically inactive QDs as discussed in Chapter 2.<sup>8-10</sup> Additionally, batch-wise synthesizing QDs can produce QDs with slightly different photophysical properties which would impact the performance of the LEDs produced,<sup>11-12</sup> This batch-wise difference could also be enhanced when scaling to industrial scales.<sup>12</sup> One possible solution to this batch-wise variation in the photophysical



properties of QDs is to treat the surface of the QDs post-synthesis. Jang and co-workers investigated surface treatment of zinc blende (ZB) crystal lattice CdX, X = S, Se or Te, QDs by H<sup>-</sup> generating compounds finding that the QY of PL increase upwards of 55 times compared to the pre-treated QDs.<sup>1</sup> They attributed this enhancement to the formation of CdO shell, which protects the light-emitting core from the surroundings resulting in the dramatic increase in the QY of PL. Additionally, during the H<sup>-</sup> treatment of the QDs gas is formed and the emission slightly blue-shifts.<sup>1</sup> The oxidation of the surface is thought to occur by the removal of surface ligands by H<sup>-</sup> which allows for oxygen migration to the surface resulting in the CdO layer.<sup>1</sup> This mechanism was then studied by Tsui and co-workers, where proton NMR was used to analyze the hydrogen gas that was formed during deuterated H<sup>-</sup> (D<sup>-</sup>) treatment of CdSe QDs.<sup>3</sup> In their NMR study, they did not observe the formation of D<sub>2</sub> which indicates that the surface ligands are not desorbed during the H<sup>-</sup> treatment,<sup>3</sup> a vital step in the formation of CdO shell.<sup>1</sup>

The conclusion of Jang and co-workers was further investigated by Subila and co-workers, where wurtzite (WZ) and ZB CdSe QDs were investigated.<sup>2</sup> They reported that the QY of PL before H<sup>-</sup> treatment for ZB and WZ QDs to be 37.5% and 4.6%, respectively. After H<sup>-</sup> treatment the QY of PL for ZB QDs is slightly modified, while the QY of PL for WZ QDs is enhanced as Jang and co-workers reported. It is likely that the crystal lattice was QZ not ZB because the characterization was performed visual, while Subila and co-workers characterized the QDs via XRD.<sup>1-2</sup> Subila and co-workers observed that ZB QDs naturally form a CdO layer, resulting in the difference between the QY of PL for ZB (37.5%) and WZ (4.6%). This CdO layer also makes ZB CdSe QDs stable in oxygen atmospheres, where WZ CdSe QDs PL is dramatically reduced within 6 hours.<sup>2</sup> From this work, the mechanism of PL enhancement of CdX, X = S, Se or Te, by H<sup>-</sup> treatment is unclear due to seemingly conflicting reports for ZB QDs. Additional

investigations are needed to provide a mechanism to describes the process of  $\text{H}^-$  treatment that leads to the dramatic enhancement of the QY of PL that resolves the conflictions between experimental results.<sup>1-3</sup>

### 5.1.1. Hypothetical Mechanisms of PL Enhancement

The mechanism of PL enhancement is likely the result of removing surface trap states by etching the surface (removal of ions causing the trap states),  $\text{H}^-$  passivating dangling bonds of surface  $\text{Cd}^{2+}$  or reducing the QDs generating the  $\text{H}_2$  ( $\text{D}_2$ ). These general mechanisms are from experimental reports investigating the surface of QDs.<sup>2</sup> Etching of the surface by  $\text{H}^-$  would likely remove ions that are weakly bound to the QDs surface that could be responsible for trap state formation. This would change the stoichiometry of the surface of the QD, from the work by Wei and co-workers Cd-rich surface-emission spectra are dominated by band edge emission, while Se-rich surface is either non-emissive or emit from trap states.<sup>13</sup> This would imply if  $\text{H}^-$  treatment removes surface  $\text{Se}^{2-}$ , the surface would become Cd-rich, resulting in emission from the band edge states that are optically active. The second general mechanism for PL enhancement would strongly passivate surface ions dangling bonds, the interaction between surface  $\text{Cd}^{2+}$  and  $\text{H}^-$  should be very strong and  $\text{H}^-$  could passivate the dangling bonds more efficiently compared to L-type ligands such as amines. The final general mechanism has been reported by Subila and co-workers where they observed  $\text{D}_2$  formation when treating QDs with deuterated hydride sources.

To determine the most possible mechanism for the above, we will use DFT and TDDFT to simulate the morphology changes during  $\text{H}^-$  treatment. From the QD model, the crystal lattice will be WZ, because the ZB surface naturally oxidized to for the CdO shell that does not respond to  $\text{H}^-$  treatment. The QY of PL will be approximated by comparing the oscillator strength of the lowest excited state,  $S_1$ . This approximation is based on Kasha's rule that states the emission

occurs from the lowest excited state.<sup>14</sup> This approximation is valid for QDs because the nuclear rearrangement upon optical excitation is insignificant for QDs.<sup>15</sup> All calculations were performed at the level of theory discussed in section 3.3.4 using CPCM to implicitly include solvent effect for propylamine. The nature of the emissive states was characterized by natural transition orbitals (NTOs)<sup>16</sup> and visualized via VMD<sup>17</sup> with isovalue of 0.02.

## **5.2. Results and Discussion**

The investigation into the mechanism of PL enhancement of CdX, X = S, Se or Te, was atomically simulated by stoichiometric (magic size) and non-stoichiometric QDs. We will start our investigation by reacting H<sup>-</sup> to surface Se<sup>-</sup> and Cd<sup>2+</sup> ions in (CdSe)<sub>33</sub> QDs, where we found that H<sup>-</sup> can elongate the QD-Se bond resulting in trap state formation, and H<sup>-</sup> strongly binds to surface Cd<sup>2+</sup> minorly perturbing the emissive state. Then we will investigate the effect of H<sup>-</sup> on non-stoichiometric QDs, from these simulations we will formula the atomic-level mechanism for PL enhancement.

### **5.2.1. H<sup>-</sup> Treatment of Stoichiometric QDs**

Here we will investigate the effect of H<sup>-</sup> treatment of magic size (CdSe)<sub>33</sub> QDs on its photophysical properties. The model system of (CdSe)<sub>33</sub> has a C<sub>3</sub>-axis that runs perpendicular to the crystal layers, which should result in 7 surface Cd<sup>2+</sup> and 7 surface Se<sup>2-</sup> that are not equivalent by symmetry reducing the possible binding sites from 42 to 14 for H<sup>-</sup> treatment. In section 5.2.1.1. we will provide evidence that this assumption is valid. This assumption will then be used to study reacting H<sup>-</sup> with surface Se<sup>2-</sup> (section 5.2.1.2.) and Cd<sup>2+</sup> (section 5.2.1.3.).

#### **5.2.1.1. C<sub>3</sub>-Axis of (CdSe)<sub>33</sub> QDs**

In this section, we will investigate whether the C<sub>3</sub>-axis causes surface ions to be symmetrically equivalent. The layer investigated will be layer A, Figure 5.1.a, that has 3 surface

$\text{Se}^{2-}$  that are 3-coordinated, 3 surface  $\text{Cd}^{2+}$  that are 3-coordinated, and 3 surface  $\text{Cd}^{2+}$  that are 2-coordinated. The systems utilized to investigate whether surface ions are symmetric equivalent two systems were investigated: pre-treated  $\text{CdSe}_{33}$  QDs, and post-treated CdSe QDs. In this section and section 5.2.1, pre-treated QDs refer to QDs before  $\text{H}^+$  treatment that is fully passivated by methylamine. the pre-treated QDs are magic size  $(\text{CdSe})_{33}$  QDs. For sections 5.2.2.1 through 5.2.2.4 with non-stoichiometric QDs, pre-treated QDs are fully passivated with methylamine with the stoichiometry in the title of the section. For all sections, post-treated QDs are QDs with at least one  $\text{H}^+$  passivating either surface  $\text{Se}^{2-}$ , Figure 5.1.c, or  $\text{Cd}^{2+}$ , Figure 5.1.d.

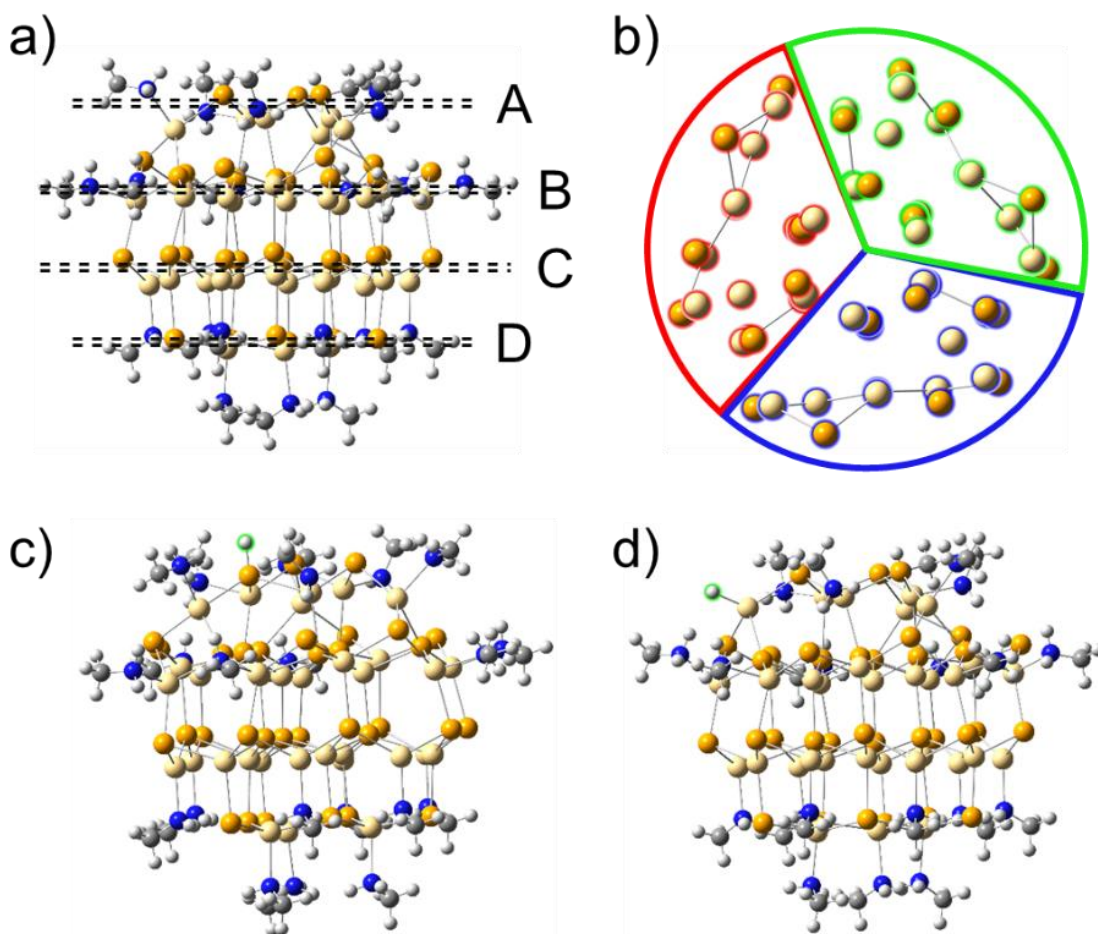


Figure 5.1. Magic size CdSe QDs utilized in this chapter. a) magic size  $(\text{CdSe})_{33}$  QD passivated by 21 methylamines labeling Layers A-D. b) magic size  $(\text{CdSe})_{33}$  QD without surface passivation demonstrating the  $C_3$ -axis symmetry. c) example of  $\text{H}^+$  passivation of surface  $\text{Se}^{2-}$  on Layer A d) example of  $\text{H}^+$  passivation of surface  $\text{Cd}^{2+}$  on Layer A.

From the optimized geometry with and without  $H^-$  treatment the first observable investigated was the deviation of “heavy” atoms (non-hydrogen) by rotating the structures to align the suspected chemically equivalent atoms, this was done by rotating the pre-treated QD by  $120^\circ$  or  $240^\circ$  and the post-treated QDs to align the  $Y-H^-$ ,  $Y = Se$  or  $Cd$ , bond, Figure 5.2. From the rotated geometry the root-mean-square deviation (RMSD) from the sets of structures was computed because the visual inspection of the rotated geometry shows that the ligands atoms (C and N) are the only atoms that greatly differ, Table 5.1. The RMSD for the QD ions is quite small ranging from  $0.08 \text{ \AA}$  to  $0.10 \text{ \AA}$  compared to the ligand RMSD that is around 3 times greater ranging from  $0.24 \text{ \AA}$  to  $0.30 \text{ \AA}$ . From the RMSD values and visual inspection, the morphology of the QD should follow the  $C_3$ -axis, which greatly reduces the number of possible binding sites that are needed to be investigated to determine the mechanism for PL enhancement.

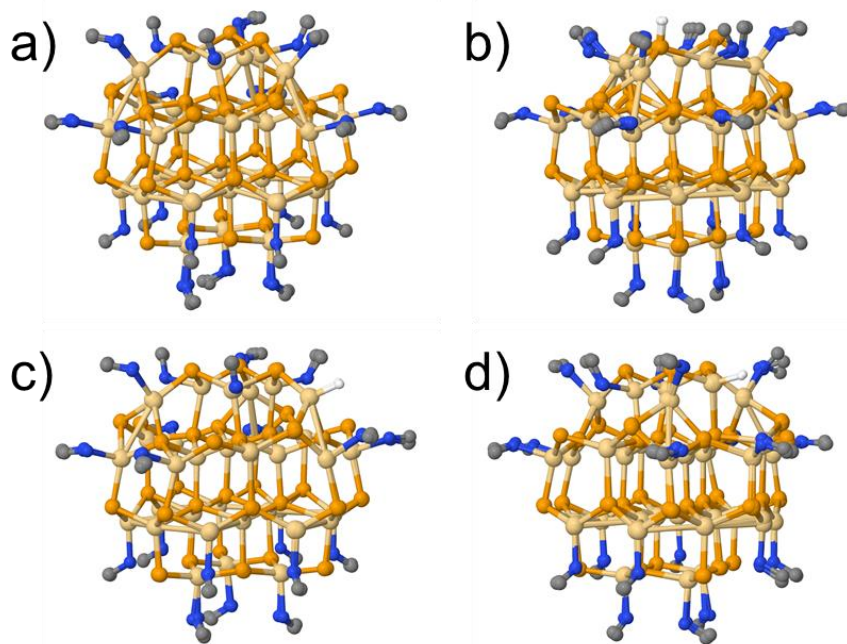


Figure 5.2. Rotating QDs by  $0^\circ$  (reference geometry),  $120^\circ$ , and  $240^\circ$  with various surface passivation demonstrating the  $C_3$ -axis of  $(CdSe)_{33}$  QDs, hydrogens are omitted in the methylamine. a) 21 methylamines passivated QDs b) hydride passivating 3 coordinated  $Se^{2-}$  ions c) hydride passivating 2 coordinated  $Cd^{2+}$  ions d) hydride passivating 3 coordinated  $Cd^{2+}$  ions.

Table 5.1. Bond lengths, binding energy and RMSD for the three possible binding sites on 2 coordinated  $\text{Se}^{2-}$ , 2 and 3 coordinated  $\text{Cd}^{2+}$  for hydride passivation on Layer A. The RMSD reference geometry is  $A_1$  where  $A_2$  and  $A_3$  are rotated to superimpose over  $A_1$  the values are only QD atoms and ligands without the hydrogens.

	2-Se Post-treatment			2-Cd Post-treatment			3-Cd Post-treatment		
	$A_1$	$A_2$	$A_3$	$A_1$	$A_2$	$A_3$	$A_1$	$A_2$	$A_3$
Bond Length ( $\text{\AA}$ )									
Cd-Se	2.92	2.92	2.95	2.81	2.80	2.81	2.83	2.85	2.83
	3.01	2.96	2.95	2.95	2.92	2.92	2.84	2.89	2.84
	3.01	3.14	3.09	2.96	2.95	2.95	3.00	2.94	3.00
Se-H	1.51	1.51	1.51	--	--	--	--	--	--
Cd-H	--	--	--	-1.88	-1.89	-1.89	-1.87	-1.87	-1.87
Binding Energy (eV)									
QD-H	0.166	0.200	0.179	-2.198	-2.190	-2.217	-2.135	-2.134	-2.115
RMSD ( $\text{\AA}$ )									
QD	Ref.	0.097	0.085	Ref.	0.077	0.089	Ref.	0.106	0.106
Ligand	Ref.	0.242	0.272	Ref.	0.248	0.275	Ref.	0.301	0.241

To support the idea of reducing the number of possible binding sites by 3, we compared the  $B_e$  and absorption spectra for the 9 confirmations of  $\text{H}^-$  at the QD. The  $B_e$  of the 2-coordinated  $\text{Se}^{2-}$  ions on layer A and 2- and 3-coordinated  $\text{Cd}^{2+}$  show well agreement varying on the order of thermal fluctuation (25.7 meV), Table 5.1 and Figure 5.3. The absorption spectra computed for these geometries also has very slight difference, Figure 5.4.a-c. Interestingly, QDs where surface  $\text{Se}^{2-}$  are treated by  $\text{H}^-$  have optical transitions that are orders of magnitude greater than the pre-treated QDs. QDs with surface passivation by only MA are red-shift by around 2.25 eV, Figure 5.4.c. The optically active transitions around 0.75 eV were investigated by artificially removing the [Se-H] fragment from the surface of  $A_1$  treated QD. This system is referred to as  $A_1$  far post-treated. Comparing the NTOs for  $A_1$  post-treated,  $A_1$  far post-treated and pre-treated QDs indicate that the optically bright transitions around 0.75 eV for  $A_1$  post-treatment are the result of Se-vacancy on the surface, Table 5.2. The NTOs for the first two optical excited states are optically inactive for  $A_1$  far post-treatment compared to the optically active states for  $A_1$

post-treatment, this is because  $A_1$  far post-treatment is a charge transfer (CT) state between the [Se-H] fragment and QD. The next optically active states for  $A_1$  far post-treatment show localization on the treatment site, which indicates a trap state for  $H^-$  treatment around surface  $Se^{2-}$ , Table 5.2. Analyzing the transitions for  $A_1$  post-treatment show highly delocalized states for the first few transitions, but  $S_{10}$  and  $S_{11}$  transitions show localization around the [Se-H] fragment. From this data, we can conclude that the highly optically active low energy transitions are likely caused by Se-vacancies on the surface that become optically active due to the highly confined nature of our model system compared to experimental QDs.<sup>18</sup>

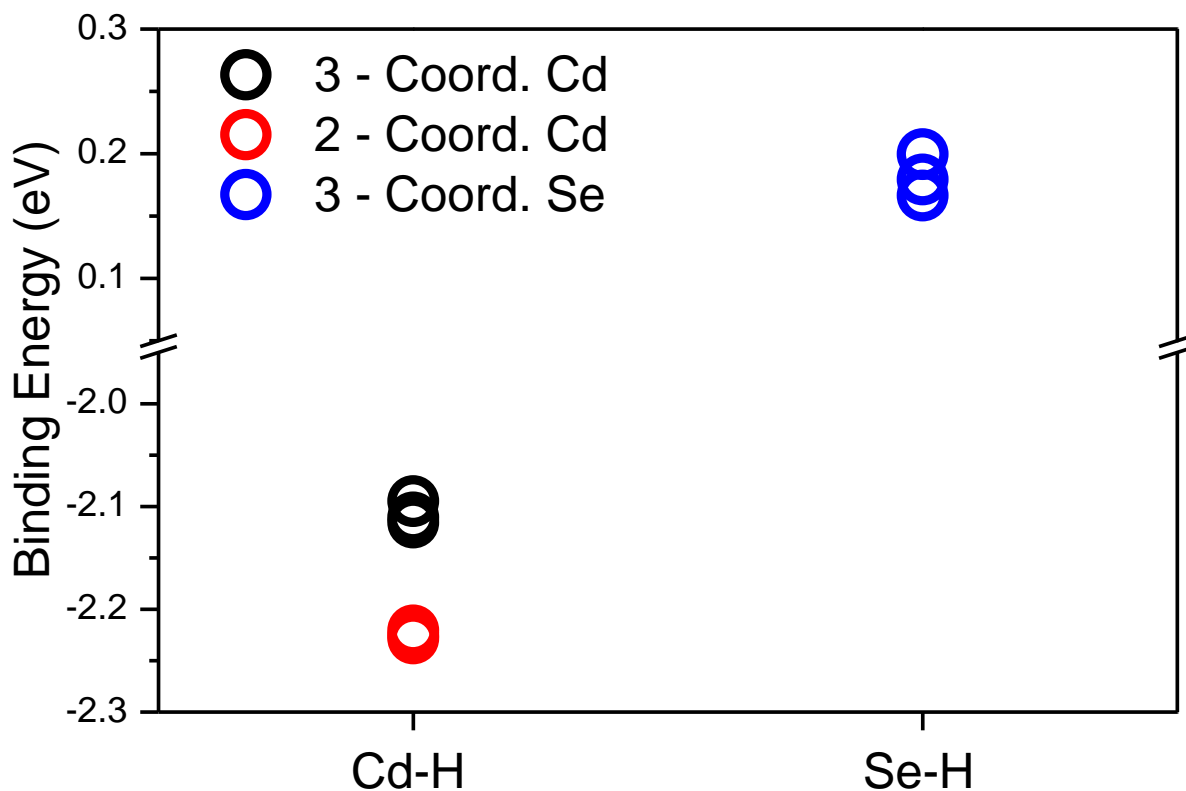
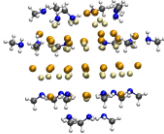
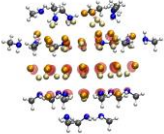
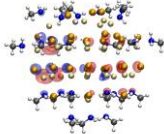
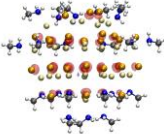
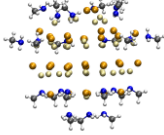
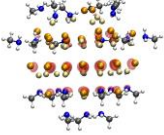
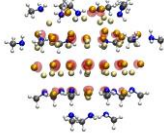
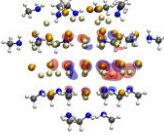
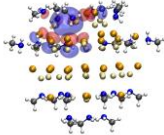
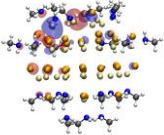
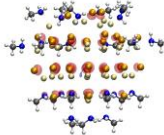
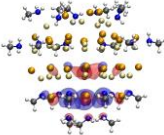
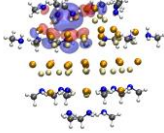
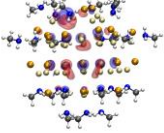
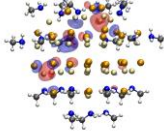
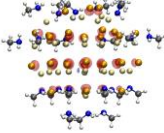


Figure 5.3. Binding energy of  $H^-$  to surface ions in Layer A. The black circles are the binding energy for 3 coordinated surface  $Cd^{2+}$ , red circles are the binding energy for 2 coordinated surface  $Cd^{2+}$ , and blue circles are the binding energy for surface  $Se^{2-}$ . The positive Binding energy of  $H^-$  to surface  $Se^{2-}$  in Layer A is likely a result of the increased bond length between the  $Se^{2-}$  and neighboring  $Cd^{2+}$ .

Table 5.2. Natural transition orbitals (NTOs) comparing A<sub>1</sub> post-treatment with the Se-H fragment near and far. The NTOs for S<sub>1</sub> and S<sub>2</sub> are plotted with the next two most optically active transitions.

	A <sub>1</sub> Far Post-treatment		A <sub>1</sub> Post-treatment		
	HOTO	LUTO	HOTO	LUTO	
S <sub>1</sub> 2.31 eV <i>f</i> = 0.000			S <sub>1</sub> 0.53 eV <i>f</i> = 0.531		
S <sub>2</sub> 2.31 eV <i>f</i> = 0.000			S <sub>2</sub> 0.51 eV <i>f</i> = 0.514		
S <sub>4</sub> 2.78 eV <i>f</i> = 0.217			S <sub>10</sub> 1.54 eV <i>f</i> = 0.034		
S <sub>9</sub> 2.84 eV <i>f</i> = 0.115			S <sub>11</sub> 1.58 eV <i>f</i> = 0.012		



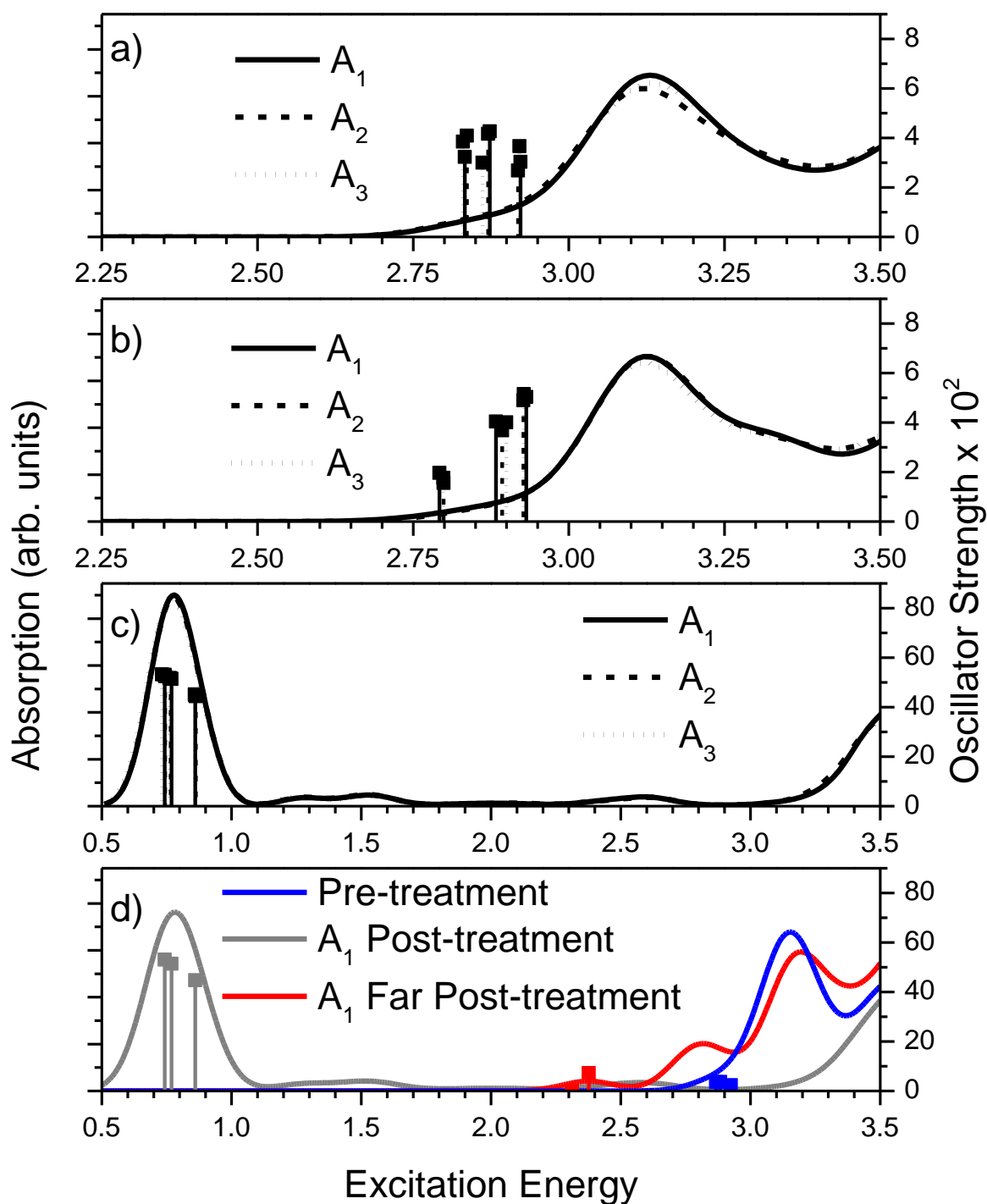


Figure 5.4. Absorption spectra for  $(\text{CdSe})_{33}$  QDs with a single  $\text{H}^-$  passivating Layer A. a) 2 coordinated  $\text{Cd}^{2+}$  b) 3 coordinated  $\text{Cd}^{2+}$  c) 3 coordinated  $\text{Se}^{2-}$  d) comparing 3 coordinated  $\text{Se}^{2-}$  geometries Near and Far to amine passivated QDs. The Far geometry was obtained by artifactually moving the Se-H fragment from the QDs surface.

### 5.2.1.2. $H^-$ Treatment of Surface $Se^{2-}$ on Magic Size CdSe QDs

In section 5.2.1.1. we provided evidence that the  $C_3$ -axis can be used to reduce the possible number of binding configurations of  $H^-$  to surface  $Se^{2-}$  ion from 21 to 7. Here we will investigate the effect of  $H^-$  treatment of surface  $Se^{2-}$  in magic size QDs, where  $H^-$  reacts with all layers of the QD. We will compare the post-treated QDs to the fully passivated amine magic size QDs. The optically bright transitions observed for  $H^-$  treatment of surface  $Se^{2-}$  ( $A_1$ ,  $A_2$ , and  $A_3$ ) is also observed for  $B_1$  and  $B_2$   $H^-$  treatment of surface  $Se^{2-}$ , Figure 5.5. Investigating these optically active states shows similar nature as  $A_1$  post-treatment (Figure 5.4.d, Table 5.2.), indicating  $B_1$  and  $B_2$  would also be the result of Se-vacancies after  $H^-$  treatment that is optically active due to the strong confinement, Table 5.3.<sup>18</sup> Layers C and D, absorption spectrum are similar to the  $A_1$  far post-treatment, but  $S_1$  is optically active and red-shifted by  $\sim 1.0$  eV compared to the pre-treatment. The nature of the emissive states is CTs from surface states located near the treatment site.

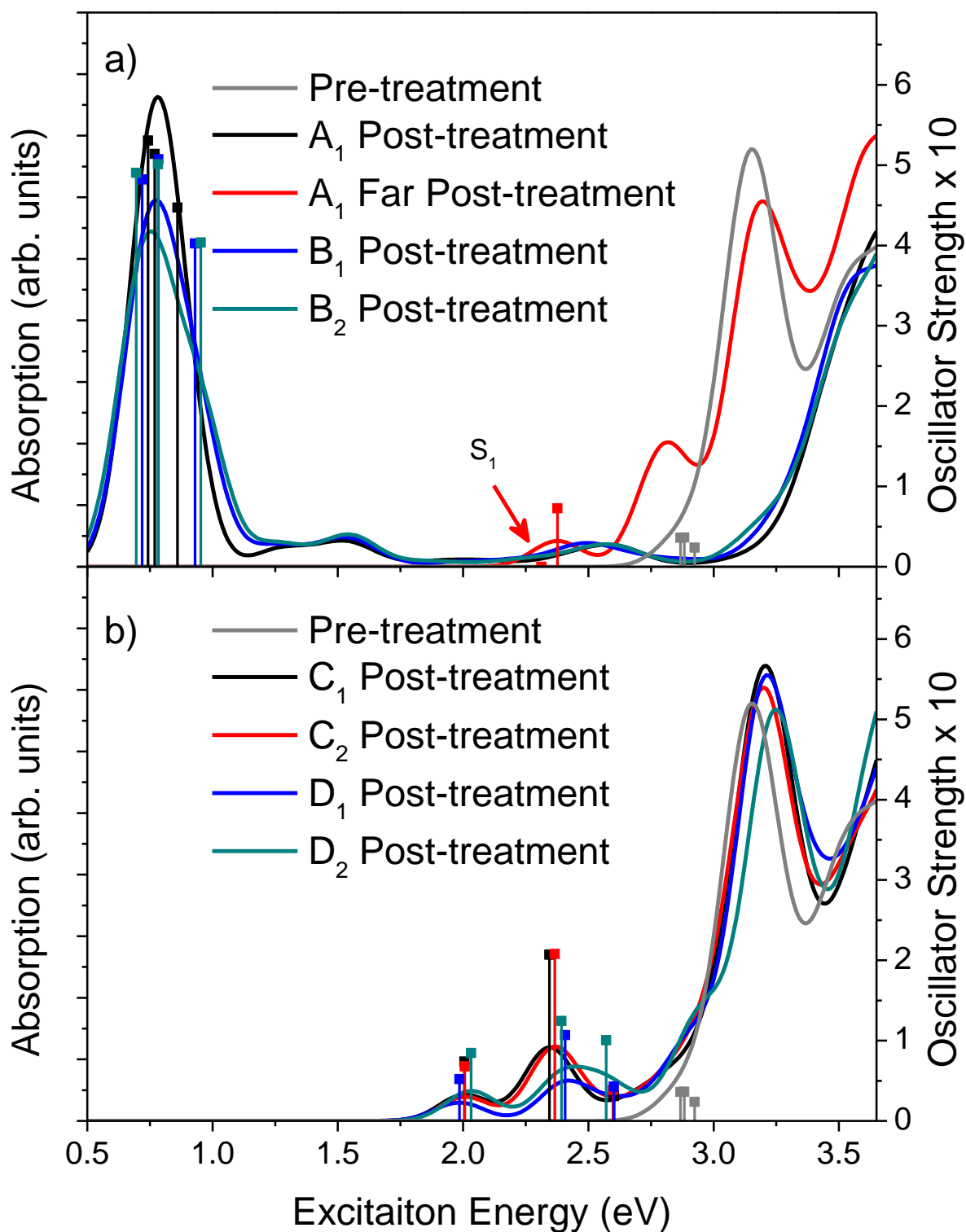


Figure 5.5. Absorption spectra for pre- and post-treatment of surface  $\text{Se}^{2-}$  with the first three transition oscillator strength plotted with vertical lines. The first state ( $S_1$ ) is optically inactive for  $A_1$  Far Post-treatment and is indicated by the red arrow.

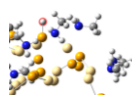
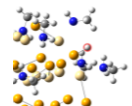
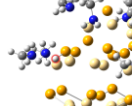
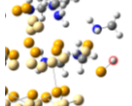
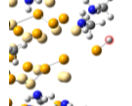
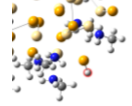
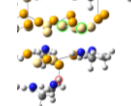
Table 5.3. NTOs for  $S_1$  transitions plotted in Figure 5.5. surface  $\text{Se}^{2-}$  treatment by  $\text{H}^-$ .

	HOTO	LUTO		HOTO	LUTO
$A_1$ 0.74 eV $f = 0.5306$			$C_1$ 2.00 eV $f = 0.0740$		
$A_1$ Far 2.31 eV $f = 0.0000$			$C_2$ 2.01 eV $f = 0.0679$		
$B_1$ 0.72 eV $f = 0.4821$			$D_1$ 1.99 eV $f = 0.0520$		
$B_2$ 0.70 eV $f = 0.4903$			$D_2$ 2.03 eV $f = 0.0846$		
Post-treatment Pre-treatment 2.87 eV $f = 0.0360$					

From the absorption spectrum, we can conclude that merely treating surface  $\text{Se}^{2-}$  would not result in an enhancement in PL. Considering the  $B_e$  of  $\text{H}^-$  to the surface of the QD through  $\text{Se}^{2-}$ , we see that layers A and B have relatively weak interaction, which could be due to being in a quasi-stable state caused by the surface retaining the  $[\text{Se-H}]$  where the stable structure would have the fragment detached similarly to layers C and D that has high  $B_e$  of  $\text{H}^-$  to the surface of the QD, Table 5.4. The nature of the  $\text{H}^-$  also changes when attached to surface  $\text{Se}^{2-}$  going from negative ( $\text{H}^-$ ) to positive ( $\text{H}^+$ ). Along with the oxidation of the  $\text{H}^-$  layers C and D show significant elongation of at least one Cd-Se bond indicating that the  $[\text{Se-H}]$  fragment tends to

detach from the surface of the QD. The elongation of the [Se-H] fragment for B<sub>1</sub> and D<sub>2</sub> appear to be similar; visually inspecting the atoms around the binding site show that both B<sub>1</sub> and D<sub>2</sub> the [Se-H] fragment does not jut out from the surface, Table 5.4. However, there is additional surface reconstruction (“surface healing”) that occurs for D<sub>2</sub> that is not present for B<sub>1</sub>. The green highlighted atoms for D<sub>2</sub> in Table 5.4. are Cd<sup>2+</sup> atoms that interatomic distance reduces significantly upon H<sup>-</sup> treatment. This surface healing is likely the result for the large negative B<sub>e</sub> for D<sub>2</sub> compared to the positive B<sub>e</sub> for B<sub>1</sub>. This removal of surface Se<sup>2-</sup> would result in Cd-rich surfaces that are known to be highly emissive.<sup>11</sup> We expect that a second H<sup>-</sup> would result in the formation of H<sub>2</sub>Se which could then detach from the surface, this will be investigated in section 5.3.1. and 5.3.3.

Table 5.4. Structure and structural parameters for H<sup>-</sup> reacting with surface Se<sup>2-</sup> on layers A-D.

	A <sub>1</sub>	B <sub>1</sub>	B <sub>2</sub>	C <sub>1</sub>	C <sub>2</sub>	D <sub>1</sub>	D <sub>2</sub>
Structure							
							
Bond Length (Å)							
	2.92	2.94	2.82	2.80	2.74	2.81	2.94
Cd-Se	3.01	2.94	3.00	3.98	3.89	3.91	2.95
	3.01	3.87		4.41	4.30		3.95
Se-H	1.51	1.51	1.50	1.52	1.52	1.51	1.51
Binding Energy (eV)							
QD-H	0.166	0.075	-0.166	-1.080	-1.016	-1.011	-1.142
NBO (e <sup>-</sup> )							
H	0.095	0.076	0.094	0.048	0.046	0.057	0.076

### 5.2.1.3. H<sup>-</sup> Treatment of Surface Cd<sup>2+</sup> on Magic Size CdSe QDs

The second general mechanism for PL enhancement is the strong interaction between surface Cd<sup>2+</sup> and H<sup>-</sup> that would efficiently passivate the dangling bond generated by

undercoordination with  $\text{Se}^{2-}$ . In this section, we will investigate the effect of passivating surface  $\text{Cd}^{2+}$  by a single  $\text{H}^-$  on magic size  $(\text{CdSe})_{33}$  QDs. The absorption spectrum generated by  $\text{H}^-$  treatment on layers A-D shows a slight difference between the pre-treated QDs and the post-treated QDs, Figure 5.6. However, the emissive state does not increase; in fact, the oscillator strength of  $S_1$  decreases compared to the pre-treated QD and redshifts, this contradicts the experimental observations.<sup>1-3</sup> Characterizing the nature of the emissive state ( $S_1$ ) shows that these states are different from the pre-treated QD by localizing around the  $\text{H}^-$  treated  $\text{Cd}^{2+}$  site, Table 5.5. The Cd-Se bond lengths for  $\text{Cd}^{2+}$  treatment by  $\text{H}^-$  are not elongated as seen in Table 5.4. and the  $\text{H}^-$  remains negatively charged which is likely responsible for the increased  $B_e$  between  $\text{H}^-$  and QD for  $\text{Cd}^{2+}$  treatment compared to  $\text{Se}^{2-}$ . The  $B_e$  of  $\text{H}^-$  to surface  $\text{Cd}^{2+}$  ranges from -2.1 eV to -2.7 eV which is much higher compared to the  $B_e$  compared to methylamine that ranges from -0.4 eV to -0.8 eV. This would imply that  $\text{H}^-$  would readily replace the methylamine on the surface of the QD and explain why Jang and co-workers found that prolonged  $\text{H}^-$  treatment results in the precipitation of the QDs.<sup>1</sup>

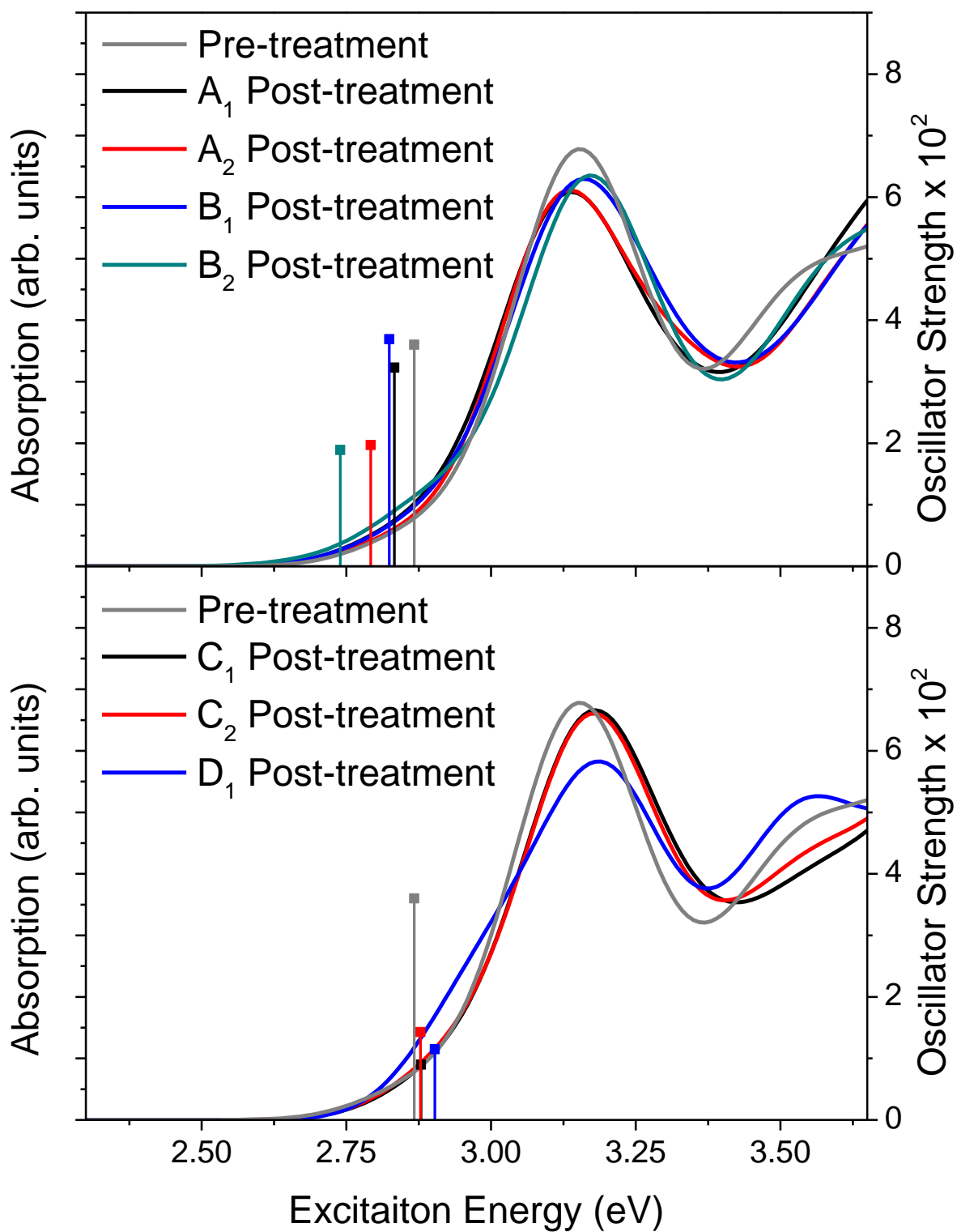


Figure 5.6. Absorption spectra for pre- and post-treatment of surface Cd<sup>2+</sup> with the first transition oscillator strength plotted with a vertical line.

Table 5.5. NTOs for  $S_1$  transitions plotted in Figure 5.6. surface  $Cd^{2+}$  treatment by  $H^-$ .

	HOTO	LUTO		HOTO	LUTO	
Post-treatment	$A_1$ 2.83 eV $f = 0.0323$			$C_1$ 2.88 eV $f = 0.009$		
	$A_2$ 2.79 eV $f = 0.0197$			$C_2$ 2.88 eV $f = 0.0143$		
	$B_1$ 2.82 eV $f = 0.0369$			$D_1$ 2.90 eV $f = 0.0115$		
	$B_2$ 2.74 eV $f = 0.0189$					
	Pre-treatment 2.87 eV $f = 0.0360$					

### 5.2.2. $H^-$ Treatment of Non-Stoichiometric QDs

The observation of detaching of [Se-H] fragment and strong binding of  $H^-$  to surface  $Cd^{2+}$  when  $H^-$  is performed on magic size CdSe QDs is the basis for investigating the mechanism for PL enhancement by  $H^-$  treatment for non-stoichiometric QDs we will use the method for surface enrichment used in Chapter 4. This investigation will be in two parts, single-ion enrichment, and enrichment by four ions.



### 5.2.2.1. $H^-$ Treatment of $Cd_{33}Se_{34}$ QDs

In this section we will investigate if reacting Se enriched surface with  $H^-$  could produce  $H_2Se$  that transforms the surface for Se-rich to Cd-rich that are expected to be optically active and result in PL enhancement. The structures used in this section are generating by the schematic representation presented in Figure 5.7.

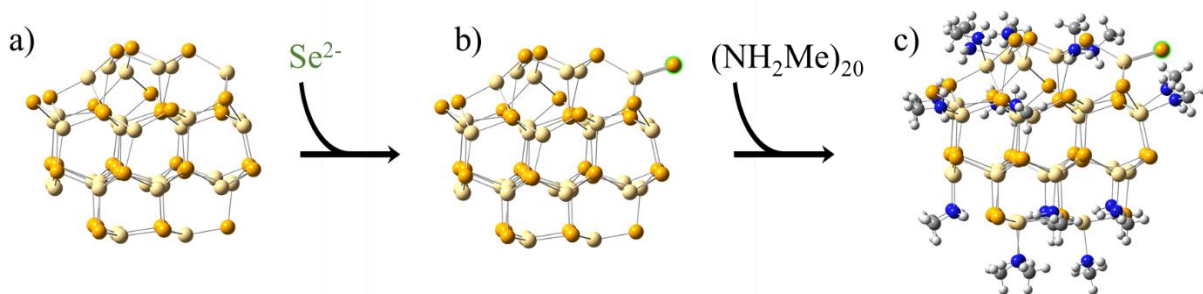


Figure 5.7. Schematic surface enriched by a single  $Se^{2-}$  ions of bare magic size  $(CdSe)_{33}$  QD followed by surface passivation by 20 methylamines. a) bare magic size  $(CdSe)_{33}$  QD b) bare  $Cd_{33}Se_{34}$  QD c) methylamine passivated  $Cd_{33}Se_{34}$  QD.

All layers were investigated by enriching the surface by a single  $Se^{2-}$ , but layers A and B absorption and emissive states are shown because these layers have both 2- and 3-coordinated  $Cd^{2+}$ . The structures were optimized with and without  $H^-$  treatment. The addition of a single  $Se^{2-}$  to the surface of the QD results in trap states compared to magic size  $(CdSe)_{33}$  QDs, Figure 5.8. After  $H^-$  treatment the system is comprised of the QD and  $H_2Se$  which are both neutral molecules, thus, we consider the charge of the post-treated system to be neutral. The absorption and emission properties are then recovered to the magic size QD, showing more delocalized states compared to the  $Cd_{33}Se_{34}$  QD pre-treatment, Table 5.6. The formation of  $H_2Se$  was observed in all cases except for  $B_1$  where the step-like nature between layers A and B result in the second  $H^-$  migrating to  $Se^{2-}$  on layer A, this configure is optically active which could be due to our artificially remove the charge from the system effectively passivating the surface with  $H^+$ . The bond length between the 34<sup>th</sup>  $Se^{2-}$  and the surface  $Cd^{2+}$  is shown in Table 5.7. showing that

the  $\text{H}_2\text{Se}$  when formed is weakly bound to the surface. This conclusion is supported by the  $B_e$  comparison between  $\text{H}_2\text{Se}$  and methylamine, Table 5.7. These simulations indicated that  $\text{H}^-$  treatment of Se-rich QDs would react producing  $\text{H}_2\text{Se}$  that would likely result in Cd-rich QDs, in the next section we will investigate whether  $\text{H}^-$  treatment of surface  $\text{Cd}^{2+}$  would result in enhancement of PL.

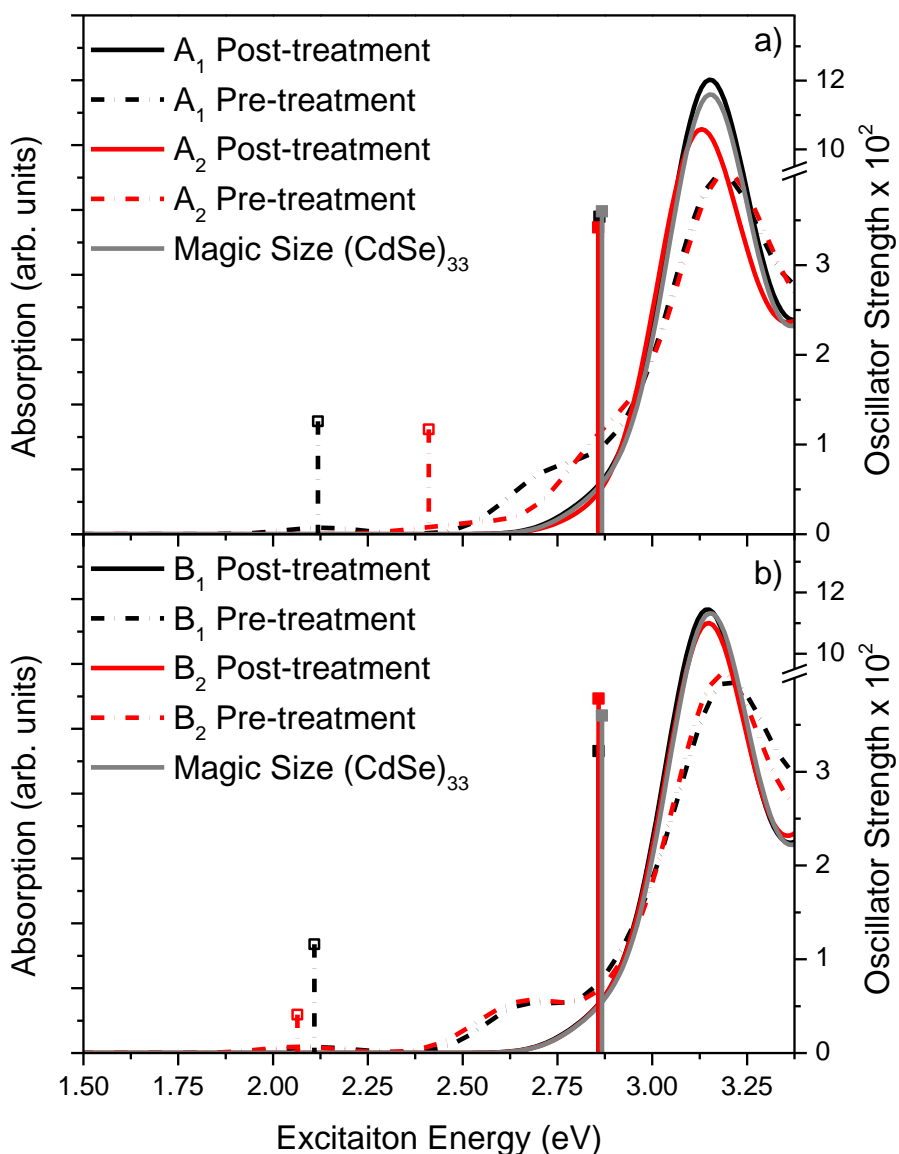


Figure 5.8. Absorption Spectra for  $\text{Cd}_{33}\text{Se}_{34}$  passivated by methylamine pre- and post-treatment vs. magic size  $(\text{CdSe})_{33}$  QDs with the first transition oscillator strength is plotted with a vertical line. The dashed (solid) lines represent the pre-treated (post-treated) QDs. a) layer A b) layer B.

Table 5.6. NTOs for  $S_1$  transitions plotted in Figure 5.8. surface  $\text{Se}^{2-}$  treatment by two  $\text{H}^-$  resulting in neutral QD and  $\text{H}_2\text{Se}$ .

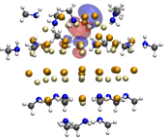
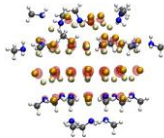
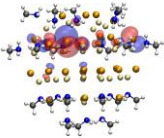
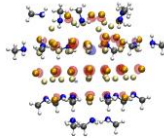
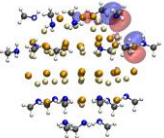
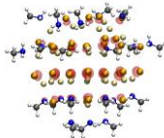
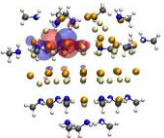
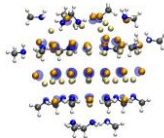
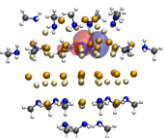
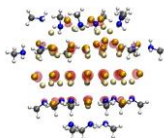
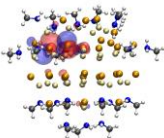
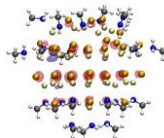
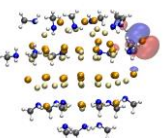
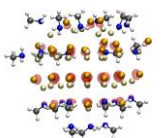
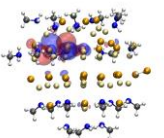
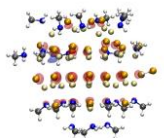
	Pre-treatment		Post-treatment		
	HOTO	LUTO	HOTO	LUTO	
$A_1$ 2.12 eV $f = 0.013$			$A_1$ 2.86 eV $f = 0.035$		
$A_2$ 2.41 eV $f = 0.012$			$A_2$ 2.86 eV $f = 0.034$		
$B_1$ 2.11 eV $f = 0.012$			$B_1$ 2.86 eV $f = 0.032$		
$B_2$ 2.06 eV $f = 0.004$			$B_2$ 2.86 eV $f = 0.038$		

Table 5.7. Structural parameters for  $\text{Cd}_{33}\text{Se}_{34}$  treated by 2  $\text{H}^-$  resulting in neutral QD and  $\text{H}_2\text{Se}$ .

	$A_1$	$B_1$	$B_2$	$C_1$	$C_2$	$D_1$	$D_2$
Bond Length ( $\text{\AA}$ )							
QD-( $\text{SeH}_2$ )	4.9	--	4.8	5.4	3.7	3.8	3.9
Binding Energy (eV)							
QD-( $\text{SeH}_2$ )	-0.23	--	-0.24	-0.27	-0.09	0.10	-0.10
QD- $\text{NH}_2\text{Me}$	-0.40	-0.58	-0.40	-0.38	-0.80	-0.51	-0.35
NBO ( $e^-$ , total)							
$\text{H}_2\text{Se}$	-0.077	--	0.080	-0.052	0.078	0.073	0.070

### 5.2.2.2. $\text{H}^-$ Treatment of $\text{Cd}_{34}\text{Se}_{33}$ QDs

The generation of  $\text{Cd}_{34}\text{Se}_{33}$  QDs was performed similarly to  $\text{Cd}_{33}\text{Se}_{34}$  but  $\text{Cd}^{2+}$  was added, followed by a single  $\text{H}^-$  on the enriched  $\text{Cd}^{2+}$  site. Then the positive charged QD was passivated

by a second  $H^-$ , the placement of this second  $H^-$  is unknown. Thus, we considered four scenarios based on the fact that  $H^-$  can react with both surface  $Se^{2-}$  and  $Cd^{2+}$ , and spatial distribution of charge along the QD's surface: 2  $H^-$ -Cd (far), 2  $H^-$ -Cd (near), 1  $H^-$ -Cd +1  $H^-$ -Se (far) and 1  $H^-$ -Cd +1  $H^-$ -Se (near). This is depicted in Figure 5.9. The results of  $H^-$  treatment were then compared to the pre-treated  $Cd_{34}Se_{33}$  QDs absorption spectrum. Here we will show the results for layer  $B_1$  because this layer has 2-coordinated surface  $Se^{2-}$  which should be the most reactive for the non-stoichiometric  $Cd^{2+}$  enrichment. We found that  $H^-$  treatment for the cases where the second  $H^-$  reacts with surface  $Se^{2-}$  result in trap states similar to the case where  $H^-$  reacts with surface  $Se^{2-}$  on stoichiometric  $(CdSe)_{33}$  QDs, Figure 5.10. These trap states are Se-vacancy states that are optically active because the electron and hole are squeezed together in our highly confined QDs.<sup>18</sup> The cases where the second  $H^-$  reacts with a second surface  $Cd^{2+}$  we observe the blue shift in the energy of  $S_1$  but the oscillator strength is not increased dramatically as seen in the experimental results, Table 5.8.

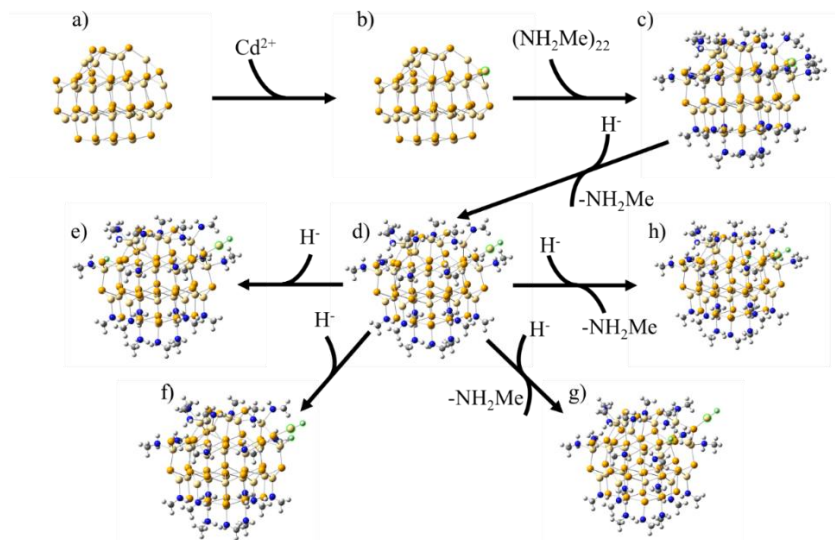


Figure 5.9. Schematic surface enriched by a single  $Cd^{2+}$  ion. This starts from bare magic size  $(CdSe)_{33}$  QD (a), where a single  $Cd^{2+}$  is placed on the surface (b). The  $Cd_{34}Se_{33}$  QD surface is then passivation by 22 methylamines (c). The fully passivated QD exchanges the methylamine on the non-stoichiometric  $Cd^{2+}$  is exchanged for the first  $H^-$  (d). The placement of the second  $H^-$  has four possible binding sites: far  $Cd^{2+}$  (e), near  $Cd^{2+}$  (f), near  $Se^{2-}$  (g), and far  $Se^{2-}$  (h).

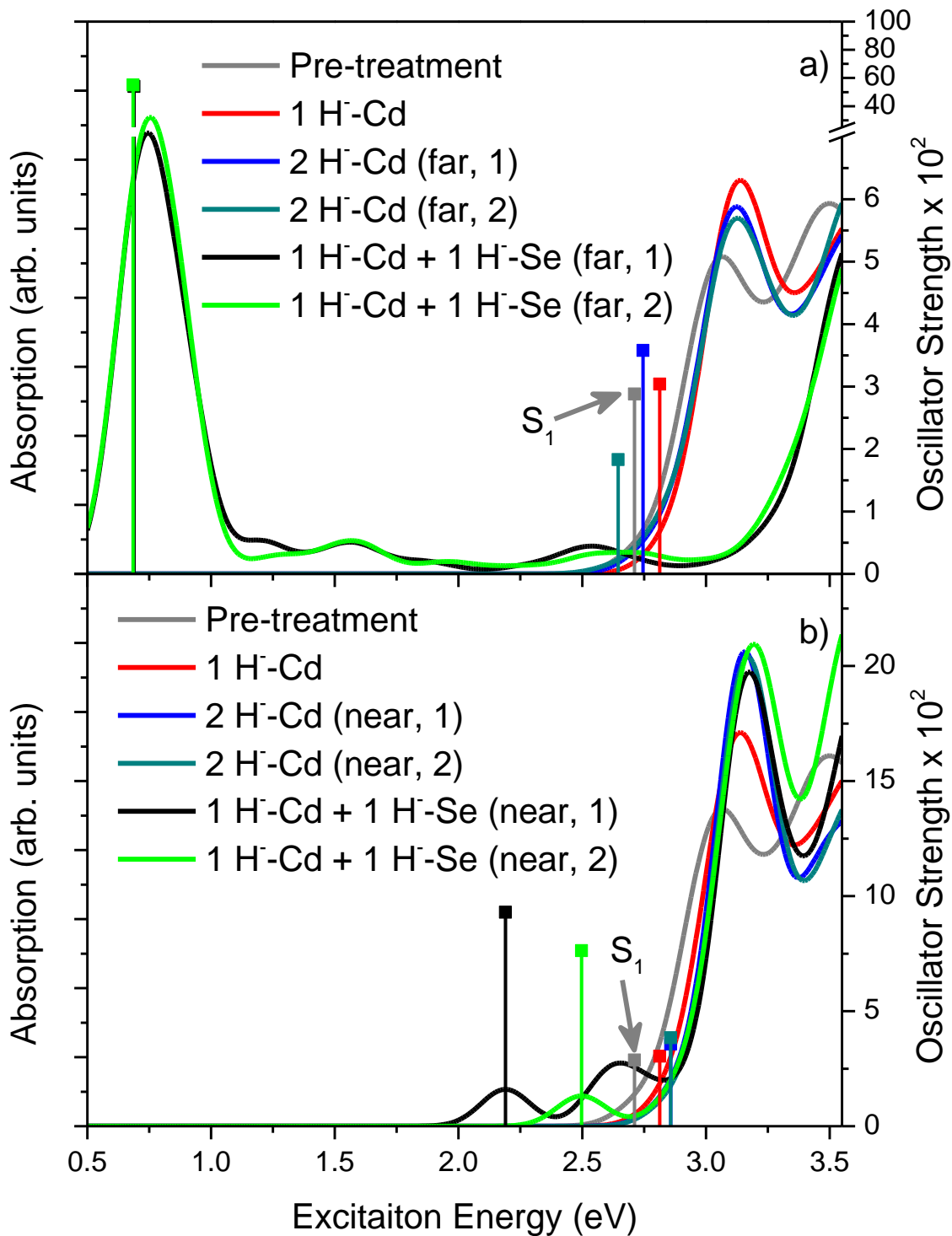


Figure 5.10. Absorption Spectra for Cd<sub>34</sub>Se<sub>33</sub> with pre- (22 methylamine) and post-treatment (21 methylamine and H<sup>-</sup>) on layer B<sub>1</sub> with the first transition oscillator strength plotted with vertical lines. The first transitions (S<sub>1</sub>) for the pre-treated systems are indicated by the arrow. a) the second H<sup>-</sup> was place far from the enriched Cd-H fragment b) the second H<sup>-</sup> was place near the enriched Cd-H fragment.

Table 5.8. NTOs for  $S_1$  transitions plotted in Figure 5.10. surface treatment of  $Cd_{34}Se_{33}$  by  $H^-$  on layer  $B_1$ .

		HOTO	LUTO		HOTO	LUTO
Pre-treatment				1 H-Cd		
2.71 eV				2.81 eV		
$f = 0.029$				$f = 0.030$		
		Far		Near		
2 H <sup>-</sup> -Cd	2.75 eV			2.86 eV		
	$f = 0.036$			$f = 0.036$		
2 H <sup>-</sup> -Cd	2.65 eV			2.86 eV		
	$f = 0.018$			$f = 0.038$		
1 H <sup>-</sup> -Cd + 1 H <sup>-</sup> -Se	0.69 eV			2.19 eV		
	$f = 0.540$			$f = 0.093$		
1 H <sup>-</sup> -Cd + 1 H <sup>-</sup> -Se	0.68 eV			2.50 eV		
	$f = 0.551$			$f = 0.076$		

The enhancement of the PL observed in the experimental studies is like the result of Cd-rich surfaces that are more dominated by  $Cd^{2+}$  ions, in section 5.4 we will investigate  $Cd_{37}Se_{33}$  to investigate the effect of  $H^-$  treatment on the surface where  $Cd^{2+}$  enrichment is relatively high. In this section we will use the fact that reacting with surface  $Se^{2-}$  by the second  $H^-$  results in surface trap states associated with surface  $Se^{2-}$ , thus, we will exclude the possibility of reacting with surface  $Se^{2-}$ .

### 5.2.2.3. $H^-$ Treatment of $Cd_{33}Se_{37}$ QDs

From sections 5.1.2.1 and 5.3.1, we showed that  $H^-$  tends to elongate the Cd-Se bond length for  $Se^{2-}$  that are treated by  $H^-$  and that Se-rich surface can produce  $H_2Se$  which would effectively produce Cd-enriched QDs. Here we will expand this to highly enriched QD with 4 additional  $Se^{2-}$ , Figure 5.11. From section 5.3.1, the charge of the final system was neutralized since both the QD and  $H_2Se$  should be neutral. We followed this concept here, where the final structure after reaction with 8  $H^-$  charge was neutral. Additionally, the intermediate structure with 4  $H^-$  reacting with the 4 non-stoichiometric  $Se^{2-}$  was also oxidized. This is based on the fact that the  $[Se-H]$  fragment would likely have a charge of minus one because from section 5.1.2.1 the  $H^-$  became  $H^+$  after treatment of surface  $Se^{2-}$ . Thus, the total charge of the intermediate geometry was set to negative 4 instead of negative 12.

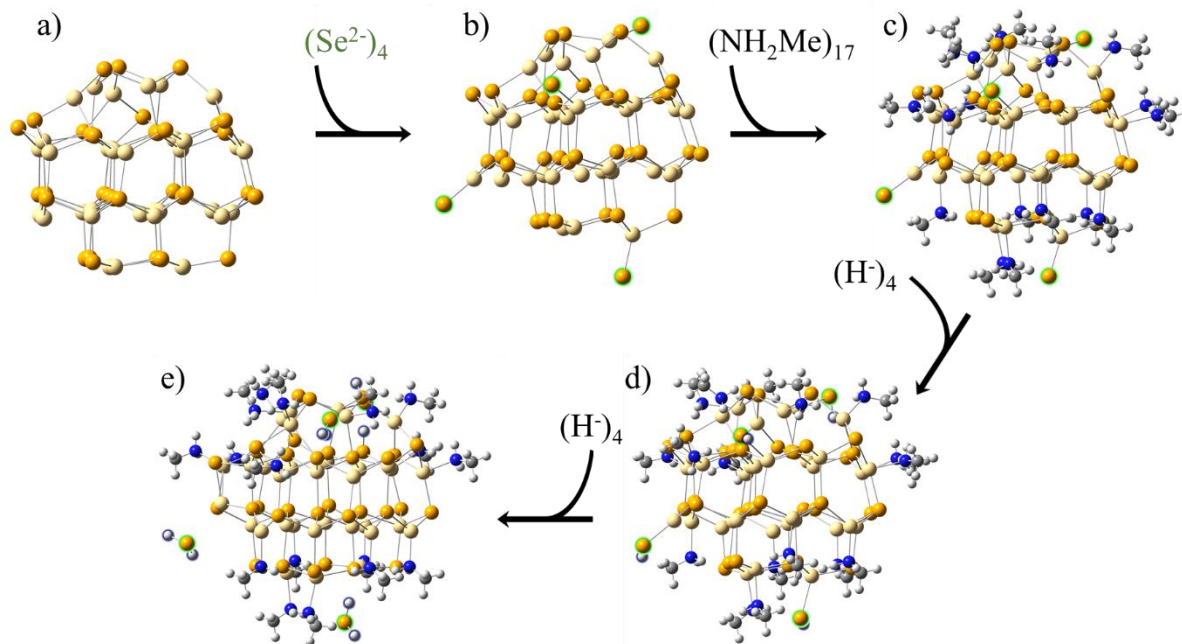


Figure 5.11. Schematic surface enriched by a four  $Se^{2-}$  ions. This starts from bare magic size  $(CdSe)_{33}$  QD (a), where a four  $Se^{2-}$  are places on the surface (b). The  $Cd_{33}Se_{37}$  QD surface is then passivation by 17 methylamines (c). Then four  $H^-$  react with the non-stoichiometric  $Se^{2-}$  (d) followed by a second reaction of four  $H^-$  on the same non-stoichiometric  $Se^{2-}$  resulting in a neutral system (e).

The optical properties of the Se-enriched geometries investigated here, Figure 5.11.c-e, were compared to the optical properties of magic size CdSe QDs, Figure 5.12. Although the oscillator strength of the  $H^-$  treated QDs were not dramatically increased compared to the pre-treated Se-rich QDs, there was  $\sim 0.5$  eV blue shift in the energy of  $S_1$  to the energy range of the magic size QD, Table 5.9. The nature of the transition is still localized compared to magic size QD, however, this could be because there are four surface  $Cd^{2+}$  that are no longer passivated by ligands. This unpassivation of surface  $Cd^{2+}$  is likely not to occur in experimental conditions where ample coordination ligands are available, which would result in the optical transition of post-treatment to become similar or identical to the magic size QD that is 2 times more optically active compared to the Se-rich QD.

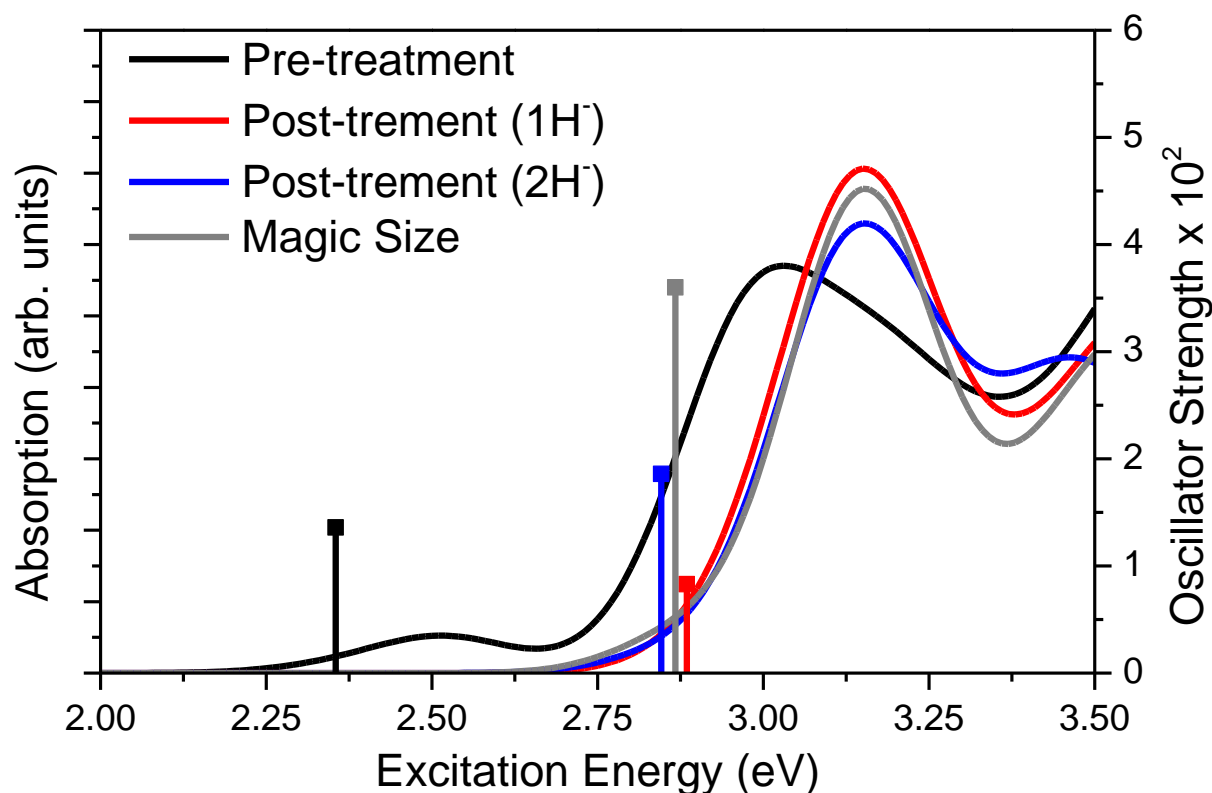
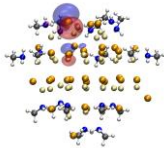
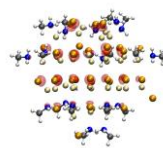
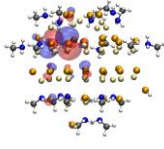
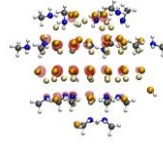
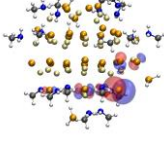
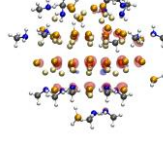
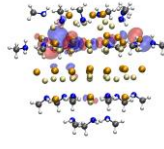
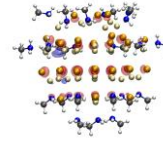


Figure 5.12. Absorption Spectra of  $Cd_{33}Se_{37}$  Se-enriched QDs pre- and during  $H^-$  treatment compared to magic size  $(CdSe)_{33}$  QD, where the oscillator strength of  $S_1$  is plotted with the vertical line.



Table 5.9. NTOs for  $S_1$  transitions plotted in Figure 5.14. surface treatment of  $Cd_{37}Se_{33}$  by  $H^-$ .

	HOTO	LUTO
Pre-treatment 2.35 eV $f = 0.014$		
Post-treatment (1H <sup>-</sup> ) 2.88 eV $f = 0.008$		
Post-treatment (2H <sup>-</sup> ) 2.85 eV $f = 0.019$		
Magic Size 2.87 eV $f = 0.0360$		

#### 5.2.2.4. $H^-$ Treatment of $Cd_{37}Se_{33}$ QDs

The previous section showed that  $H^-$  treatment of Se-rich QDs, would likely result in the formation of  $H_2Se$  removing non-stoichiometric  $Se^{2-}$ . The optical properties of the treated QDs are similar to the magic size and are likely to become the magic size QD which would increase the PL by 2 times. However, this increase pales in comparison to the 55 times increase in PL QY. Additional treatment of surface  $Se^{2-}$  could result in Cd-rich QDs. In this section, we will investigate whether Cd-rich QDs would increase the oscillator strength of the emissive state compared to the pre-treated QDs. The question of placing the second  $H^-$  was partially addressed in section 5.2.2, where trap states are formed when the second  $H^-$  reacts with surface  $Se^{2-}$ . Here we will only consider the passivation of surface  $Cd^{2+}$  near and far from the non-stoichiometric  $Cd^{2+}$  when the second  $H^-$  reacts with the surface, Figure 5.13.

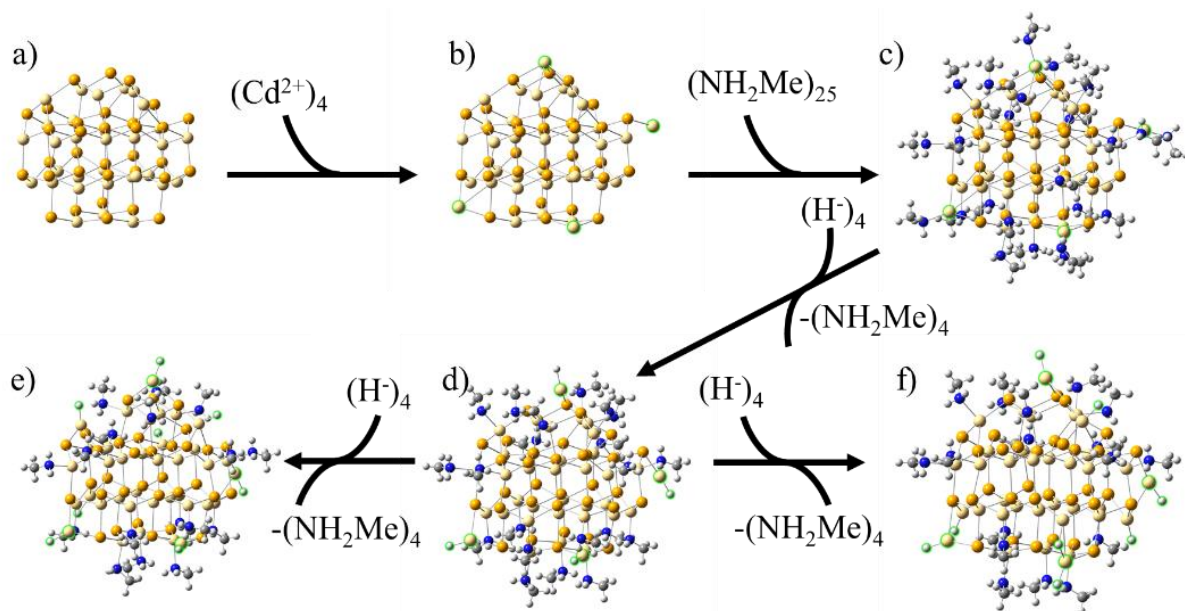


Figure 5.13. Schematic surface enriched by four Cd<sup>2+</sup> ions. This starts from bare magic size (CdSe)<sub>33</sub> QD (a), where a four Cd<sup>2+</sup> are places on the surface (b). The Cd<sub>37</sub>Se<sub>33</sub> QD surface is then passivation by 25 methylamines (c). The fully passivated QD exchanges the four methylamines on the non-stoichiometric Cd<sup>2+</sup> ions (d). The second reaction by four H<sup>-</sup> was only performed on far Cd<sup>2+</sup> (e) and near Cd<sup>2+</sup> (f) ions.

Investigating the emissive properties of the pre-treated, single H<sup>-</sup> per non-stoichiometric Cd<sup>2+</sup> and 2 H<sup>-</sup> per non-stoichiometric Cd<sup>2+</sup>, shows the blue shift observed in experimental studies but no dramatic increase in PL (oscillator strength of S<sub>1</sub>), Figure 5.14 and Table 5.10. The largest enhancement our simulations show is a 2x enhancement, for panel c the third configuration investigated. Interestingly, this transition is brighter than the ideal surface simulated from magic size (CdSe)<sub>33</sub> QD which would be expected to be the brightest. Comparing the nature of the excitation for configuration 3 to 1 shows that the post-treated QDs for configuration 3 with the second H<sup>-</sup> on an adjacent Cd<sup>2+</sup> is the most delocalized, Table 5.14.

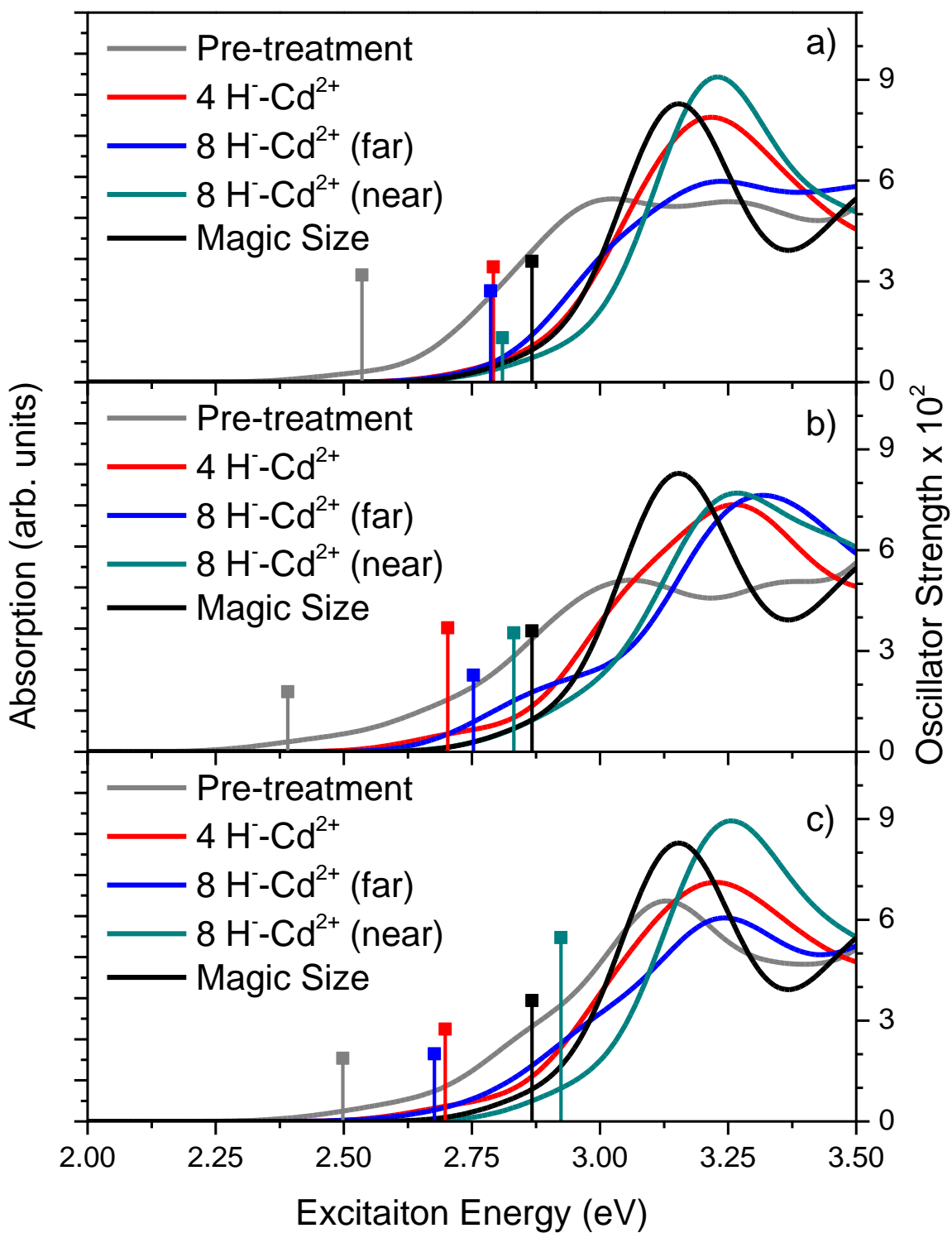
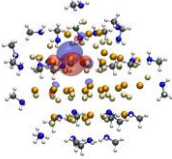
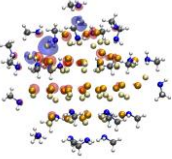
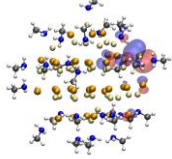
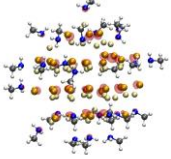
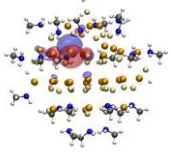
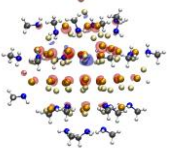
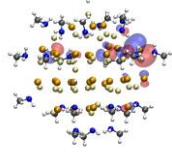
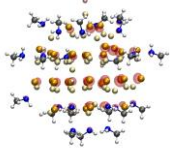
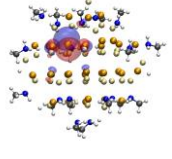
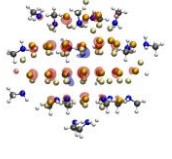
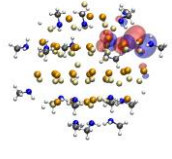
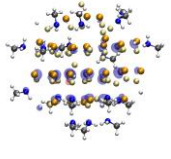
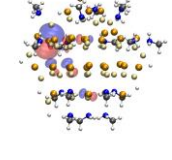
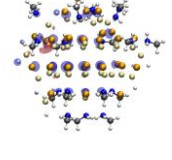
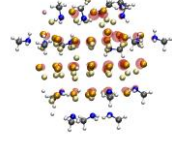
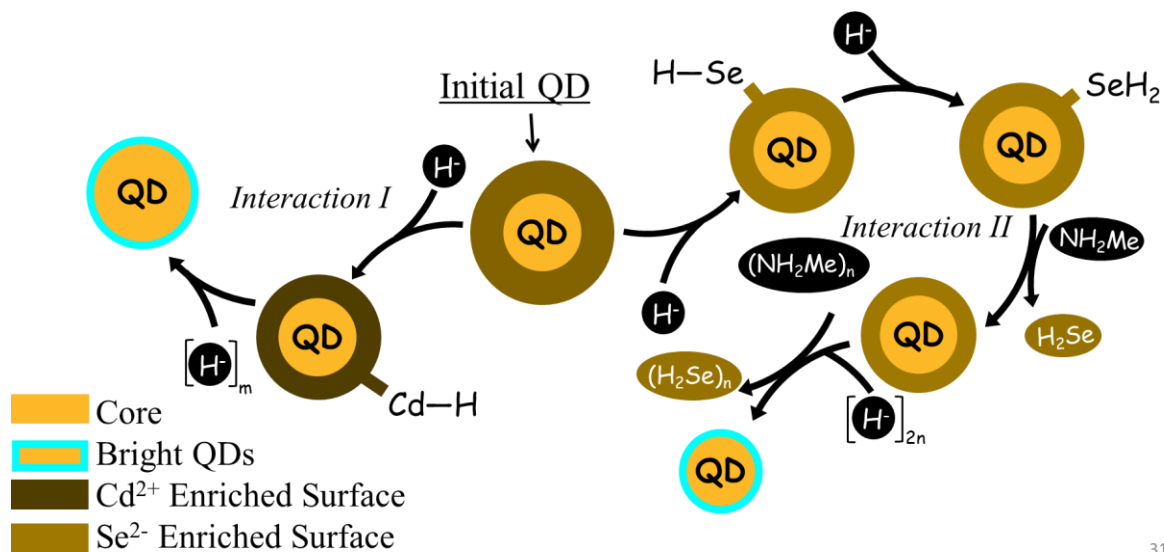


Figure 5.14. Absorption Spectra of Cd<sub>37</sub>Se<sub>33</sub> Cd-enriched QDs pre- and during H<sup>-</sup> treatment compared to magic size (CdSe)<sub>33</sub> QD, where the oscillator strength of S<sub>1</sub> is plotted with the vertical line. a) configuration 1 b) configuration 2 c) configuration 3.

Table 5.10. NTOs for  $S_1$  transitions plotted in Figure 5.14. surface treatment of  $Cd_{37}Se_{33}$  by  $H^-$ .

		Configuration 1		Configuration 3		
		HOTO	LUTO	HOTO	LUTO	
Pre-treatment	2.54 eV $f = 0.032$			2.50 eV $f = 0.019$		
	4 $H^-Cd^{2+}$			2.70 eV $f = 0.028$		
8 $H^-Cd^{2+}$ (far)	2.79 eV $f = 0.027$			2.68 eV $f = 0.020$		
	8 $H^-Cd^{2+}$ (near)	2.81 eV $f = 0.013$			2.92 eV $f = 0.055$	

Combining the observation from stoichiometric (magic size), section 5.2.1, and non-stoichiometric QDs, section 5.2.2, we propose the following mechanism for PL enhancement by  $H^-$  treatment, Figure 5.15. In this mechanism,  $H^-$  can interact with the QD in two ways in addition to the reduction proposed by Tsui and co-workers.<sup>3</sup> The interaction of the  $H^-$  is likely driven primarily by the kinetic in experimental studies, meaning that the type of interaction of incoming  $H^-$  can go through either interaction mechanism. Firstly,  $H^-$  can react with surface  $Cd^{2+}$  that efficiently passivated the dangling bonds as shown in Figure 5.12. The second interaction is the removal of surface  $Se^{2-}$  by  $H^-$  generating  $H_2Se$  that readily desorbs from the QDs surface being replaced by methylamine. These interactions would result in optically active QDs.



31

Figure 5.15. Proposed mechanism for enhancement of QY of PL by H<sup>-</sup> treatment.

### 5.3. Conclusions

The proposed mechanism for PL enhancement is proposed based on our DFT and TDDFT calculations simulating the treatment of H<sup>-</sup> on stoichiometric and non-stoichiometric CdSe QDs. Three pathways are likely responsible for the enhancement of PL observed in experimental studies.<sup>1-3</sup> The first pathway was indirectly reported by Tsui and co-workers where they obscured the formation of D<sub>2</sub> from deuterated H<sup>-</sup> sources, where the QD is reduced. In this study, we did not investigate this effect. Cd-rich surfaces are likely reduced causing the surface to become less positive, charged QDs have been shown to undergo non-radiative relaxation through trion states.<sup>19</sup> The second pathway for PL enhancement is the removal of surface Se<sup>2-</sup> ions that are responsible for trap states. The third and final pathway is the passivation of surface Cd<sup>2+</sup> by H<sup>-</sup> that efficiently caps the dangling bonds of 2- and 3-coordinated Cd<sup>2+</sup>. From our simulations the largest increase in the oscillator strength of the lowest transition was two times the pre-treated QDs. This enhancement is dramatically smaller compared to the 55 times enhancement seen in experimental studies. We suspect that the 55 times enhancement is the

result of “turning” on the emissive properties of QDs that were completely optically inactive before H<sup>-</sup> treatment. In contrast, in our modeling the “non-treated” QDs have a perfect surface passivations, which is likely not the case in experimental studies. The perfect surface passivations increases the “non-treated” QDs’ optical properties making the improvement by H<sup>-</sup> treatment being less pronounced in our modeling compared to the significant improvement observed in experimental studies.

#### 5.4. References

1. Jang, E.; Jun, S.; Chung, Y.; Pu, L., Surface treatment to enhance the quantum efficiency of semiconductor nanocrystals. *J. Phys. Chem. B* **2004**, *108* (15), 4597-4600.
2. Subila, K.; Kishore Kumar, G.; Shivaprasad, S.; George Thomas, K., Luminescence properties of CdSe quantum dots: role of crystal structure and surface composition. *J. Phys. Chem. Lett.* **2013**, *4* (16), 2774-2779.
3. Tsui, E. Y.; Hartstein, K. H.; Gamelin, D. R., Selenium Redox Reactivity on Colloidal CdSe Quantum Dot Surfaces. *J. Am. Chem. Soc.* **2016**, *138* (35), 11105-11108.
4. Hetsch, F.; Zhao, N.; Kershaw, S. V.; Rogach, A. L., Quantum dot field effect transistors. *Mater. Today* **2013**, *16* (9), 312-325.
5. Somers, R. C.; Bawendi, M. G.; Nocera, D. G., CdSe nanocrystal based chem-/bio-sensors. *Chem. Soc. Rev.* **2007**, *36* (4), 579-591.
6. Hetsch, F.; Xu, X.; Wang, H.; Kershaw, S. V.; Rogach, A. L., Semiconductor nanocrystal quantum dots as solar cell components and photosensitizers: material, charge transfer, and separation aspects of some device topologies. *J. Phys. Chem. Lett.* **2011**, *2* (15), 1879-1887.
7. Yang, Y.; Zheng, Y.; Cao, W.; Titov, A.; Hyvonen, J.; Manders, J. R.; Xue, J.; Holloway, P. H.; Qian, L., High-efficiency light-emitting devices based on quantum dots with tailored nanostructures. *Nat. Photonics* **2015**, *9* (4), 259.
8. Kilina, S.; Ivanov, S.; Tretiak, S., Effect of Surface Ligands on Optical and Electronic Spectra of Semiconductor Nanoclusters. *J. Am. Chem. Soc.* **2009**, *131* (22), 7717-7726.
9. Puzder, A.; Williamson, A.; Gygi, F.; Galli, G., Self-healing of CdSe nanocrystals: first-principles calculations. *Phys. Rev. Lett.* **2004**, *92* (21), 217401.
10. Kilina, S. V.; Tamukong, P. K.; Kilin, D. S., Surface Chemistry of Semiconducting Quantum Dots: Theoretical Perspectives. *Acc. Chem. Res.* **2016**, *49* (10), 2127-2135.
11. Wei, H. H.-Y.; Evans, C. M.; Swartz, B. D.; Neukirch, A. J.; Young, J.; Prezhdo, O. V.; Krauss, T. D., Colloidal semiconductor quantum dots with tunable surface composition. *Nano Lett.* **2012**, *12* (9), 4465-4471.
12. Jeong, D.-W.; Park, J. Y.; Kim, T.-S.; Seong, T.-Y.; Kim, J.-Y.; Ko, M. J.; Kim, B. S., Fine Tuning of Colloidal CdSe Quantum Dot Photovoltaic Properties by Microfluidic Reactors. *Electrochim. Acta* **2016**, *222*, 1668-1676.

13. Wei, N.; Li, L.; Zhang, H.; Wang, W.; Pan, C.; Qi, S.; Zhang, H.; Chen, H.; Chen, X., Characterization of the Ligand Exchange Reactions on CdSe/ZnS QDs by Capillary Electrophoresis. *Langmuir* **2019**, *35* (14), 4806-4812.
14. Kasha, M., Characterization of electronic transitions in complex molecules. *Discuss Faraday Soc.* **1950**, *9*, 14-19.
15. Gong, K.; Kelley, D. F.; Kelley, A. M., Resonance Raman excitation profiles of CdS in pure CdS and CdSe/CdS core/shell quantum dots: CdS-localized excitons. *J. Chem. Phys.* **2017**, *147* (22), 224702.
16. Martin, R. L., Natural transition orbitals. *J. Chem. Phys.* **2003**, *118* (11), 4775-4777.
17. Humphrey, W.; Dalke, A.; Schulten, K., VMD: visual molecular dynamics. *J. Mol. Graph.* **1996**, *14* (1), 33-38.
18. Miller, J. B.; Dandu, N.; Velizhanin, K. A.; Anthony, R. J.; Kortshagen, U. R.; Kroll, D. M.; Kilina, S.; Hobbie, E. K., Enhanced luminescent stability through particle interactions in silicon nanocrystal aggregates. *ACS Nano* **2015**, *9* (10), 9772-9782.
19. Galland, C.; Ghosh, Y.; Steinbrück, A.; Sykora, M.; Hollingsworth, J. A.; Klimov, V. I.; Htoon, H., Two types of luminescence blinking revealed by spectroelectrochemistry of single quantum dots. *Nature* **2011**, *479* (7372), 203-207.

## 6. INFLUENCE OF SURFACE THIOL/THIOLATE PASSIVATION ON THE PHOTOPHYSICS OF CDS QUANTUM DOTS

In this chapter, the effect of passivating the surface of the QD by thiol derivatives will be studied. Thiol derivatives, like  $\text{H}^-$  treatment, are thought to undergo multiple types of ligands exchange including L- and X-type. Thiol can undergo both of these pathways because the neutral thiol ligand can donate lone pairs to surface  $\text{Cd}^{2+}$  or undergo deprotonated resulting in thiolate, a conjugate base, that can react with surface  $\text{Cd}^{2+}$ . The effect of thiolate on the surface has been studied experiential with a bifunctional thiol derivative that can be used to take the QDs into the aqueous phase, that results in thiolate formation causing the PL to be quenched.<sup>1</sup>

Thiol can be utilized in the syntheses of so-called “giant” CdSe/CdS core/shell QDs as the sulfur precursor, these core/shell QDs have been shown to have suppressed blinking making them ideal for LED applications,<sup>2-3</sup> however, under high influence of light and temperature the QY of PL of the “giant” CdSe/CdS QDs produced with thiol as a precursor become optically inactive. The details of the irreversible quenching of the PL properties are unknown. In this chapter, I will investigate the irreversible quenching by investigating whether the surface is able to abstract the acidic proton in thiol resulting in thiolate formation and protonation of surface  $\text{Se}^{2-}$ .

### 6.1. Introduction

From chapter 2, the surface of colloidal QDs is dynamically passivated by ligand which results in desorption and adsorption of ligands. This causes the PL properties to fluctuation in a process called blinking, blinking is not ideal for LEDs because the overall luminosity of the device could greatly vary.<sup>3-9</sup> To address the issue of dynamic surface passivation by ligand “giant” core/shell QDs were synthesized showing suppressed blinking as a result of passivating



the light-emitting core by a shell of inorganic material.<sup>5-6, 8, 10</sup> The syntheses of the “giant” CdSe/CdS has been performed by successive ionic layer adsorption and reaction (SILAR)<sup>2, 6-7, 11</sup> and high-temperature continuous-injection (HTCI).<sup>4</sup> Investigating the photophysical properties of these “giant” CdSe/CdSe QDs via single dot spectroscopy where the QDs are exposed to high influence of light and temperatures shows that HTCI is initially more optically active compared to SILAR QDs. However, the PL of HTCI QDs quickly undergoes irreversible bleaching while SILAR QDs show reversible bleaching under high influence of light and temperature.<sup>2</sup> The reversible bleaching of SILAR QDs can be explained by charging of the QD under high influence of light, while the irreversible bleaching of HTCI is through trap states.<sup>2</sup> The surface of these QDs is vastly different. SILAR QDs are synthesized with sulfur powder which results in surfaces that are passivated by oleate, where HTCI are synthesized using 1-octylthiol that likely result in the surface being passivated by thiol functionalized ligands. I believe the trap states that cause the irreversible bleaching are associated with the thiol ligands because previous studies investigating  $\beta$ -mercaptoethanol (BME) found that thiolate formation, loss of the acidic proton bounded to S, results in quenching of the PL. In this study, thiolate formation was caused by deprotonation of BME through the aqueous solvent.<sup>1</sup> In the single dot experiments, the QDs are deposited on glass and the solvent is removed which would prevent the solvent from deprotonating the thiol that could then result in passivating the surface with thiolate.

In this chapter, I will study whether the surface of the QD is capable of deprotonating surface thiol which would result in thiolate formation without the need of protic solvents causing the irreversible bleaching observed in the single dot spectroscopy study.<sup>2</sup> The study of the full core/shell system is computationally infeasible, however, as described in section 3.3.2. when surface trap states are formed the surface of the QD only needs to be studied because these trap

states could be within the bandgap of the core. This assumption allows us to simulate the surface of the “giant” CdSe/CdSe core/shell QD by magic size  $(\text{CdS})_{33}$  QD, Figure 6.1.

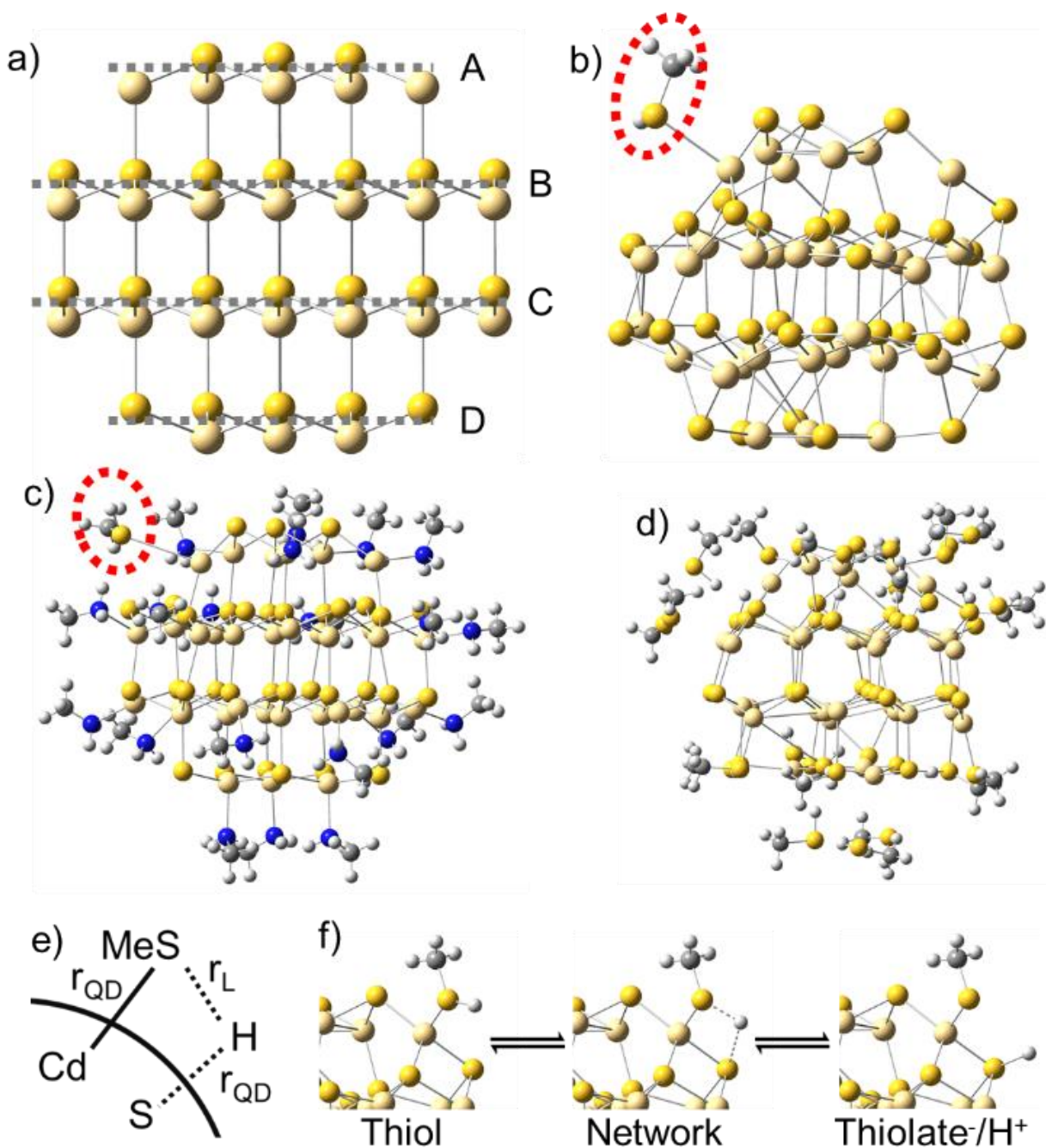


Figure 6.1. Model system used to study surface abstraction of the acidic proton in thiol. a) magic size  $(\text{CdS})_{33}$  QD with layers A-D denoted b) single passivated  $(\text{CdS})_{33}$  with thiol c) fully passivated  $(\text{CdS})_{33}$  with 20 methylamines (MA) and one thiol d) fully passivated  $(\text{CdS})_{33}$  with 21 thiol e) Schematic diagram illustrating the three bond lengths shown in Fig. 3. f) Interconversion between thiol and thiolate where the QDs extracts  $\text{H}^+$ .

## 6.2. Results and Discussion

Investigating whether the surface is capable of deprotonating thiol causing thiolate associated trap states was performed in apolar (propylamine, PAM,  $\epsilon = 4.9912$ ) and polar (acetonitrile, ACN,  $\epsilon = 35.688$ ) solvents via CPCM.<sup>12-13</sup> This was done to simulate the effect of solvents in various experimental conditions and to modulate the surface dipole that is likely responsible for proton extraction. The apolar solvent PAM will be assumed to approximate the dielectric of the atmosphere in the experimental conditions where irreversible bleaching of PL was observed. In this work, I will consider three thiol (methanethiol) derivatives that interacts with the surface of the QD: 1) thiol (HSR) 2) thiolate/H ( $\text{SR}^-/\text{H}^+$ ) 3) thiolate ( $\text{SR}^-$ ). At the beginning of this study, I will investigate a single thiol derivative and the effect it has on the photophysical properties. Then I will investigate QDs that are fully passivated by thiol derivatives. These simulations will revival an atomic level understanding of the effect of the surface on thiolate formation which could result in the irreversible photobleaching observed in the single dot spectroscopy experiment.<sup>2</sup>

### 6.2.1. Surface Passivation by a Single Thiol Derivative

In this section, the passivation of magic size  $(\text{CdS})_{33}$  QDs by a single thiol derivative will be investigated. There will be two types of surface passivation schemes used in this section bare (Figure 6.1.b) and amine surface (Figure 6.1.c). This was done because the surface dipole of the QD is changed when passivating the surface with methylamines (MA) compared to bare QDs, the surface dipole I believe is responsible for the deprotonation of thiol (HSR) to thiolate ( $\text{SR}^-/\text{H}^+$ ), where surface  $\text{S}^{2-}$  abstract the  $\text{H}^+$  from the thiol. Conventionally, the emissive properties of surface with increased surface passivation should become more emissive since surface dangling bonds are passivating reducing sites for surface trap states. If it is true that the surface can

deprotonate thiol resulting in surface passivation of  $\text{Cd}^{2+}$  by  $\text{SR}^-$  and  $\text{S}^{2-}$  by  $\text{H}^+$  is responsible for PL quenching this would be counterintuitive. This counterintuitive trend could be explained by the ligand states being destabilized when the charged  $\text{SR}^-$  ligand interacts with the surface, this destabilization has been observed for the CdSe-N719 dye-sensitized QD. That has the dye state shift within the bandgap of the CdSe QD when the N719 dye was deprotonated and interacted through the charged functional group.<sup>14</sup>

The binding energy ( $B_e$ ) of the three thiol derivatives was computed for both solvents on layers A-D, Figure 6.2. The thiol ligand weakly interacts with the surface of the QD with fully passivated or bare surfaces but is around an order of magnitude larger compared to thermal fluctuation meaning that thiol would be thermally stable on the surface of the QD. The  $B_e$  thiol pales in comparison to the bind of  $\text{SR}^-$  with or without  $\text{H}^+$  passivating surface  $\text{S}^{2-}$ . In the apolar solvent PAM, the stabilization is around 2.0 eV while in ACN (polar) the stabilization energy is reduced to approximately 1.0 eV. This reduction in the stabilization when the surface abstracts the acidic proton is likely caused to the inversely proportional dependence of the Coulombic or dipole-dipole interaction between the oppositely charged surface  $\text{Cd}^{2+}$  and  $\text{SR}^-$ .<sup>15</sup> From the  $B_e$  it would appear that the surface would be thermodynamically favored to remove the proton from the HSR ligand resulting in  $\text{SR}^-/\text{H}^+$  on the surface.

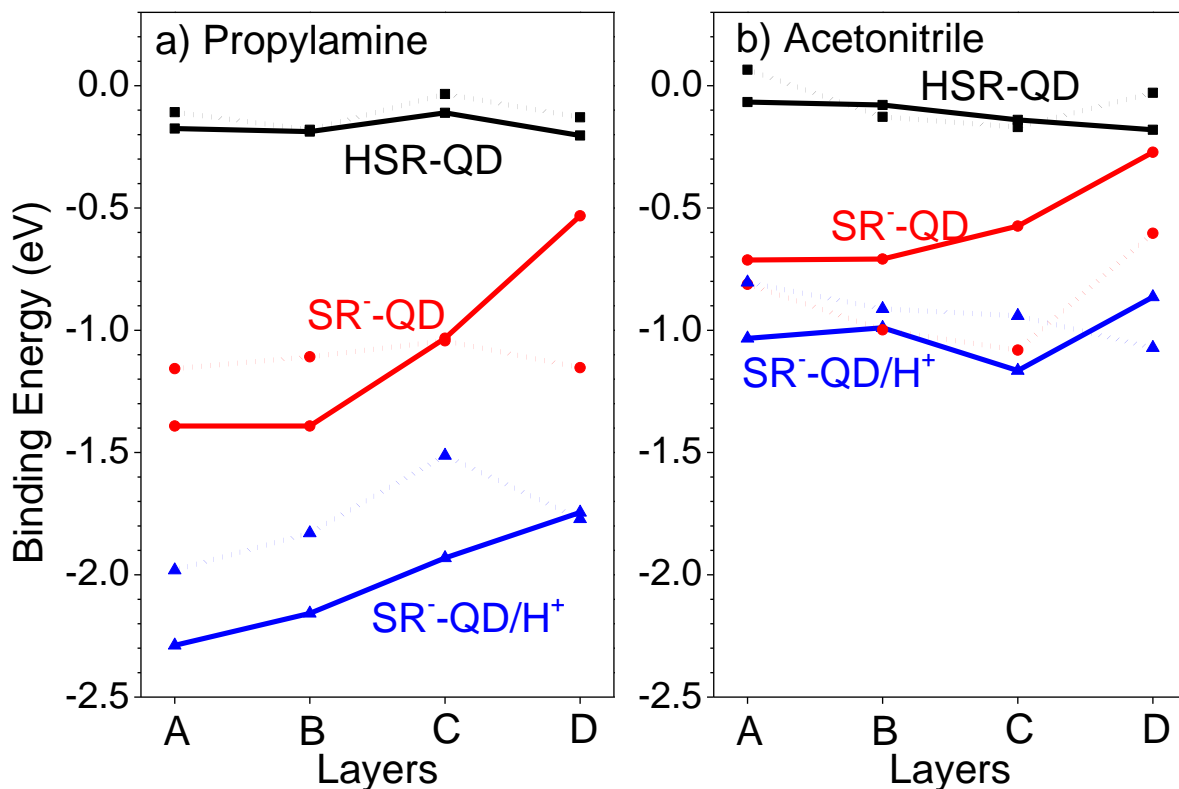


Figure 6.2. Binding energy ( $B_e$ ) of thiol derivative to QDs in propylamine (a) and acetonitrile (b) on layers A-D. Solid (dashed) lines represent passivation by 20 MA (bare) with a single thiol derivative, HSR (black),  $SR^-$  (red), or  $SR^-/H^+$  (blue) QDs.

Although, there is a thermodynamic driving force to convert HSR into  $SR^-/H^+$  on the surface of the QD at 0 K the equilibrium geometry for all layers except for layer C show that HSR interacts as a L-type ligand. This analyzation was done by comparing the bond lengths shown in Figure 6.1.e. that are plotted in Figure 6.3. for both bare and amine passivated CdS QDs. The bond length between the surface and the ligand can also explain why in ACN the  $B_e$  of  $SR^-/H^+$  is reduced because the bond length between the surface and the ligand is elongated (0.1-0.5 Å) indicating a reduction in the interaction as observed in the  $B_e$ . The only surface that facilitates interconversion between HSR and  $SR^-/H^+$  is layer C, where both amine and bare passivated surfaces the  $H^+$  is shared between surface  $S^{2-}$  and the ligand, Figure 6.3. The bond length reduction between the ligand and surface sulfurs does not change the nature of the initial

passivation but mixes nature. This observation is similar to hydrogen bonding in bulk water; thus, we refer to this as surface networking ( $N_S$ ).

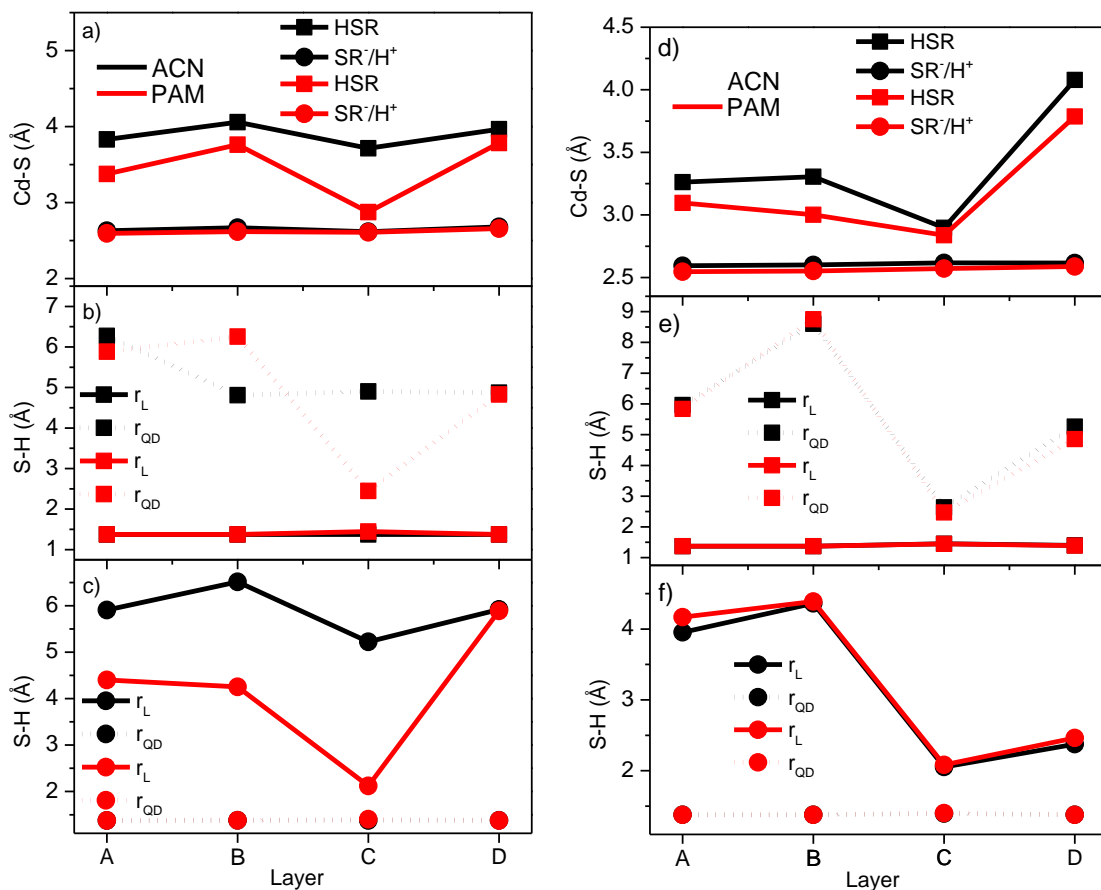


Figure 6.3. Bond length of fully passivated (a-c) and bare (d-f) QDs with one HSR or  $SR^-/H^+$  on the surface. Panels a and d bond length between the surface ( $Cd^{2+}$ ) and ligand (S), panels b and e bond lengths between the surface and ligand sulfur to  $H^+$  for HSR initial passivation, panels c and f bond lengths between the surface and ligand sulfur to  $H^+$  for  $SR^-$  initial passivation.

The networking between the surface for layer C could provide insight into how charging the thiol ligand affects the ligand-based electronic states which could provide the trap states observed in experiments.<sup>1-2, 16</sup> To investigate the shifting of the electronic states PDOS plots were generated for layers A and C, Figure 6.4. and 6.5. The destabilization observed for N719 dye in the VB when charged is also seen when HSR is deprotonated forming  $SR^-$  and  $SR^-/H^+$ , where the ligand-based states are somewhat stabilized when  $H^+$  is placed on the surface for layer

A. From the PDOS for layer A it is expected that the emissive properties of  $\text{SR}^-$  to be very low due to the hybridization of the QD and ligand-based states, Figure 6.4. Additionally, there is a shoulder in the VB edge that is QD associated with all initial passivation for layer C PDOS, Figure 6.5.

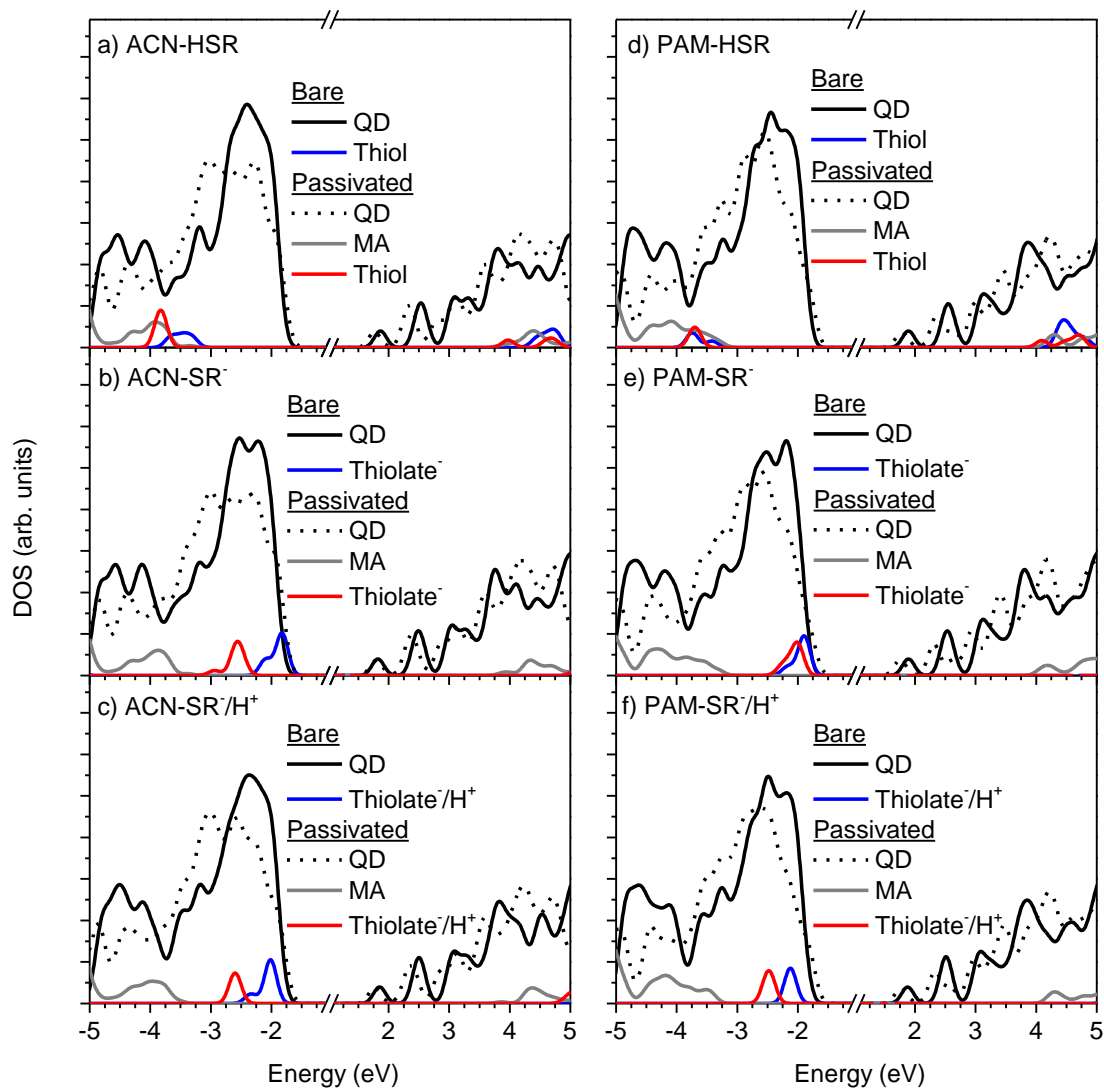


Figure 6.4. Projected Density of State (PDOS) for fully passivated QDs and singly passivated of HSR (a and d),  $\text{SR}^-$  (b and e), and  $\text{SR}^-/\text{H}^+$  (c and f) on layer A in ACN and PAM. The PDOS for the thiol derivatives is multiplied by 3 to aid in visualization.

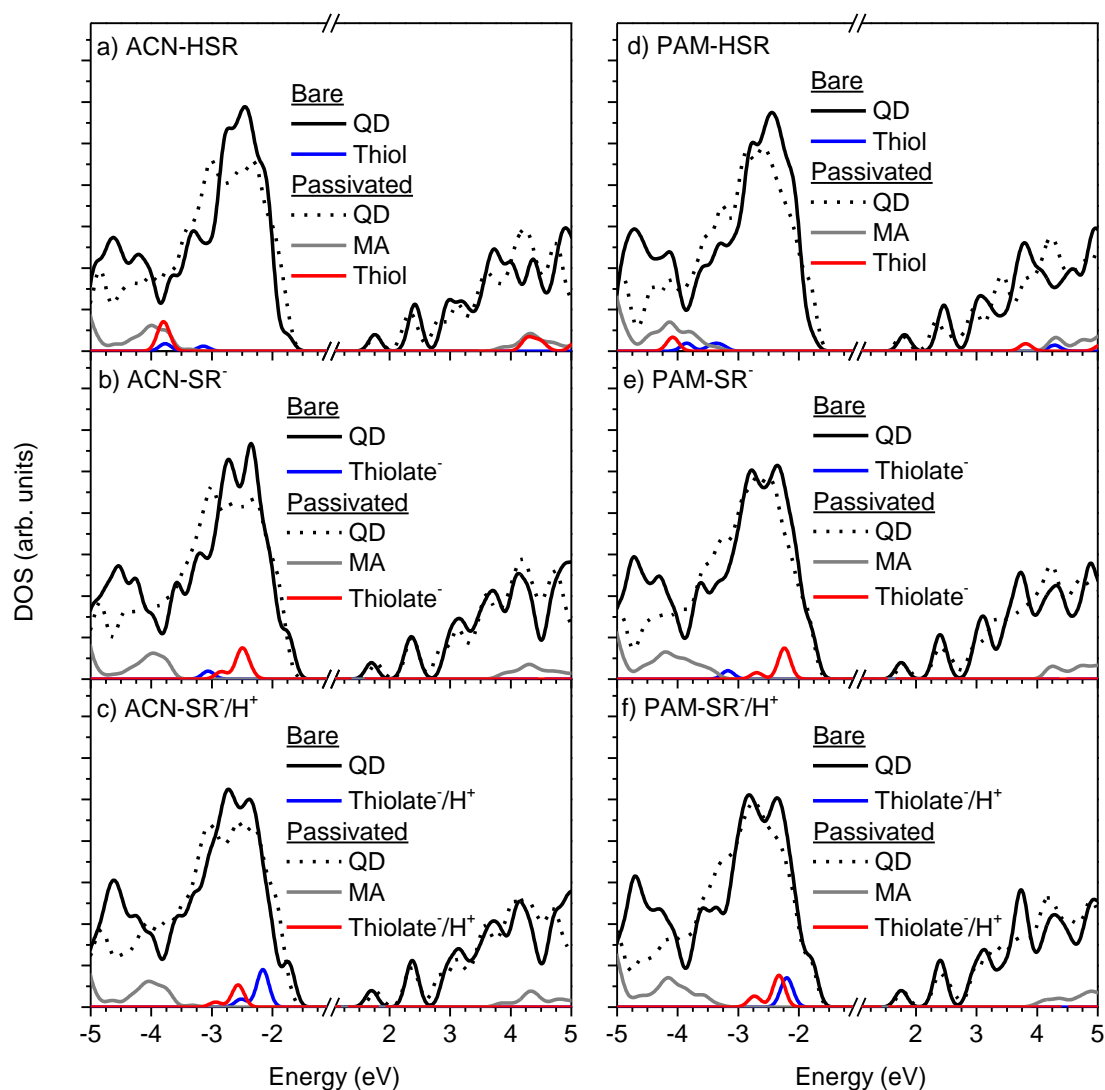


Figure 6.5. Projected Density of State (PDOS) for fully passivated QDs and singly passivated of HSR (a and d),  $\text{SR}^-$  (b and e), and  $\text{SR}^-/\text{H}^+$  (c and f) on layer C in ACN and PAM. The PDOS for the thiol derivatives is multiplied by 3 to aid in visualization.

The perturbation of the QD states near the VB edge should affect the optical properties and therefore the emissive properties of these QDs passivated by thiol derivatives. The emissive properties will be approximated by computing the oscillator strength of the lowest singlet state ( $S_1$ ), this is in accordance with the Kasha's rule.<sup>17</sup> Computing the absorption spectra for thiol derivative passivated structures in Figures 6.4. and 6.5. are plotted in Figure 6.6. From Figure



6.6., the networking causes the bare CdS QDs with  $SR^-$  and  $SR^-/H^+$  to have low energy transitions that are reduced in intensity compared to the magic size and HSE QDs. This would support the hypothesis that thiolate formation either by the solvent or the surface would result in quenching of PL that is observed in experimental studies.<sup>1-2</sup> Computing NTOs for these transitions show that the trap state is not located on the ligand but the ligand causes a localization of the HOTO that is responsible for the decrease in oscillator strength, Table 6.1.

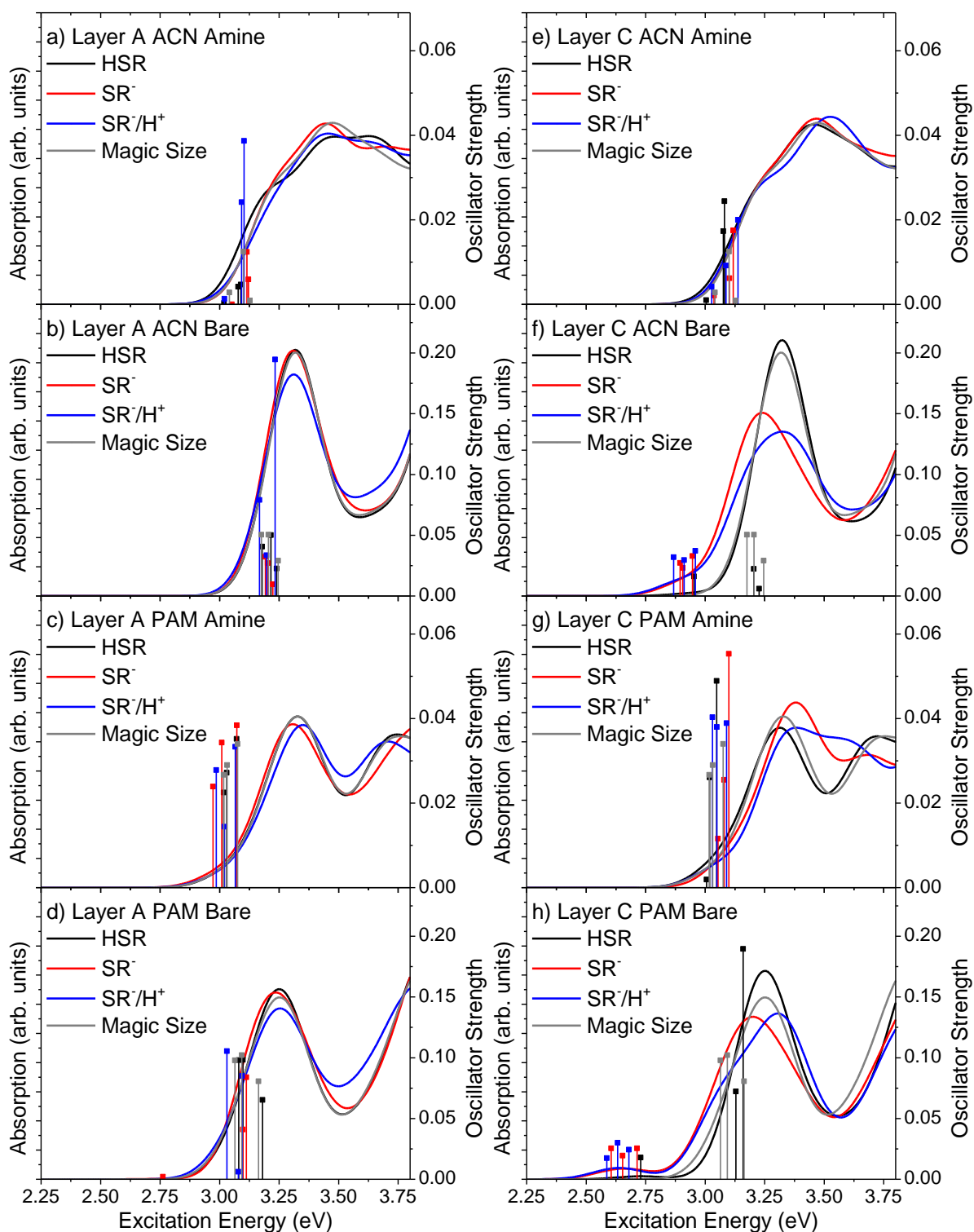


Figure 6.6. Absorption spectra for Layer A and C with a singlet thiol derivative passivating amine and bare QDS.

Table 6.1. NTOs for  $S_1$  for the QDs with HSR and  $SR^-/H^+$  initial passivation from Figure 6.6.

		Amine		Bare			
		HOTO	LUMO	HOTO	LUMO		
HSR	ACN	Layer A 3.02 eV $f = 0.0003$			Layer A 3.18 eV $f = 0.0408$		
		Layer C 3.00 eV $f = 0.0010$			Layer C 2.95 eV $f = 0.0163$		
	PAM	Layer A 3.02 eV $f = 0.0227$			Layer A 3.08 eV $f = 0.0985$		
		Layer C 3.01 eV $f = 0.0019$			Layer C 2.73 eV $f = 0.0180$		
$SR^-/H^+$	ACN	Layer A 3.02 eV $f = 0.0013$			Layer A 3.17 eV $f = 0.0794$		
		Layer C 3.03 eV $f = 0.0042$			Layer C 2.87 eV $f = 0.0321$		
	PAM	Layer A 2.99 eV $f = 0.0280$			Layer A 3.03 eV $f = 0.1059$		
		Layer C 3.03 eV $f = 0.0403$			Layer C 2.59 eV $f = 0.0172$		

The observed red-shifted reduced optical active states for QDs with  $SR^-$  passivating the surface  $Cd^{2+}$  indicates that the presents of  $SR^-$  on the surface can result in ligand-induced traps states, the question of whether HSR and be converted into  $SR^-/H^+$  is unanswered by placing a

single thiol derivative on the surface of CdS QDs. To address this question, two initial conditions for fully HSR and  $\text{SR}^-/\text{H}^+$  passivated CdS QDs were prepared.

### 6.2.2. Fully Passivated CdS QDs by HSR and $\text{SR}^-/\text{H}^+$ Ligand

In the previous section, QDs passivated by a single thiol derivative was investigated finding that the formation of  $\text{SR}^-/\text{H}^+$  on the surface would result in ligand-induced trap states by introducing CT states, proton abstraction by surface  $\text{S}^{2-}$  is thermodynamically favorable from 0.5-2.0 eV, and networking reduces the destabilization of the ligand states. Here I will investigate whether the presence of neighboring thiol derivatives will result in the conversation between HSR to  $\text{SR}^-/\text{H}^+$ . If  $\text{SR}^-/\text{H}^+$  is formed this is likely irreversible because of the thermodynamic driving force of 0.5-2.0 eV which would explain why HTCI “giant” CdSe/CdS QDs undergo irreversible photobleaching.

The equilibrium structures of the initial passivation of CdS QDs by HSR and  $\text{SR}^-/\text{H}^+$  were obtained, from these structures were encountered a second type of networking, this networking was between neighboring ligands ( $N_L$ ). The surface passivation was then investigated by counting the number of each type of ligands on the surface for HSR,  $\text{SR}^-/\text{H}^+$ , surface networking, and ligand networking, Table 6.2. Comparing the relative numbers of ligands that remain in the initial confirmation supports the irreversibility of  $\text{SR}^-/\text{H}^+$  formation by surface abstraction of the  $\text{H}^+$  because around 5 times more  $\text{SR}^-$  remain after optimization compared to the HSR. Additionally, the number of surface networking ( $N_S$ ) is relatively high compared to ligand networking ( $N_L$ ). From the previous section, the formation of  $\text{SR}^-/\text{H}^+$  resulted in perturbation of the electronic structure causing the optical activity of  $S_1$  to decrease. For full passivation by thiol derivative results in more dramatic differences between HSR and  $\text{SR}^-/\text{H}^+$   $S_1$ , Figure 6.7.

Table 6.2. The instances of HSR,  $\text{SR}^-/\text{H}^+$ ,  $N_s$ , and  $N_L$  on the surface of CdS QDs fully passivated by thiol derivatives based (HSR, and  $\text{SR}^-/\text{H}^+$ ) on the bond lengths between sulfurs (ligand and QD's surface) to the  $\text{H}^+$ .

System	HSR	$\text{SR}^-/\text{H}^+$	$N_s$	$N_L$
PAM HSR	3	0	10	8
PAM $\text{SR}^-/\text{H}^+$	0	14	7	0
ACN HSR	3	0	12	6
ACN $\text{SR}^-/\text{H}^+$	0	15	6	0

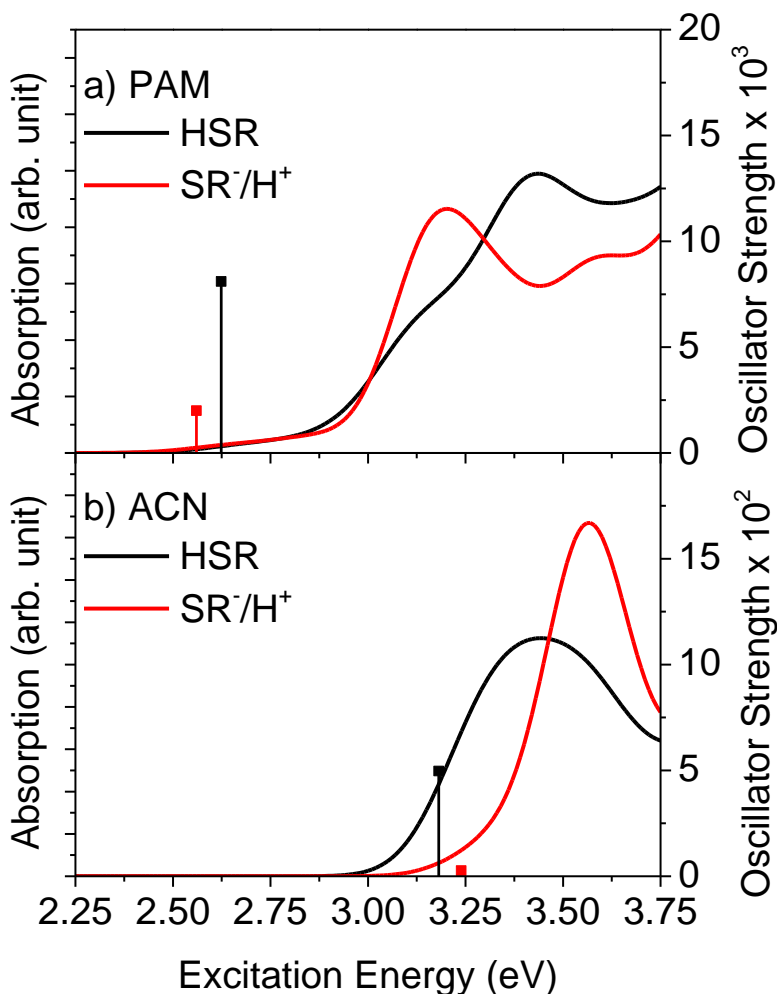
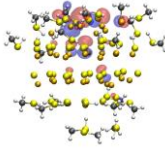
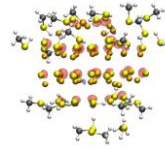
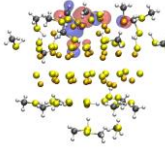
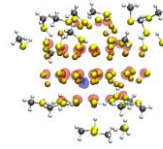
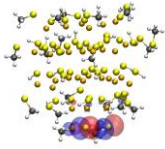
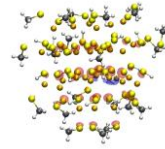
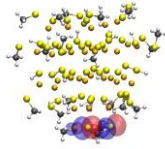
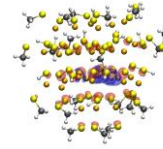


Figure 6.7. Absorption of QDs fully passivated by 21 HSR or  $\text{SR}^-/\text{H}^+$  in PAM and ACN. The oscillator strength for  $S_1$  is plotted with the vertical lines.

The nature of  $S_1$  for the four systems with fully thiol derivative passivations shows that the reduction in optical activity is due to the localization of the HOTO on the ligands passivating

layer D, Table 6.3. This localization is apparent in the PDOS for these systems, where the  $SR^-/H^+$  states are far within the bandgap of the QD. The stabilization of the ligand localized state when networking observed for layer C  $SR^-/H^+$  is also seen for full passivation. This stabilization of the networking states between ligands ( $N_L$ ) is increased compared to the stabilization resulting in networking between the ligand and surface ( $N_s$ ), Figure 6.8. The destabilization of the HSR in PAM shifts the ligand-based states above the QD band edge and significantly modifies the QD VB edge compared to HSR in ACN, these explains why the oscillator strength of  $S_1$  for HSR in PAM (0.008) is much smaller compared to HSR in ACN (0.050).

Table 6.3. NTOs for  $S_1$  for QDs initially passivated by HSR and  $SR^-/H^+$ . The black (red) vertical lines in Figure 6.7 are characterized by NTOs with the name of HSR ( $SE^-/H^+$ ).

		ACN		PAM	
		HOTO	LUTO	HOTO	LUTO
HSR	$S_1$				
	3.18eV			2.62eV	
	0.050 <i>f</i>			0.008 <i>f</i>	
$SR^-/H^+$	$S_1$				
	3.24eV			2.56eV	
	0.003 <i>f</i>			0.002 <i>f</i>	

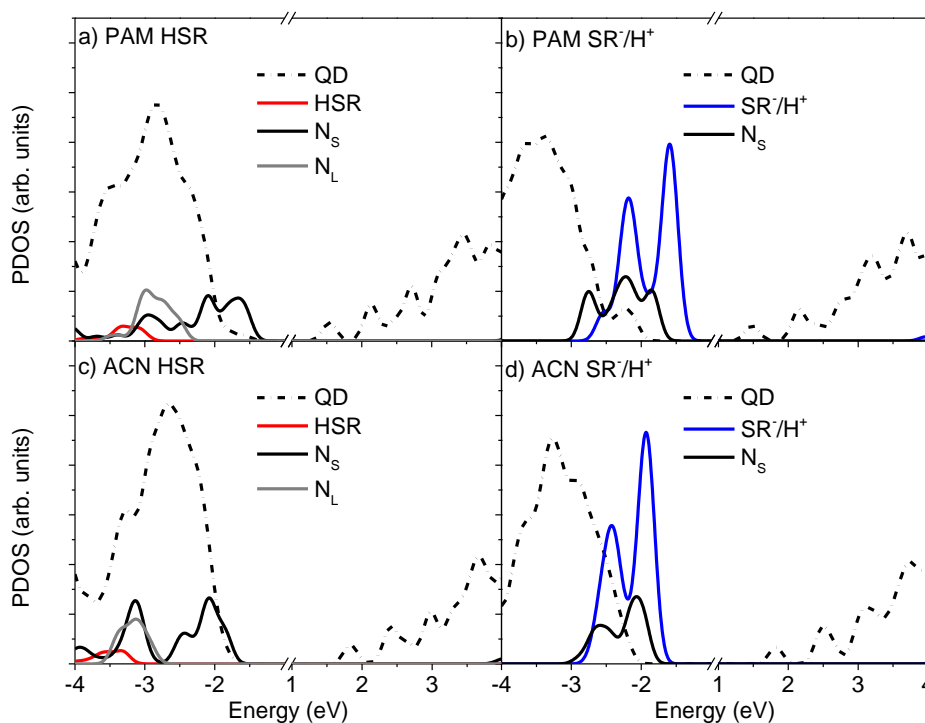


Figure 6.8. PDOS for QDs initially passivated by 21 HSR (a and c) and 21  $\text{SR}^-/\text{H}^+$  (b and d). Dashed black lines QD state, red lines HSR, blue  $\text{SR}^-/\text{H}^+$ , black  $N_s$ , and grey  $N_L$ .

The conclusions from passivation QDs with a single thiol derivative are supported by the electronic and optical properties of QDs passivated by HSR and  $\text{SR}^-/\text{H}^+$ , where the formation of thiolate on the surface results in ligand-based trap states that are shown in the PDOS of the systems. The stabilization of surface networking is seen for the fully passivated QDs by HSR and  $\text{SR}^-/\text{H}^+$ , however, this stabilization is increased when neighboring ligands networking which shifts the  $N_L$  states near the HSR states. Additionally, the thermodynamic driving force predicted by the  $B_e$  of a single ligand seems to prevent the formation of HSR from the initial passivation of  $\text{SR}^-/\text{H}^+$ , which could be the causes for the irreversible nature of the photobleaching observed by Orfield and co-workers.<sup>2</sup>

### 6.3. Conclusions

Our DFT and TDDFT based simulations bring atomic-level insight into the irreversible bleaching observed in experimental studies on HTCI QDs,<sup>2</sup> we found that the surface of CdS is

capable of abstracting  $H^+$  for HSR which in turns results in  $SR^-/H^+$  formation. This formation then destabilizes the occupied ligand-based states towards and even above the QDs band edge. These ligand-based states cause localization of the hole on the thiolate ligand reducing the optical activity of the emissive state. This reduced optical activity is expected to cause the irreversible bleaching. Although, we did not investigate the effect of thermalization on the equilibrium between thiol and thiolate, we did find that the binding of  $SR^-/H^+$  is 1.0 eV to 2.0 eV higher compared to HSR. This  $B_e$  implies that the proton extraction by the surface is thermodynamically favorable and could result in the irreversible photothermal-bleaching observed by Orfield and co-workers. Additionally, the formation of the ligand-based trap states by the formation of  $SR^-/H^+$  could explain why PTC, Chapter 4 ligand, shows an increase in hole extraction. Conjugated thiol derivatives could be utilized in QD based PV devices, where the ligand-based trap states formed by converting HSR into  $SR^-/H^+$  could achieve similar results as PTC derivatives without the decomposition of PTC into the aniline derivative and carbon disulfide.

#### 6.4. References

1. Jeong, S.; Achermann, M.; Nanda, J.; Ivanov, S.; Klimov, V. I.; Hollingsworth, J. A., Effect of the thiol– thiolate equilibrium on the photophysical properties of aqueous CdSe/ZnS nanocrystal quantum dots. *J. Am. Chem. Soc.* **2005**, *127* (29), 10126-10127.
2. Orfield, N. J.; Majumder, S.; McBride, J. R.; Yik-Ching Koh, F.; Singh, A.; Bouquin, S. J.; Casson, J. L.; Johnson, A. D.; Sun, L.; Li, X., Photophysics of thermally-assisted photobleaching in “giant” quantum dots revealed in single nanocrystals. *ACS Nano* **2018**, *12* (5), 4206-4217.
3. Galland, C.; Ghosh, Y.; Steinbrück, A.; Sykora, M.; Hollingsworth, J. A.; Klimov, V. I.; Htoon, H., Two types of luminescence blinking revealed by spectroelectrochemistry of single quantum dots. *Nature* **2011**, *479* (7372), 203-207.
4. Chen, O.; Zhao, J.; Chauhan, V. P.; Cui, J.; Wong, C.; Harris, D. K.; Wei, H.; Han, H.-S.; Fukumura, D.; Jain, R. K., Compact high-quality CdSe–CdS core–shell nanocrystals with narrow emission linewidths and suppressed blinking. *Nat. Mater.* **2013**, *12* (5), 445-451.
5. Chen, Y.; Vela, J.; Htoon, H.; Casson, J. L.; Werder, D. J.; Bussian, D. A.; Klimov, V. I.; Hollingsworth, J. A., “Giant” multishell CdSe nanocrystal quantum dots with suppressed blinking. *J. Am. Chem. Soc.* **2008**, *130* (15), 5026-5027.



6. Ghosh, Y.; Mangum, B. D.; Casson, J. L.; Williams, D. J.; Htoon, H.; Hollingsworth, J. A., New insights into the complexities of shell growth and the strong influence of particle volume in nonblinking “giant” core/shell nanocrystal quantum dots. *J. Am. Chem. Soc.* **2012**, *134* (23), 9634-9643.
7. Mahler, B.; Spinicelli, P.; Buil, S.; Quelin, X.; Hermier, J.-P.; Dubertret, B., Towards non-blinking colloidal quantum dots. *Nat. Mater.* **2008**, *7* (8), 659-664.
8. Vela, J.; Htoon, H.; Chen, Y.; Park, Y. S.; Ghosh, Y.; Goodwin, P. M.; Werner, J. H.; Wells, N. P.; Casson, J. L.; Hollingsworth, J. A., Effect of shell thickness and composition on blinking suppression and the blinking mechanism in ‘giant’ CdSe/CdS nanocrystal quantum dots. *J. Biophotonics* **2010**, *3* (10-11), 706-717.
9. Zhang, A.; Dong, C.; Liu, H.; Ren, J., Blinking behavior of CdSe/CdS quantum dots controlled by alkylthiols as surface trap modifiers. *J. Phys. Chem. C* **2013**, *117* (46), 24592-24600.
10. Pal, B. N.; Ghosh, Y.; Brovelli, S.; Laocharoensuk, R.; Klimov, V. I.; Hollingsworth, J. A.; Htoon, H., ‘Giant’CdSe/CdS core/shell nanocrystal quantum dots as efficient electroluminescent materials: strong influence of shell thickness on light-emitting diode performance. *Nano Lett.* **2012**, *12* (1), 331-336.
11. Yang, Y.; Zheng, Y.; Cao, W.; Titov, A.; Hyvonen, J.; Manders, J. R.; Xue, J.; Holloway, P. H.; Qian, L., High-efficiency light-emitting devices based on quantum dots with tailored nanostructures. *Nat. Photonics* **2015**, *9* (4), 259.
12. Barone, V.; Cossi, M.; Tomasi, J., Geometry optimization of molecular structures in solution by the polarizable continuum model. *J. Comput. Chem.* **1998**, *19* (4), 404-417.
13. Cossi, M.; Barone, V.; Cammi, R.; Tomasi, J., Ab initio study of solvated molecules: a new implementation of the polarizable continuum model. *Chem. Phys. Lett.* **1996**, *255* (4-6), 327-335.
14. Cui, P.; Tamukong, P. K.; Kilina, S., Effect of Binding Geometry on Charge Transfer in CdSe Nanocrystals Functionalized by N719 Dyes to Tune Energy Conversion Efficiency. *ACS Appl. Nano Mater.* **2018**, *1* (7), 3174-3185.
15. Mahan, G., Local-field corrections to coulomb interactions. *Phys. Rev.* **1967**, *153* (3), 983.
16. Baker, D. R.; Kamat, P. V., Tuning the emission of CdSe quantum dots by controlled trap enhancement. *Langmuir* **2010**, *26* (13), 11272-11276.
17. Kasha, M., Characterization of electronic transitions in complex molecules. *Discuss Faraday Soc.* **1950**, *9*, 14-19.

## 7. PHONON-DRIVEN ENERGY RELAXATION IN PBS/CDS AND PBSE/CDSE CORE/SHELL QUANTUM DOTS

In Chapters 4, 5 and 6, I studied the effect of ligands on the morphology of the QD' surface. Here I will focus on encapsulating the core of PbX, X = S or Se, with a shell of CdX, X = S or Se, to generate PbX/CdX, X = S or Se, core/shell QDs. This encapsulation is achieved by ion reactive ion exchange of surface  $\text{Pb}^{2+}$  by  $\text{Cd}^{2+}$  ions. These core/shell QDs are well studied for their ability to undergo multi-exciton generation (MEG) through carrier multiplication (CM). From experimental studies, the increase in CM is the result of band engineering that provides an intermediate state associated with the interface between the core and shell which allows CM to outcompete carrier cooling.<sup>1-5</sup> In this work, I will investigate whether the intermediate states generated by the core shell interface can reduce the hole cooling significantly providing atomic level evidence for the experimental hypothesis why the core/shell QDs have enhanced CM efficiencies compared to the bulk or homogenous QDs.<sup>6</sup>

### 7.1. Introduction

Colloidal QDs show great promise in solar cell applications<sup>1,7-11</sup> because they are broad band absorbers with high molar absorption coefficients,<sup>12</sup> and photostable,<sup>13-14</sup> but the most advantageous property is their ability to undergo CM. CM produces multiple pairs of charge carriers from a single photon which increases the theoretical limit for a single junction solar cell from 33%<sup>15</sup> to 46%.<sup>16</sup> However, the efficiency of most QD based PV devices are relatively low which is likely the result of the surface of the QDs. The electronic properties of QDs are highly sensitive to the environment as describe in chapter 2.<sup>17-18</sup>

The heterogenous core/shell QDs have addressed in part the sensitivity to the environment by encapsulating the core of the QD by a shell of a second semiconducting

material.<sup>11, 19-20</sup> The class of core/shell QDs that are particularly interesting are quasi-type-II core/shell QDs because the band structure is thought to reduce the relaxation of the hole while satisfying the energy requirements to undergo CM. For a system to undergo CM the energy of the charge carriers should be more than twice that of the band gap. One example of quasi-type-II core/shell QDs are PbX/CdX, X = S or Se, where the CB is delocalized over the entire QD and the VB is localized on the core.<sup>4</sup> This system has been shown to reduce the lattice mismatch that can result in electronic trap state on the interface between the core and shell.<sup>20-21</sup>

Experimental and theoretical (effective mass approximation, EMA) studies have shown that the ratio of the core radius to shell thickness to greatly influence the efficiency of CM, where CM is enhanced when the core radius and shell thickness are approximately equal.<sup>1</sup> EMA modeling assumes ideal interfaces, however, it is known that the lattice mismatch can influence the electronic properties of the core/shell QDs. First principle calculations, such as density functional theory (DFT), can address these issues, although they are limited to smaller size QDs (<3 nm in diameter).<sup>17, 22</sup> Toward this direction, DFT-based simulations have been applied to CdS(e)/ZnS(e) and CdSe/CdS QDs focusing on the effect of their interface<sup>23-24</sup> and the core-to-shell ratio<sup>25-26</sup> on the electronic structure<sup>27</sup> and optical response,<sup>28</sup> as well as on structural features.<sup>29</sup> However, DFT-based simulations of the carrier cooling mediated by electron-phonon couplings in core/shell QDs have not been reported yet, whereas it is a key process in photoexcited dynamics affecting CM, charge transfer, and emission in nanostructures. NAMD simulations were performed to gain an atomic level understanding of carrier cooling in PbX/CdX, X = S or Se, core/shell QDs.

## 7.2. Result and Discussion

Here, we perform nonadiabatic molecular dynamics (NAMD), NAMD is described in detail in Chapter 3.2.3.2., based on DFT to study the effect of the vibrational motion on the charge carrier relaxation in PbX/CdX ( $X = S, Se$ ) core/shell QDs. While holding  $\sim 1$  nm size of the core and the shell, we focus on the role that the anion type of the core/ shell structures plays in the electron and hole cooling, comparing PbSe/CdSe and PbS/CdS QDs. Our NAMD calculations reveal that despite many similarities in the electronic structure and phonon spectra of PbSe/CdSe and PbS/CdS QDs, electron cooling happens about twice faster in PbS/CdS than in PbSe/CdSe because of the stronger electron coupling to higher energy optical phonons in structures with sulfur anions. Our results imply that weaker electron-phonon couplings in PbSe/CdSe QDs provide conditions allowing for CM to outpace energy dissipation even in the structures with a thin monolayer-shell. These fundamental insights are important in establishing design principles for improving performance of heterostructured nanomaterials for energy applications.

### 7.2.1. Ground State Properties

The electronic properties of PbX/CdX,  $X = S$  or  $Se$ , core/shell QDs has been shown to be quasi-type-II,<sup>1</sup> where the VB edge is located on the core and CB edge is delocalized over the entire QDs.<sup>4</sup> The electronic properties using the method described in section 3.3.3. and 3.3.5. are shown in Figure 7.1 for the ground state equilibrium geometry demonstrating the quasi-type-II electronic distribution, which in-part justifying our relatively small model system. It is known that the PBE functional underestimates the bandgap of systems,<sup>30-31</sup> this underestimation can affect the NACT due to their inverse proportionality to the energy gap between states. However, the shape of the electronic bands has been shown to be overall unchanged for the homogenous

QDs.<sup>32-33</sup> The electronic properties of the equilibrium geometry for PbSe/CdSe core/shell QDs was compared when computed with PBE<sup>34</sup> and HSE,<sup>35</sup> Figure 5.2. From this comparison, the major difference is the sub-gaps in the VBs and CBs. This decreased energy difference between the states will increase the carrier cooling when utilizing PBE for the electronic structure calculations that are used to obtain the NACT used in FSSH-NAMD.

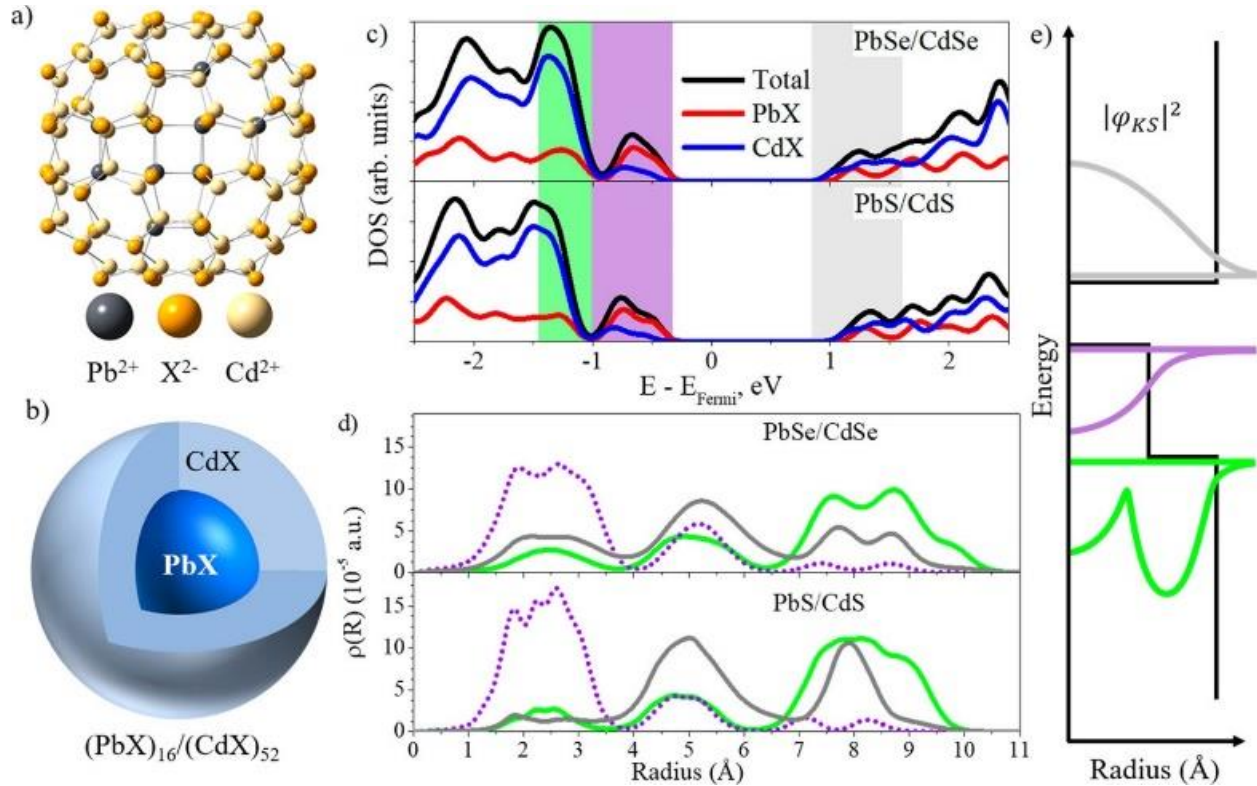


Figure 7.1. Electronic properties of PbX/CdX, X = S or Se, core/shell QDs at the ground state equilibrium geometry. a) atomic structure b) schematic representation c) PDOS for the core/shell QDs d) Normalized radial distribution of electronic density, average of electronic states shaded by colored regions in panel c e) Schematic representation of quasi-type II electronic structure of PbX/CdX QDs.

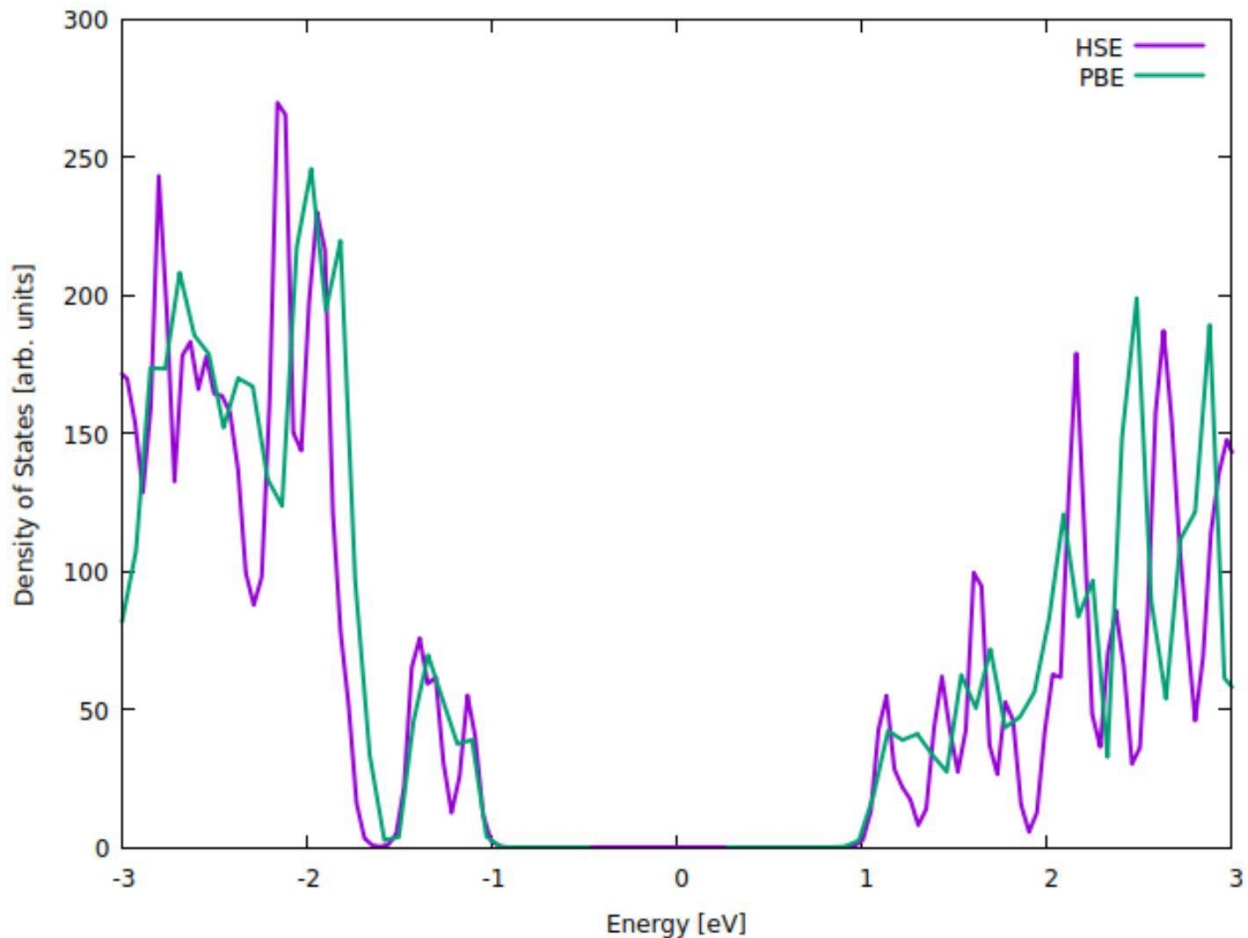


Figure 7.2. Comparing DOS generated by PBE and HSE functionals for PbSe/CdSe core/shell QDs. This comparison was done by shifting the VB by  $-0.447$  eV and CB by  $0.242$  eV to align the band edges between PBE and HSE.

### 7.2.2. Thermalization

The thermalization of the core/shell QDs to 300 K reduces the quasi-type-II nature of the very small core/shell QDs. The monolayer of CdX, X = S or Se, is flexible which results in the hybridization of the “core” states with shell contribution compared to the equilibrium geometry. The ensemble average of the PDOS is shown in Figure 7.3, where the VB edge is still dominated by core with significant contribution of the shell that is the result of the small size of the monolayer shell. The ensemble average was done for the NAMD trajectories where the initial conditions were the first 300 timesteps of the BOA GS MD trajectory.

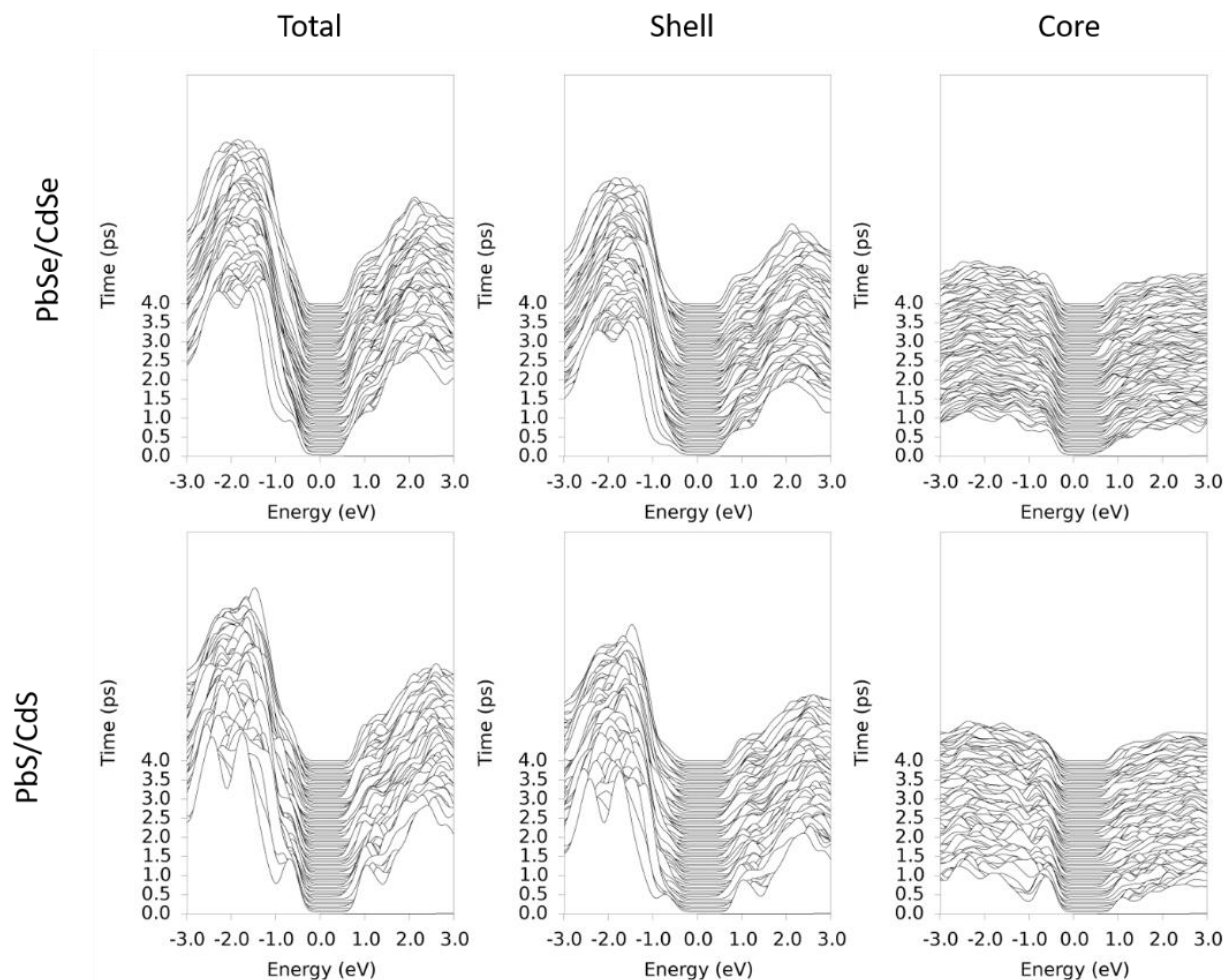


Figure 7.3. Ensemble average of the PDOS evolving in time of PbSe/CdSe (a-c) and PbS/CdS (d-f). (a) and (d) the total DOS; (b) and (e) the PDOS contributed by the atoms in the shell (CdSe and CdS, respectively) and (c) and (f) contributed by the atoms in the core (PbSe and PbS, respectively). The subgaps that distinguishes the core and shell contributions to the electronic states (at  $\sim 0.75$  eV below HOMO) are reduced due to the thermal motion (especially in PbSe/CdSe QD), compared to the DOS at 0 K.

### 7.2.3. Excited State Properties

The absorption spectra were computed using the independent particle approximation for PbS/CdS and PbSe/CdSe core/shell QDs for the ground state equilibrium and thermalized systems, Figure 7.4. and 7.5. The lowest energy absorption peak ( $\sim 1.6$  eV for  $X = \text{Se}$  and  $\sim 1.8$  eV for  $X = \text{S}$ ) involves symmetric optical transitions with CdS(e). This symmetry is due to the quasi-type-II nature of both PbX/CdX QDs, since the frontier orbitals are associated with the

PbX core that has symmetric VB and CB near the energy gap and, correspondingly, similar effective masses of the electron and the hole.<sup>36-37</sup> This result agrees with the nature of the  $1S_e-1S_h$  core-based transitions obtained by EMA<sup>3</sup> for PbX/CdX QDs with core and shell sizes of  $\sim 2$  nm. These optically active transitions contribute to the core-associated IR emission experimentally observed at  $\sim 0.95$  eV for the 4 nm PbSe/CdSe with the 1.5 nm core.<sup>3</sup> Since our model of the PbSe/CdSe QD has much smaller core (of 0.85 nm), the calculated optically active lowest energy transition is blue-shifted due to the strong confinement. Next paired peaks (1.8-2.1 eV for X = Se) can be assigned to the core-contributed  $1S_e-1P_h$  and  $1S_h-1P_e$  transitions.<sup>3, 8</sup> While these transitions are formally forbidden mixed parity transitions, they are experimentally observed in the absorption spectra of PbSe(S) QDs and rationalized by the contribution of quadrupole optical transitions<sup>38</sup> and a transient Stark effect imposed by an excitation of the hot electron-hole pair resulting in the symmetry breaking and redistribution of optical transition strength to dipole forbidden transitions.<sup>39</sup> Despite its asymmetric nature, we assign  $1S_{e,h}-1P_{h,e}$  transitions as symmetric ones, because the energy splitting between  $1S_{h,e}$  and  $1P_{h,e}$  associated states in PbX/CdX falls in the range of the chosen thermal correction,  $\Delta E = 0.12$  eV, for symmetric transitions with  $|E_h| = |E_e| \pm \Delta E$ .



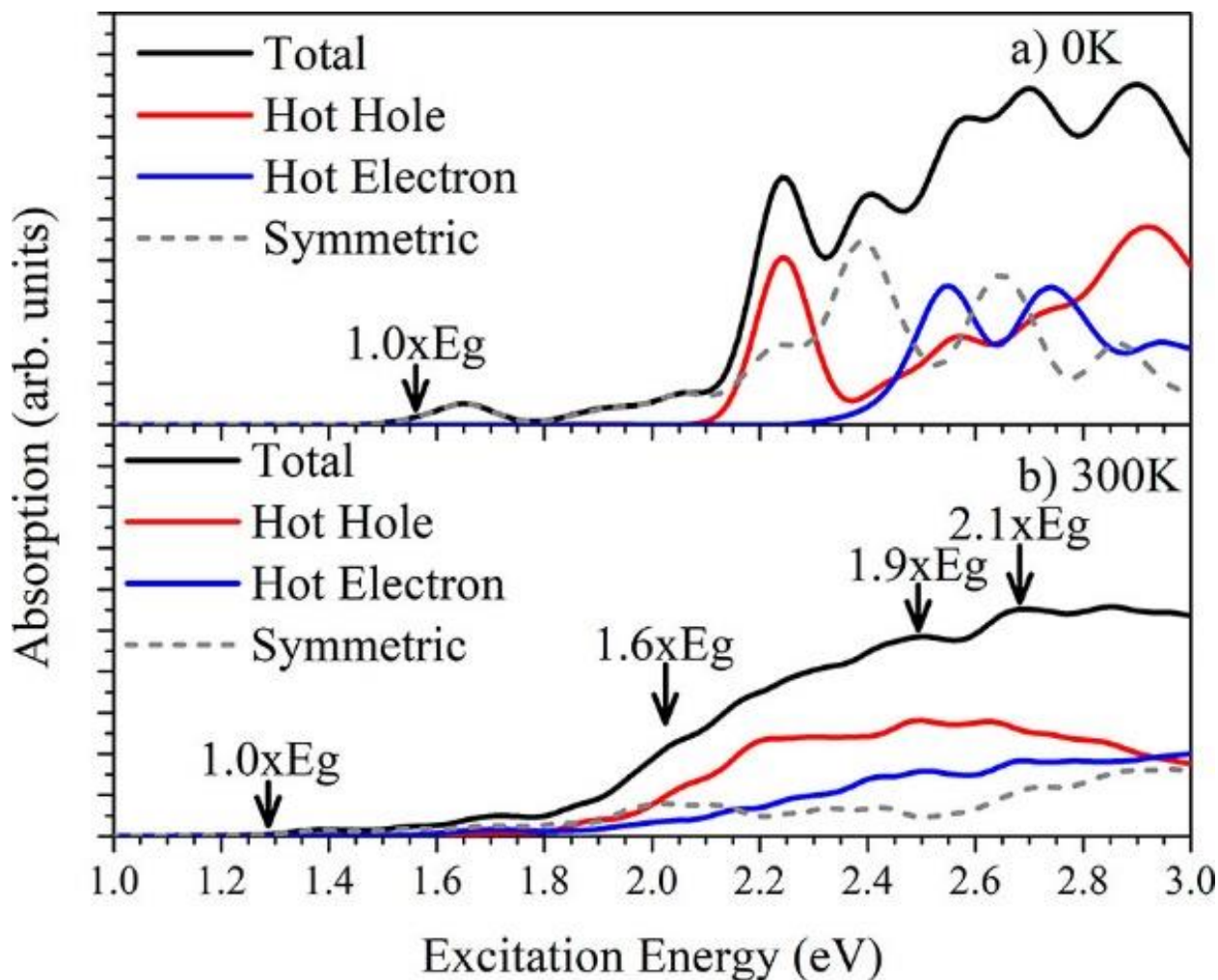


Figure 7.4. Absorption spectrum of PbSe/CdSe QDs decomposed into three types of excitations (hot holes, hot electrons, and symmetric). Absorption spectrum at 0 (a) and 300 K averaged over the QD ensemble constructed from 30 randomly selected conformations from NAMD trajectory (b). The vertical black arrows indicate the averaged energy of the HOMO-LUMO gap ( $1.0 \times E_g$ ) and the initial excitations of  $1.6 \times E_g$ ,  $1.9 \times E_g$ , and  $2.1 \times E_g$ . These excitation energies were selected as initial conditions for the NAMD simulations that are distinct in their energy and nature having predominantly hot hole and hot electron transitions at  $1.9 \times E_g$  and  $2.1 \times E_g$ , while significant contributions of symmetric transitions at  $1.6 \times E_g$ .

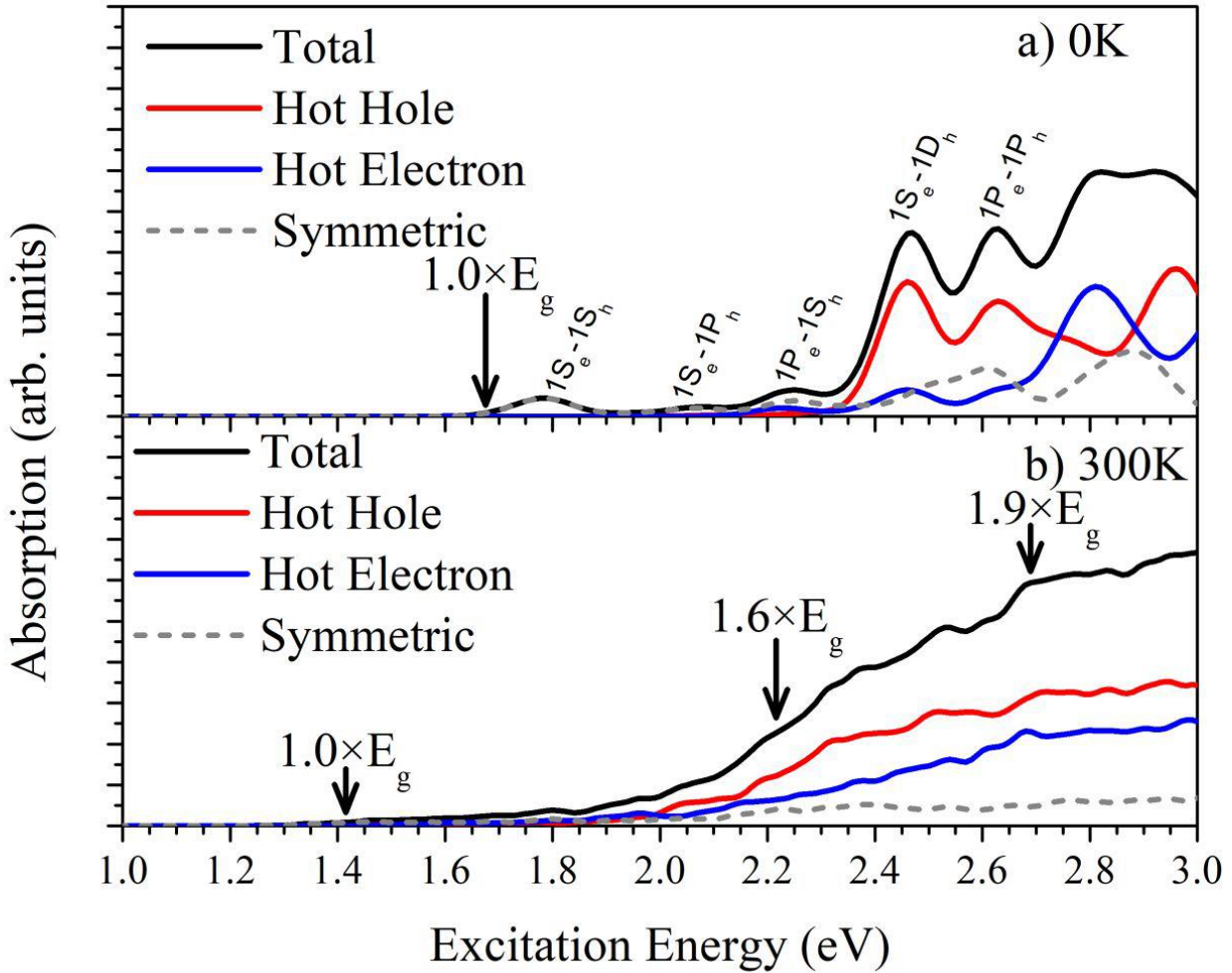


Figure 7.5. Absorption spectrum of PbS/CdS QDs decomposed into three types of excitations (hot holes, hot electrons and symmetric). (a) Absorption spectrum at 0 K. Indexes depict the types of the envelope function of the optical transition, according to the effective-mass approximation. (b) Thermalized absorption spectra at 300 K averaged over the QD ensemble constructed from 30 randomly selected conformations from the NAMD trajectories. The vertical black arrows indicate the averaged energy of the HOMO-LUMO gap ( $1.0 \times E_g$ ) and the initial excitations of  $1.6 \times E_g$  and  $1.9 \times E_g$ .

The asymmetric transitions involving hot holes (red lines in Figure 7.4. and 7.5.), with the energy of holes significantly larger than electron's energy ( $|E_h| > |E_e| + \Delta E$ ), dominate the next highly intensive absorption peak at the energy of  $\sim 1.5 \times E_g$ , Figure 7.4.a for PbSe/CdSe and Figure 7.5.a for PbS/CdS. The asymmetric nature of these bright transitions is dictated by the strong core-shell delocalized character of both electron and hole states, with much higher density of states for holes (compare green and gray regions of DOS in Figure 7.1c). According to EMA

calculations,<sup>1</sup> this peak can be associated with  $1S_e-1D_h$  transitions, followed by the symmetric  $1P_e-1P_h$  ( $\sim 1.6 \times E_g$ , Figure 7.4a) transitions. These well distinct optically active transitions are expected to contribute to the shell-originated emission experimentally observed at  $\sim 2.4$  eV for the 4 nm PbSe/CdSe having 1.5 nm shell.<sup>3</sup> For the energy range larger than  $1.6 \times E_g$ , hot electron transitions ( $|E_e| > |E_h| + \Delta E$ ) start to play a part at the high-energy absorption bands, with a well pronounced contribution at the energy of  $\sim 1.9 \times E_g$  and higher (blue lines in Figure 7.4. for X = Se and Figure 7.5. for X = S). For both QDs, the thermalized absorption spectra averaged over 30 random conformations qualitatively agree with those at 0 K, Figures 7.4.b and 7.5.b. However, optical peaks are significantly broadened and red-shifted due to thermal fluctuations.

Overall, our core/shell QD models reproduce well-distinct optically active peaks at the near IR range originated from the core and at the visible range originated from the shell that can be associated with the dual emission experimentally observed in the larger size PbSe/CdSe QDs. Note that the direct comparison of the calculated and experimental spectra is problematic because of the difference in the size of the core and the shell between the computational models and the experimental samples. Thus, the agreement between experimental and calculated energies of these peaks are affected by two factors: (i) The stronger confinement of the core ( $\sim 0.9$  nm) and the shell ( $\sim 1.1$  nm), compared to the experimental QDs having both the core and the shell  $> 1.5$  nm, leads to blue shifts of the spectral peaks. (ii) The PBE functional underestimates the energy gaps leading to redshifts of the peaks.

#### **7.2.4. NAMD Simulation of Charge Carrier Cooling**

Phonon-mediated charge carrier relaxation in PbX/CdX QDs is shown in Figure 7.6. for the excitation at  $2.1 \times E_g$  ( $1.9 \times E_g$  and  $1.6 \times E_g$ , Figures 7.7. and 7.8., respectively). Comparing

excitations with different constraints-all optically allowed transitions, only hot electrons, and only hot holes at the given energy range-one can see that excitation at  $1.6 \times E_g$  is mainly governed by symmetric transitions (Figure 7.8.), at  $1.9 \times E_g$  it is dominated by hot electrons (Figure 7.7.), while at  $2.1 \times E_g$  dynamics has a highly mixed character including symmetric, hot hole, and hot electron contributions for both QDs (Figure 7.6.). However, independent of the initial excitation and its symmetry nature, the energy relaxation happens about twice faster in the PbS/CdS than in the PbSe/CdSe QDs, as depicted in Figure 7.6.a. While holes are cooling faster than electrons because of their stronger NACTs, the difference in relaxation time between two QDs is more pronounced for electrons ( $\sim 2$  times slower for  $X = \text{Se}$ ) than holes ( $\sim 1.4$  times slower for  $X = \text{Se}$ ) when single-exponential fitting is used, Tables 7.1 and 7.2. This implies that electrons play an important role in slower energy relaxation of PbSe/CdSe, compared to PbS/CdS QDs, resulting in their overall relaxation time of 0.61-0.65 ps for PbSe/CdSe and 0.39-0.41 ps for PbS/CdS, slightly speeding up with the excitation energy.

Table 7.1. Ensemble average of the Non-Adiabatic Coupling Terms (NACTs) and the excited state lifetimes. The average initial NACTs for nearest neighbors (NN), second nearest neighbors (SNN) and average coupling over the entire range for all simulations. The lifetime of the excited states were found by a four-state irreversible kinetic model ( $\tau_{KM}$ ) and single exponential fitting ( $\tau_{SE}$ ).

Initial Excitation	X	NN (meV)		SNN (meV)		Ave. N (meV)		$\tau_{KM}$ (ps)		$\tau_{SE}$ (ps)		
		Hole	Elec.	Hole	Elec.	Hole	Elec.	Hole	Elec.	Hole	Elec.	
All	1.6xEg	Se	20.5	13.0	7.9	4.0	12.6	7.7	0.81	0.62	0.56	0.74
		S	28.9	21.2	13.4	6.7	18.3	12.7	0.56	0.45	0.39	0.30
	1.9xEg	Se	22.1	15.2	8.9	4.9	13.6	9.1	0.80	0.84	0.54	0.65
		S	30.8	25.3	14.9	9.5	19.6	15.4	0.55	0.53	0.39	0.33
	2.1xEx	Se	22.4	17.2	9.0	5.9	13.7	10.3	0.81	0.87	0.52	0.64
		S	31.0	26.7	15.0	10.7	19.6	16.4	0.58	0.55	0.38	0.33
Hot Electron	1.6xEg	Se	12.1	13.7	3.4	4.3	7.2	8.2	0.62	0.84	0.43	0.68
		S	22.1	22.9	7.7	7.7	13.6	13.8	0.28	0.56	1.31	0.34
	1.9xEg	Se	13.8	15.7	4.4	5.1	8.4	9.3	0.66	0.98	0.67	0.63
		S	24.1	25.3	8.6	9.5	14.7	15.4	0.38	0.63	0.47	0.34
	2.1xEg	Se	16.3	17.2	5.8	5.9	10.0	10.3	0.69	1.02	0.55	0.62
		S	24.5	27.0	8.9	11.0	15.0	16.6	0.39	0.68	0.43	0.34
Hot Hole	1.6xEg	Se	20.5	12.1	7.9	3.6	12.6	7.4	0.83	0.53	0.53	0.85
		S	28.9	19.3	13.3	5.3	18.3	11.6	0.60	0.39	0.38	0.28
	1.9xEg	Se	22.3	12.5	9.0	3.7	13.6	7.5	0.93	0.62	0.51	0.74
		S	30.8	19.7	14.9	6.1	19.6	11.9	0.67	0.35	0.38	0.30
	2.1xEg	Se	22.4	12.2	9.0	3.7	13.7	7.3	0.98	0.63	0.51	0.69
		S	31.0	20.0	15.0	6.2	19.6	12.0	0.70	0.44	0.39	0.33

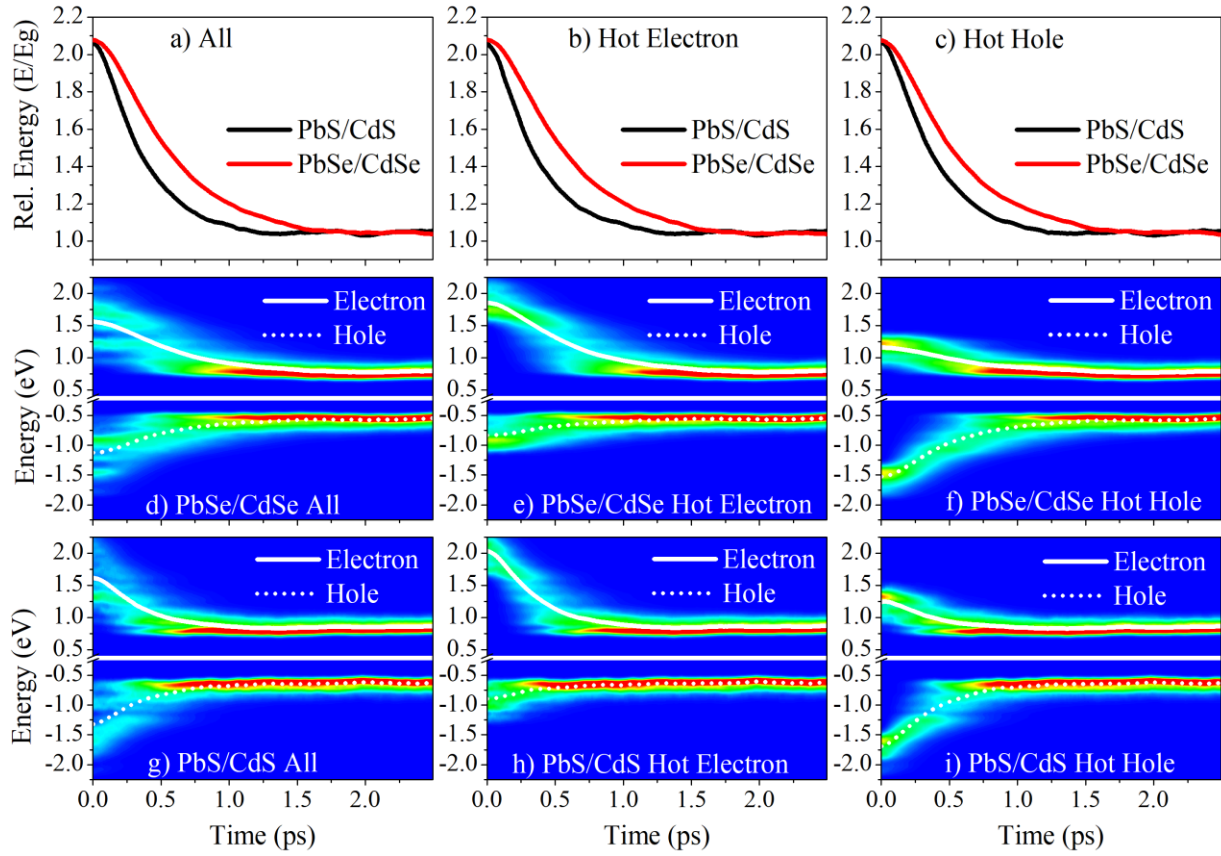


Figure 7.6. Time evolution of the initial excitation at  $2.1 \times E_g$  in PbX/CdX QDs. (a)-(c) Relaxation of the average energy of the photoexcited electron-hole in PbS/CdS (black lines) and PbSe/CdSe (red lines), shown as a ratio between the excited energy and the energy gap ( $E/E_g$ ). (d)-(i) Evolution of the electron and the hole wave packets with the magnitude varying from blue (minimum) to red (maximum) according to the rainbow color scheme. The white lines represent the ensemble average energy for the hole (dotted lines) and electron (solid lines) relaxation. The initial excitation includes all optically active transitions at the given energy (a), (d) and (g), optically active transitions involving only high-energy hot electrons (b), (e) and (h), and optically active transitions involving only high-energy hot holes (c), (f) and (i).

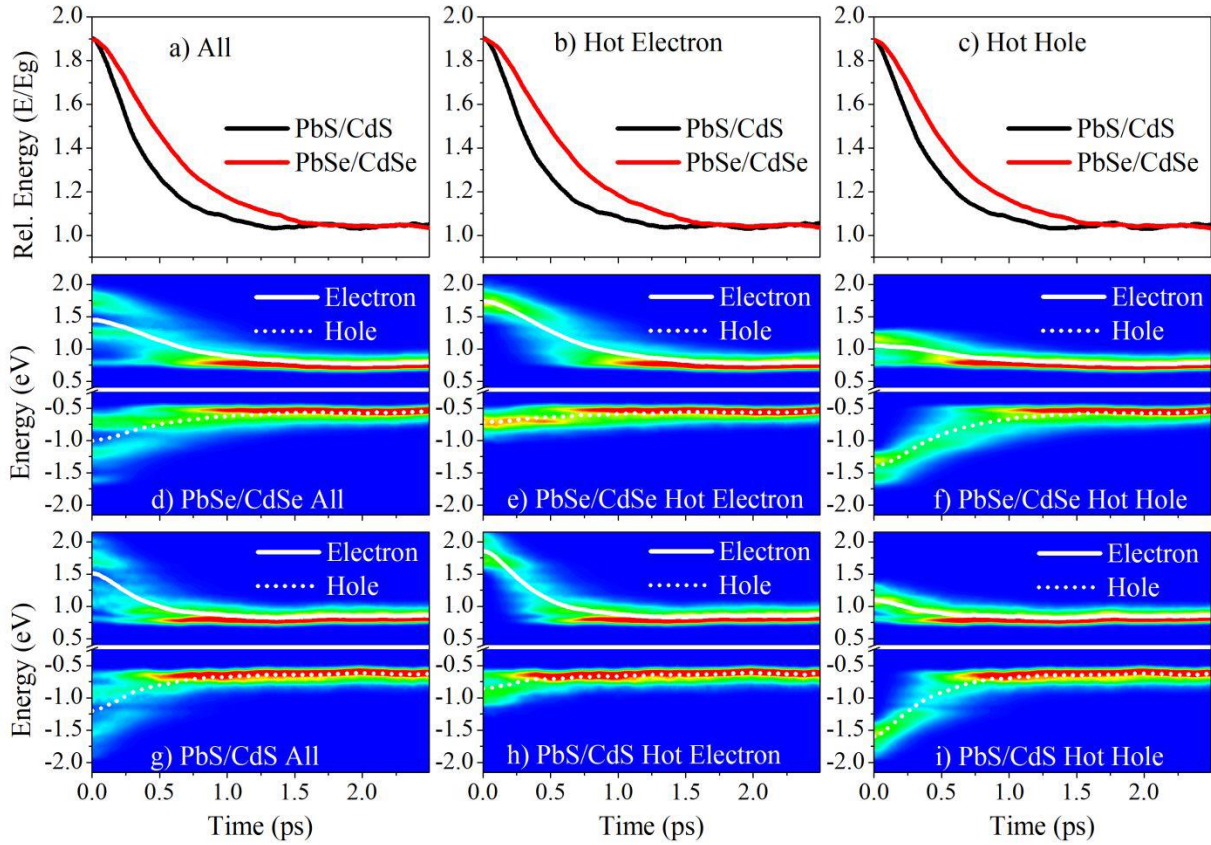


Figure 7.7. Time evolution of the initial excitation at  $1.9 \times E_g$  in  $PbX/CdX$  with  $X=S$  or  $Se$ . (a)-(c) Relaxation of the average energy of the photoexcited electron-hole in  $PbS/CdS$  QD (blacklines) and  $PbSe/CdSe$  QD (red lines), shown as a ratio between the excited energy and the energy gap ( $E/E_g$ ). (d)-(i) Evolution of the electron and the hole wave packets with the magnitude varying from blue (minimum) to red (maximum) according to the rainbow color scheme. The white lines represent the ensemble average energy for the hole (dotted lines) and electron (solid lines) relaxation. The initial excitation includes all optically active transitions at the given energy (a), (d) and (g), optically active transitions involving only high-energy hot electrons (b), (e) and (h), and optically active transitions involving only high-energy hot holes (c), (f) and (i).

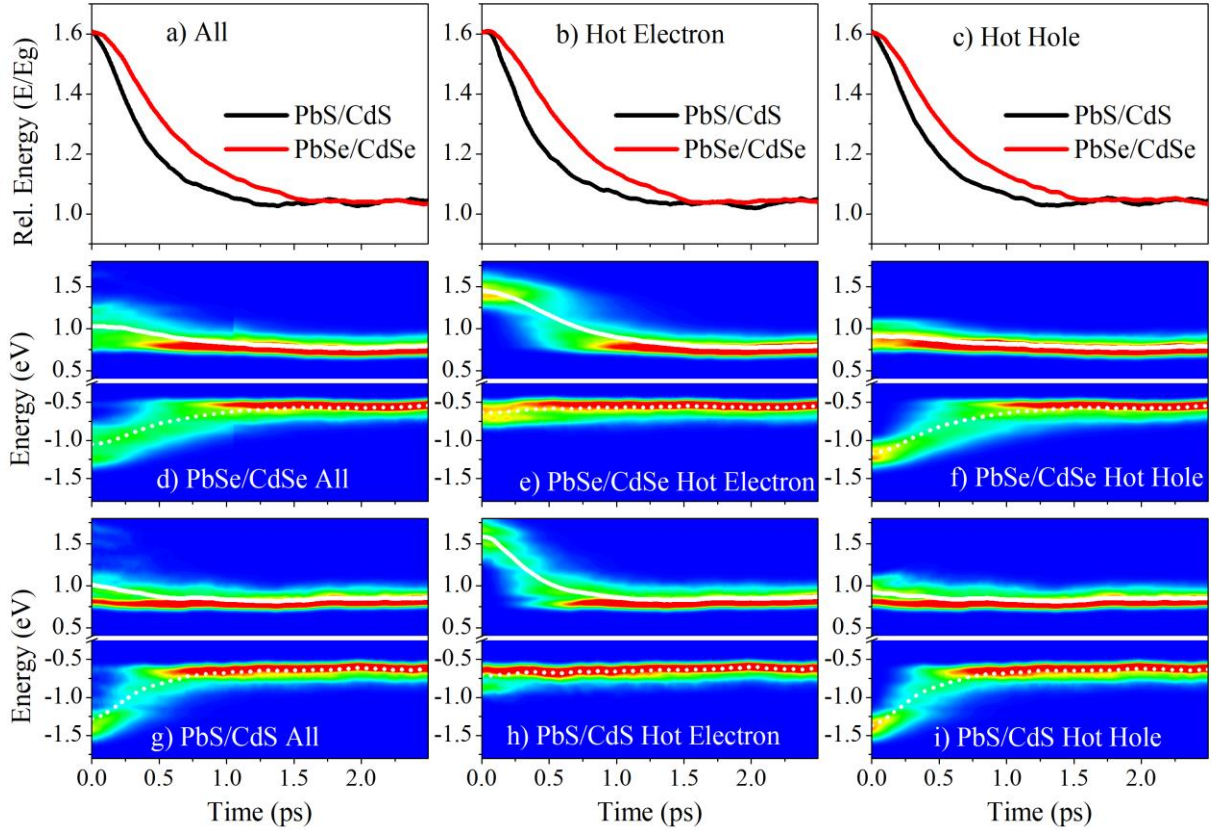


Figure 7.8. Time evolution of the initial excitation at  $1.9 \times E_g$  in  $PbX/CdX$  with  $X=S$  or  $Se$ . (a)-(c) Relaxation of the average energy of the photoexcited electron-hole in  $PbS/CdS$  QD (blacklines) and  $PbSe/CdSe$  QD (red lines), shown as a ratio between the excited energy and the energy gap ( $E/E_g$ ). (d)-(i) Evolution of the electron and the hole wave packets with the magnitude varying from blue (minimum) to red (maximum) according to the rainbow color scheme. The white lines represent the ensemble average energy for the hole (dotted lines) and electron (solid lines) relaxation. The initial excitation includes all optically active transitions at the given energy (a), (d) and (g), optically active transitions involving only high-energy hot electrons (b), (e) and (h), and optically active transitions involving only high-energy hot holes (c), (f) and (i).

Despite stronger average NACTs for holes than for electrons, hole relaxation times are comparable and even slightly slower than electrons, especially, in the  $PbS/CdS$  QD, Table 7.1.

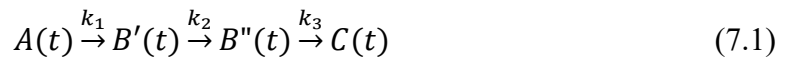
This trend emerges from a well-pronounced discontinuity in the population distribution of hole states deep inside the VB of the  $PbS/CdS$  QDs, Figure 7.6.g. Similar but less pronounced and short-living discontinuity also present in hole dynamics of the  $PbSe/CdSe$  QD, Figure 7.6.d.

These discontinuities in the population distribution take place at the energy range where the



interface states between the PbX core and the CdX shell contribute. Note that there are no subgaps at the DOS of both QDs corresponding to the states associated with the population discontinuity (Figure 7.6.). In other words, the interface-originated states are available, but these states are not populated during NAMD due to their weak couplings to phonons. Electron dynamics also exhibits a long-living discontinuity in the population distribution of the interface-originated states inside the CB of the PbSe/CdSe, while it is not appearing for the PbS/CdS QD. As such, the interface-originated states very weakly coupled to phonons slow down relaxation of holes, which is partially compensated by strong hole-phonon couplings rationalizing nearly the same relaxation rates of holes and electrons in PbS/CdS QDs. On the other hand, a discontinuity in electron population distribution of PbSe/CdSe QDs explains twice slower electron relaxation time in PbSe/CdSe compared to PbS/CdS QDs.

Discontinuities in the carrier population distribution also point to the complicated not level-to-level character of the relaxation dynamics, which is beyond single-exponential behavior for both QDs. In contrast to simulated dynamics in the pristine PbX and CdX QDs,<sup>40</sup> the intermediate states play a significant role in carrier relaxation of the core/shell PbX/ CdX QDs. To address this trend, a four-state irreversible kinetic model is used.



Where  $A(t)$  is the population of the initial state,  $B'(t)$  is the population of the first band of intermediate states,  $B''(t)$  is the population of the second band of intermediate states,  $C(t)$  is the population of the final state (HOMO-2 – HOMO or LUMO – LUMO+2 for the hole and electrons, respectively),  $k_1$  is the rate of going from  $A(t)$  to  $B'(t)$ ,  $k_2$  is the rate of going from  $B'(t)$  to  $B''(t)$ , and  $k_3$  is the rate of going from  $B''(t)$  to  $C(t)$ . Solving the ordinary differential equations result in the analytical form for describing the population as:

$$\alpha = k_2 - k_1; \quad \beta = k_3 - k_1; \quad \gamma = k_3 - k_2 \quad (7.2)$$

$$A(t) = A_0 e^{-k_1 t} \quad (7.3)$$

$$B'(t) = \frac{k_1 A_0}{\alpha} (e^{-k_1 t} - e^{-k_2 t}) \quad (7.4)$$

$$B''(t) = \frac{k_1 k_2 A_0}{\alpha \beta \gamma} (\gamma e_1^{-k_1 t} - \beta e^{-k_2 t} + \alpha e^{-k_3 t}) \quad (7.5)$$

$$C(t) = A_0 + C_0 - A(t) - B'(t) - B''(t) \quad (7.6)$$

The population of the excited states where then fit resulting in elementary lifetimes inversely to the rate, the overall lifetime is the sum of elementary lifetimes:

$$\tau_{lt} = \frac{1}{k_1} + \frac{1}{k_2} + \frac{1}{k_3} \quad (7.7)$$

Figures 7.10., Figure 7.11. and Figure 7.12. show the accuracy of the four-state irreversible kinetic model to the NAMD population. Similar methodology has been used to study the population of the excited state during excited state molecular dynamics.<sup>41-42</sup> The kinetic model demonstrates that the initial state loses its population in less than 0.2 ps, with twice faster rate for electrons and three times faster for holes in the PbS/CdS, compared to the PbSe/CdSe QDs (see  $\tau_1$  in Table 7.2.). However, the carriers are than trapped at the intermediate states spending 0.4-0.9 ps at these states with only 1.2 times difference between PbS/CdS and PbSe/CdSe relaxation time, (see  $\tau_2$  and  $\tau_3$  in Table 7.2.). The kinetic model provides the total relaxation times for electrons and holes of 0.8-0.9 ps for PbSe/CdSe and 0.5-0.6 ps for PbS/CdS, slightly increasing with the excitation energy, Table 7.1.

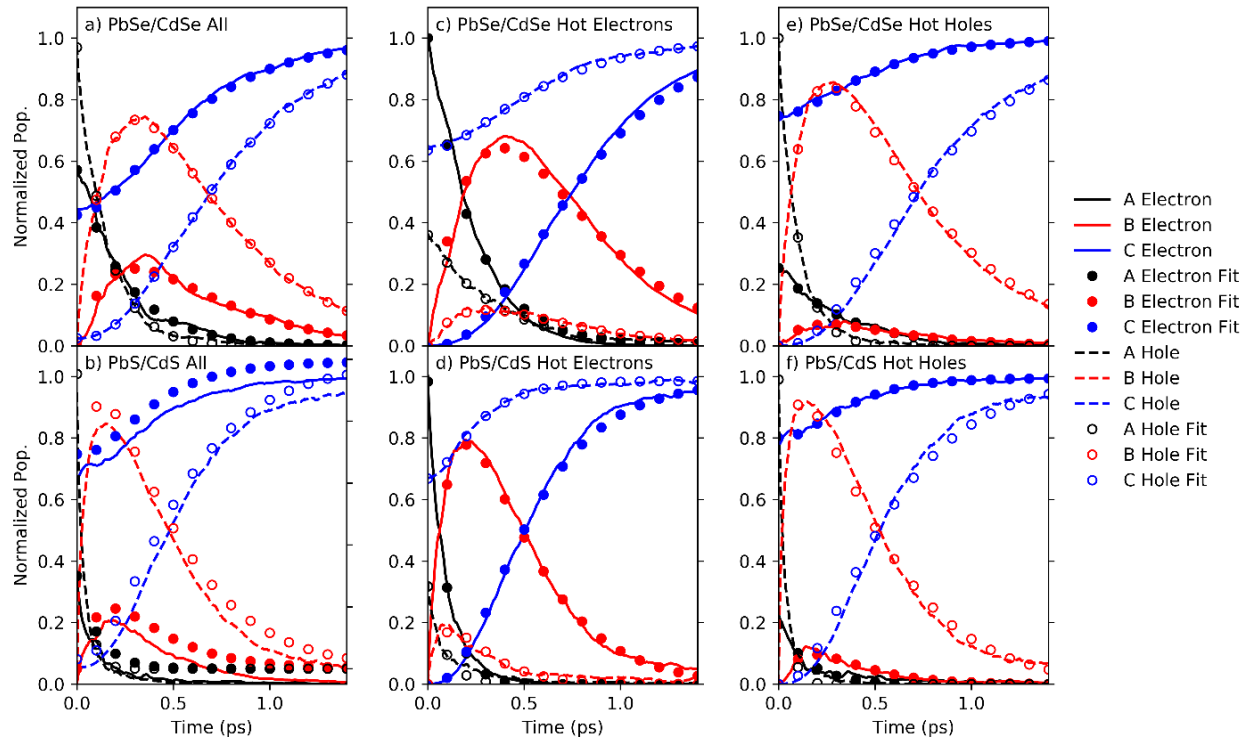


Figure 7.9. Population of the excited state during NAMD excited at  $1.6 \times E_g$  in PbX/CdX QDs, with X=S and Se. These populations were used in the four-state kinetic model in Eqs 7.1-7.7. The solid lines represent the ensemble population average obtained from NAMD of excited electrons. Fitting functions obtained from Eqs 7.1-7.7 are indicated by the filled circles. The dashed lines represent the ensemble average populations obtained from NAMD simulations of excited holes. Fitting functions obtained from Eqs 7.1-7.7 are indicated by the empty circles. The time-dependent ensemble populations were generated by monitoring the populations during the NAMD simulations: Line A is comprised of the initially excited states, line C comprises the first three MOs for occupied and unoccupied orbitals (final state), and line B is the sum of the populations of all other orbitals (intermediate states). Population analysis for PbSe/CdSe (a) and PbS/CdS (b) QDs, with initial conditions including all optical transitions at the investigated energy range. Population analysis for PbSe/CdSe (c) and PbS/CdS (d) QDs, with initial conditions including only hot electron transitions at the investigated energy range. Population analysis for (e) PbSe/CdSe and PbS/CdS (f) QDs, with initial conditions including only hot hole transitions at the investigated energy range.

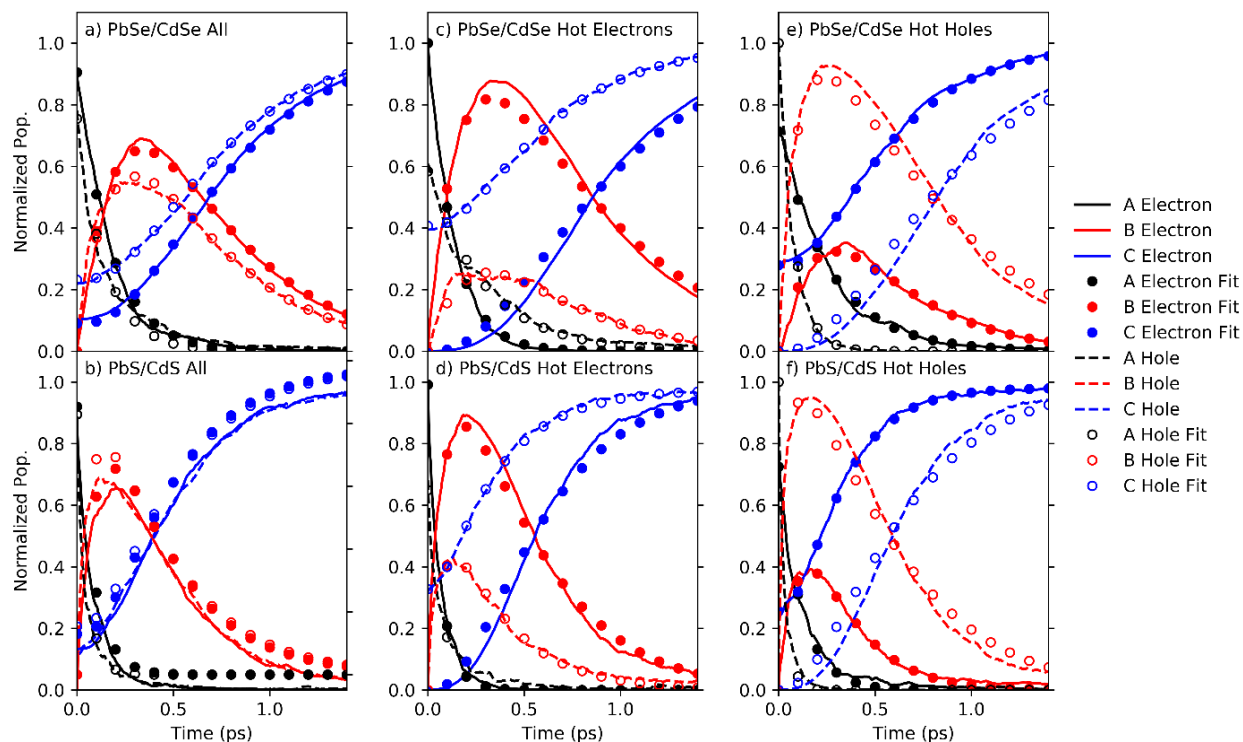


Figure 7.10. Time evolution of the population of the state initially excited at  $1.9 \times E_g$  in PbX/CdX QDs, with X=S and Se. These populations were used in the four-state kinetic model in Eqs 7.1-7.7. The solid lines represent the ensemble population average obtained from NAMD of excited electrons. Fitting functions obtained from Eqs 7.1-7.7 are indicated by the filled circles. The dashed lines represent the ensemble average populations obtained from NAMD simulations of excited holes. Fitting functions obtained from Eqs 7.1-7.7 are indicated by the empty circles. The time-dependent ensemble populations were generated by monitoring the populations during the NAMD simulations: Line A is comprised of the initially excited states, line C comprises the first three MOs for occupied and unoccupied orbitals (final state), and line B is the sum of the populations of all other orbitals (intermediate states). Population analysis for PbSe/CdSe (a) and PbS/CdS (b) QDs, with initial conditions including all optical transitions at the investigated energy range. Population analysis for PbSe/CdSe (c) and PbS/CdS (d) QDs, with initial conditions including only hot electron transitions at the investigated energy range. Population analysis for (e) PbSe/CdSe and PbS/CdS (f) QDs, with initial conditions including only hot hole transitions at the investigated energy range.

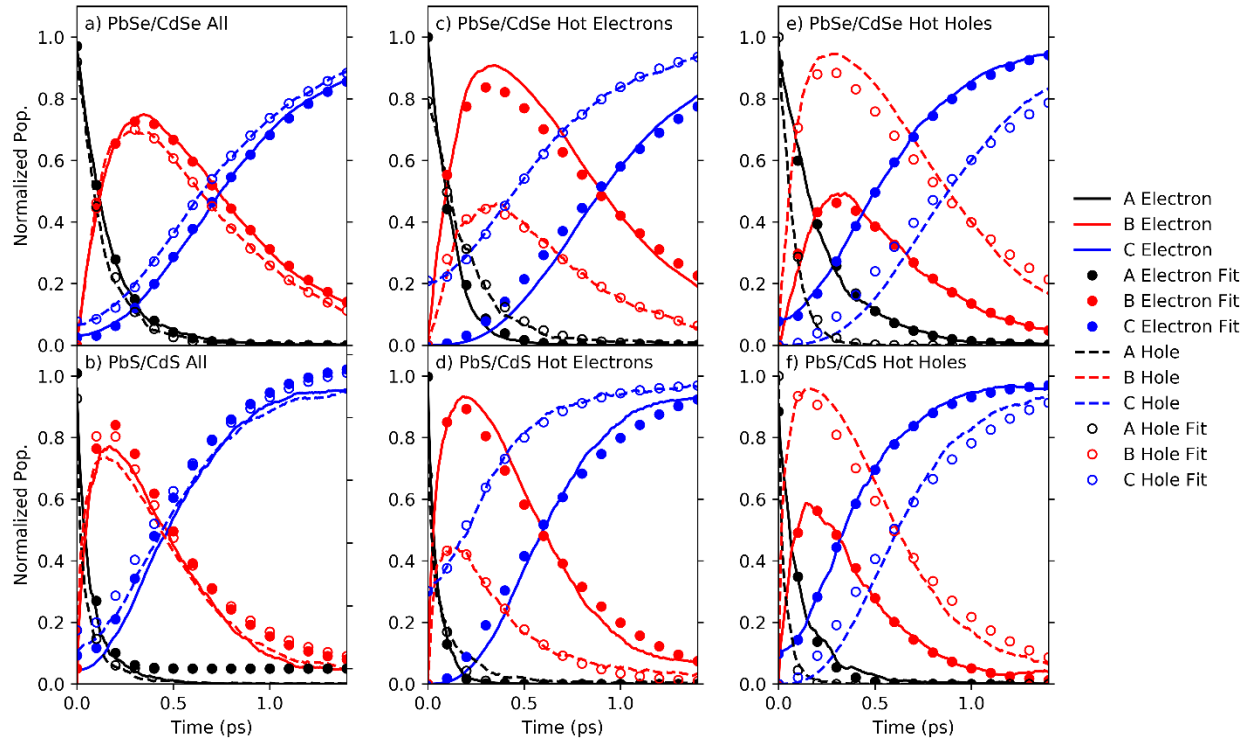


Figure 7.11 Population of the excited state during NAMD excited at  $2.1 \times E_g$  in PbX/CdX QDs, with X=S and Se. These populations were used in the four-state kinetic model in Eqs 7.1-7.7. The solid lines represent the ensemble population average obtained from NAMD of excited electrons. Fitting functions obtained from Eqs 7.1-7.7 are indicated by the filled circles. The dashed lines represent the ensemble average populations obtained from NAMD simulations of excited holes. Fitting functions obtained from Eqs 7.1-7.7 are indicated by the empty circles. The time-dependent ensemble populations were generated by monitoring the populations during the NAMD simulations: Line A is comprised of the initially excited states, line C comprises the first three MOs for occupied and unoccupied orbitals (final state), and line B is the sum of the populations of all other orbitals (intermediate states). Population analysis for PbSe/CdSe (a) and PbS/CdS (b) QDs, with initial conditions including all optical transitions at the investigated energy range. Population analysis for PbSe/CdSe (c) and PbS/CdS (d) QDs, with initial conditions including only hot electron transitions at the investigated energy range. Population analysis for (e) PbSe/CdSe and PbS/CdS (f) QDs, with initial conditions including only hot hole transitions at the investigated energy range.

Table 7.2. Relaxation rates obtained from four-state kinetic model and single exponential fitting. The fitting to the four-state kinetic model shows that relaxation in the PbS/CdS QD is faster than in the PbSe/CdSe QD. The lifetimes found by the single exponential qualitatively agrees with the four-state kinetic model except for hole relaxation at the initial excitation of  $1.6 \times E_g$  with hot electrons. This discrepancy is rationalized by the fact that initial conditions for these simulations have the hole populated very close to the frontier MOs, which results in the initial and the final states being almost the same leading to nearly flat ensemble average energy for the hole.

Initial Excitation	X	$\tau_1$ (ps)	$\tau_2$ (ps)	$\tau_3$ (ps)	$\tau_{int.}$ (ps)	$\tau_{tot.}$ (ps)	$\tau_{SE}$ (ps)	
Electron								
All	$1.6 \times E_g$	Se	0.25	0.37	0.00	0.37	0.62	0.74
		S	0.11	0.27	0.06	0.34	0.45	0.30
	$1.9 \times E_g$	Se	0.17	0.43	0.24	0.67	0.84	0.65
		S	0.08	0.33	0.12	0.45	0.53	0.33
	$2.1 \times E_g$	Se	0.16	0.29	0.42	0.71	0.87	0.64
		S	0.07	0.30	0.18	0.48	0.55	0.33
Hot Electron	$1.6 \times E_g$	Se	0.24	0.30	0.30	0.61	0.84	0.68
		S	0.09	0.24	0.24	0.47	0.56	0.34
	$1.9 \times E_g$	Se	0.13	0.42	0.42	0.85	0.98	0.63
		S	0.06	0.28	0.28	0.57	0.63	0.34
	$2.1 \times E_g$	Se	0.12	0.45	0.45	0.89	1.02	0.62
		S	0.05	0.32	0.32	0.63	0.68	0.34
Hot Hole	$1.6 \times E_g$	Se	0.33	0.19	0.00	0.19	0.53	0.85
		S	0.15	0.21	0.03	0.24	0.39	0.28
	$1.9 \times E_g$	Se	0.27	0.29	0.05	0.35	0.62	0.74
		S	0.12	0.21	0.03	0.24	0.35	0.30
	$2.1 \times E_g$	Se	0.24	0.34	0.06	0.39	0.63	0.69
		S	0.11	0.28	0.05	0.33	0.44	0.33
Hole								
All	$1.6 \times E_g$	Se	0.15	0.26	0.40	0.66	0.81	0.56
		S	0.04	0.29	0.23	0.52	0.56	0.39
	$1.9 \times E_g$	Se	0.15	0.42	0.24	0.65	0.80	0.54
		S	0.05	0.36	0.14	0.50	0.55	0.39
	$2.1 \times E_g$	Se	0.14	0.45	0.22	0.67	0.81	0.52
		S	0.05	0.36	0.17	0.54	0.58	0.38
Hot Electron	$1.6 \times E_g$	Se	0.35	0.27	0.00	0.27	0.62	0.43
		S	0.08	0.19	0.00	0.20	0.28	1.31
	$1.9 \times E_g$	Se	0.29	0.32	0.05	0.37	0.66	0.67
		S	0.08	0.30	0.01	0.31	0.38	0.47
	$2.1 \times E_g$	Se	0.22	0.42	0.06	0.47	0.69	0.55
		S	0.07	0.30	0.01	0.32	0.39	0.43
Hot Hole	$1.6 \times E_g$	Se	0.10	0.37	0.37	0.74	0.83	0.53
		S	0.03	0.28	0.28	0.57	0.60	0.38
	$1.9 \times E_g$	Se	0.08	0.43	0.43	0.85	0.93	0.51
		S	0.03	0.32	0.32	0.64	0.67	0.38
	$2.1 \times E_g$	Se	0.08	0.45	0.45	0.90	0.98	0.51
		S	0.03	0.34	0.34	0.67	0.70	0.39

A lower sensitivity of the relaxation time to the initial excitation energy in PbX/CdX QDs, compared to those in pristine PbX and CdX QDs,<sup>40</sup> is rationalized by the excitation over the interface-associated states for all cases, so that the carriers (especially hot holes) are trapped at the interface states even when excited at lower  $1.6 \times E_g$  energy range. Overall, the

intermediate states associated with the core/shell interface trap the carriers slowing down relaxation and mainly define the overall relaxation time for both QDs, while the phonon couplings with initially excited states govern the difference in relaxation times between PbS/CdS and PbSe/CdSe QDs.

The role of the interface states in slowing charge carrier relaxation is the best seen for the excitation at  $1.6 \times E_g$ , where the asymmetric hot hole optical transitions dominate. For PbSe/CdSe QDs, the average relaxation time of holes is about 1.5 times slower compared to electrons (Table 7.2.), despite three times faster relaxation time of holes than electrons from their initial state (Table 7.2.). The overall slowing of hole cooling is governed by much longer lifetime of their interface-associated intermediate states that is 3-4 times longer than for electrons (Table 7.2.). In contrast, in the pristine PbSe QDs of 1 and 2 nm in size, it was calculated that holes relax faster than electrons with the relaxation time of 0.5 vs 0.8 ps and 0.8 vs 1.4 ps, respectively, depending on the QD size.<sup>40, 43</sup> This difference in relaxation trends between the core/shell and pristine QDs well agrees with experimentally detected dynamics of the shell-associated emissive peak at the visible range of 4 nm PbSe/ CdSe QDs with a thick shell.<sup>1, 3</sup> It was observed that the shell emission lifetime is controlled by relaxation of a shell-localized hole resulting in noticeably longer (6-10 ps) hole cooling,<sup>1</sup> compared to those in the core-only PbSe QDs excited at the same energy range (0.25-2.6 ps).<sup>44</sup> Note that the smaller size of our computational QD models results in a strong confinement effect. The confinement enhances tunneling of the wave functions at the interface leading to a higher degree of delocalization between the core and shell orbitals, in contrast to stronger localization of hole states at the thicker shell in larger PbSe/CdSe QDs used in experiments.<sup>1, 3</sup> Such a delocalization of the core-shell orbitals increases nonadiabatic

couplings and speeds up relaxation rates in small QDs with a thin shell, compared to QDs with the shell larger than 2 nm.

Figure 7.12. shows the spectra of phonons coupled to various hole and electron states, as obtained from fast Fourier transform (FFT) of the electronic states evolving along the adiabatic trajectories. In both QDs, the initially excited electron (dashed red lines in Figure 7.12.c and d) and hole states (dashed black lines in Figure 7.12.c and d) are coupled to similar phonons, with the largest contribution from acoustic phonons having frequencies less than  $100 \text{ cm}^{-1}$ . Strong couplings to acoustic phonons in  $\text{PbS}^{45}$  and  $\text{CdSe}^{46}$  QDs have been experimentally confirmed by low-temperature spectroscopy. Our calculations show that these lower frequency phonons are mainly associated with Pb-Pb, Cd-Pb, and Cd-Cd vibrations. The nature of these vibrations is depicted in Figure 7.13, showing the phonon frequencies associated with the thermal motion of the pairs of nearest atoms in QDs. Despite more pronounced couplings to slightly lower frequency acoustic phonons ( $25\text{-}40 \text{ cm}^{-1}$ ) of hot electrons, compared to hot holes ( $60\text{-}80 \text{ cm}^{-1}$ ) in the PbS/CdS QD, the nature of these phonons is similar, demonstrating strong couplings of both hot electrons and hot holes to the surface (Cd-Cd) and interfacial (Cd-Pb) vibrations for both QDs. However, the overall phonon spectra contributing to hot carrier dynamics are much broader having higher intensity for the PbS/CdS QD, compared to those of the PbSe/CdSe QD. As such, more acoustic phonons at the various frequencies and with higher NA couplings are available to mediate depopulation of the initially excited state of the PbS/CdS QD, rationalizing much faster relaxation rates of the initial states in the PbS/CdS QDs than in the PbSe/CdSe QD.



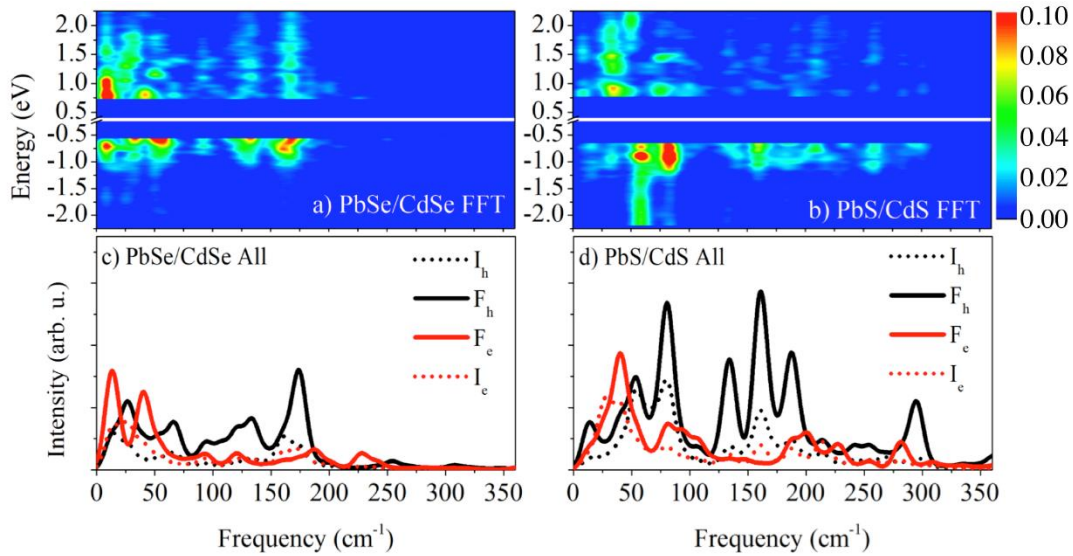


Figure 7.12. Electron-phonon couplings contributing from various electron and hole states involved in NAMD simulations of PbX/CdX QDs. The Fourier Transform (FT) of the electronic states evolving along the adiabatic trajectory as a function of the phonon frequency of PbSe/CdSe (a) and PbS/CdS (b) QDs, varying from blue (minimum) to red (maximum) according to the rainbow color scheme. FT data averaged over the final (solid lines) and initial (dotted lines) electron (red) and hole states (black) excited at  $2.1 \times E_g$  in PbSe/CdSe (c) and PbS/CdS (d) QDs. The values of electron-phonon couplings of PbSe/CdSe QDs are multiplied by 2 for better comparison to those of PbS/CdS QDs.

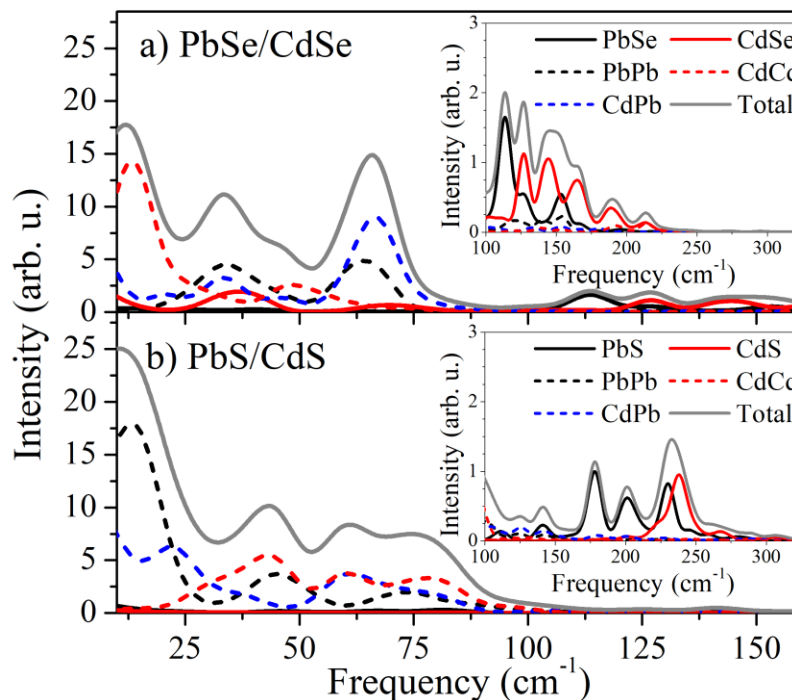


Figure 7.13. Vibrational spectrum for PbSe/CdSe (a) and PbS/CdS (b) QDs decomposed over the contributions of various atom-atom pairs. The low frequency portion of the vibration spectra are dominated by the vibrations between pairs of metals, whereas the high frequency portion originates from the vibration of metal chalcogenides pairs associated with optical phonons.

In both QDs, the initially excited electron and hole states demonstrate weak, but noticeable couplings to phonons at the range of 150-200  $\text{cm}^{-1}$ , which are more pronounced for hot electrons than for hot holes, Figures 7.13.a and b and S11. These frequencies are mainly associated with the core Pb-S vibrations in the PbS/CdS QD, Figure 7.13.b inset. In contrast, both core Pb-Se ( $\sim 160 \text{ cm}^{-1}$ ) and shell Cd-Se ( $\sim 180 \text{ cm}^{-1}$ ) vibrations contribute at this frequency range in the PbSe/CdSe QD, Figure 7.14.a, inset. However, for PbS/CdS QD, optical phonons with frequencies higher than 200  $\text{cm}^{-1}$  also contribute to dynamics of hot electrons, Figure 7.12.b and d. These high frequency phonons mainly originate from shell-associated vibrations (Cd-Se bond stretching, Figure 7.13.b). As such, both QDs exhibit some contributions of both core- and shell-originated phonons to the dynamics of excited states. However, in the case of holes, these phonons mainly contribute to the states closer to the energy gap with the energy  $< -1.2 \text{ eV}$  (after the edge between green and purple shaded areas in Figure 7.1c).

It is important to note that the density of states of cold holes ( $E_h < -1.2 \text{ eV}$ ) is lower, compared to hot holes (Figure 7.4. and 7.5.). This means that the energy splitting between nearest states is increasing, so that only higher energy phonons can contribute to hole jumps between these states. Negligibly weak couplings of holes at the energy of  $\sim -1.2 \text{ eV}$  with high frequency phonons ( $> 100 \text{ cm}^{-1}$ ) explains the appearance of the long-living intermediate states associated with the core/shell interface that traps holes and significantly slows down relaxation rates in both systems. On the other side, contributions of high frequency optical phonons<sup>47</sup> ( $> 200 \text{ cm}^{-1}$ ) to relaxation of both hot and cold electrons in the PbS/ CdS QD, which are not available in the PbSe/CdSe QD,<sup>46</sup> rationalize almost twice faster relaxation time of electrons in the PbS/CdS QD.

For both QDs, the final electron and hole states at the edges of the bandgap exhibit noticeable couplings not only to acoustic phonons, but also to higher energy optical phonons, with the mainly core contributions at 100-170  $\text{cm}^{-1}$  (Pb-Se) and 130-180  $\text{cm}^{-1}$  (Pb-S) and the dominant shell contributions at frequencies  $>180 \text{ cm}^{-1}$  (Cd-Se) and  $>240 \text{ cm}^{-1}$  (Cd-S). More pronounced contributions of bulk-like optical phonons to the final electron/hole states is rationalized by stronger localization of their orbitals at the inner part of the QD, compared to more delocalized nature of hot charge carriers. In PbS/CdS QDs, couplings to much higher frequency optical phonons of electronic states nearer to the energy gap, where states are more discrete, provides faster charge carrier relaxation to the final state compared to those of PbSe/CdSe QDs rationalizing about twice faster relaxation rates in PbS/CdS systems.

Experiments show lower CM yields in PbS than in PbSe QDs of similar energy gaps.<sup>9</sup> This is an indication of a difference in the competing energy relaxation channels, such as phonon-mediated relaxation, that favors CM in PbSe QDs.<sup>9</sup> These measurements have estimated more than twice as large energy loss rate due to phonon emission in PbS than in PbSe that is translated into an approximately 2-fold reduction in the CM yield in PbS compared to PbSe, despite very similar biexciton lifetimes as a function of confinement energy in both nanomaterials. Our computational results well explain the difference in the CM yield between these two nanomaterials, while also confirm that the trend is not changed in the PbX/ CdX core/shell structures.

### **7.3. Conclusion**

In summary, our simulations reveal that despite many similarities in both electronic structure and phonon spectra of PbSe/CdSe and PbS/CdS QDs, rates of charge carrier relaxation differ greatly in these systems, with about twice faster energy relaxation in the PbS/CdS, than in

the PbSe/ CdSe QDs. In contrast to the state-to-state character of photoexcited relaxation in pristine PbX and CdX QDs, the intermediate states play a key role in relaxation dynamics in the core/shell QDs. As such, a simple exponential model is not a good approximation for relaxation of the excitation in the core/shell structures and the four-state irreversible kinetic model is suggested instead. Negligibly small couplings of hot holes originated from the interface states to the core-originated high frequency phonons ( $>100\text{ cm}^{-1}$ ) explain appearance of the long-living intermediate states that trap holes and slow down their relaxation rates for both QDs. On the other hand, strong couplings of high frequency optical phonons ( $>200\text{ cm}^{-1}$ ) to cold holes and both to hot and cold electrons in the PbS/CdS QD, which are not available in the PbSe/CdSe QD, rationalize almost twice-faster relaxation time of carriers in the PbS/CdS ( $\sim 0.5\text{ ps}$ ) than in PbSe/CdSe ( $\sim 0.9\text{ ps}$ ) QDs. These findings well agree with strikingly lower carrier multiplication yields experimentally observed in pristine PbS QDs than those in PbSe QDs, rationalized by competing energy-loss processes governed by stronger electron-phonon couplings in PbS compared to PbSe nanomaterials.<sup>9</sup> Our calculations confirm that this trend is not changed in the core/shell structures. Similar to the pristine QDs,<sup>48</sup> a high degree of the confinement in the modeled core/shell QDs enhances electron delocalization over the core and the shell raising electron couplings to phonons and, thus, suppressing the phonon bottleneck. Nonetheless, our results imply that even at a monolayer-shell and a 1 nm core, the PdSe/CdSe QD exhibits  $\sim 1\text{ ps}$  rates of carrier cooling with the overall energy dissipation slowing to a higher degree compared to the PbS/CdS QDs. Thus, PbSe/ CdSe QDs provide conditions allowing for CM to outpace energy dissipation and positively contribute to the PV efficiency.

## 7.4. References

1. Cirloganu, C. M.; Padilha, L. A.; Lin, Q.; Makarov, N. S.; Velizhanin, K. A.; Luo, H.; Robel, I.; Pietryga, J. M.; Klimov, V. I., Enhanced carrier multiplication in engineered quasi-type-II quantum dots. *Nat. Commun.* **2014**, *5* (1), 1-8.
2. Garcí'a-Santamarí'a, F.; Chen, Y.; Vela, J.; Schaller, R. D.; Hollingsworth, J. A.; Klimov, V. I., Suppressed Auger Recombination in Giant Nanocrystals Boosts Optical Gain Performance. *Nano Lett.* **2009**, 3482-3488.
3. Lin, Q.; Makarov, N. S.; Koh, W. K.; Velizhanin, K. A.; Cirloganu, C. M.; Luo, H.; Klimov, V. I.; Pietryga, J. M., Design and synthesis of heterostructured quantum dots with dual emission in the visible and infrared. *ACS Nano* **2015**, *9* (1), 539-47.
4. Piryatinski, A.; Ivanov, S. A.; Tretiak, S.; Klimov, V. I., Effect of quantum and dielectric confinement on the exciton– exciton interaction energy in type II core/shell semiconductor nanocrystals. *Nano Lett.* **2007**, *7* (1), 108-115.
5. Stewart, J. T.; Padilha, L. A.; Bae, W. K.; Koh, W.-K.; Pietryga, J. M.; Klimov, V. I., Carrier multiplication in quantum dots within the framework of two competing energy relaxation mechanisms. *J. Phys. Chem. Lett.* **2013**, *4* (12), 2061-2068.
6. Nootz, G.; Padilha, L. A.; Levina, L.; Sukhovatkin, V.; Webster, S.; Brzozowski, L.; Sargent, E. H.; Hagan, D. J.; Van Stryland, E. W., Size dependence of carrier dynamics and carrier multiplication in PbS quantum dots. *Phys. Rev. B* **2011**, *83* (15), 155302.
7. Midgett, A. G.; Luther, J. M.; Stewart, J. T.; Smith, D. K.; Padilha, L. A.; Klimov, V. I.; Nozik, A. J.; Beard, M. C., Size and Composition Dependent Multiple Exciton Generation Efficiency in PbS, PbSe, and PbS x Se<sub>1-x</sub> Alloyed Quantum Dots. *Nano Lett.* **2013**, *13* (7), 3078-3085.
8. Padilha, L. A.; Stewart, J. T.; Sandberg, R. L.; Bae, W. K.; Koh, W.-K.; Pietryga, J. M.; Klimov, V. I., Aspect ratio dependence of auger recombination and carrier multiplication in PbSe nanorods. *Nano Lett.* **2013**, *13* (3), 1092-1099.
9. Stewart, J. T.; Padilha, L. A.; Qazilbash, M. M.; Pietryga, J. M.; Midgett, A. G.; Luther, J. M.; Beard, M. C.; Nozik, A. J.; Klimov, V. I., Comparison of carrier multiplication yields in PbS and PbSe nanocrystals: the role of competing energy-loss processes. *Nano Lett.* **2012**, *12* (2), 622-628.
10. Zhao, H.; Chaker, M.; Wu, N.; Ma, D., Towards controlled synthesis and better understanding of highly luminescent PbS/CdS core/shell quantum dots. *J. Mater. Chem.* **2011**, *21* (24), 8898-8904.
11. Chen, Y.; Vela, J.; Htoon, H.; Casson, J. L.; Werder, D. J.; Bussian, D. A.; Klimov, V. I.; Hollingsworth, J. A., “Giant” multishell CdSe nanocrystal quantum dots with suppressed blinking. *J. Am. Chem. Soc.* **2008**, *130* (15), 5026-5027.
12. Moreels, I.; Lambert, K.; De Muynck, D.; Vanhaecke, F.; Poelman, D.; Martins, J. C.; Allan, G.; Hens, Z., Composition and size-dependent extinction coefficient of colloidal PbSe quantum dots. *Chem. Mater.* **2007**, *19* (25), 6101-6106.
13. Resch-Genger, U.; Grabolle, M.; Cavaliere-Jaricot, S.; Nitschke, R.; Nann, T., Quantum dots versus organic dyes as fluorescent labels. *Nat. Methods* **2008**, *5* (9), 763.
14. Larson, D. R.; Zipfel, W. R.; Williams, R. M.; Clark, S. W.; Bruchez, M. P.; Wise, F. W.; Webb, W. W., Water-soluble quantum dots for multiphoton fluorescence imaging in vivo. *Science* **2003**, *300* (5624), 1434-1436.

15. Shockley, W.; Queisser, H. J., Detailed balance limit of efficiency of p-n junction solar cells. *J. Appl. Phys.* **1961**, *32* (3), 510-519.
16. Hanna, M.; Nozik, A., Solar conversion efficiency of photovoltaic and photoelectrolysis cells with carrier multiplication absorbers. *J. Appl. Phys.* **2006**, *100* (7), 074510.
17. Kilina, S.; Kilin, D.; Tretiak, S., Light-driven and phonon-assisted dynamics in organic and semiconductor nanostructures. *Chem. Rev.* **2015**, *115* (12), 5929-5978.
18. Tan, L.; Li, P.; Sun, B.; Chaker, M.; Ma, D., Stabilities related to near-infrared quantum dot-based solar cells: the role of surface engineering. *ACS Energy Lett.* **2017**, *2* (7), 1573-1585.
19. García-Santamaría, F.; Chen, Y.; Vela, J.; Schaller, R. D.; Hollingsworth, J. A.; Klimov, V. I., Suppressed Auger recombination in “giant” nanocrystals boosts optical gain performance. *Nano Lett.* **2009**, *9* (10), 3482-3488.
20. Kim, S.; Fisher, B.; Eisler, H.-J.; Bawendi, M., Type-II quantum dots: CdTe/CdSe (core/shell) and CdSe/ZnTe (core/shell) heterostructures. *J. Am. Chem. Soc.* **2003**, *125* (38), 11466-11467.
21. Lin, Q.; Makarov, N. S.; Koh, W.-k.; Velizhanin, K. A.; Cirloganu, C. M.; Luo, H.; Klimov, V. I.; Pietryga, J. M., Design and synthesis of heterostructured quantum dots with dual emission in the visible and infrared. *ACS Nano* **2014**, *9* (1), 539-547.
22. Kilina, S. V.; Tamukong, P. K.; Kilin, D. S., Surface Chemistry of Semiconducting Quantum Dots: Theoretical Perspectives. *Acc. Chem. Res.* **2016**, *49* (10), 2127-2135.
23. Kilina, S. V.; Neukirch, A. J.; Habenicht, B. F.; Kilin, D. S.; Prezhdo, O. V., Quantum zeno effect rationalizes the phonon bottleneck in semiconductor quantum dots. *Phys. Rev. Lett.* **2013**, *110* (18), 180404.
24. Kilin, D. S.; Tsemekhman, K.; Prezhdo, O. V.; Zenkevich, E. I.; von Borczyskowski, C., Ab initio study of exciton transfer dynamics from a core-shell semiconductor quantum dot to a porphyrin-sensitizer. *J. Photochem. Photobiol. A* **2007**, *190* (2-3), 342-351.
25. Cui, X.; Wang, X.; Yang, F.; Cui, Y.; Yang, M., Shell effect on the electron and hole reorganization energy of core-shell II-VI nanoclusters. *Chem. Phys.* **2017**, *494*, 72-77.
26. Kocovski, V.; Eriksson, O.; Gerard, C.; Sarma, D.; Rusz, J., Influence of dimensionality and interface type on optical and electronic properties of CdS/ZnS core-shell nanocrystals—A first-principles study. *J. Chem. Phys.* **2015**, *143* (16), 164701.
27. Giberti, F.; Vörös, M. r.; Galli, G., Design of heterogeneous chalcogenide nanostructures with pressure-tunable gaps and without electronic trap states. *Nano Lett.* **2017**, *17* (4), 2547-2553.
28. Sowers, K. L.; Hou, Z.; Peterson, J. J.; Swartz, B.; Pal, S.; Prezhdo, O.; Krauss, T. D., Photophysical properties of CdSe/CdS core/shell quantum dots with tunable surface composition. *Chem. Phys.* **2016**, *471*, 24-31.
29. Mahboub, M.; Xia, P.; Van Baren, J.; Li, X.; Lui, C. H.; Tang, M. L., Midgap States in PbS Quantum Dots Induced by Cd and Zn Enhance Photon Upconversion. *ACS Energy Lett.* **2018**, *3* (4), 767-772.
30. Albert, V. V.; Ivanov, S. A.; Tretiak, S.; Kilina, S. V., Electronic structure of ligated CdSe clusters: Dependence on dft methodology. *J. Phys. Chem. C* **2011**, *115* (32), 15793-15800.
31. Janesko, B. G.; Henderson, T. M.; Scuseria, G. E., Screened hybrid density functionals for solid-state chemistry and physics. *Phys. Chem. Chem. Phys.* **2009**, *11* (3), 443-454.

32. Cui, P.; Javed, M.; Vogel, D. J.; Kilina, S., Phonon-Mediated Ultrafast Hole Transfer from Photoexcited CdSe Quantum Dots to Black Dye. In *Computational Photocatalysis: Modeling of Photophysics and Photochemistry at Interfaces*, American Chemical Society: 2019; Vol. 1331, pp 137-156.
33. Kilina, S.; Velizhanin, K. A.; Ivanov, S.; Prezhdo, O. V.; Tretiak, S., Surface Ligands Increase Photoexcitation Relaxation Rates in CdSe Quantum Dots. *ACS Nano* **2012**, *6* (7), 6515-6524.
34. Perdew, J., Electronic Structure of Solids' 91, edited by Ziesche, P. and Eschrig, H.(Berlin: Akademie-Verlag) p. 11; Perdew, JP and Wang, Y., 1992. *Phys. Rev. B* **1991**, *45* (13), 244.
35. Krukau, A. V.; Vydrov, O. A.; Izmaylov, A. F.; Scuseria, G. E., Influence of the exchange screening parameter on the performance of screened hybrid functionals. *J. Chem. Phys.* **2006**, *125* (22), 224106.
36. Liljeroth, P.; van Emmichoven, P. A. Z.; Hickey, S. G.; Weller, H.; Grandidier, B.; Allan, G.; Vanmaekelbergh, D., Density of states measured by scanning-tunneling spectroscopy sheds new light on the optical transitions in PbSe nanocrystals. *Phys. Rev. Lett.* **2005**, *95* (8), 086801.
37. Wise, F. W., Lead salt quantum dots: the limit of strong quantum confinement. *Acc. Chem. Res.* **2000**, *33* (11), 773-780.
38. Peterson, J. J.; Huang, L.; Delerue, C.; Allan, G.; Krauss, T. D., Uncovering forbidden optical transitions in PbSe nanocrystals. *Nano Lett.* **2007**, *7* (12), 3827-3831.
39. Trinh, M. T.; Sfeir, M. Y.; Choi, J. J.; Owen, J. S.; Zhu, X., A hot electron-hole pair breaks the symmetry of a semiconductor quantum dot. *Nano Lett.* **2013**, *13* (12), 6091-6097.
40. Kilina, S. V.; Kilin, D. S.; Prezhdo, V. V.; Prezhdo, O. V., Theoretical study of electron-phonon relaxation in PbSe and CdSe quantum dots: evidence for phonon memory. *J. Phys. Chem. C* **2011**, *115* (44), 21641-21651.
41. Lystrom, L.; Zhang, Y.; Tretiak, S.; Nelson, T., Site-Specific Photodecomposition in Conjugated Energetic Materials. *J. Phys. Chem. A* **2018**, *122* (29), 6055-6061.
42. Bricker, W. P.; Shenai, P. M.; Ghosh, A.; Liu, Z.; Enriquez, M. G. M.; Lambrev, P. H.; Tan, H.-S.; Lo, C. S.; Tretiak, S.; Fernandez-Alberti, S., Non-radiative relaxation of photoexcited chlorophylls: theoretical and experimental study. *Sci. Rep.* **2015**, *5*, 13625.
43. Kilina, S. V.; Craig, C. F.; Kilin, D. S.; Prezhdo, O. V., Ab initio time-domain study of phonon-assisted relaxation of charge carriers in a PbSe quantum dot. *J. Phys. Chem. C* **2007**, *111* (12), 4871-4878.
44. Schaller, R. D.; Pietryga, J. M.; Goupalov, S. V.; Petruska, M. A.; Ivanov, S. A.; Klimov, V. I., Breaking the phonon bottleneck in semiconductor nanocrystals via multiphonon emission induced by intrinsic nonadiabatic interactions. *Phys. Rev. Lett.* **2005**, *95* (19), 196401.
45. Krauss, T. D.; Wise, F. W., Coherent acoustic phonons in a semiconductor quantum dot. *Phys. Rev. Lett.* **1997**, *79* (25), 5102-5105.
46. Baker, J. A.; Kelley, D. F.; Kelley, A. M., Resonance Raman and photoluminescence excitation profiles and excited-state dynamics in CdSe nanocrystals. *J. Chem. Phys.* **2013**, *139* (2), 024702-1-12.
47. Krauss, T. D.; Wise, F. W., Raman-scattering study of exciton-phonon coupling in PbS nanocrystals. *Phys. Rev. B* **1997**, *55* (15), 9860-9865.

48. Kilina, S. V.; Kilin, D. S.; Prezhdo, O. V., Breaking the phonon bottleneck in PbSe and CdSe quantum dots: time-domain density functional theory of charge carrier relaxation. *ACS Nano* **2009**, 3 (1), 93-99.



## 8. CONCLUSION

In this work, computational methods were employed to provide atomic level insight for several open research questions on the effect of surface passivation by organic and inorganic ligands on II-VI and IV-II QDs. We focused on questions related to the photophysical properties of these QDs for LED and PV applications.

We first investigated whether the decomposition products of DMPTC interact with the surface of CdSe QDs. It is known that DMPTC decomposes in protic solvents such as methanol, methanol is used to precipitate the QDs during the ligand exchange process. We found that simplifying the DMPTC ligand by VTC ligands provides reasonable agreement for the  $B_e$  and electron distribution. This simplification reduces the computational cost, making it possible to simulate full surface passivation by VTC. Our calculations show that when  $VTC^-$  fully passivates the surface of non-stoichiometric QDs it strongly binds whereas,  $VTC^-$  does not bind to the surface of stoichiometric QDs due to strong electrostatic repulsion. The products of decomposition such as DMA and TEA do bind to the surface of stoichiometric QDs. This implies that the surface would be partially passivated by DMA and/or TEA. This is a novel discovery because the conventional picture of ligand exchange is mass-action picture.<sup>1</sup> This research shines the light on how simplify the ligand exchange of DMPTC, yielding exchange of “native” ligands with only the ligands of interest.

Next, we investigated the mechanism of the QY of PL enhancement by  $H^-$  treatment that results in approximately a 55 times increase in QY of PL of CdS QDs.<sup>2</sup> In this work, we found that  $H^-$  interacts with the surface of the QD in two scenarios: 1) removing surface  $Se^{2-}$  2) capping dangling bonds of surface  $Cd^{2+}$ . Surface  $Se^{2-}$  are removed by the formation of  $H_2Se$  gas, which eliminates trap states localized around surface  $Se^{2-}$ . This effectively produces Cd-rich surfaces

that then  $H^-$  can passivate the surface leading to the enhancement of PL. From our calculations, the emissive state oscillator strength only increased by a factor of 2 not order of magnitude as seen in experimental studies.<sup>2-4</sup> However, we have compared QDs with ideal surface passivation, where in experimental samples it is likely that the pre-treated QDs have non-ideal surfaces which result in optically inactive QDs.  $H^-$  treatment results, in making these optically inactive QDs optically active, which our comparison would not capture since our  $H^-$  pretreated models are already have optically active transitions. This justifies our predicted mechanism of PL enhancement by  $H^-$  treatment.

The cause of the irreversible photo-thermal bleaching of HTCI core/shell QDs was investigated. From experimental work, the cause of the bleaching of HTCI is unknown.<sup>5</sup> We hypothesize that thiol ligand passivating the surface of HTCI core/shell QDs are responsible for the photo-thermal bleaching because SILAR core/shell QDs only photo-thermal bleach after protracted exposure to high influence of light and high temperatures.<sup>5</sup> The thiol ligands can undergo deprotonation resulting in thiolate ligands passivating the surface of the QD. We found that the formation of thiolate ligands results in ligand-based trap states that are thermodynamically more stable compared to thiol. Thus, the formation of thiolate during the heating and irradiation of the QDs would result in trap states that are irreversibly formed resulting in irreversible photo-thermal bleaching of HTCI core/shell QDs.

Finally, we investigated whether the interfacial associated states are responsible for the reduced relaxation rates of the charge carriers in  $PbX/CdX$ ,  $X = S$  or  $Se$ , core/shell QDs. This reduction in relaxation was proposed to make CM outcompete charge carrier cooling which could result in more efficient solar cells.<sup>6-10</sup> From our NAMD simulations, the interfacial associated states dramatically increase the excited state lifetimes, reducing the relaxation rate for

the hole. Comparing PbS/CdS to PbSe/CdSe core/shell QDs, we found that the heavier PbSe/CdSe relax upwards of 2 times slower compared the lighter PbS/CdS. Thus, PbS/CdS core/shell QDs are less likely to undergo CM compared to PbSe/CdSe core/shell QDs. Overall, our studies have demonstrated that DFT-based simulations are reliable tools for providing important insights into mechanism of photoexcited process taking place at the organic-inorganic surfaces and interfaces in nanomaterials that complement experimental findings.

### 8.1. References

1. Anderson, N. C.; Hendricks, M. P.; Choi, J. J.; Owen, J. S. Ligand exchange and the stoichiometry of metal chalcogenide nanocrystals: spectroscopic observation of facile metal-carboxylate displacement and binding. *J. Am. Chem. Soc.* **2013**, *135* (49), 18536-18548.
2. Jang, E.; Jun, S.; Chung, Y.; Pu, L. Surface treatment to enhance the quantum efficiency of semiconductor nanocrystals. *J. Phys. Chem. B* **2004**, *108* (15), 4597-4600.
3. Subila, K.; Kishore Kumar, G.; Shivaprasad, S.; George Thomas, K. Luminescence properties of CdSe quantum dots: role of crystal structure and surface composition. *J. Phys. Chem. Lett.* **2013**, *4* (16), 2774-2779.
4. Tsui, E. Y.; Hartstein, K. H.; Gamelin, D. R. Selenium Redox Reactivity on Colloidal CdSe Quantum Dot Surfaces. *J. Am. Chem. Soc.* **2016**, *138* (35), 11105-11108.
5. Orfield, N. J.; Majumder, S.; McBride, J. R.; Yik-Ching Koh, F.; Singh, A.; Bouquin, S. J.; Casson, J. L.; Johnson, A. D.; Sun, L.; Li, X. Photophysics of thermally-assisted photobleaching in “giant” quantum dots revealed in single nanocrystals. *ACS Nano* **2018**, *12* (5), 4206-4217.
6. Cirloganu, C. M.; Padilha, L. A.; Lin, Q.; Makarov, N. S.; Velizhanin, K. A.; Luo, H.; Robel, I.; Pietryga, J. M.; Klimov, V. I. Enhanced carrier multiplication in engineered quasi-type-II quantum dots. *Nat. Commun.* **2014**, *5* (1), 1-8.
7. Garcí'a-Santamarí'a, F.; Chen, Y.; Vela, J.; Schaller, R. D.; Hollingsworth, J. A.; Klimov, V. I. Suppressed Auger Recombination in Giant Nanocrystals Boosts Optical Gain Performance. *Nano Lett.* **2009**, 3482-3488.
8. Midgett, A. G.; Luther, J. M.; Stewart, J. T.; Smith, D. K.; Padilha, L. A.; Klimov, V. I.; Nozik, A. J.; Beard, M. C. Size and Composition Dependent Multiple Exciton Generation Efficiency in PbS, PbSe, and PbS x Se1-x Alloyed Quantum Dots. *Nano Lett.* **2013**, *13* (7), 3078-3085.
9. Stewart, J. T.; Padilha, L. A.; Bae, W. K.; Koh, W.-K.; Pietryga, J. M.; Klimov, V. I. Carrier multiplication in quantum dots within the framework of two competing energy relaxation mechanisms. *J. Phys. Chem. Lett.* **2013**, *4* (12), 2061-2068.
10. Zhang, J.; Gao, J.; Church, C. P.; Miller, E. M.; Luther, J. M.; Klimov, V. I.; Beard, M. C. PbSe quantum dot solar cells with more than 6% efficiency fabricated in ambient atmosphere. *Nano Lett.* **2014**, *14* (10), 6010-6015.